Collision geometry and event plane dependence of two particle correlations in $\sqrt{s_{\mathrm{NN}}} = 200$ GeV Au+Au collisions at RHIC-STAR

Ryo AOYAMA

February 2019

Collision geometry and event plane dependence of two particle correlations in $\sqrt{s_{\mathrm{NN}}} = 200$ GeV Au+Au collisions at RHIC-STAR

Ryo AOYAMA

Doctoral Program in Physics

Submitted to the Graduate School of
Pure and Applied Sciences
in Partial Fullfillment of the Requirements
for the Degree of Doctor Philosophy in
Science

at the
University of Tsukuba

abstract

Protons and neutrons which are the constituent of atoms are composed of quarks and gluons, fundamental elements of nuclear matter. Quarks and gluons are confined in the hadrons by the strong interaction and they cannot live apart. However, at the extremely high temperature and density, quarks and gluons (partons) are de-confined from a hadron and fly freely like a plasma. The new state is called Quark-Gluon Plasma (QGP). QGP is expected to exist in the early stage of universe or high-density neutron star. Therefore, it is important to understand the properties of QGP because it is a clue to understand the properties of early stage of the universe or neutron star. Experimentally, relativistic heavy-ion collisions is a unique tool to create QGP on earth.

Partons can scatter with large momentum transfer in the early stage of high-energy nuclear collisions. The hard scattered partons are created back-to-back and fragment into di-jet pairs. The partons lose their energies in the hot and dense matter and observed as jets. Thus, jets are a good probe to study energy-loss mechanisms of hard-scattered partons in the QGP. Two-particle correlations with high-p_T particles as proxies for the jets are established-robust method to investigate energy loss of jets. The effect of partonic energy loss has been observed for residual high-p_T correlated yield after background subtraction in central collisions. On the other hand, correlation shapes with intermediate-p_T particles in heavy-ion collisions are rather modified compared with p+p collisions; near-side correlation shapes are broadened into longitudinal direction and away-side structures are double peaked.

Two-particle correlations with trigger angle ϕ_s selections with respect to the second-order event plane lead to difference of path length in the medium. Path-length dependent suppression of high-p_T correlated yield and modification of correlation shapes with intermediate-p_T particles are observed with event-plane dependent correlations in 20-60 % centrality by the previous study at RHIC. Especially for intermediate-p_T correlations, double-peaked structures have been observed with mid-plane to out-of-plane trigger selections even after v_2, v_3 and v_4 contributions are subtracted by the STAR experiment.

In this thesis, two-particle correlations with trigger angle selections with respect to the second-order event plane have been performed in $\sqrt{s_{\mathrm{NN}}} = 200$ GeV Au+Au collision data taken by the RHIC-STAR experiment. Difference of correlation shapes between in-plane and out-of-plane is enhanced in mid-central collisions compared with central and peripheral collisions where the difference of path length is large. The integrated yields are small at mid-plane triggers and are large at out-of-plane trigger, which is observed with lower trigger and associate p_T from central to mid-central collisions. With selecting higher associate p_T in mid-central to peripheral collisions, the integrated

yields increase with long path length, which indicates the contribution of re-distribution is dominant in this region. The integrated yields with selecting higher associate p_T are enhanced with long path length, which indicates the contribution of re-distribution is dominant. Integrated yields are plotted as a function of simple path length calculated by Glauber Monte-Carlo. The integrated yields do not scale well in 0.5-2 GeV/c associate p_T, while the integrated yields scale in 2-4 GeV/c associate p_T comapred with lower associate p_T. This is because path-length dependent enhancement or suppression cannot be described by simple path length in lower associate p_T. The azimuthal anisotropy of integrated yield have been calculated and compared with that of single particle. The $v_2^{Y,corr}$ and $v_4^{Y,corr}$ decrease with increasing p_T^a, The $v_2^{Y,corr}$ are larger than single particle v_2 with 0.5-2 (GeV/c) p_T on the near side for all centrality bins, and they are also larger than single particle v_2 in 2-4 (GeV/c) p_T from central to mid-central collisions. The $v_2^{Y,corr}$ increases with increasing p_T^a with 2-4 (GeV/c) trigger particles on the away side in mid-central collisions. Near-side peaks with two in-plane trigger bins shift to in-plane direction. This result support the view that jets emitted from the short path-length direction with less energy loss. Near-side peaks with out-of-plane lower p_T trigger particles shift to out-of-plane trigger direction. This result suggests that low-p_T particles emitted from the long path-length direction are associated with energy re-distributed particles. Away side yield with higher trigger and associate particles composing jets are emitted more towards shorter path length direction. In addition, azimuthal correlations are compared with AMPT model with including string melting and quenching model and the roughly reproduce the away-side shape of the experimental data from mid-central to peripheral collisions. However, near-side peak in AMPT is much smaller than real data.

As a new approach of event selections to determine the collision geometry, the length of flow vector q_2 which is proportional to v_2 are selected and the measurement of two-particle correlations has been performed. In the real experiment, participant eccentricity cannot be directly selected, and thus the length of flow vectors have been used to restrict the initial eccentricity. The v_2 increases linearly with increasing q_2 in all centrality bins, and therefore q_2 selections works as global event characterization. Correlation shapes are modified by trigger angle ϕ_s and q_2 selections in mid-central collisions especially for in-plane and out-of-plane trigger bins. The q_2 dependence of integrated yield is observed for in-plane and out-of-plane trigger slices where the difference of path length is caused by q_2 selections; the integrated yields are enhanced with increasing q_2, which means that the integrated yield of the out-of-plane trigger is enhanced with increasing path length and the integrated yield of the in-plane trigger is enhanced with decreasing path length. While the integrated yield are suppressed with increasing ϕ_s (corresponding to increasing path length), the yield in the in-plane trigger slice are suppressed with increasing path length and the yield in the out-of-plane trigger slice are enhanced with increasing path length. This observation could be interpreted as follows: the effect of jet penetration is dominant in the in-plane direction, and the effect of energy re-distribution is dominant in the out-of-plane direction. Therefore, collective expansion could be thought to have effect on the jet-like particle productions.

We point out that correlated yield cannot scale with simple path length and collective expansion could be thought to have effect on the jet-like particle productions.

Contents

List of Figures

List of Tables

Acknowledgements

First of all, I would like to express my gratitude to Prof. Y. Miake for giving me an opportunity to study in the field of heavy-ion physics and to gave me a critical comments for my study. I would like to really appreciated Prof. S. Esumi. His invitation led me to this field and his encouragement led me to doctoral course. I learned many things from him, heavy-ion physics, analysis techniques and experiment. My study was improved by his diverse perspectives on physics. I cannot thank him too much. I appreciate Prof. T. Chujo for his useful advice and comments. I would like to express my gratitude to Prof. M. Inaba for his kind care and support during my stay at BNL. I would like to thank Prof. H. Masui for his useful and critical advice for flow physics and STAR experiments. I appreciate Prof. B. Oliver, Prof. S. Sakai, Dr. Y. Watanabe and Prof. N. Novitzky for their useful suggestions and comments. Prof. Sakai and Dr. Watanabe told me how to estimate systematic uncertainties before QM2018. I appreciate Mr. S. Kato for his setup of computer systems of the laboratory. I also grateful to Prof. A. Ozawa for his careful reading my thesis and giving worthful comments and suggestions. I would like to my grate appreciation to Dr. T. Niida and Dr. T. Todoroki, Dr. S. Mizuno, Dr. H. Nakagomi and Dr. N. Tanaka for their kindness support, comments and friendship. I learned a lot of analysis and computer techniques from them. Especially, STAR collaborators, Dr. Niida, Dr. Todoroki and Dr. Mizuno, taught me a computer system and support my English presentation at the PWG meeting. Dr. Todoroki told me analysis techniques and we discussed physics on two-particle correlations, which was helpful for me. I often discussed physics with Dr. Tanaka because we had similar analysis topic and we talked about TV animation and comics. I would like to appreciate Dr. T. Nonaka and Mr. T. Sugiura, co-worker for the STAR experiment, for their friendship. We discussed a lot about the physics and went to BNL and physics conferences together. Dr. Nonaka told me how to start a data analysis at STAR, and that was helpful for me. Thanks for his driving during BNL trip, we enjoyed our meals. I would like to acknowledge Mr. R. Hosokawa. His kind support and advice is useful for me, and discussion of jet physics with him is worthful. We often went for dinner together (often went to a bento shop) when we are extremely busy for preparation for the conference. I appreciate Mr. J.Lee, Mrs. I. Sakatani, Mr. T. Shioya, Mr. M. Hirano and Mr. H. Yamamoto for their friendship as my colleagues. I could not enjoy my laboratory life without them. I also appreciate my colleagues of our laboratory, Dr. H. Yokoyama, Dr. J. Bhom, Dr. D. Watanabe, Mr. K. Ohshima, Ms. H. Ozaki, Mr. T. Kobayashi, Mr. K. Kihara, Mr. W. Sato, Mr. K. Ito, Mr. B. Kim, Mr. R. Koyama, Ms. S. Kudo, Mr. K. Matsunaga, Ms. M. Chang, Mr. Y. Fukuda, Mr. K. Sato, Mr. Y. Rebaza, Mr. H. Jeong, Mr. T. Ichisawa, Mr. H. Kato, Mr. D. Kawana, Mr. Y. Kawamura, Mr. T. Suzuki,

Chapter 1

Introduction

It is well known that the matter around us consists of atoms. The atoms are the smallest constituent that has the chemical element and they have nuclei in the center which consists of nucleus and electrons. Nucleus consists of protons and neutrons. Moreover, protons and neutrons consist of three quarks. Thus, the matter has a hierarchical structure. At present, the elementary particles are categorized into Fermion and Boson which is summarized in Fig.1.1 [1]. The fermion composes the matter and follows Fermi-Dirac statistics. Moreover, quarks and leptons are recognized as a fermion by Standard Model of particle physics. It is known that there are six type of quarks and six types of leptons, and quarks have intrinsic properties which include electric charge, mass, color charge and spin. The boson is categorized into gauge bosons which mediate the interactions between particles and Higgs boson which gives a mass to the particles and have been discovered in July 2012. Ordinarily, quarks and gluons are confined in hadrons and cannot move freely. With extremely high temperature, quarks and gluons could move freely just like a "plasma" state of quarks and gluons. That state is called Quark-Gluon Plasma (QGP). QGP is expected to exist in the early stage of universe or high-density neutron star. Therefore, it is important to understand the properties of QGP because it is a clue to understand the properties of early stage of the universe or neutron star.

In this chapter, we introduce Quantum Chromodynamics (QCD) theory and the relativistic heavy-ion collisions.

1.1 Quantum Chromodynamics

The strong interaction between quarks and gluons is described by Quantum Chromodynamics (QCD) which is a gauge field theory. Quarks are elemental building blocks of the matter and carry the quantum number which is called color charge, which is analogous to the electric charge in Quantum Electrodynamics (QED). In QED, photons mediate the electromagnetic interaction. On the other hand in QCD, gluons mediate the strong interaction. While photons carry no electric charge and do not interact with each other, gluons carry color charges and interact with other color

Figure 1.1: Elementary particles included in Standard Model [1]

charges. The QCD Lagrangian density is given as

$$\mathcal{L} = \sum_f^{N_f} \bar{q}_f(i\gamma^\mu D_\mu - m_f)q_f - \frac{1}{4}F_{\mu\nu}^a F_a^{\mu\nu}, \tag{1.1}$$

where f is a flavor of quarks ($f = 1, 2, 3$), q_f is the quark field of flavor f, γ^μ is a Dirac matrix, m_f is an invariant mass. $F_{\mu\nu}^a$ is the gluon-field strength tensor with color index a (a = 1-8) and defined as,

$$F_{\mu\nu}^a = \delta_\mu A_\nu^a - \delta_\nu A_\mu^a + g f_{abc} A_\mu^b A_\nu^c, \tag{1.2}$$

where A_μ^a is the gluon field and g is the dimensionless strength of quark-gluon and gluon-gluon interaction defined as $g \equiv \sqrt{4\pi\alpha_s}$, and f_{abc} is the structure constant of SU(3). The parameter α_s is the coupling constant of strong interaction which can be calculated by perturbative QCD (pQCD) [2] as

$$\alpha_s(Q^2) = \frac{1}{\beta_0 \ln(Q^2/\lambda^2)}, \tag{1.3}$$

where λ is the QCD scale parameter. Here, β_0 is given by

$$\beta_0 = \frac{33 - 2f_N}{12\pi}, \tag{1.4}$$

where N_f is the number of active quark flavors. The covariant derivative D_μ of QCD is defined as,

$$D_\mu = \delta_\nu + ig\frac{\lambda_a}{2}A_\nu^a, \tag{1.5}$$

where λ_a is the eight Gell-Mann matrices. The running coupling constant for the strong interaction becomes small at a short distance between color charges by the anti-screening feature of the color charge because the gluons are not neutral in color. This behavior is called asymptotic freedom, because the quarks and gluons act as free particles at shorter distances. Because of this QCD behavior, pQCD calculation can only be performed only in interactions with a large momentum transfer (Q). As seen in Fig.1.2, the summary of measurements of running coupling constant are very good agreement with the calculation by pQCD up to large momentum transfer region.
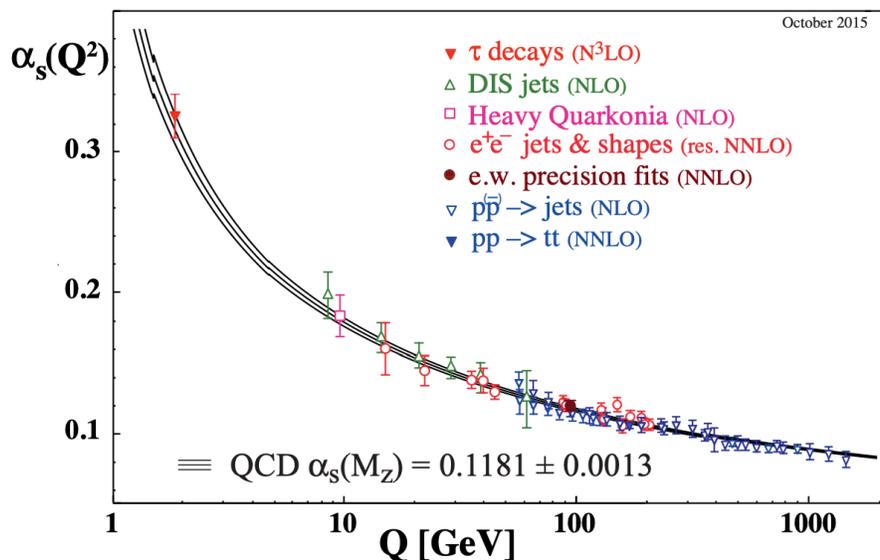
Figure 1.2: Summary of measurements of coupling constant α_s as a function of the energy scale Q [3].

On the other hand, the fact that the strength of coupling rises up at larger distances could suggest a possibility of confinement of quarks. However, the perturbative theory is invalid at this point. The correct form of the quark-(anti)quark potential are tried to derive either from pure QCD or its combination with other theory [4]. Conversely, the theory that quarks are always bound into colorless matter would be valid because they are never observed as free particles. Therefore, the quark potential is assumed to have the empirical form within framework of string model [5, 6] as,

$$V_{strong}(r) = -\frac{4}{3}\frac{\alpha_s}{r} + kr. \tag{1.6}$$

The first term of Eq.(1.6) is analogous to Coulomb potential that is dominant at small distances. The second term is dominant at large distances. According to [5, 6], when a high energy "string" is created between two quarks, energy density rises up with the distance between quarks increasing

until the distance reaches a certain critical distance r_c, where the energy density between the quarks is extremely high to create a new quark-anti-quark pair. The new quarks immediately interact with the original quarks and reduce the potential and once again form colorless objects.

1.1.1   Quark-Gluon Plasma

Lattice QCD calculations are one of the powerful method that has non-perturbative method. The lattice QCD calculations on thermodynamic behavior of quarks and gluons at finite temperature and density predict a phase transition phenomena of nuclear matter at a high temperature and density that is a release of quarks and gluons from hadron's confinement [7]. Fig.1.3 shows energy density ε and 3 times the pressure $3p$ over biquadrate of temperature T^4 as a function of temperature T. According to the Lattice QCD calculation, ε/T^4 and $3p/T^4$ rise rapidly at the vertical band (185−195 MeV). Since the term ε/T^4 corresponds to the number of degrees of freedom, this large jump indicates that a phase transition to the new state of matter called **Quark-Gluon Plasma (QGP)**.
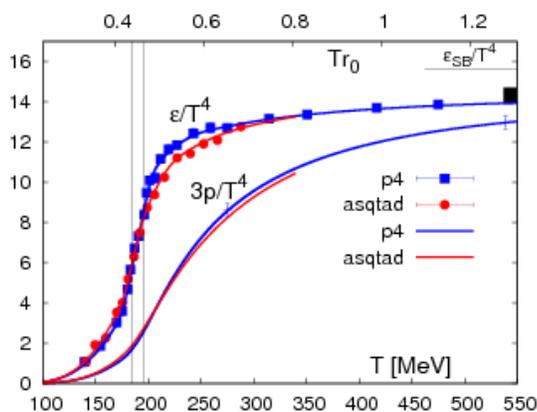
Figure 1.3: The energy density and three times the pressure divided by biquadrate temperature T^4 calculated by Lattice QCD as a function of temperature T [7].

1.2   Relativistic heavy-ion collisions

As introduced in Sect.1.1, the phase transition to the QGP is predicted at the extremely high temperature and density. Experimentally, relativistic heavy-ion collision is a unique tool to achieve such a state of matter on earth. Two heavy-ions such as Cu, Au or Pb are accelerated to nearly speed of light and collided at the high energy. In theory of relativity, the energy of four-vector, a term of time, is not invariant with respect to the Lorentz transformation, and thus the energy observed from a certain inertial frame of reference and that from other one is different. Here, the parameter s which is invariant to Lorentz transformation is defined by four-momenta of two nucleons

p_1 and p_2 as

$$s = (p_1 + p_2)^2, \tag{1.7}$$

where $\sqrt{s}$ correspond to the total energy of two nucleons observed from the center of gravity frame. Thus, $\sqrt{s}$ is defined as collision energy. Furthermore, the collision energy per nucleon-nucleon pair is expressed as $\sqrt{s_{\text{NN}}}$. Currently, several experiments of relativistic heavy-ion collisions have been carried out at Relativistic Heavy Ion Collider (RHIC) and the Large Hadron Collider (LHC) Table.1.1. While the experiments in Alternating Gradient Synchrotron (AGS) and Super Proton Synchrotron (SPS) were carried out with fixed-target mode, the experiments in RHIC and LHC have been carried out with collider-mode at top collision energy. Since each colliding nucleus has an energy moving to opposite direction, the maximum collision energy become higher in collider mode than in fixed-target mode. RHIC is the first heavy-ion collider of the world and located at Brookhaven National Laboratory (BNL). LHC is the largest heavy-ion collider of the world and located at the European Organization for Nuclear Research (CERN) in Switzerland. The previous experiments are summarized in 1.1.

Table 1.1: Summary of relativistic heavy ion collisions at AGS, SPS, RHIC and LHC

Year	Accelerators	Location	Species	Collision Energy(GeV)
1986	AGS	BNL	^{16}O, ^{28}Si	5.4
1992			^{197}Au	4.8
1986	SPS	CERN	^{16}O, ^{32}S	19.4
1994			^{208}Pb	17.4
2000	RHIC	BNL	^{197}Au	130
2001			^{197}Au	200
2003			d-^{197}Au	200
2003-2004			^{197}Au	200, 62.4
2005			^{63}Cu	200, 62.4, 22.4
2007			^{200}Au	200
2008			d-^{197}Au	200, 62.4
2010			^{197}Au	200, 62.4, 39, 11.5, 7.7
2011			^{197}Au	200, 19.6, 27
2012			^{238}U	193
2012			^{63}Cu-^{197}Au	200
2014			^{197}Au	200, 14.6
2014			^{3}He-^{197}Au	200
2015			p-^{197}Au	200
2015			p-^{197}Al	200
2016			^{197}Au	200
2016			d-^{197}Au	200, 62.4, 19.6, 39
2017			^{197}Au	54
2018			^{96}Zr	200
2018			^{96}Ru	200
2018			^{197}Au	27
2010	LHC	CERN	^{208}Pb	2760
2011			^{208}Pb	2760
2013			p-^{208}Pb	5020
2015			^{208}Pb	5020
2016			p-^{208}Pb	5020, 8160
2017			^{129}Xe	5440
2018			^{208}Pb	5440

1.2.1 Collision geometry

Fig.1.4 shows a schematic picture of participant-spectator picture before (left) and after (right) collision. The longitudinal length of colliding nuclei accelerate to nearly speed of light deflate to $2R/\gamma$ (Lorentz contraction), where R is a radius of the nucleus and γ is Lorentz factor. Here, b is an impact parameter, which is the distance between the centers of two nuclei. In case of collision with $b > 0$, the collision is called peripheral collisions. The degree of overlapping region is named "centrality", which can be determined by multiplicity in the experiment. In peripheral collisions, the collision can be explained by participant-spectator picture. The region participating in the collision is called "participant" and the rest part is called "spectator". The following statements are the characteristics of the picture:

- Since the de Broglie wavelength of a nucleon is much shorter than the size of nucleus, the relativistic heavy-ion collisions can be described by nucleon-nucleon collisions.

- The mean free path of the nucleon-nucleon collisions is shorter than the radius of the colliding nuclei.

- Since the velocity of nuclei is much faster than the Fermi motion of nucleons in the nuclei, the move of nucleons by Fermi motion during the crossing of nuclei is negligible.
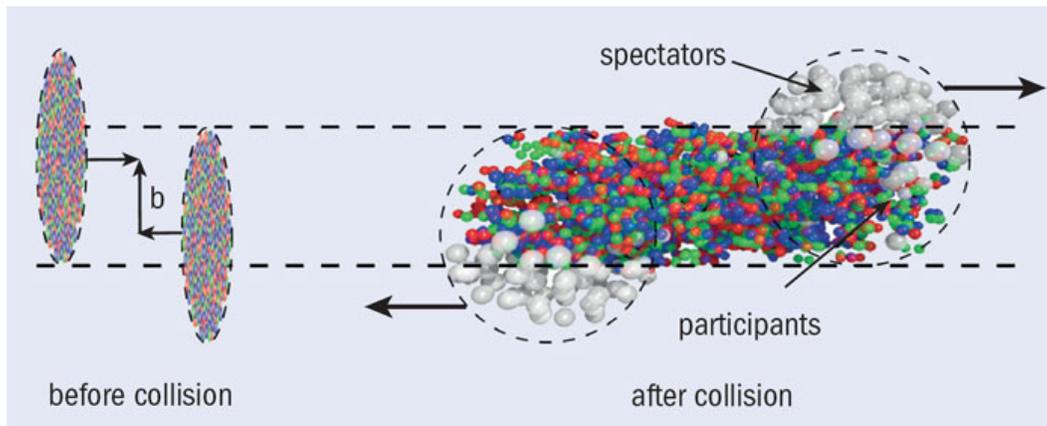
Figure 1.4: A schematic picture of participant-spectator picture before (left) and after collision (right) [8]. Impact parameter b is defined as the distance between the centers of two colliding nuclei.

The number of participant nucleons N_{part} and the number of nucleon-nucleon collisions in an event N_{coll} can be determined by impact parameter based on Glauber Model [9]. The following statements are assumption of Glauber Model:

- Nucleons travel straight lines and do not change its orbit.

- Nucleus-nucleus collision happens from individual inelastic nucleon-nucleon interactions.

- Cross-section of the inelastic nucleon-nucleon interaction is independent of the number of nucleon-nucleon collisions N_{coll}.

Wood-Saxon potential ρ_A of nucleons which has a mass number A based on Glauber Model is defined as

$$\rho_A(r) = \frac{\rho_{A,0}}{1 + \exp((r - R_A)/a_A)}, \tag{1.8}$$

where R_A is radius of nucleus, a_A a diffusion parameter and $\rho_{A,0}$ is a normalization factor to satisfy $\int d^3 r \rho_A(r) = A$. For example, the parameters in Au+Au collision at $\sqrt{s_{NN}} = 200$ GeV are $A = 197$, $R_A = 6.38$ fm and $a_A = 0.54$ fm and the cross section σ_0 of p+p collisions at $\sqrt{s_{NN}} = 200$ GeV is $\sigma_0 = 42$ mb [3]. The nuclear thickness function $T_A(x, y)$ is defined as

$$T_A(x, y) = \int_{-\infty}^{\infty} dz \rho_A(x, y, z). \tag{1.9}$$

The density function of the number of participants $n_{part}(x, y; b)$ in a nucleus collision is given by

$$\begin{aligned} n_{part}(x, y; b) &= T_A(x + b/2, y) \left\{ 1 - \left[1 - \frac{\sigma_0 T_B(x - b/2, y)}{B} \right]^B \right\} \\ &+ T_B(x + b/2, y) \left\{ 1 - \left[1 - \frac{\sigma_0 T_A(x + b/2, y)}{A} \right]^A \right\} \end{aligned} \tag{1.10}$$

where A and B are mass number of colliding nuclei. Thus, the number of participants N_{part} as a function of impact parameter b can be obtained by the integral of n_{part} in x-y plane as

$$N_{part}(b) = \int dx dy n_{part}(x, y; b). \tag{1.11}$$

The density function of the number of binary collisions n_{coll} is given by the product of σ_0, T_A and T_B as

$$n_{coll}(x, y; b) = \sigma_0 T_A(x + b/2, y) T_B(x + b/2, y). \tag{1.12}$$

Thus, the number of binary collisions N_{coll} is obtained as

$$N_{part}(b) = \int dx dy n_{coll}(x, y; b). \tag{1.13}$$

Fig.1.5 shows the Glauber Monte-Carlo simulation in Au+Au collisions performed by the PHOBOS experiment [10]. In this study, centrality is determined by Glauber Model by Monte-Carlo approach.

1.2.2   Space-time evolution

In this subsection, space-time evolution of the created system is described with separating the time scale which is supposed by Bjorken [11]. Fig.1.6 shows a schematic picture of space-time evolution of relativistic heavy-ion collisions which can be divided in three stages: parton cascade (pre-equilibrium), QGP phase, freeze out. The "space" in the longitudinal direction corresponds to the horizontal axis and the "time" corresponds to the vertical axis, and two nuclei collide at $t = 0$ and $z = 0$.
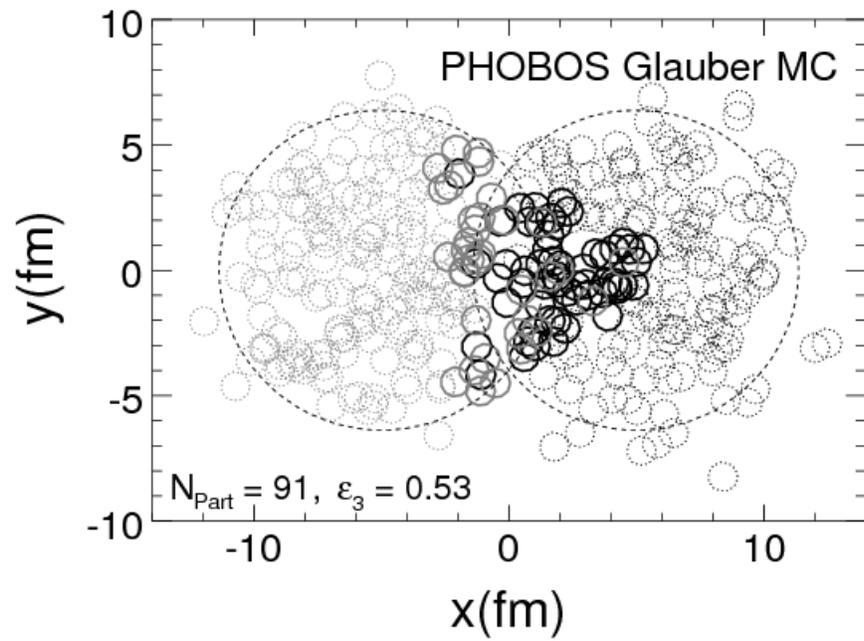
Figure 1.5: The PHOBOS Glauber Monte-Carlo simulation in $\sqrt{s_{\mathrm{NN}}} = 200$ GeV Au+Au collisions [10].
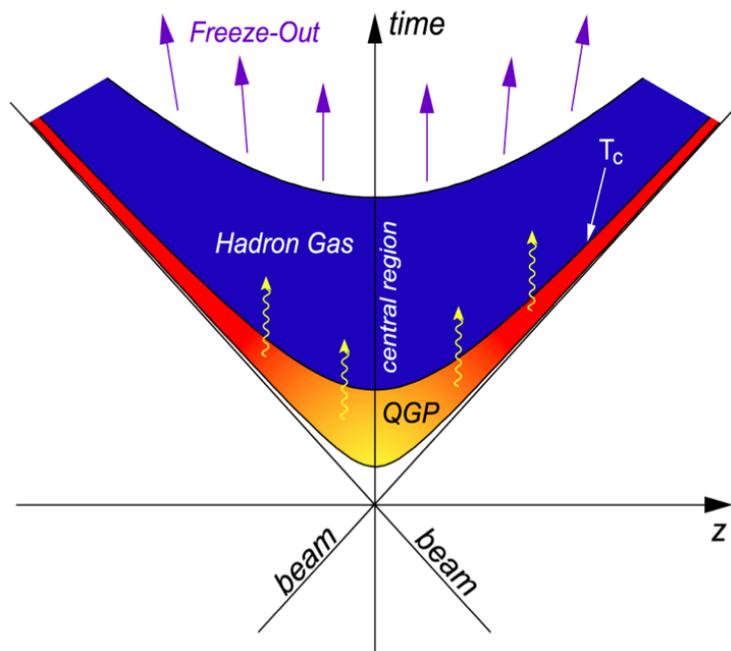
Figure 1.6: Space-time evolution

Parton Cascade stage (Pre-equilibrium)

Parton-parton scatterings occur in the initial stage of nucleon collisions. The mechanics are described by several models, such as the color-string models [12], the color glass condensate (CGC) [13, 14], and the pQCD models [2], but the mechanics have not been understood well. The entropy increases with multiple scattering of partons that is called parton cascade and QCD matter reaches local thermal equilibrium at a certain time τ_0 and QGP phase is formed. Typical time τ_0 at RHIC top energy is 1 fm/c or less, which is expected by calculation with hydrodynamical models [15].

QGP phase

QGP expands toward transverse and longitudinal directions due to the internal pressure. Once the QCD matter reaches the local thermal equilibrium, the evolution of the system can be described by the relativistic hydrodynamics. In the relativistic hydrodynamics, energy-momentum tensor $T^{\mu\nu}$ and the baryon number current j_B^μ are given by

$$T^{\mu\nu} = (\varepsilon + P)u^\mu u^\nu - g^{\mu\nu}P, \qquad (1.14)$$

$$j_B^\mu = n_B u^\mu, \qquad (1.15)$$

where ε is the local energy density, P is the pressure, u^μ is a fluid four-velocity which is defined as $u^\mu = \gamma(1, u_x, u_y, u_z)$ and n_B is the baryon number. Here, $T^{\mu\nu}$ and j_B^μ are conserved as

$$\delta_\mu T^{\mu\nu} = 0, \qquad (1.16)$$

$$\delta_\mu j_B^\mu = 0. \qquad (1.17)$$

The system cools down and the phase transition from QGP phase to hadron phase occur at critical temperature T_c.

Freeze out

The hadron-gas system expands with inelastic scattering between hadrons and the temperature drops down. After the hadron-hadron interactions ends at a certain temperature, the species of hadrons no longer change, which is called chemical freeze-out. The elastic scattering of hadrons ends finally, which is called kinetic freeze-out, and after that particles enter into detectors.

1.3   Experimental observables

In this section, the experimental observables which is related to this study are presented. Before moving on the introduction, rapidity y is defined as follows:

$$y = \frac{1}{2}\ln\left(\frac{E + p_z}{E - p_z}\right) = \frac{1}{2}\ln\left(\frac{t + z}{t - z}\right), \qquad (1.18)$$

where the second and third formula can be connected with the following relation : $\beta_z = p_z/E = z/t$. E, p_z, transverse mass m_T and t and z can be written as

$$E = m_T \cosh y, \tag{1.19}$$

$$p_T = \sqrt{p_x^2 + p_y^2}, \tag{1.20}$$

$$p_z = m_T \sinh y, \tag{1.21}$$

$$m_T = \sqrt{E^2 - p_z^2} = \sqrt{p_T^2 + m_0^2}, \tag{1.22}$$

$$t = \tau \cosh y, \tag{1.23}$$

$$z = \tau \sinh y, \tag{1.24}$$

$$\tau = \sqrt{t^2 - z^2}, \tag{1.25}$$

where τ is the formation time.

1.3.1 Energy density

The energy density achieved in the experiment si given by Bjorken formula [11] as

$$\varepsilon_{Bj} = \frac{1}{\pi R^2 \tau} \frac{dE_T}{dy}, \tag{1.26}$$

where R is the radius of nucleus in Wood-Saxon model and E_T is the transverse energy. Fig.1.7 shows the Bjorken energy density measured as a function of N_{part} estimated by Glauber Monte-Carlo in three different collision energies [16]. In the most central collisions at $\sqrt{s_{\mathrm{NN}}} = 200$ GeV, $\varepsilon_{Bj}\tau$ reaches above 5 GeVfm$^{-2}c^{-1}$. If the typical value $\tau = 1$ fm/c, the estimated Bjorken energy density is larger than the critical energy density predicted by lattice QCD calculations, and the created matter in Au+Au collisions at RHIC top energy reaches to QGP phase.

1.3.2 Radial flow

Transverse momentum distribution (p_T spectra) is important because transverse momenta are generated after collisions. By seeing p_T spectra, we can obtain the information of the the condition in the late stage and entire information of space-time evolution of the system. Transverse momentum (mass) distribution can be written with invariant cross-section as

$$E\frac{d^3\sigma}{dp^3} = \frac{1}{2\pi p_T}\frac{d^2\sigma}{dp_T dy} \tag{1.27}$$

$$= \frac{1}{2\pi m_T}\frac{d^2\sigma}{dm_T dy} \tag{1.28}$$

$$\propto \exp(-\frac{m_T}{T}) \tag{1.29}$$

where T is the inverse slope parameter which is interpreted as the temperature of the system at the kinetic freeze-out. Fig.1.8 shows transverse mass distribution in Au+Au collisions [17]. In high energy p+p and p+A collisions, the inverse slope parameters T in various particle species,
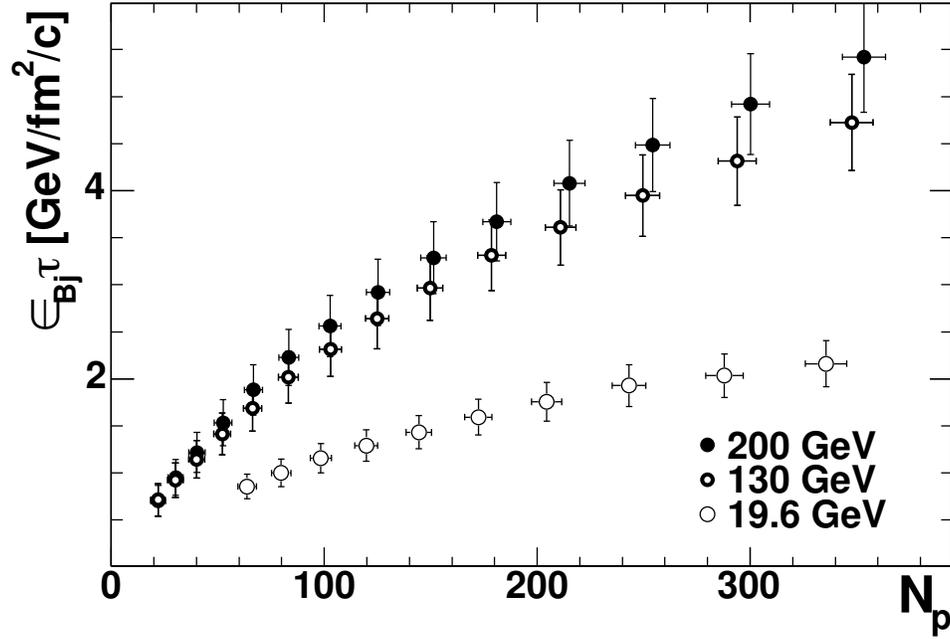
Figure 1.7: Bjorken Energy density multiplied by the formation time τ measured by the PHENIX experiment[16].
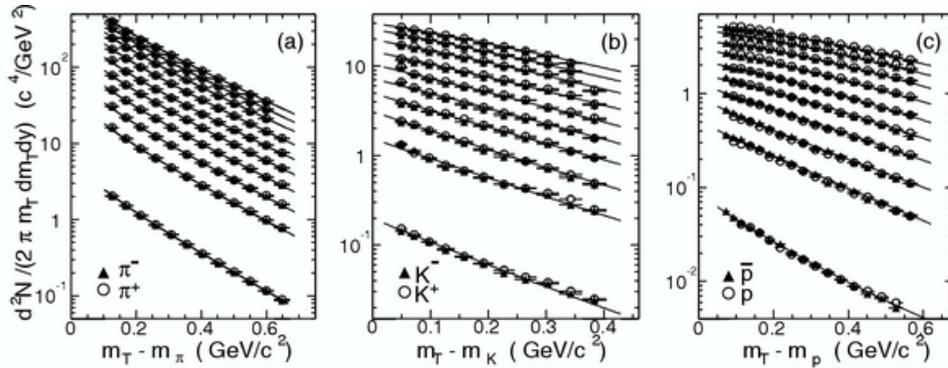
Figure 1.8: Invariant yield as function of transverse mass for $\pi^{\pm}$, $K^{\pm}$, and inclusive p and $\bar{p}$ at mid-rapidity ($|y| < 0.1$) for pp (bottom) and Au+Au events from 70-80% (second bottom) to the 0-5% centrality (top) [17]. Open markers represent positive particles and solid markers represent negative particles.

which is known as m_T scaling [18]. This fact suggests that the inverse slopes in different hadrons would have similar values. Fig.1.9 shows the inverse slopes as a function of hadron mass in three different centrality classes [19]. The inverse slopes increase with increasing particle masses and m_T scaling hold. This result indicates the radial collective expansion of the system, which means all the produced particles have common velocity in transverse direction. The inverse slope is represented as

$$T = T_f + \frac{1}{2} m \langle \beta \rangle^2, \tag{1.30}$$

where β is radial flow velocity and T_f is the freeze-out temperature. The estimated T_f is ~ 177 MeV in most central collisions. The blast-wave model which is phenomenological hydrodynamical model can describe the effect of radial flow of the mass spectra in low m_T region [20]].
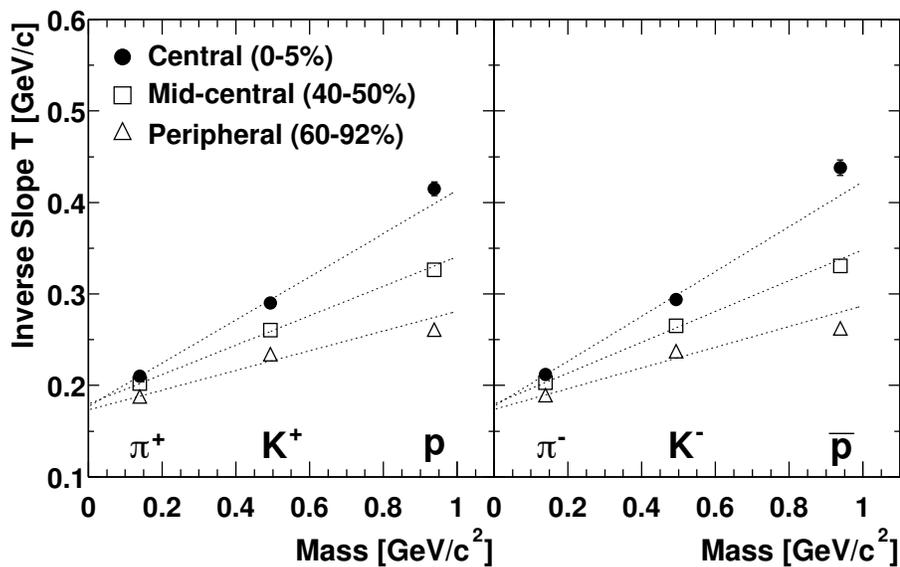
Figure 1.9: Mass and centrality dependence of inverse slope parameters T in m_T spectra for positive (left) and negative (right) particles [20].

1.3.3 Azimuthal anisotropy

Azimuthal anisotropy of emitted particles in momentum space has been studied because it is expected to be sensitive to the early stage of collisions. In non-central heavy-ion collisions, the overlapping region of two nuclei has spatial anisotropy like an almond depicted in Fig.1.10. The reaction plane is defined as the plane formed by the beam direction and the vector of impact parameter. Moreover, since the number of participants is finite in nucleus-nucleus collisions, the shape of participant region fluctuates event-by-event due to the fluctuations of nucleons and can form a n-sided polygon. The spatial deformation is converted into a momentum space by the
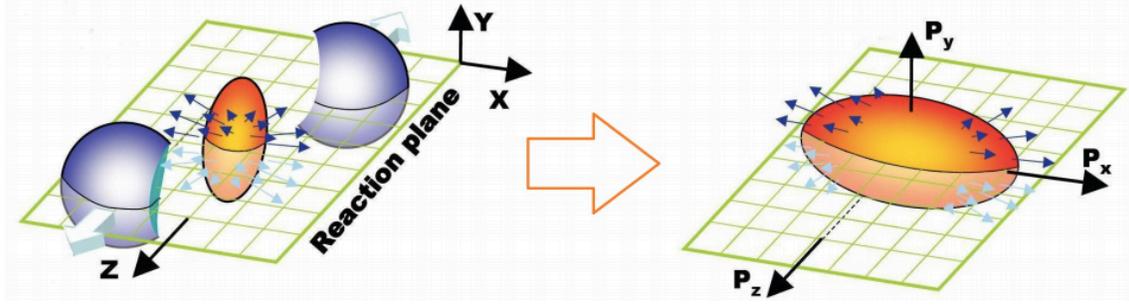
Figure 1.10: Image of non-central nucleus-nucleus collisions (left) and collective flow of the medium toward the direction of reaction plane in momentum space (right).

collective flow of the QGP and higher-order harmonic flow is observed.   The eccentricity of the participant region ε_n and n-th order participant plane Ψ_n^{PP} is given by [10, 21] as

$$\varepsilon_n = \frac{\sqrt{\langle r^2 \cos(n\phi_{part})\rangle^2 + \langle r^2 \sin(n\phi_{part})\rangle^2}}{\langle r^2 \rangle}, \tag{1.31}$$

$$\Psi_n^{PP} = \frac{1}{n} \tan^{-1} \left(\frac{\langle r^2 \sin(n\phi_{part})\rangle}{\langle r^2 \cos(n\phi_{part})\rangle} \right), \tag{1.32}$$

where ϕ_{part} is an azimuthal angle of participant nucleon. Here, Ψ_n^{PP} represents the long axis which initial shape of the system is diagnosed as n-sided polygon. Fig.1.11 shows initial eccentricity ε_2 as a function of N_{part} simulated by Glauber Monte-Carlo in Au+Au collisions at $\sqrt{s_{\mathrm{NN}}} = 200$ GeV. The average eccentricity represented by lack data point become larger with smaller N_{part} (peripheral collisions).

The azimuthal distribution of emitted particles can be written by Fourier series expansion as

$$\frac{dN}{d\phi} = 1 + \sum 2v_n \cos[n(\phi - \Psi_n)], \tag{1.33}$$

where ϕ is the azimuthal angle of emitted particles in a laboratory frame and Ψ_n is the azimuthal angle of the event plane which corresponds to the direction with most emitted particles are observed. In the real experiment, the second-order event plane Ψ_2 is often measured instead of reaction plane but their directions are not necessarily the same because of participant density fluctuations. Fourier coefficients v_n denote the magnitude of flow which defined as

$$v_n = \langle \cos[n(\phi - \Psi_n)]\rangle . \tag{1.34}$$

Model calculations have done to explain v_2 and v_3 as a function of N_{part} by different setup and compared with the results from the PHENIX experiment [22]. Initial conditions and shear viscosity over entropy density η/s in hydrodynamical calculations are combined with MC-KLN+$4\pi\eta/s = 2$, Glauber+$4\pi\eta/s = 1$ (1) [23] and (2) [24] and UrQMD+$4\pi\eta/s = 0$ [25]. For the results of v_2, all the model calculations shown in Fig.1.12 almost reproduce the experimental results. Glauber model
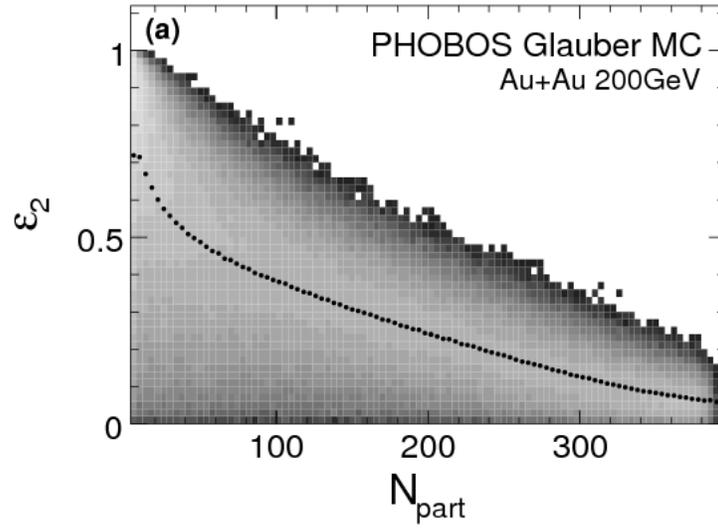
Figure 1.11: The second-order participant eccentricity ε_2 as a function of N_{part} in Au+Au collisions [10].

reproduce also v_3. However, v_3 by MC-KLN do not reproduce the experimental results in spite of the same parameter as that for v_2. Thus, the measurements of v_n can constrain the initial condition and the degree of viscosity of the system.
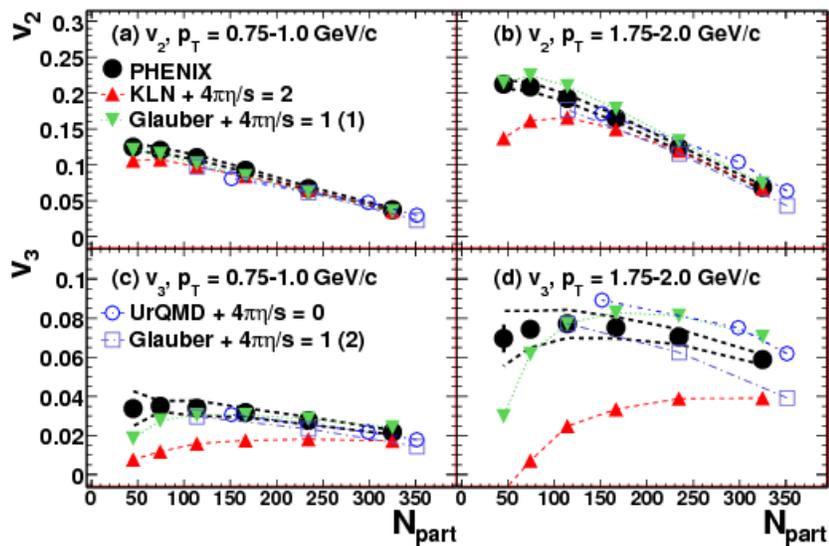
Figure 1.12: v_2 and v_3 as a function of N_{part} for two different p_T ranges in Au+Au collisions at $\sqrt{s_{NN}} = 200$ GeV by the PHENIX experiment [22]. The results are compared with theoretical models.

1.4   Jets and parton energy loss

In earlier stage in the high energy nuclear collisions, parton pairs with high momentum are produced in a back-to-back direction by hard scattering of partons in the nucleons. The recoiled partons radiate gluon bremsstrahlung into small angles in the original trajectory and the gluons radiate another gluon again or produce $q\bar{q}$ pairs. When the distance between created $q\bar{q}$ pair become larger than ~ 1 fm, the energy flux tube between the quarks become high, which is sufficient to create a new $q\bar{q}$ pair. The created quark paris combine with the rest of free quarks. Thus, the shower of hadrons which is called jets is created in the same direction as initial hard scattered partons. In heavy-ion collisions, partons interact with the hot and dense matter and lose their energy, which is called jet quenching. The image of hard scattering is shown in Fig.1.13. Investigation of the modification of high-p_T hadrons will help us to understand the energy loss mechanism in the QGP.

1.4.1   Experimental results of jet quenching

In this subsection, several results about high-p_T particles is presented.
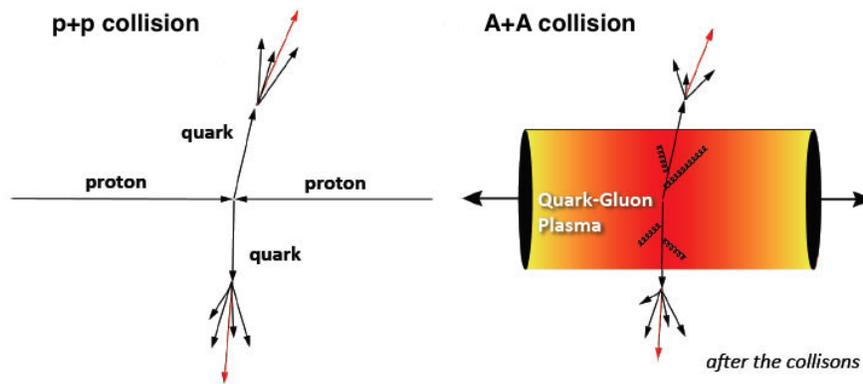
Figure 1.13: Image of hard scattering in vacuum (p+p collisions) and parton energy loss in the QGP (A+A collisions).

Nuclear modification factor : R_{AA}

The nuclear modification factor R_{AA} is the ratio of particle yields in heavy-ion collisions to that in p+p collisions which is scaled by N_{coll} as

$$R_{AA} = \frac{d^2 N^{AA}/dp_T d\eta}{N_{coll} d^2 N^{pp}/dp_T d\eta}, \tag{1.35}$$

where N^{AA} and N^{pp} are the number of particles in A+A collisions and p+p collisions, respectively. R_{AA} is one of the probes to quantify the suppression of particle yields due to the energy loss in the QGP. [26] shows R_{AA} of π^0, η and direct photon measured by the PHENIX experiment [26, 27]. Left figure of Fig.1.14 shows R_{AA} with different particle species in central Au+Au collisions. R_{AA} of π^0 and η is smaller than 1 (around 0.2), which means that the yields in Au+Au collisions are strongly suppressed compared with p+p collisions. On the other hand, R_{AA} of high-p_T direct photons is consistent with unity within statistical and systematic uncertainties though high-p_T direct photons are produced in hard scattering processes. This is because direct photons do not have color charge and do not interact with QGP. Right figure of Fig.1.14 shows R_{AA} of π^0 in five different centrality classes and minimum bias. The more peripheral the centrality becomes, the less suppression of π^0 yield, which means the existence of path length dependent energy loss.

Two-particle correlations

While R_{AA} gives information about single particle (jet) suppression, two-particle correlations give information about recoil particles (jets) with respect to the leading jets. Two-particle correlations are obtained by measuring the relative azimuthal and pseudorapidity $\eta = -\ln(\tan(\theta/2))$ position of associated particles with respect to that of trigger particles. In order to obtain correlated-yield distribution, subtraction of combinatorial background which mainly comes from collective flow is needed. Fig.1.15 shows high-p_T triggered and high-p_T associated di-hadron correlations after background subtraction in p+p, d+Au and central Au+Au collisions at $\sqrt{s_{\mathrm{NN}}} = 200$ GeV by the
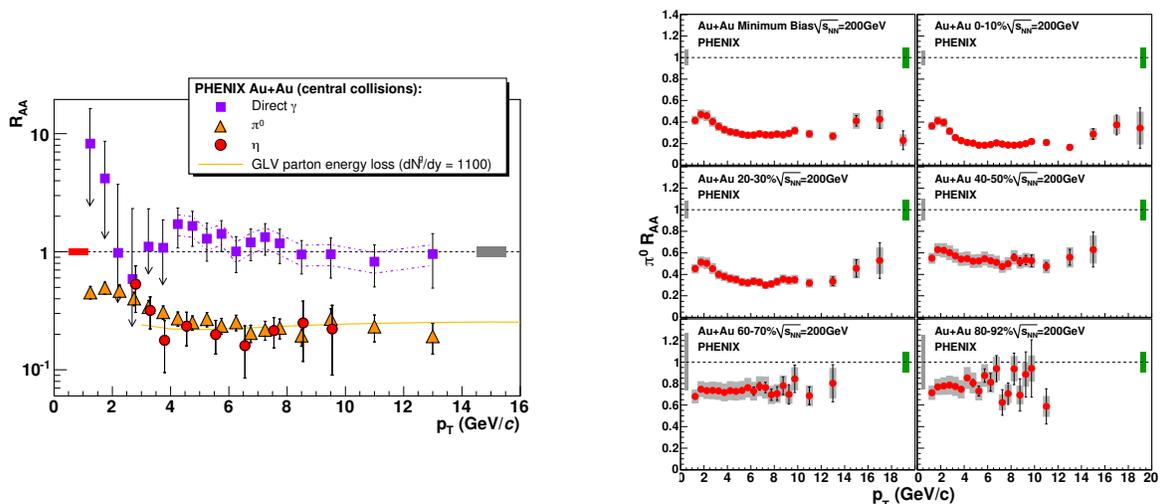
Figure 1.14: R_{AA} with different particle species, direct photon, π^0 and η, in Au+Au central collisions [26] (Left) R_{AA} of π^0 in various centrality bins in Au+Au collisions at $\sqrt{s_{NN}} = 200$ GeV by the PHENIX experiment [27] (Right).

STAR experiment [28]. The clear two peaks is observed in d+Au and p+p collisions in $\Delta\phi = 0$ (near side) and $\Delta\phi = \pi$ (away side) which is the typical dijet topology as observed in Panel (b). Therefore, no jet quenching effect can be observed in minimum bias d+Au collisions. However, in Au+Au collisions, clear peak is observed in the near side, but the away-side peak is disappeared due to jet modification in the QGP.

According to the energy loss model, parton energy loss in the QGP is affected by the particle types and the properties of the QGP, such as running coupling constant, temperature and in-medium path length [29]. The model reproduces the results of $dN/d\eta$, p_T spectra and azimuthal jet-like di-hadron correlations.

The STAR experiment has measured di-hadron correlations with various p_T combinations. Fig.1.17 shows trigger p_T and centrality and trigger p_T dependence of di-hadron correlations [30]. Fig.1.17 shows centrality dependence of azimuthal distributions of correlated yield with 2.5-3, 3-4, 4-6, 6-10 (GeV/c) trigger and 1-2.5 (GeV/c) associate particles in 0-12, 20-40, 40-60 and 60-80 %. In 60-80 % centrality, the yield in Au+Au collisions is almost similar to that in d+Au mini-mum bias collisions and is enhanced with higher trigger p_T in both near side and away side due to the effect of parton fragmentation. In more central collisions, significant increase of correlated yield is observed both in near side and away side compared to d+Au collisions and the relative increase is larger with lower trigger p_T. While correlations with higher p_T triggers are dominated by the component of jet fragmentation, those with lower p_T triggers are contributed from coales-cence quark from bulk partonic matter [31, 32], shower thermal coalescence [33] or re-heating of the medium by the passage of high-energy partons [34]. In peripheral collisions, near-side yield with full acceptance is similar with that in $|\Delta\eta| < 0.7$ and d+Au collisions, which indicates that the near-side long range correlations called "ridge" [35] decreases with peripheral collisions as shown in
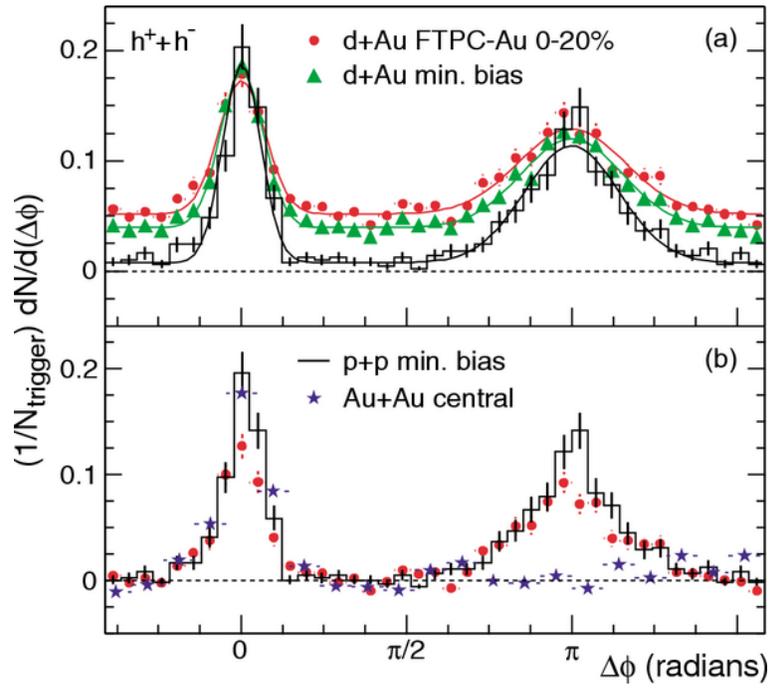
Figure 1.15: Azimuthal di-hadron correlations in minimum bias d+Au (a) and in p+p and central Au+Au collisions (b) at $\sqrt{s_{\mathrm{NN}}} = 200$ GeV by the STAR experiment [28]. Trigger and associate p_T ranges are $4 < p_T^t < 6$ (GeV/c) and $2 < p_T^a < p_T^t$ (GeV/c), respectively.

Fig.1.16 because an effect of jet fragmentation is expected in small $\Delta\eta$ range.   In central collisions,
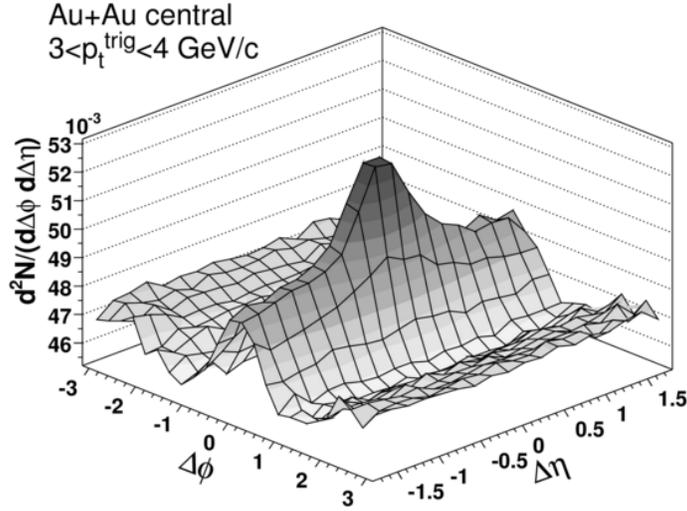
Figure 1.16: Azimuthal di-hadron correlations with $3< p_T^{trig} <4$ (GeV/c) trigger and $2< p_T^{trig} < p_T^{asso}$ (GeV/c) associate in central in Au+Au collisions at $\sqrt{s_{\rm NN}} = 200$ GeV by the STAR experiment [35].

double-peaked structures are observed with lower triggear p_T, which was indicated in [36]. Some models are suggested to explain the double-peaked structures : Mach-cone shock wave [37], QCD Cherenkov radiations [38], 3D hydrodynamical calculation simulated with local density fluctuations in the initial state [39]. Here, the background contributions considered for Au+Au collisions in [30] is only the second-order harmonic flow. Azimuthal di-hadron correlations with subtracting v_2, v_3 and v_4 have been measured at the PHENIX [40]. According to the thesis [40], correlations with intermediate trigger p_T ($p_T < 4$ GeV/c) show suppression or broadening of away-side structure in 0-10 % and double-peaked structure in 10-50 % centrality by at most 1σ significance.
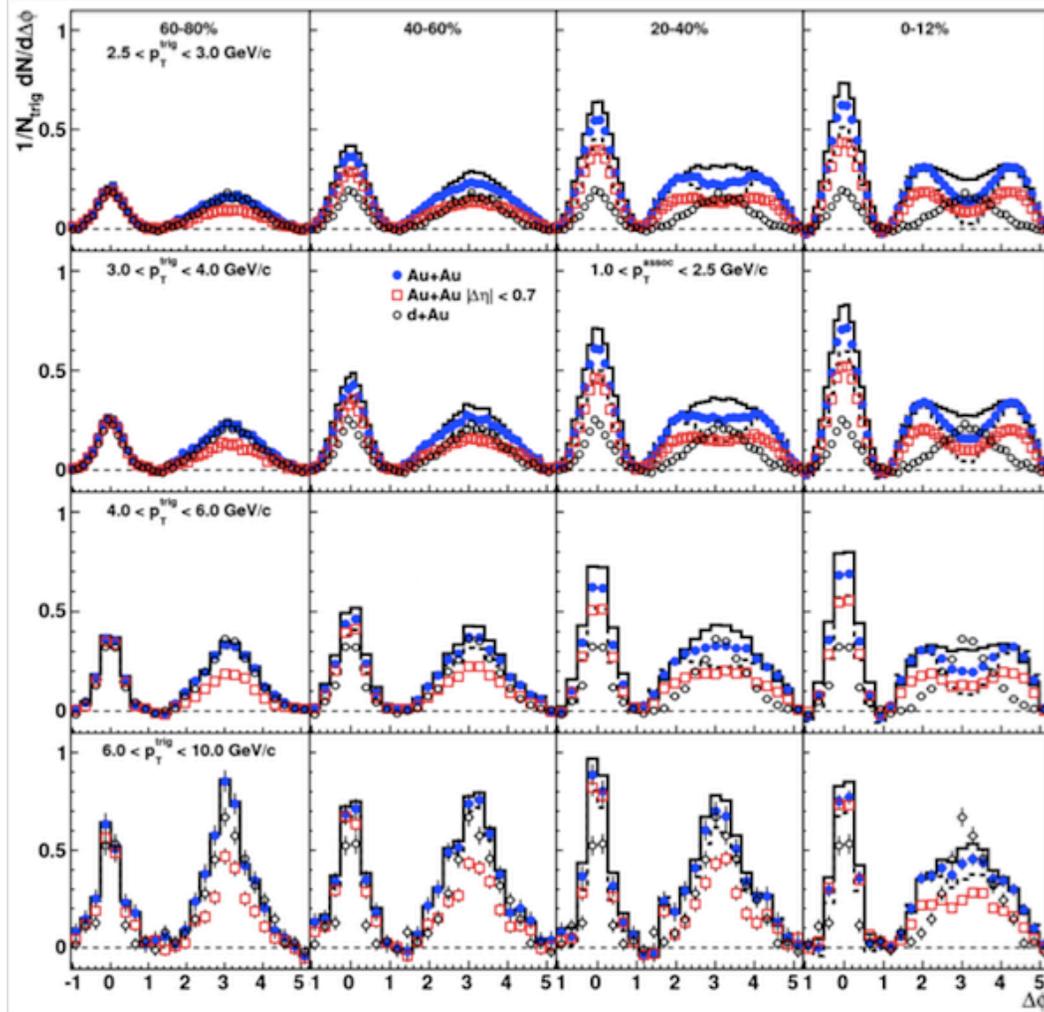
Figure 1.17: Azimuthal di-hadron correlations with 2.5-3, 3-4, 4-6 and 6-10 (GeV/c) trigger (from left to right) and 1-2.5 (GeV/c) associate in 60-80, 40-60, 20-40 and 0-12 % centrality (from top to bottom) in Au+Au collisions (blue : full acceptance, red : $|\Delta\eta| < 0.7$) and in minimum bias d+Au collisions (open black) at $\sqrt{s_{NN}} = 200$ GeV by the STAR experiment [30].

1.4.2 Path-length dependent jet modification

   The path length of jets in the medium can be controlled by selecting the direction of emitted particles with respect to the event plane due to the deformation of initial collision geometry. Longer (shorter) path length is expected for out-of-plane (in-plane) direction. The high-p_T two-particle correlations have been measured with scanning the trigger angle direction with respect to the second-order event plane $\phi_s = \phi^t - \Psi_2$ performed by the PHENIX experiment [41]. Fig.1.18 shows I_{AA} which is the ratio of correlated yield in heavy-ion collisions to that in p+p collisions. In this measurement, contributions from v_2 and $v_4 \{\Psi_2\}$ have been subtracted. Near-side yields are almost consistent with unity within statistical and systematic uncertainties and independent of trigger angle. On the other hand, away-side yields are more suppressed with increasing trigger particle's direction with respect to the second-order event plane (in-medium path length).
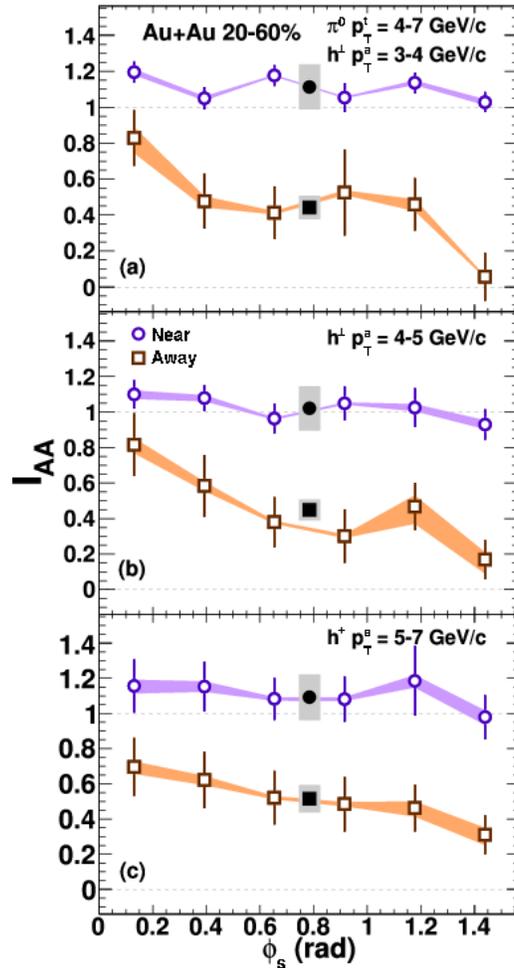
Figure 1.18: p_T and trigger angle dependence of nuclear jet suppression factor I_{AA} in 20-60 % Au+Au collisions performed by the PHENIX experiment[41].
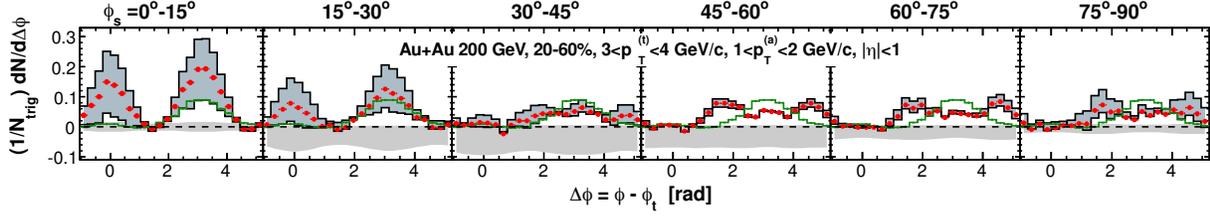
Figure 1.19: Di-hadron correlations with trigger angle selections with respect to the second-order event plane Ψ_2 with 3-4⊗1-2 (GeV/c) in Au+Au collisions (Red) and in d+Au minimum bias as a reference (Green) at $\sqrt{s_{\mathrm{NN}}} = 200$ GeV by the STAR experiment [42].

The STAR experiment has also measured an event-plane dependent di-hadron correlations in intermediate-p_T range where near-side ridge is observed [42]. Fig.1.19 shows long-range ($|\Delta\eta| > 0.7$) azimuthal distributions of di-hadron correlations with trigger angle selections with respect to the second-order event plane with 3-4⊗1-2 (GeV/c) in 20-60 % Au+Au collisions and those without trigger angle selections in minimum bias d+Au collisions. In this measurement, contributions from v_2, v_3, $v_4\{\Psi_4\}$ and $v_4\{\Psi_2\}$ are subtracted. Trigger-angle-dependent jet modification is observed compared with d+Au collisions. Near-side ridge yields are suppressed more with out-of-plane trigger in Au+Au collisions and also suppressed in d+Au collisions. On the other hand, the away-side ridge yields become lower and broadened with more out-of-plane trigger and shows double-peaked structure.

1.5 Event Shape Engineering

In order to study evolution of the system more detailedly, further constraint of initial geometry is needed because initial geometry is related to shape of evolution. In general, the initial collision shape is determined by centrality which is strongly related to impact parameter. However, the event-by-event eccentricity largely fluctuates in a fixed centrality bin as shown in Fig.1.11 and that results in event-by-event fluctuations of v_n. Fig.1.20 shows probability distribution of v_2, v_3 and v_4 in Pb-Pb collisions at $\sqrt{s_{\mathrm{NN}}} = 2.76$ TeV measured with the ATLAS detectors [43]. Large fluctuations of v_n are observed in a fixed centrality bin and the fluctuation is larger with peripheral collisions.

Recently, Event Shape Engineering (ESE) technique was proposed as a new tool to control event-by-event fluctuating v_n [44]. The method of ESE technique is to select the initial shape with
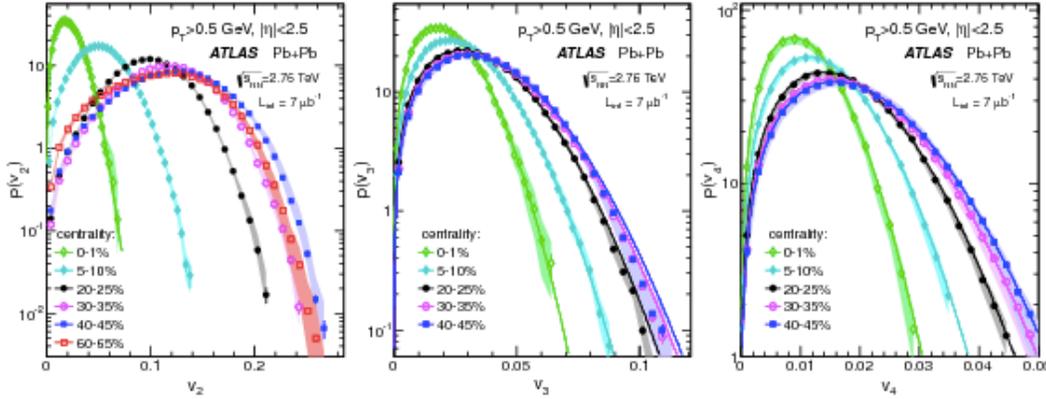
Figure 1.20: The probability distribution of v_2 (left), v_3 (middle) and v_4 (right) in various centrality bins in Pb-Pb collisions at $\sqrt{s_{\mathrm{NN}}} = 2.76$ TeV by the ATLAS experiment [43].

flow vector q_n, which is given in the same way as initial eccentricity,

$$Q_{n,x} = \sum_i^M \cos(n\phi_i), \tag{1.36}$$

$$Q_{n,y} = \sum_i^M \sin(n\phi_i), \tag{1.37}$$

$$q_n = \frac{\sqrt{Q_{n,x}^2 + Q_{n,y}^2}}{\sqrt{M}}, \tag{1.38}$$

where M is the multiplicity of a subsystem, ϕ_i is the azimuthal angle of the particle. The strong point of ESE technique is possibility to extract effect of difference of the event shape with fixing the system size. Ref.[44] has pointed out that ESE will have an important role on investigation of double-bump strutcutre in jet-like di-hadron correlations, measurement of azimuthally sensitive femtoscopy and an estimate of the background effects in chiral magnetic effect (CME) studies. Azimuthal sensitive HBT measurements with q_2 and q_3 selections as ESE have been performed by Ref.[45] and ALICE have also applied q_2 selections as ESE to charge-dependent two- or three-particle correlations to investigate v_2 dependence of Chiral Magnetic Effect signal [46]. Recent studies with ESE are introduced in the following paragraphs.

Fig.1.21 shows v_2 as a function of p_T with q_2 selection in various subsystems in Pb-Pb collisions at $\sqrt{s_{\mathrm{NN}}} = 2.76$ eV with the ALICE detectors [47]. If the q_2 is selected so as to be the same ratio of v_2 in ESE-selected events to the q_2 unbiased events between various q_2 selections, the p_T dependence of the ratio is almost nothing as seen in bottom panel. Large q_2 selected events have larger v_2 and small q_2 selected events have smaller v_2 events than q_2 unbiased events. This result suggests that non-flow contributions do not affect on p_T dependence because pseudo-rapidity gap is quite different between V0C ($-3.7 < \eta < -1.7$) and TPC ($|\Delta\eta| = 0.1$ for q_2 selection and v_2 measurements). Fig.1.5 shows the ratio of p_T spectra of identified charged hadrons in top (Left)

and bottom (Right) 10 % q_2 selected events to those in q_2 unbiased events. p_T spectra are enhanced (suppressed) with large (small) q_2 selections and the enhancement (suppression) become stronger with higher p_T. The ratio of the spectra is fitted by blast-wave function [48] and the parameter of boost velocity is extracted. The boost velocity is larger (smaller) with large (small) q_2 selections, which suggests that radial flow also changes with q_2 selections.
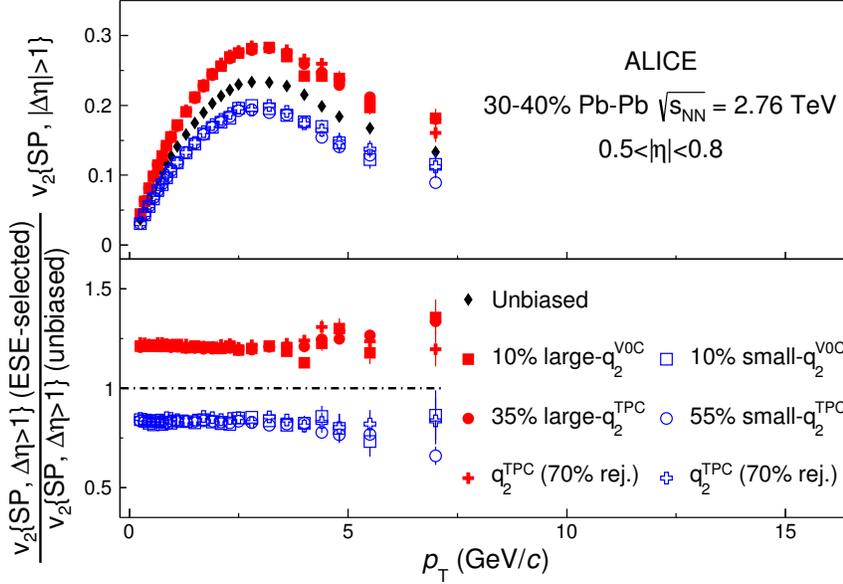
Figure 1.21: v_2 as a function of p_T with q_2 selections at various subsystems (top) and the ratio of v_2 with q_2 selection to the q_2 unbiased events (bottom) in Pb-Pb 30-40 % centrality at $\sqrt{s_{\mathrm{NN}}} = 2.76$ TeV by the ALICE experiment [47].

The correlations between flow harmonics have been measured by the ATLAS experiments in order to study how initial geometry effects affect final-state azimuthal anisotropy [49]. Fig.1.23 shows correlation between v_n at lower p_T ($0.5 \leq p_T \leq 2$ GeV/c) and v_n at higher p_T ($3 \leq p_T \leq 4$ GeV/c) with selecting q_n in 5 % centrality intervals measured by the ATLAS experiment [49]. Going from central collisions to peripheral collisions, v_n first increases and then decreases along both axes, which reflects the characteristic centrality dependence of v_n. The rate of decrease is larger at higher p_T, which result in "boomerang-like" structure. This centrality dependence at higher-p_T regions do not conflict with viscous-damping effects on v_n expected by hydrodynamic calculations [50]. Fig.1.24 shows the correlation between v_2 and v_3 with selecting q_n in 5 % centrality intervals measured by the ATLAS experiment [49]. The v_2 and v_3 are always anticorrelated with each other within given centrality while they are positively correlated with centrality. The boomerang-like structure in this case results from weak centrality dependence of v_3. The ε_2-ε_3 correlations calculated via MC Glauber model [51] and MC-KLN model [52] are almost consistent with experimental data, which reveals the v_2-v_3 anticorrelation originates from initial geometry effects.
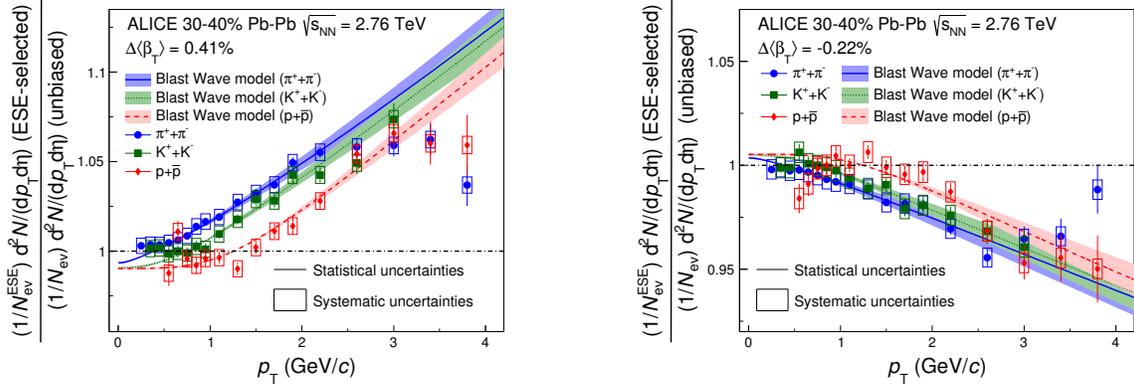
Figure 1.22: Identified charged hadron spectra ratio with large (left) small (right) q_2 selections in Pb-Pb 30-40 % centrality at $\sqrt{s_{\mathrm{NN}}} = 2.76$ TeV by the ALICE experiment [47].
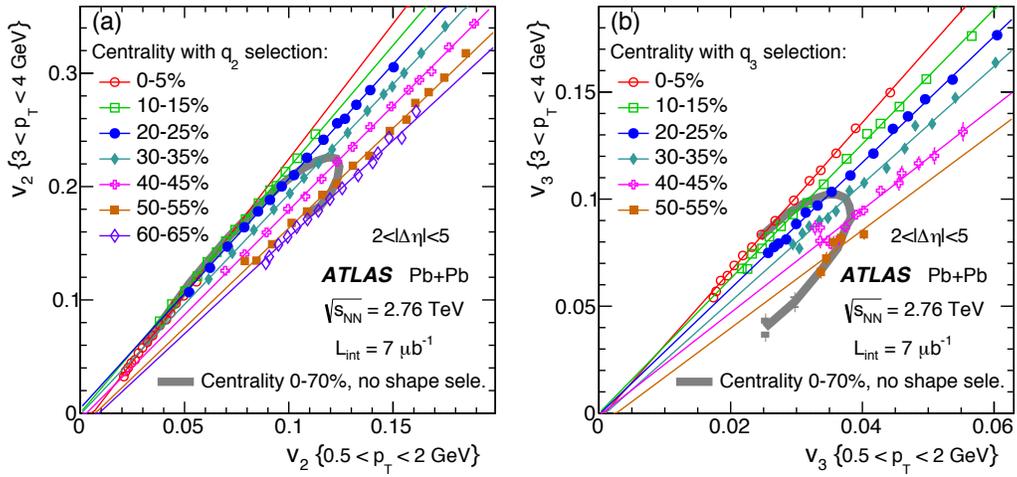
Figure 1.23: The correlation between v_n at lower p_T ($0.5 \leq p_T \leq 2$ GeV/c) and v_n at higher p_T ($3 \leq p_T \leq 4$ GeV/c) with selecting q_n in 5 % centrality intervals measured by the ATLAS experiment [49].
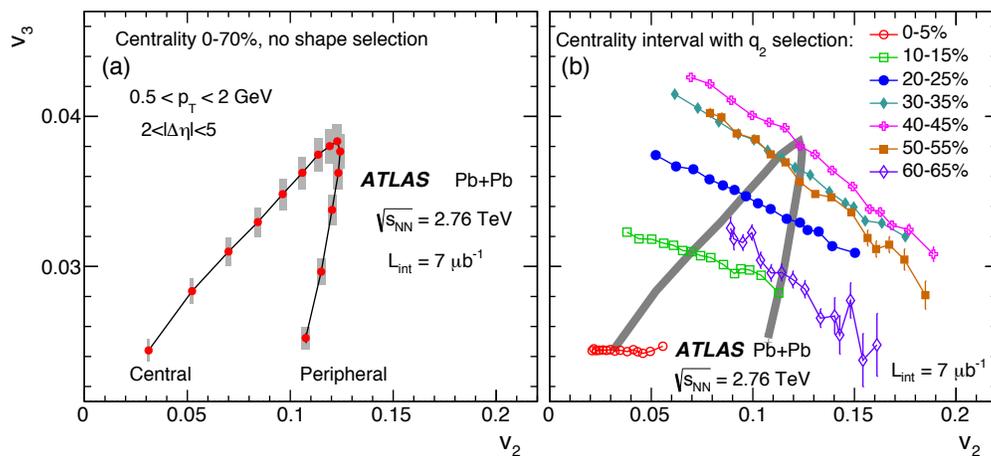
Figure 1.24: The correlation between v_2 and v_3 with selecting q_n in 5 % centrality intervals measured by the ATLAS experiment [49].

1.6 Motivation of this thesis

Information of partonic energy loss or that of bulk response to the traverse of high energy partons are provided by the measurements of di-hadron correlations with various p_T combinations. According to the previous studies, event-plane dependence of near-side and away-side structure has been measured, which suggests that the effect of jet penetration and energy re-distribution is strongly affected by in-medium path length of jets. However, in the previous studies, event-plane dependent di-hadron correlations have been measured in wide centrality steps, specifically in 0-20 and 20-60 % centrality. Therefore, those measurements with fine centrality bins are important to understand how jet modification and their energy re-distributions to the medium are related to the initial energy density and in-medium path length of initial partons. In this study, event-plane dependent two-particle correlations have been measured with fine centrality bins with higher statistics data taken in 2011 by the STAR detectors.

We can determine the centrality based on the event multiplicity because they are well correlated. Centrality is one of the probes to determine initial collision geometry. However, when centrality is changed from central to peripheral collisions, not only the the shape of the system but also the size of the system. Moreoever, initial geometry can fluctuate in a fixed centrality bin because of event-by-event participant fluctuations. We can separate the volume effect and shape effect by length of flow vector (q_n) selections as an event-shape engineering (ESE) technique; recently provided new tool. In addition to measurements of two-particle correlations with fine centrality bin, q_2 selections have been performed, which can constrain the initial eccentricity with average multiplicity fixed. The length of the second-order flow vector q_2 correspond to the amplitude of the second-order azimuthal anisotropy v_2. Thus, initial eccentricity selection can be translated into final-state elliptic flow selections. Therefore, we can study the relations between medium response to the passage of jets and collective expansion of the medium. Better experimental discrimination is expected for the

relation of two-particle-correlaiton shape and yield to initial density, path length and elliptic flow.

Chapter 2

Experimental setup

2.1 Relativistic Heavy Ion Collider (RHIC)

Relativistic Heavy Ion Collider (RHIC, Fig.2.1) located in Brookhaven National Laboratory (BNL)[53] in Upton, New York, is the only one of the dedicated collider for the experiment of heavy-ion collisions [54]. RHIC consists of two concentric accelerator rings, called "Blue Ring" (clockwise beam direction) and "Yellow Ring" (counter-clockwise beam direction), whose circumferential length is approximately 3.834 km. RHIC can accelerate various type of nuclear species
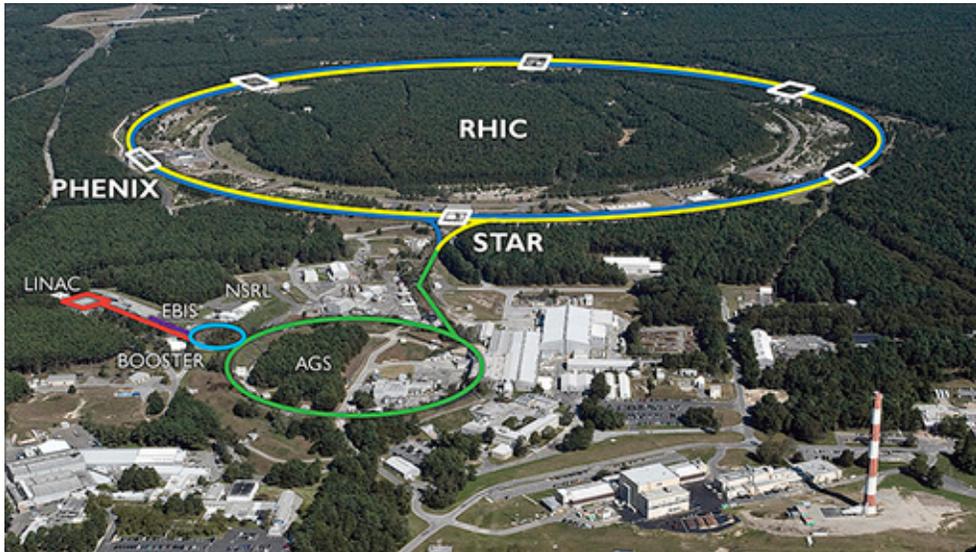
Figure 2.1: An aerial view of accelerators [55]

from A=1 (proton) to A=238 (Uranium) and can do independently in Blue Ring and Yellow Ring because RHIC contains 1,700 superconducting magnets. Before injecting beams into the RHIC, five accelerators, Electron Beam Ion Source (EBIS), Radio Frequency Quadrupole (RFQ), Linear accelerator (LINAC), the Booster Synchrotron and the Alternating Gradient Synchrotrons (AGS),

are used to accelerate gradually to the relativistic velocity. Fig.2.2 shows the procedure of acceleration of Au beam. There are six intersection of two rings at RHIC and four collaboration locate the detectors in different four points, PHENIX (8 o'clock) [56], STAR (6 o'clock) [57], PHOBOS (10 o'clock) [58] and BRAHMS (2 o'clock) [59]. PHENIX, PHOBOS and BRAHMS have been completed their operation and only STAR continues to running at RHIC.

EBIS		
Au^{32+}	17 keV/u	3.4×10^9 ions
RFQ		90%
Au^{32+}	300 keV/u	3.0×10^9 ions
Linac		90%
Au^{32+}	2 MeV/u	2.7×10^9 ions
BOOSTER		85%
Au^{32+}	70 MeV/u	2.3×10^9 ions
STRIPPER FOIL		60%
Au^{77+}	70 MeV/u	1.4×10^9 ions
AGS		90%
Au^{77+}	9 GeV/u	1.2×10^9 ions
STRIPPER FOIL		100%
Au^{79+}	9 GeV/u	1.2×10^9 ions
RHIC		
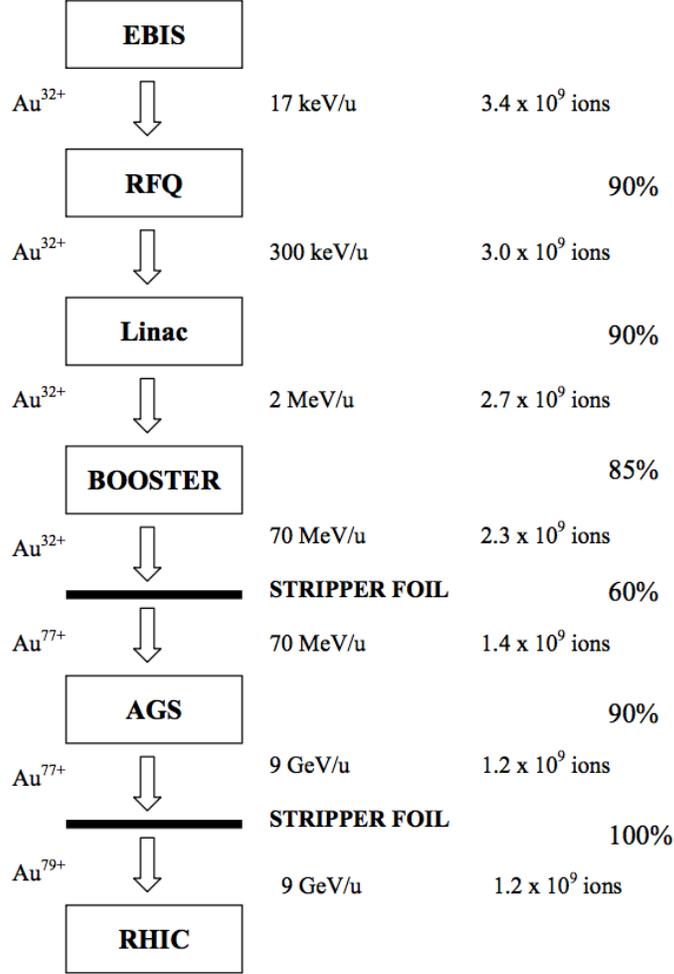
Figure 2.2: Injection step of beam [60].

2.2   Solenoidal Tracker At RHIC (STAR)

Solenoidal Tracker At RHIC (STAR) is the experiment group operating now located at 6 o'clock position in the RHIC. In 2019, the STAR Collaboration is composed of 65 institutes from 14 countries, with total of 652 collaborators. One of the main purpose of the experiment is to search Quark-Gluon Plasma (QGP) and to investigate the QCD phase diagram. At the STAR experiment,

polarized p+p and d+A collisions have been held in order to study parton distribution function inside the nuclei and for the reference as A+A collisions. Low-momentum particles are measured in order to investigate temperature of phase transition, dynamical collectivity and the effect of chiral condensation and so on. High-momentum particles are measured in order to study nuclear modification and the energy loss of colliding partons. Stopping factor of nuclear and baryon chemical potential of source of the particles can be determined by measurement of p_T spectra of baryon and anti-baryon.

STAR detectors have excellent at tracking accuracy, determination of momentum and particle identification at mid-rapidity ($0 < |\phi| < 2\pi$ and $|\eta| < 1.8$) in order to measure large number of hadrons emitted by collisions. Fig.2.3 shows overview of STAR detectors.
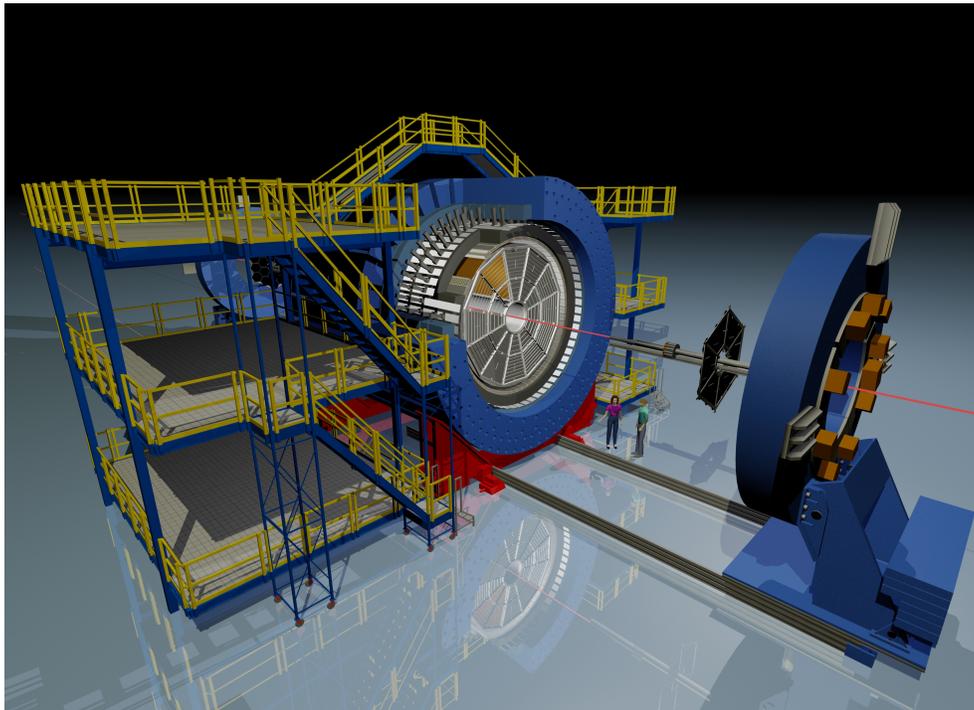
Figure 2.3: Overview of STAR detectors

2.2.1 Beam Energy Scan (BES) Program

Expoloring and understanding the nature of phase transition have been a long-standing challenge for high-energy nuclear and particle physics. Proposal of Beam Energy Scan (BES) program was published in 2010 [61]. The main goal of the BES program is to map out the QCD phase diagram by searching for the turn-off of QGP signatures, signals of QCD phase boundary and existence of a critical point in the QCD phase diagram. Beam Energy Scan I (BES-I) has been carried out from 2010 to 2014 by colliding Au-nuclei from 7.7 to 200 GeV at RHIC. It is important that physics observables are measured with various collision energies, because μ_B can be controlled by scanning

the beam energy. In order to analyze better statistics, Beam Energy Scan II (BES-II) is scheduled from 2019 to 2021 in five collision energies $\sqrt{s_{NN}}$ from 7.7 to 19.6 GeV in collider mode and in eight collision energies $\sqrt{s_{NN}}$ from 3.0 to 7.7 GeV in fixed-target mode.

2.2.2   Time Projection Chamber (TPC)

Time Projection Chamber (TPC) is a heart of the STAR detector and installed at the center of the STAR in order to record the tracks of particles, to measure their momenta and to identify particle species with energy loss by ionization in the TPC [62]. Fig.2.4 shows the schematic view of TPC. The size of is 4.2 m along beam direction which corresponds to the pseudorapidity coverage of
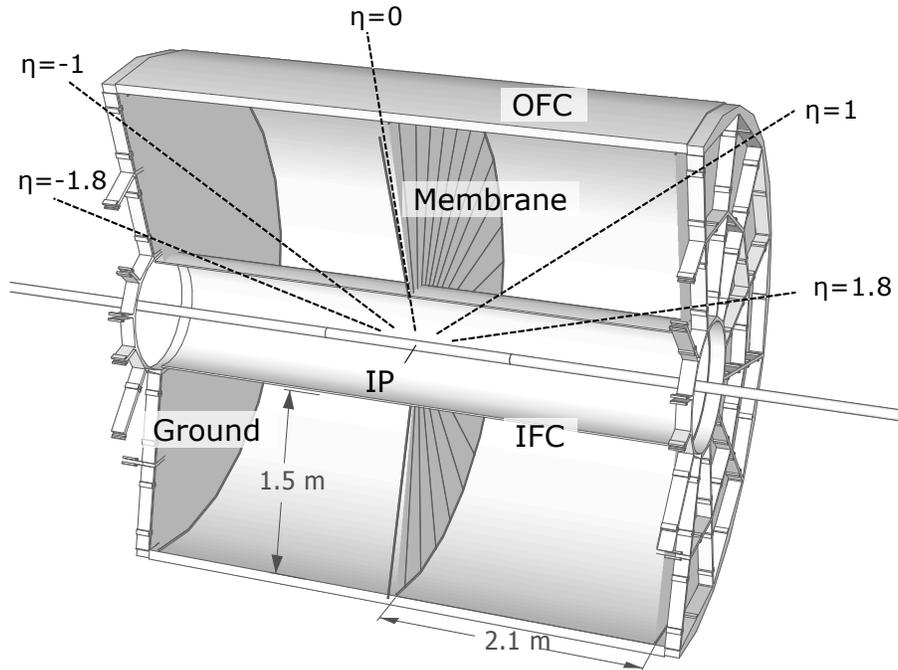
Figure 2.4: Schematic view of TPC [57]

± 1.8. Outer and inner diameter of drift volumes are 4 m and 1 m, respectively. TPC is separated by the thin Central Membrane (CM) and cathode at the center along the beam direction. The empty volume is filled with P10 gas (10 % methane and 90% argon) by 2 mbar atmospheric pressure and applied uniform electric field by 135 V/cm which is required to drift the ionized electrons toward the endcap-readout pads. The readout systems at the end cap is based on Multi-Wire Proportional Chamber (MWPC). The electron avalanche occurs at the anode wires and amplified by 1000 to 3000 gains. The ionized positive ions which is created in the avalanche induce a temporary image charge on the pads. The image charge is measured by 136,608 readout pads.

The z position of a space point is determined by the average of drift velocity and the drift time of ionized electrons from the original space point to the endcap anodes by electric field along the z

coordinate. The drift time depends on the drift velocity. But it can change by the slight change of the atmospheric pressure and the composition ratio of gasses. Thus, the effect should be minimized by two ways; change the cathode voltage corresponding to the peak in the drift velocity curve and the calibration by artificial tracks created by laser beams.

For reconstruction of tracks, space points are associated to form tracks as a first step, and the points are fitted by track model by algorithms. The signal of electron cluster is induced only on three pads for typical tracks. The x position and its width σ is given by

$$x = \frac{\sigma^2}{2w} \ln\left(\frac{h3}{h1}\right), \tag{2.1}$$

$$\sigma^2 = \frac{w^2}{\ln(h_2^2/h_1 h_3)}, \tag{2.2}$$

where h_1, h_2 and h_3 are amplitudes on each three pad and w is the pad width for the case of h_2 centered at $y = 0$. In this approach, the signals are assumed to distribute according to Gaussian distribution. The position uncertainty due to electronics noise in this method is given by

$$\Delta x = \frac{\Delta h}{h_c} \frac{\sigma^2}{2w} \sqrt{\left(1 - \frac{2x}{w}\right)^2 \exp\left(\frac{-(x+w)^2}{\sigma^2}\right) + \frac{16x^2}{w^2} \exp\left(-\frac{x^2}{w^2}\right)^2 + \left(1 + \frac{2x}{w}\right) \exp\left(\frac{-(x-w)^2}{\sigma^2}\right)} \tag{2.3}$$

where Δh is the noise, h_c is the signal amplitude under the center pad. When the signal to noise ratio is 20:1, the noise contribution is small. Helix is initial track model and the deviation from helix due to the energy loss in the gas is secondary one. The tracking efficiency depends on the electronics and the separation capability of close two hits. The two-hit resolution is 0.8 cm (in the transverse plane) and 2.7 cm (along the beam axis) in the inner sector and 1.3 cm (in the transverse plane) and 3.2 cm (along the beam axis) in the outer sector. The track merging effect due to sharing the adjacent pads by two tracks is reduced by requiring the minimum number of pad rows but cannot be completely rejected. There is 4% inefficient region due to the spaces between sectors. A fiducial cut, ignorance of any space points that fall on the last two pads by the software in order to avoid position errors and and distortion of the drift field, reduces the total acceptance to 94 %. The primary vertex is reconstructed by averaging the origins of all the tracks of charged particles. Fig.2.5 shows the resolution of primary vertex which is calculated by reconstructing primary vertex separately by each side of the TPC. We expect the resolution of 350 μm with more than 1,000 tracks.

The transverse momentum p_T, is determined by fitting the curve in the transverse $(x - y)$ plane of the vertex and the space points along the track. The momentum p is calculated by the radius of curvature and the angle of the track with respect to the beam (z) axis. This calculation works for all the primary tracks (the tracks coming from primary vertex). Fig.2.6 shows the momentum resolution of π^- and anti-protons which is simulated by embedding method. The embedding method is to embed a known track into the real data and to see how the track is reconstructed. The best relative momentum is about 2 % at $p_T \simeq 400$ MeV/c for pions.

Particle identification is capable with utilizing energy loss in the TPC gas especially for low momentum particles. Particles with $v > 0.7c$ velocities are hard separate particle species because
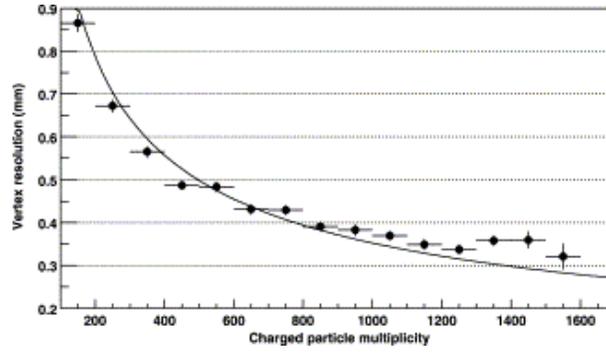
Figure 2.5: Vertex resolution of the TPC [62]
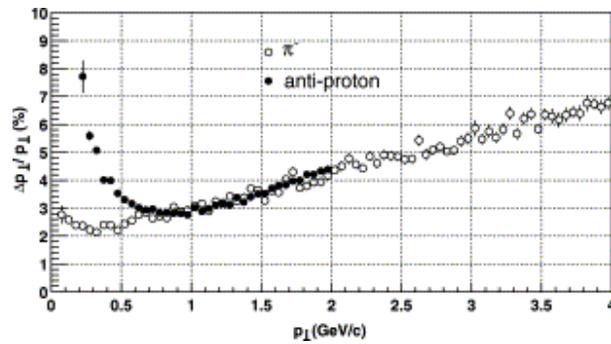
Figure 2.6: Momentum resolution of charged particles reconstructed by TPC [62]

the energy loss become mass-independent. The energy loss dE/dx is calculated by the hit points up to 45 pad rows. The accurate average dE/dx cannot be calculated because particles lose rarely hundreds of eV while usual energy loss is a few tens of eV. Thus, the typically 30 % truncated mean of the energy loss is measured by removing the cluster with the largest signal. Fig.2.7 shows the dE/dx in the TPC as a function of momentum of particle in the magnetic field 0.25 T. The resolution is 8 % for track which crosses 40 pad rows. The resolution become better in 0.5 T magnetic field because the transverse diffusion is smaller.
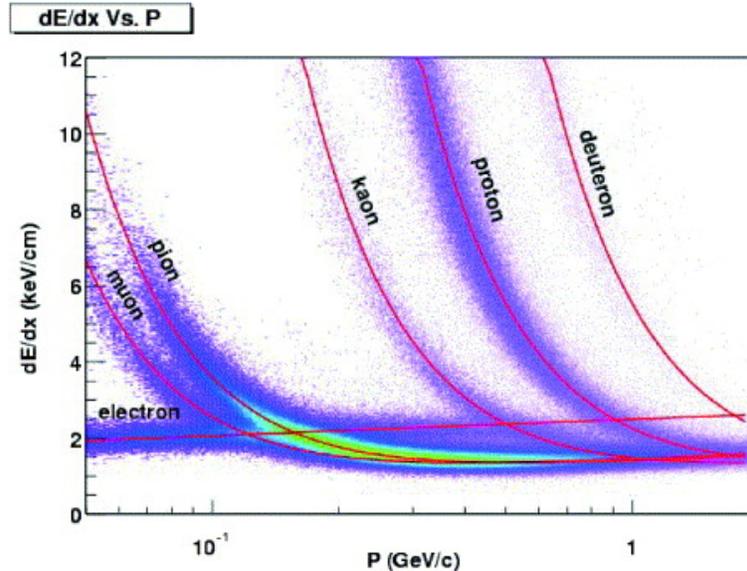
Figure 2.7: dE/dx as a function of momentum p [62]

2.2.3 Time-of-Flight (TOF)

Time-of-Flight (TOF) has been installed for particle identification utilizing differences of time of flight [63]. TOF system is constructed by Multi-gap Resistive Plate Chamber (MRPC). Fig.2.8 shows a side (upper) and end (lower) view of MRPC for TOF system. The MRPC for STAR consists of a stack of resistive plates with six gas gaps by 220 μm in between them. The resistive plate ($\sim 10^{13}\Omega$/cm volume and $10^5\Omega$ surface, respectively) is made of float glass and the thickness of glass is 0.54 mm. High voltages $\sim$ 14 kV are applied between two electrodes. During operation, the MRPCs are set in the gas 90-95% Freon R-134a and additional mixture of isobutane and SF6 for the reduction of the streamers. The stop time resolution is $\sim$ 80 ps achieved in Au+Au collisions at RHIC top energy. The number of TOF tray is 120 and they installed for full azimuthal coverage with $|\eta| < 0.9$ for pseudorapidity coverage around the TPC.

As shown in the Fig.2.7, the particle identification is capable in $p \leq 0.7$ GeV/c for pion and kaon and in $p \leq 1$ GeV/c for pion and proton with TPC. The momentum range for particle identification is extended to higher momentum by utilizing additional information from TOF system. TOF
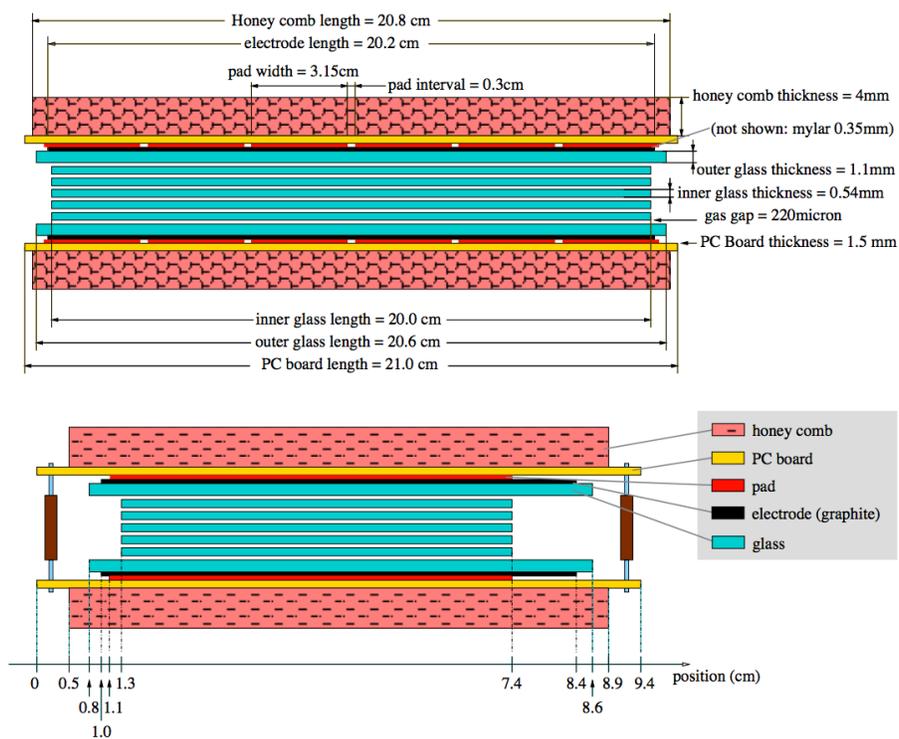
Figure 2.8: TOF view from side and end [63]

measures the time when charged particle pass through the detector after a collision occurs. The mass is given by,

$$m^2 = p^2 \left\{ \left(\frac{t}{L} \right)^2 - 1 \right\},$$

(2.4)

where L is the distance between the TOF detector and the collision vertex and t is the time difference between start time and stop time. The start time is measured with VPD systems which is explained in the following subsection. Fig.2.9 shows the inverse of β as a function of momentum of charged particles determined by TPC. It can be confirmed that separation between pion, kaon and proton is extended to higher momentum than dE/dx by TPC.
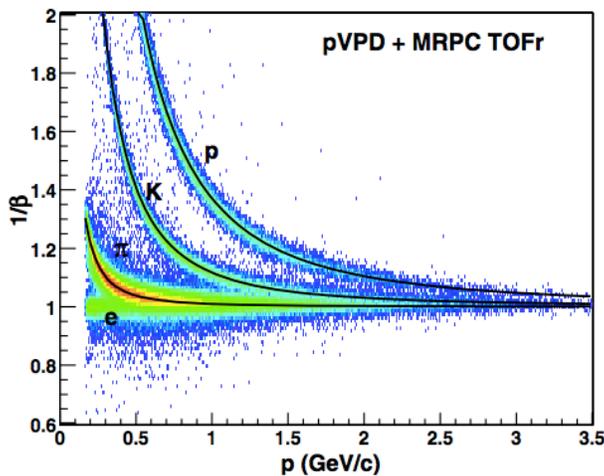
Figure 2.9: β as a function of p [63]

2.2.4 Vertex Position Detector (VPD)

Vertex position detector (VPD) has been installed as the detector which is used for start counter of TOF detector and for minimum bias trigger [64]. In the experiment, tens to hundreds of photons from neutral pion decays are emitted from the collision vertex toward close to the beam pipe. VPD measures these photons to obtain the information of event triggering. Two identical assemblies are located one on each side of the STAR, east and west. The coverage of pseudorapidity region is $4.24 \leq \eta \leq 5.1$. Each VPD assembly consists of nineteen detection units (Fig.2.11) and measures a time up to nineteen times at the maximum in each event. The primary vertex position along the beam line, Z_{vtx} is determined by the times from each VPD assemblies T_{east} and T_{west} and the speed of light c as,

$$Z_{vtx} = c(T_{east} - T_{west})/2.$$

(2.5)
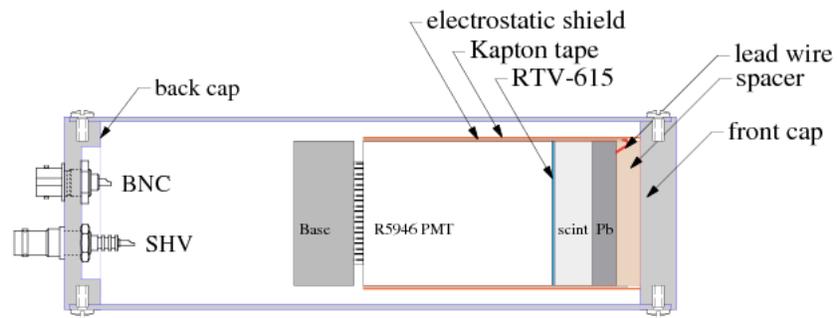
Figure 2.10: Schematic view of VPD [64]
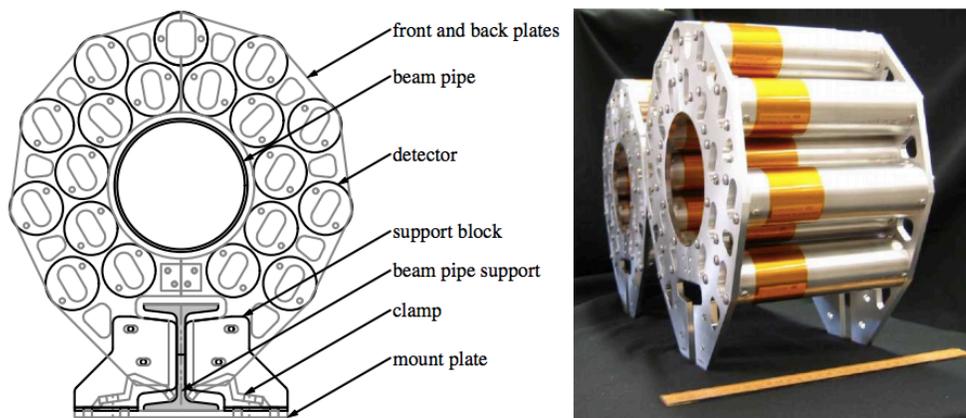
Figure 2.11: A front view of VPD [64]

The event "start time" for Time-of-Flight (TOF) detector to perform particle identification at mid-rapidity is given by,

$$T_{start} = (T_{east} + T_{west})/2 - L/c, \qquad (2.6)$$

where L is the distance between two assemblies and the center of the STAR along the beam direction. Timing resolution can be improved like $1/\sqrt{N}$, where N is the number of channels on each side which detects prompt particles. By taking the average of all the channels which detect prompt particles in an event, the resolution of Z_{vtx} is given by,

$$\sigma(Z_{vtx}) = (c/2)\sigma_{\Delta T} = (c/\sqrt{2})\sigma_{\Delta T} = (c/\sqrt{2})\sigma_0/\sqrt{N}, \qquad (2.7)$$

where T is a measured time T_{east} or T_{west}, $\sigma_{\Delta T}$ is the resolution of the time difference $T_{east} - T_{west}$, σ_T is the resolution of T_{east} or T_{west}, and σ_0 is the time resolution of a single readout detector.

Fig.2.12 shows the channel dependence of the resolution of single detector σ_0 which is performed in several beam energies. This result confirms that the time resolution become better with increase
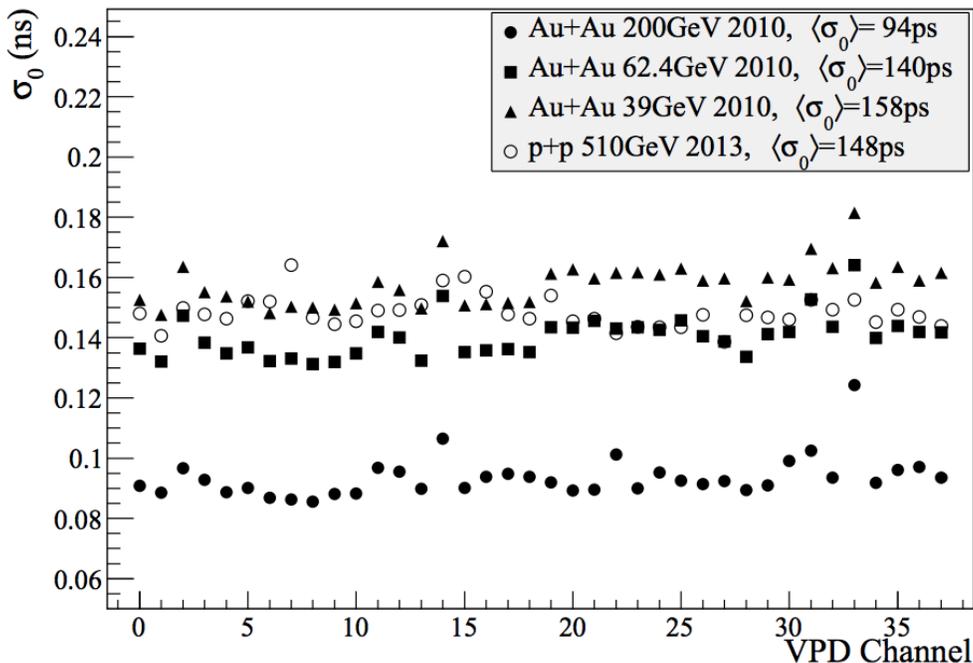
Figure 2.12: Resolutions of single detector [64].

of beam energy. VPD is doing multiple-particle timing and that makes the single detector resolution better. Thus, the resolution become better if beam energy are increased. In Au+Au collisions at top energy at RHIC $\sqrt{s_{NN}} = 200$ GeV, the start-time resolution is 20-30 ps by averaging all the channels which detect the particles, which is negligible compared with the stop time resolution of the TOF detectors (~ 80 ps).

The resolution of primary-vertex position by VPD (Z_{vtx}^{VPD}) is determined by comparison of Z_{vtx}^{VPD} and Z_{vtx}^{TPC} which is reconstructed by the primary tracks of the TPC. Fig.2.13 shows correlation

between Z_{vtx}^{VPD} and Z_{vtx}^{TPC} and Gaussian fit to the difference of vertices $\Delta Z = Z_{vtx}^{VPD} - Z_{vtx}^{TPC}$. The resolution of vertex position from the standard deviation $\sigma(\Delta Z)$ of Gaussian fit, is ~ 1 cm in Au+Au collisions.
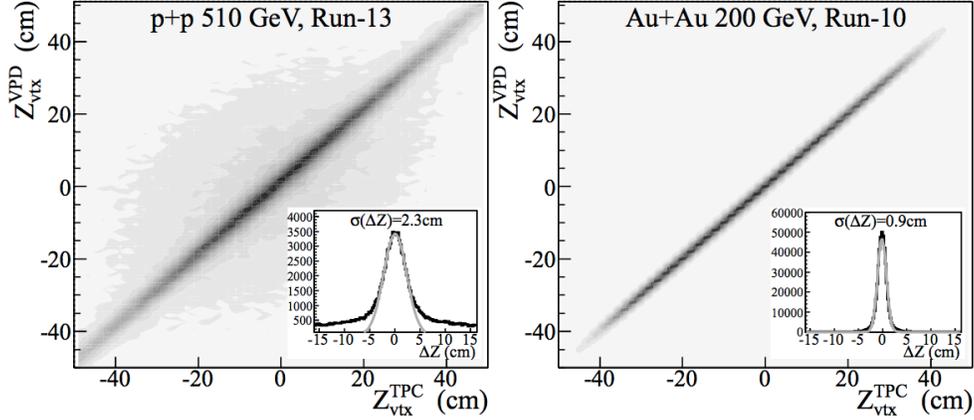
Figure 2.13: Primary vertex position determined by VPD with respect to TPC [64].

2.2.5   Zero Degree Calorimeter (ZDC)

The Zero Degree Calorimeter (ZDC) has been installed with three modules in each side by 18 m from nominal collision point of the STAR along the beam line which correspond to $\theta \leq 4$ mrad (Fig.2.14) [65].   The role of ZDC is to measure the deposited energy of neutrons of spectator in a collision. As shown in Fig.2.15 ZDC is a sampling hadron calorimeter which consists of tungsten plate, layers of undoped optical fibers and photo multiplier tubes.   The dipole magnet is located in front of ZDC for the purpose bending all charged particles and separating neutrons and other neutral particles. ZDC measures Cherenkov light produced by electron shower in a fiber. The coincidence between ZDC and VPD is used for minimum bias trigger.
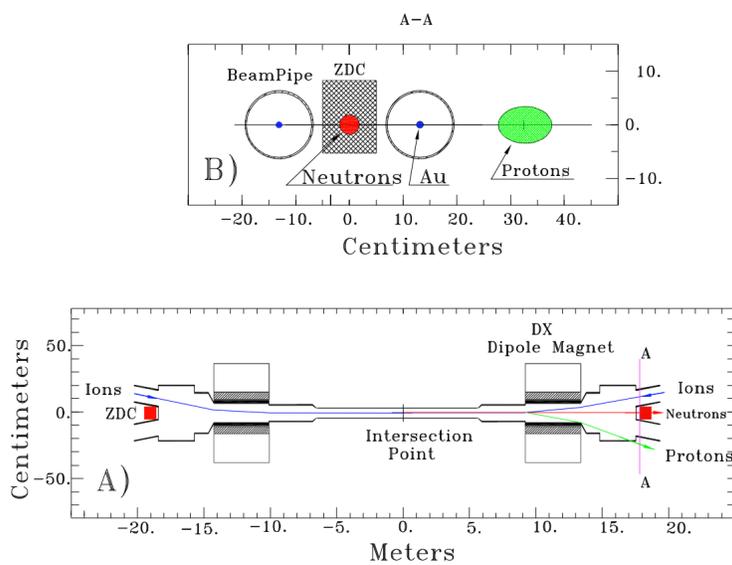
Figure 2.14:   A) Location of ZDC along a beam axis. B) The degree of deflections for neutrons, protons, and Au ions by DX magnet. [65]
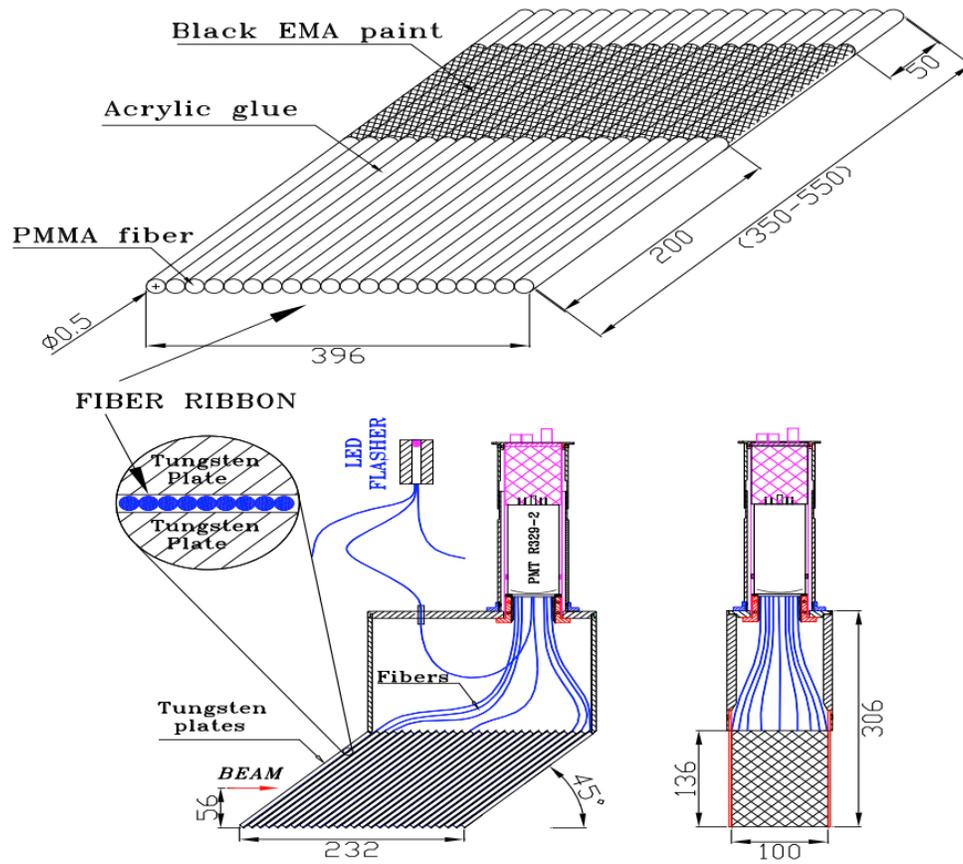
Figure 2.15: ZDC modules [65]

Chapter 3

Data analysis

Analysis methods and analytical formulae are written in this section.

3.1 Data set

The data used in this study is Au+Au collisions at $\sqrt{s_{\mathrm{NN}}} = 200$ GeV collected by the STAR detector system in 2011. The number of events is about 500 million events before run and event selections.

3.1.1 Quality assurance

Run-by-run quality assurance (Run QA) was done by checking mean value of event and track variables. Firstly, bad trigger which has large fluctuations run-by-run mean value for $\langle Vz \rangle$, $\langle Vr \rangle$ and $\langle \eta \rangle$ and are excluded from the analysis. The remaining runs which has outlier value $\pm 3\sigma$ from mean value of each trigger conditions are excluded from the analysis (Fig.3.1).

3.1.2 Event and track selection

The event and track selections used in this study are summarized in Table.3.1. The difference between z position of vertex determined by TPC (V_z^{TPC}) and that by VPD (V_z^{VPD}) is required less than 3 cm in order to remove pile-up events. Additional cut for rejection of pile-up events is applied base on RefMult (reference multiplicity in $|\eta| < 0.5$) and the number of tracks matched on TOF detector with requiring $\beta > 0.1$ in $|\eta| < 1$. The tracks from a primary vertex are selected with DCA < 1.0 cm and good reconstruction quality by requiring NHitsFit > 20 and NHitsFit/NHitsPos $>$ 0.52. The acceptance of tracks are limited in $|\eta| < 1$. At the very low momentum region ($p_T <$ 0.2 GeV/c), the tracks which have $p_T < 0.2$ (GeV/c) are not used in this study because of tracking efficiency is quite low.
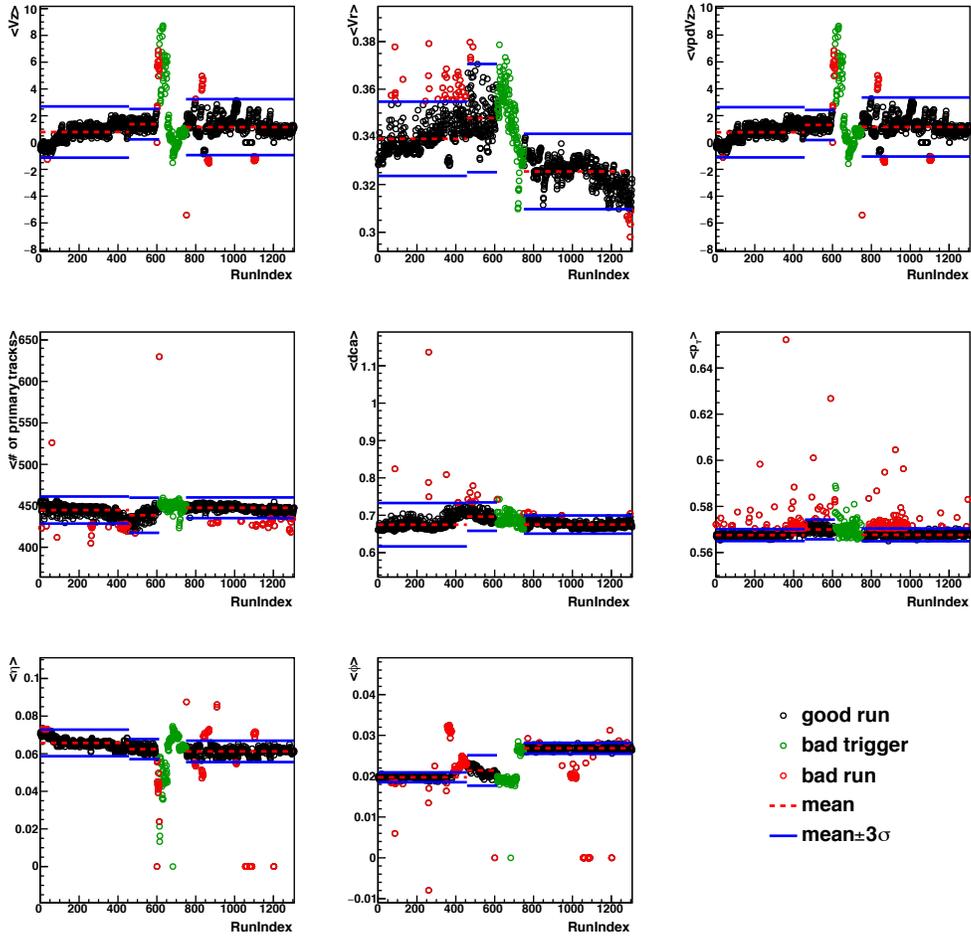
Figure 3.1: Run by run QA for Au+Au $\sqrt{s_{\mathrm{NN}}} = 200$ GeV taken in 2011 data.

Table 3.1: Event and track selections

event selections	
$|V_z|$	< 30 cm
$|V_z^{TPC} - V_z^{VPD}|$	< 3 cm
tofmatched	$>$ RefMult $\times 0.46 - 11$
track selections	
NHitsFit	> 20
NHitsFit/NHitsPos	> 0.52
DCA	< 1 cm
$|\eta|$	< 1
p_T	> 0.2 (GeV/c)

3.2   Centrality determination

Centrality is a good probe for determination of initial geometry. The definition of centrality is the degree of overlapping region of two colliding nuclei in heavy-ion collisions. Centrality is defined by RefMult which is the multiplicity of charged particles measured by TPC within $|\eta| < 0.5$. RefMult has V_z and luminosity dependence, and therefore that is corrected (named RefMultCorr). After those corrections, RefMultCorr is fitted by the simulation of Glauber Monte-Carlo and the simulated distribution is divided into centrality bins because measured multiplicity distribution cannot be directly used for centrality determination due to drop of trigger efficiency in peripheral collisions. Fig.3.2 shows centrality divided RefMultCorr distribution.

3.3   Higher-Order Azimuthal Anisotropy and Event Plane

In this section, the higher-order azimuthal anisotropy of emitted particles and the Fourier expansion of azimuthal distribution with respect to the event plane are introduced. The analysis method of measurement of higher-order azimuthal anisotropy and reconstruction of event plane are also written in this section.

3.3.1   Azimuthal Anisotropy

Azimuthal distributions of emitted particles ($dN/d\phi$) can be written by the Fourier number series with considering periodic boundary condition as follows,

$$\frac{dN}{d\phi} = \frac{x_0}{2\pi} + \frac{1}{\pi}\sum_{n=1}\{x_n\cos(n\phi) + y_n\sin(n\phi)\} \tag{3.1}$$

$$= \frac{x_0}{2\pi}\left\{1 + \sum_{n=1}\left[\frac{x_n}{x_0}\cos(n\phi) + \frac{y_n}{x_0}\sin(n\phi)\right]\right\}, \tag{3.2}$$
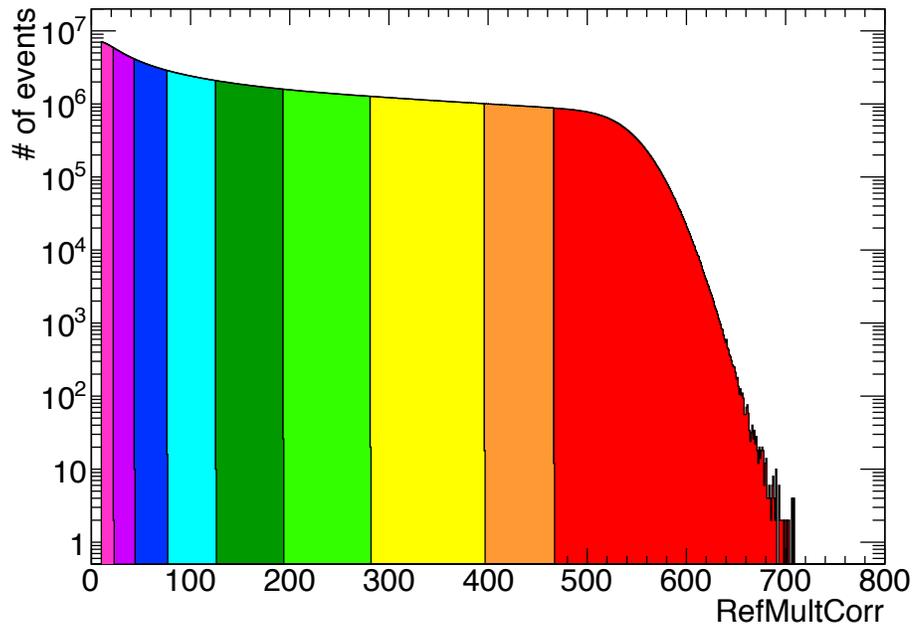
Figure 3.2: V_z and luminosity dependence corrected RefMult (RefMultCorr) distribution for each centrality bin in $\sqrt{s_{\mathrm{NN}}} = 200$ GeV. (Color online) red is 0-5%, orange is 5-10 %, yellow is 10-20 %, light green is 20-30 %, green is 30-40 %, light blue is 40-50 %, blue is 50-60 %, magenta is 60-70 %, violet is 70-80 %.

where the r and ϕ represent the azimuthal distribution and azimuthal the angle of emitted particles. The Fourier coefficient x_n and y_n can be determined by integration as follows,

$$x_n = \int_0^{2\pi} d\phi \frac{dN}{d\phi} \cos(n\phi) \tag{3.3}$$

$$y_n = \int_0^{2\pi} d\phi \frac{dN}{d\phi} \sin(n\phi). \tag{3.4}$$

These integration are translated into the summation of all the particles detected in subevents as follows,

$$\int_0^{2\pi} d\phi \frac{dN}{d\phi} \cos(n\phi) = \sum_i^M w_i \cos(n\phi_i) \equiv Q_x \tag{3.5}$$

$$\int_0^{2\pi} d\phi \frac{dN}{d\phi} \sin(n\phi) = \sum_i^M w_i \sin(n\phi_i) \equiv Q_y \tag{3.6}$$

where i represent the index of all particles up to the multiplicity M of the detector, ϕ_i is azimuthal angle of i-th particles and w_i is the weighting factor, for example p_T, multiplicity and ADC value. The w_i is necessary in order to obtain better resolution of the event plane. A vector $\mathbf{Q} = (Q_x, Q_y)$ is called "flow (Q) vector" and used for event plane determination in the experimental way. Here, Ψ_n is defined as n-th order event plane and correspond to the minor axis of the n-th order polygon,

$$\Psi_n = \frac{1}{n} \tan^{-1}(y_n/x_n), \quad 0 < \Psi_n < \frac{2\pi}{n}. \tag{3.7}$$

Then, the azimuthal distribution $dN/d\phi$ can be re-written with event planes Ψ_n as follows,

$$\frac{dN}{d\phi} = \frac{x_0}{2\pi} \left\{ 1 + \sum_{n=1} \left[\frac{x_n}{x_0} \cos(n\phi) + \frac{y_n}{x_0} \sin(n\phi) \right] \right\} \tag{3.8}$$

$$= \frac{x_0}{2\pi} \left\{ 1 + \sum_{n=1} [v_n \cos\{n(\phi - \Psi_n)\}] \right\}, \tag{3.9}$$

where v_n is the amplitude of azimuthal anisotropy of each harmonics. v_n is defined as

$$v_n = \frac{\sqrt{x_n^2 + y_n^2}}{x_0}, \tag{3.10}$$

$$x_0 = M \langle w \rangle \tag{3.11}$$

In the experimental case, the measured azimuthal distribution of particles $r^{(measured)}(\phi)$ can be written as

$$r^{obs}(\phi) = \frac{x_0}{2\pi} \left\{ 1 + \sum_{n=1} \left[v_n^{obs} \cos\{n(\phi - \Psi_n^{obs})\} \right] \right\}. \tag{3.12}$$

The azimuthal angle of the event plane is experimentally determined by flow vector event-by-event. The azimuthal angle of the event plane Ψ_n^{obs} which is measured in the experiment has different

angle from that of real event plane Ψ_n^{real}. Therefore, Ψ_n^{obs} can be written as a sum of the real event plane Ψ_n^{real} and the difference from the real event plane $\Delta\Psi_n$ as $\Psi_n^{obs} = \Psi_n^{real} + \Delta\Psi_n$. When plenty of number of events exist, the real anisotropy v_n can written by using the measured anisotropy v_n^{obs},

$$
\begin{aligned}
v_n^{obs} &= \left\langle \cos(n[\phi - \Psi_n^{obs}]) \right\rangle & (3.13) \\
&= \left\langle \cos(n[(\phi - \Psi_n) - (\Psi_n^{obs} - \Psi_n)]) \right\rangle & (3.14) \\
&= \langle \cos(n[(\phi - \Psi_n)] \cos(n[\Delta\Psi_n])) \rangle + \langle \sin(n[(\phi - \Psi_n)] \sin(n[\Delta\Psi_n])) \rangle & (3.15) \\
&= \langle \cos(n[(\phi - \Psi_n)]) \rangle \langle \cos(n[\Delta\Psi_n]) \rangle & (3.16) \\
&= v_n \langle \cos(n[\Delta\Psi_n]) \rangle & (3.17) \\
\therefore v_n &= \frac{v_n^{obs}}{\langle \cos(n[\Delta\Psi_n]) \rangle}. & (3.18)
\end{aligned}
$$

where sine terms should be zero because we consider symmetric distribution with respect to the event planes in the experiment and with the assumption that $\phi - \Psi_n$ and $\Delta\Psi_n$ are independent with each other. The denominator of Eq.(3.18) ($\langle \cos(n[\Delta\Psi_n]) \rangle$) is defined as "resolution" of the event plane.

3.3.2   Calibration of event plane

The angle of event plane is reconstructed in event-by-event basis. In the real experiment, the azimuthal distributions of event planes should be flat because we cannot control the reaction plane of two colliding nuclei by control the ion beam. The event planes are reconstructed with charged particles reconstructed by the TPC by utilizing flow vector as follows,

$$
Q_{n,x}^{raw} = \frac{\sum_i w_i \cos(n\phi_i)}{\sqrt{\sum_i w_i}} \tag{3.19}
$$

$$
Q_{n,y}^{raw} = \frac{\sum_i w_i \sin(n\phi_i)}{\sqrt{\sum_i w_i}} \tag{3.20}
$$

$$
\Psi_n^{raw} = \frac{1}{n} \tan^{-1}\left(\frac{Q_{n,y}^{raw}}{Q_{n,x}^{raw}}\right). \tag{3.21}
$$

where i is an index of the tracks w_i is an p_T (for $p_T > 2.0$, $w_i = 2.0$) and ϕ_i is an azimuthal angle of the charged particle.

In the experiment, the azimuthal distribution of event plane is not flat (shown by the black line in Fig.3.3) because of non-uniform acceptance due to the difference of tracking efficiency or the beam conditions. The non-uniform distribution of event planes should be corrected by two steps.

Re-centering Calibration

As a first step, "Re-centering calibration" are applied. The mean value of the flow vector should be 0 and the width of projected onto the x axis and y axis should be same. Re-centering Calibration
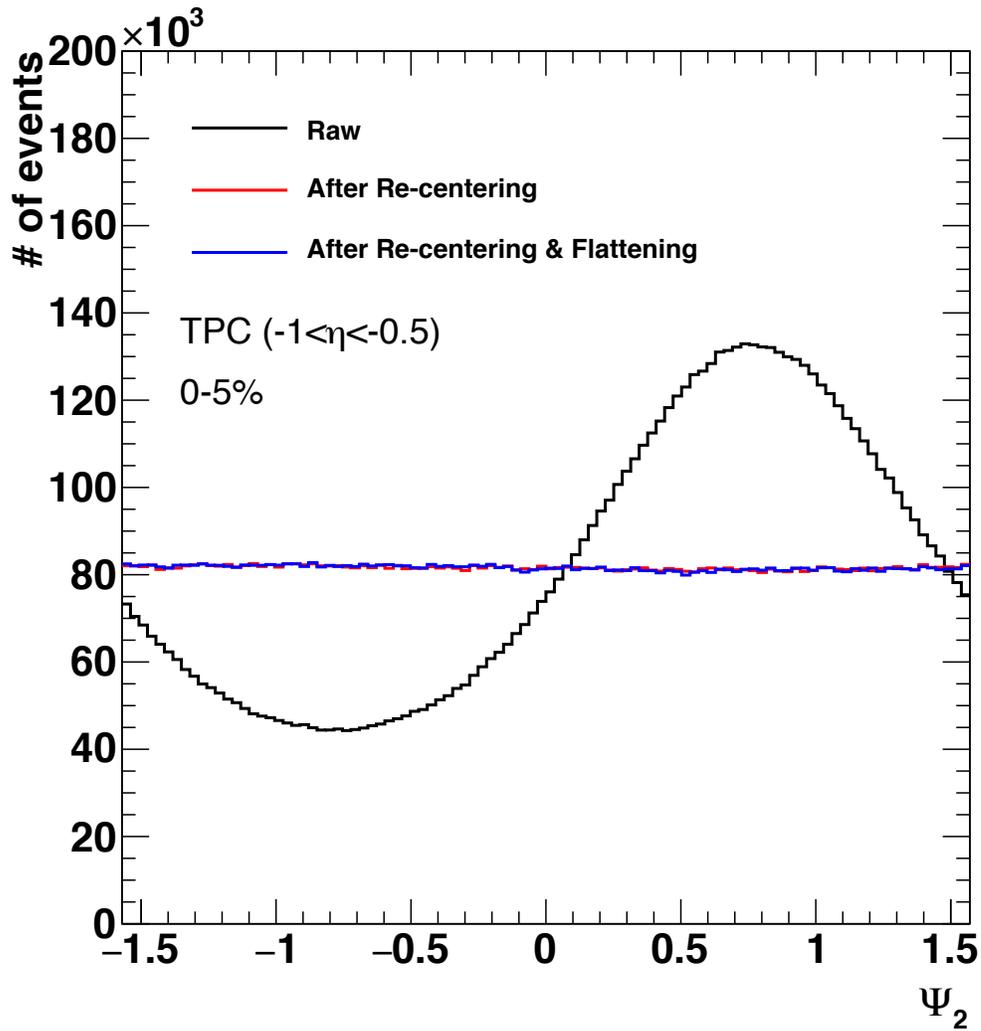
Figure 3.3: The second-order-harmonic event-plane distributions determined by the charged particles reconstructed by the TPC at $-1 < \eta < -0.5$ in 0-5 % centrality, for the no correction, after Re-centering Calibration and after Re-centering and Flattening Calibration.

can correct the observed x or y component of the flow vector respectively as follows,

$$Q_{n,x}^{rec} = \frac{Q_{n,x}^{raw} - \langle Q_{n,x}^{raw} \rangle}{\sigma_{n,x}} \tag{3.22}$$

$$Q_{n,y}^{rec} = \frac{Q_{n,y}^{raw} - \langle Q_{n,y}^{raw} \rangle}{\sigma_{n,y}} \tag{3.23}$$

$$\Psi_n^{rec} = \frac{1}{n} \tan^{-1} \left(\frac{Q_{n,y}^{rec}}{Q_{n,x}^{rec}} \right). \tag{3.24}$$

The Fig.3.4 shows the before Re-centering Calibration (left) and the after calibration (right). The mean is 0 and width is the same both for x and y component. The azimuthal distribution of the event plane shown by the red marker in the Fig.3.3 is almost corrected compared to the observed event plane distribution.

Flattening Calibration

As a second step, "Flattening Calibration" (shifting calibration) is applied. The Re-centering Calibration can almost correct the effect of the detector bias and the beam shifting as mentioned in the previous. But higher moments cannot be corrected by Re-centering Calibration. Flattening Calibration forces event plane distribution to be shifted with Fourier number series as follows,

$$n\Psi_n^{flt} \equiv n\Psi_n^{rec} + n\Delta\Psi_n^{rec} \tag{3.25}$$

$$n\Delta\Psi_n^{rec} \equiv \sum_k^N \{ A_k \cos(kn\Psi_n^{rec}) + B_k \sin(kn\Psi_n^{rec}) \}, \tag{3.26}$$

where A_k and B_k are the Fourier coefficients of event plane distributions. Fourier coefficients for cosine term can be determined by considering $\Delta\Psi_n$ is enough small case as

$$\left\langle \cos kn\Delta\Psi_n^{flt} \right\rangle = \langle \cos(kn\Psi_n^{rec} + kn\Delta\Psi_n) \rangle \tag{3.27}$$

$$= \langle \cos kn\Psi_n^{rec} \cos kn\Delta\Psi_n \rangle - \langle \sin kn\Psi_n^{rec} \sin kn\Delta\Psi_n \rangle \tag{3.28}$$

$$\simeq \langle \cos kn\Psi_n^{rec} \rangle - \langle \sin kn\Psi_n^{rec} \cdot kn\Delta\Psi_n \rangle \tag{3.29}$$

$$= \langle \cos kn\Psi_n^{rec} \rangle$$
$$\quad - \langle \sin kn\Psi_n^{rec} \cdot k \sum_k^N (A_k \cos(kn\Psi_n^{rec}) + B_k \sin(kn\Psi_n^{rec})) \rangle \tag{3.30}$$

$$= \langle \cos kn\Psi_n^{rec} \rangle - kB_k \langle \sin^2 kn\Psi_n^{rec} \rangle \tag{3.31}$$

$$= \langle \cos kn\Psi_n^{rec} \rangle - kB_k \cdot \frac{1}{2} \tag{3.32}$$

$$= 0 \tag{3.33}$$

$$B_k = \frac{2}{k} \langle \cos kn\Delta\Psi_n^{rec} \rangle. \tag{3.34}$$
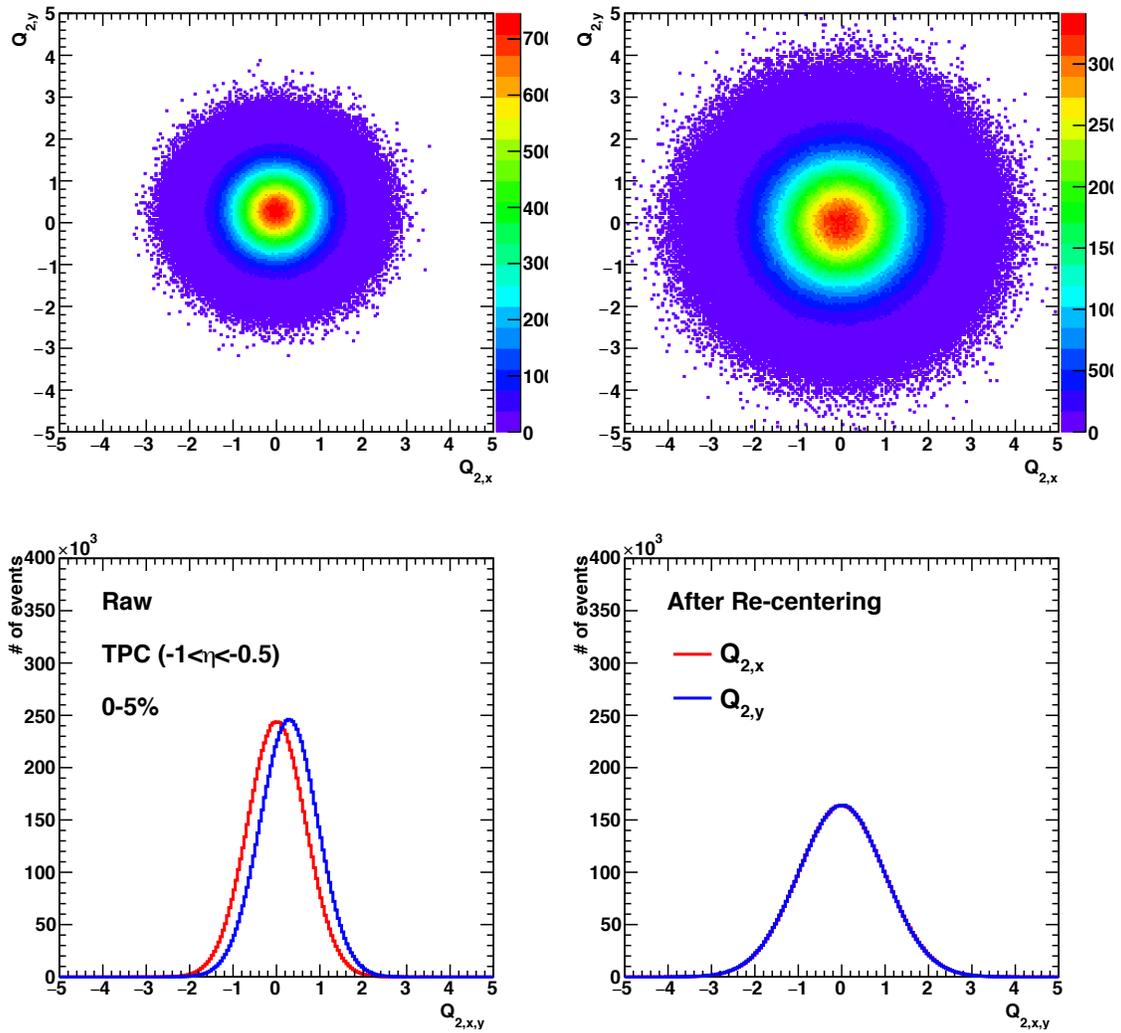
Figure 3.4: 2D (top) and projected (bottom) flow vector distributions before and after re-centering calibration in 0-5 % centrality.

Here, product of sine and cosine of different harmonics are zero because they are orthonormal. For sine term, we can calculate as

$$\left\langle \sin kn\Delta\Psi_n^{flt} \right\rangle \quad = \quad \langle \sin\left(kn\Psi_n^{rec} + kn\Delta\Psi_n\right)\rangle \tag{3.35}$$

$$= \quad \langle \sin kn\Psi_n^{rec}\cos kn\Delta\Psi_n\rangle - \langle\cos kn\Psi_n^{rec}\sin kn\Delta\Psi_n\rangle \tag{3.36}$$

$$\simeq \quad \langle\sin kn\Psi_n^{rec}\rangle + \langle\cos kn\Psi_n^{rec}\cdot kn\Delta\Psi_n\rangle \tag{3.37}$$

$$= \quad \langle\sin kn\Psi_n^{rec}\rangle$$

$$+\langle\cos kn\Psi_n^{rec}\cdot k\sum_k^N \left(A_k\cos\left(kn\Psi_n^{rec}\right) + B_k\sin\left(kn\Psi_n^{rec}\right)\right)\rangle \tag{3.38}$$

$$= \quad \langle\sin kn\Psi_n^{rec}\rangle + kA_k\left\langle\cos^2 kn\Psi_n^{rec}\right\rangle \tag{3.39}$$

$$= \quad \langle\sin kn\Psi_n^{rec}\rangle + kA_k\cdot\frac{1}{2} \tag{3.40}$$

$$= \quad 0 \tag{3.41}$$

$$A_k \quad = \quad -\frac{2}{k}\left\langle\sin kn\Delta\Psi_n^{rec}\right\rangle. \tag{3.42}$$

Flattening Calibration was done up to 8th order Fourier coefficients. The blue marker on the Fig.3.3 shows flattened event plane distribution.

3.3.3   Event Plane Resolution

In the real experiment, the event plane Ψ_n^{exp} fluctuates with respect to the real event plane Ψ_n^{real} because of the real event plane because the emitted particles from nucleus-nucleus collisions are finite. The analytical formula of the observed event plane distributions with respect to the real event plane is given by [66] as

$$\frac{dN}{d\left\{kn(\Psi_n^{exp} - \Psi_n^{real})\right\}} \quad = \quad \frac{1}{\pi}e^{\chi_n^2/2}\left\{1 + z\sqrt{\pi}\left[1 + \mathrm{erf}(z)\right]e^{z^2}\right\} \tag{3.43}$$

$$z \quad = \quad \sqrt{\frac{1}{2}}\chi_n\cos kn\left\{\Psi_n^{obs} - \Psi_n^{real}\right\}, \tag{3.44}$$

where $\chi_n = v_n\sqrt{2M}$ and $\mathrm{erf}(z)$ is the error function. The resolution of the event plane is written as

$$\left\langle\cos[kn(\Psi_n^{obs} - \Psi_m^{real})]\right\rangle = \frac{\sqrt{\pi}}{2\sqrt{2}}\chi_n e^{-\chi^2/4}\left[I_{(k-1)/2}\left(\frac{\chi^2}{4}\right) + I_{(k+1)/2}\left(\frac{\chi^2}{4}\right)\right], \tag{3.45}$$

where I_k is the modified Bessel function of the first kind [67]. This estimation is used when the following assumptions is met,

- emitted particles in the different rapidity window has no correlation with each other,

- the number of particles to be used for reconstruction of the event plane is enough larger than 1,

- the amplitude of the flow does not fluctuate in the same centrality class.

The cosine term of correlation of event planes is expanded as follows,

$$
\begin{aligned}
\left\langle \cos\left(n\left[\Psi_n^A - \Psi_n^B\right]\right)\right\rangle &= \left\langle \cos\left(n\left[\Psi_n^A - \Psi_n^{real}\right]\right) - \left(n\left[\Psi_n^B - \Psi_n^{real}\right]\right)\right\rangle \quad (3.46)\\
&= \left\langle \cos\left(n\left[\Psi_n^A - \Psi_n^{real}\right]\right)\right\rangle \left\langle \cos\left(n\left[\Psi_n^B - \Psi_n^{real}\right]\right)\right\rangle \\
&\quad + \left\langle \sin\left(n\left[\Psi_n^A - \Psi_n^{real}\right]\right)\right\rangle \left\langle \sin\left(n\left[\Psi_n^B - \Psi_n^{real}\right]\right)\right\rangle \quad (3.47)\\
&\simeq \left\langle \cos\left(n\left[\Psi_n^A - \Psi_n^{real}\right]\right)\right\rangle \left\langle \cos\left(n\left[\Psi_n^B - \Psi_n^{real}\right]\right)\right\rangle \quad (3.48)\\
&= \mathrm{Res}\left\{\Psi_n^A\right\} \mathrm{Res}\left\{\Psi_n^B\right\}, \quad (3.49)
\end{aligned}
$$

where $\mathrm{Res}\{\Psi_n^A\}$ and $\mathrm{Res}\{\Psi_n^B\}$ are the resolution of event plane A and B, respectively. Here, sin term should be 0 because the observed event planes with respect to the real event plane should are symmetric. When the detector A and B cover symmetric rapidity range and have the equivalent multiplicity, the event plane resolutions of two detectors Ψ_n^A and Ψ_n^B can be written as follows,

$$
\sqrt{\left\langle \cos\left(n\left[\Psi_n^A - \Psi_n^B\right]\right)\right\rangle} = \mathrm{Res}\left\{\Psi_n^A\right\} = \mathrm{Res}\left\{\Psi_n^B\right\} \quad (3.50)
$$

This method is called "two-subevent method". In another method, the resolution of detector A (Ψ_n^A) can be determined with correlations of three event planes, Ψ_n^B and Ψ_n^C, as follows with assuming common real event plane over all the subevents,

$$
\mathrm{Res}\{\Psi_n^A\} = \sqrt{\frac{\left\langle \cos\left\{n(\Psi_n^A - \Psi_n^B)\right\}\right\rangle \left\langle \cos\left\{n(\Psi_n^C - \Psi_n^A)\right\}\right\rangle}{\left\langle \cos\left\{n(\Psi_n^B - \Psi_n^C)\right\}\right\rangle}}. \quad (3.51)
$$

The resolutions of detector B and C are also by the same way. This method is called "three=subevent method". In this study, event planes are reconstructed with charged particles in three pseudorapidity region of the TPC, $-1 < \eta < -0.5$ (TPCe : Ψ_n^{east}), $0.5 < \eta < 1$ (TPCw : Ψ_n^{west}) and $|\eta| < 0.2$ (TPCm : Ψ_n^{mid}), and their resolutions are estimated by three-subevent method. Fig.3.5 shows correlations of event plane. The resolution of event planes are shown in the later section.
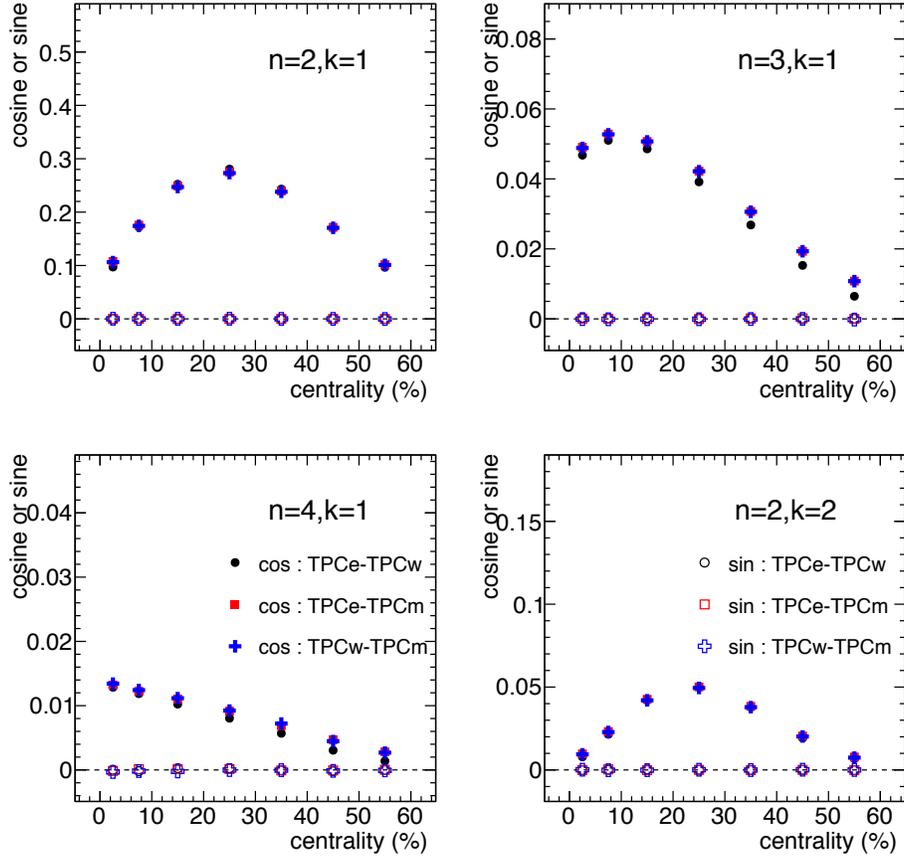
Figure 3.5: Correlations of event plane of $\left\langle \cos[kn(\Psi_n^A - \Psi_n^B)]\right\rangle$ and $\left\langle \sin[kn(\Psi_n^A - \Psi_n^B)]\right\rangle$ as a function of centrality. Solid markers represent cosine term and open markers represent sine term.

3.4   Event Shape Engineering (ESE)

Event Shape Engineering (ESE) is the method to select the flow amplitude which fluctuates event-by-event by selecting a length of flow vector [44]. ESE technique is described in this section.

3.4.1 Event Shape Engineering

The modified flow vector is used for Event Shape Engineering in order to reduce multiplicity bias in an each centrality bin as follows,

$$M = \sum_{i=0} w_i \tag{3.52}$$

$$Q_{n,x} = \frac{\sum_{i=0} w_i \cos(n\phi_i)}{\sqrt{M}} \tag{3.53}$$

$$Q_{n,y} = \frac{\sum_{i=0} w_i \sin(n\phi_i)}{\sqrt{M}} \tag{3.54}$$

$$q_n = \sqrt{Q_{n,x}^2 + Q_{n,y}^2}, \tag{3.55}$$

where q_n is the magnitude of n-th harmonic flow vector. In this study, higher-order-harmonic flow is measured in order to study how two-particle correlations are affected by q_2 selections. The selectivity of q_2 depends on v_2, the multiplicity in the pseudorapidity and the performance of the detector which means angular resolution for the second order harmonics and the linearity of the response to the multiplicity in the pseudorapidity where the detector locates. STAR has installed Beam Beam Counter (BBC) in forward and backward pseudorapidity ($3.4 < |\eta| < 5$, [68]), but the v_2 and the multiplicity at BBC region is small (System Size, Energy, Pseudorapidity, and Centrality Dependence of Elliptic Flow, PHOBOS). Thus, q_2 is selected at mid-rapidity detector TPC with taking rapidity gap from the region for measurements of di-hadron correlations and azimuthal anisotropy.

For the flow vector selection, integrated flow vector distributions are fitted by spline functions which is shown in Fig.3.6. Fig.3.7 shows the distribution of magnitude of flow vector of TPCe in 0-5% centrality with 20% steps q_2 selections. From larger q_2 bin, each bin is named q_2 : 0-20 % (top), q_2 : 20-40 %, q_2 : 40-60 %, q_2 : 60-80 %, q_2 : 80-100 % (bottom).

3.4.2 Event Plane Resolution with q_2 selections

Fig.3.8 shows event plane resolutions of TPCe, TPCw and TPCm. The resolutions of the second-order event plane in q_2 selected events are strongly biased because ESE is calibrated with itself. But for the third and the fourth order, resolutions are not strongly affected by q_2 selections.
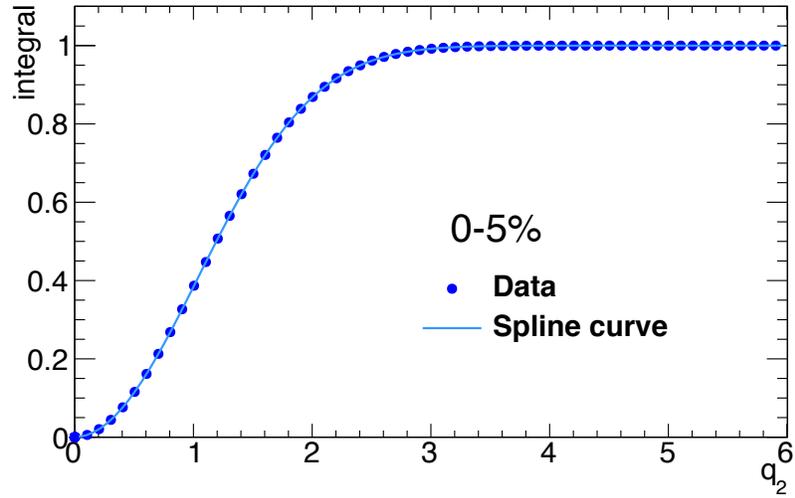
Figure 3.6: Accumulated q_2 distribution of TPCe and spline curve in 0-5 % centrality.
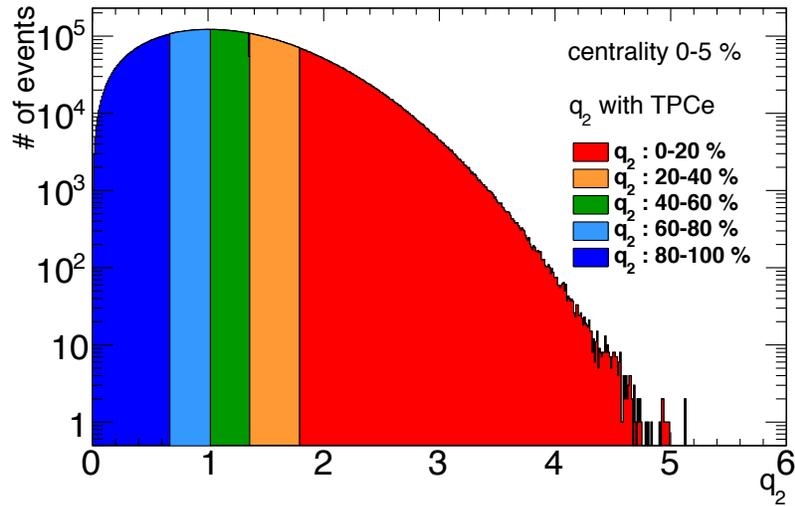
Figure 3.7: The flow vector distributions of each q_2 class of TPCe in 0-5% centrality.
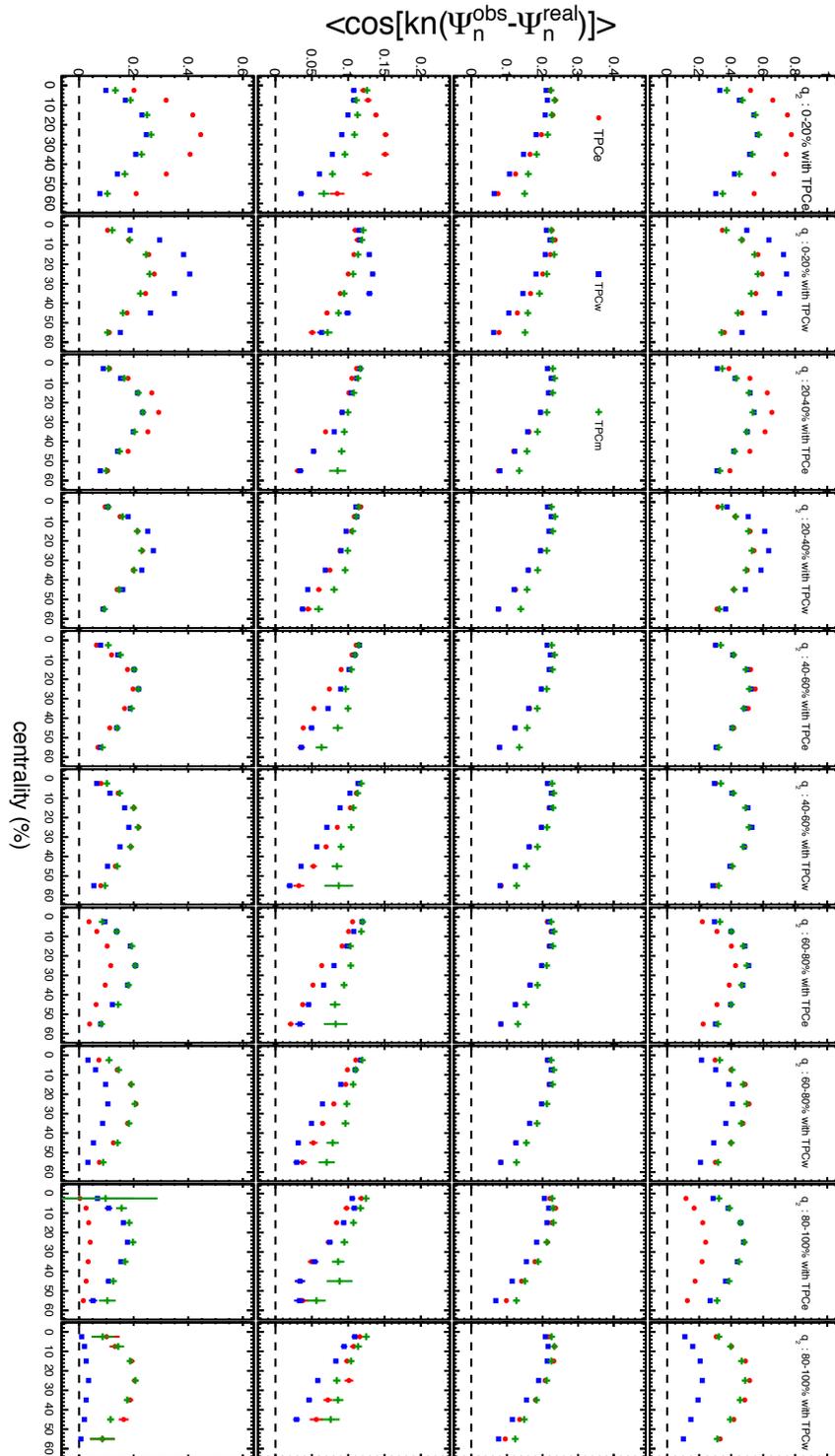
Figure 3.8: Resolutions of event plane determined by three sub-event method as a function of centrality in each q_2 class.

3.5   Measurement of two-particle correlations

Two-particle correlations have been used to study jet-like yield and azimuthal anisotropy. The two-particle spatial-proportional distribution function can be written in the ratio of distributions of two particle possibility over the product of single particle probability distributions as follows,

$$C(\Delta\phi, \Delta\eta) = \frac{P(\phi^t, \phi^a, \eta^t, \eta^a)}{P(\phi^t, \eta^t)P(\phi^a, \eta^a)}, \tag{3.56}$$

where $\phi^{t,a}$ and $\eta^{t,a}$ are azimuthal angle and pseudo-rapidity of trigger and associate particles, and $\Delta\phi = \phi^a - \phi^t$ and $\Delta\eta = \eta^a - \eta^t$ are relative angle of trigger and associate particles. In case of real data analysis, numerator means that both trigger and associate particles exist in relative angles $\Delta\phi$ and $\Delta\eta$ in the same event, and the meaning of denominator is that trigger particle and associate particle exist in relative angles $\Delta\phi$ and $\Delta\eta$ mutually independently. We can measure only pair yield in relative angles experimentally, probability P is written in the following formula,

$$P(\phi^t, \phi^a, \eta^t, \eta^a) = \frac{1}{N^{pair}}Y(\Delta\phi, \Delta\eta). \tag{3.57}$$

Then, N^{pair} is the number of all pairs. Therefore correlation function can be written as follows,

$$C(\Delta\phi, \Delta\eta) = \frac{N_{mix}^{pair}}{N_{real}^{pair}}\frac{Y_{real}^{pair}(\Delta\phi, \Delta\eta)}{Y_{mix}^{pair}(\Delta\phi, \Delta\eta)}. \tag{3.58}$$

This formula can be understood as follows. In the real experiment, event mixing means that
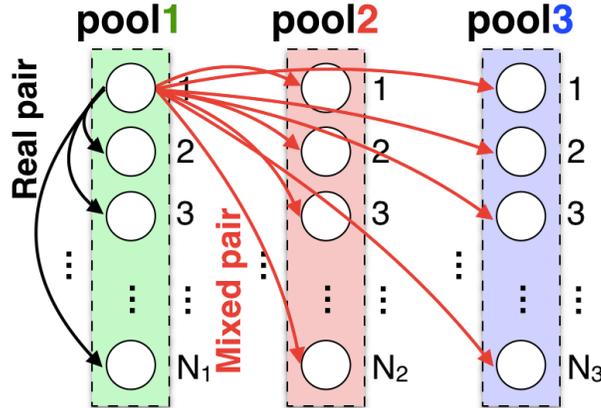
Figure 3.9: Image of taking real pairs and mixed pairs.

extracting physics signal by dividing real events which has physics signals and acceptance effects of detectors by mixed events which have only acceptance limitation effects. In order to reduce effects of collision vertex and difference of multiplicities, manually similar events are needed to make mixed events. Mixed events are calculated in the following centrality class and vertex-z class and the second-order event-plane class in order to estimate an acceptance effect,

- centrality : 5 % steps

- V_z : 6cm steps

- Ψ_2 : $\pi/8$ (rad) steps.

Two-particle correlations are measured with various p_T combinations as shown in the following list in order to comprehensively understand path-length dependence of jet modification and medium response to traverse of high momentum particles.

- trigger particles : 2-4 and 4-10 (GeV/c)

- associate particles : 0.5-1, 1-2, and 2-4 (GeV/c)

Fig.3.10 shows azimuthal relative angle distributions of real and mixed events and correlation function. As seen in the figure, the acceptance effect is corrected after divided by mixed-event pairs.
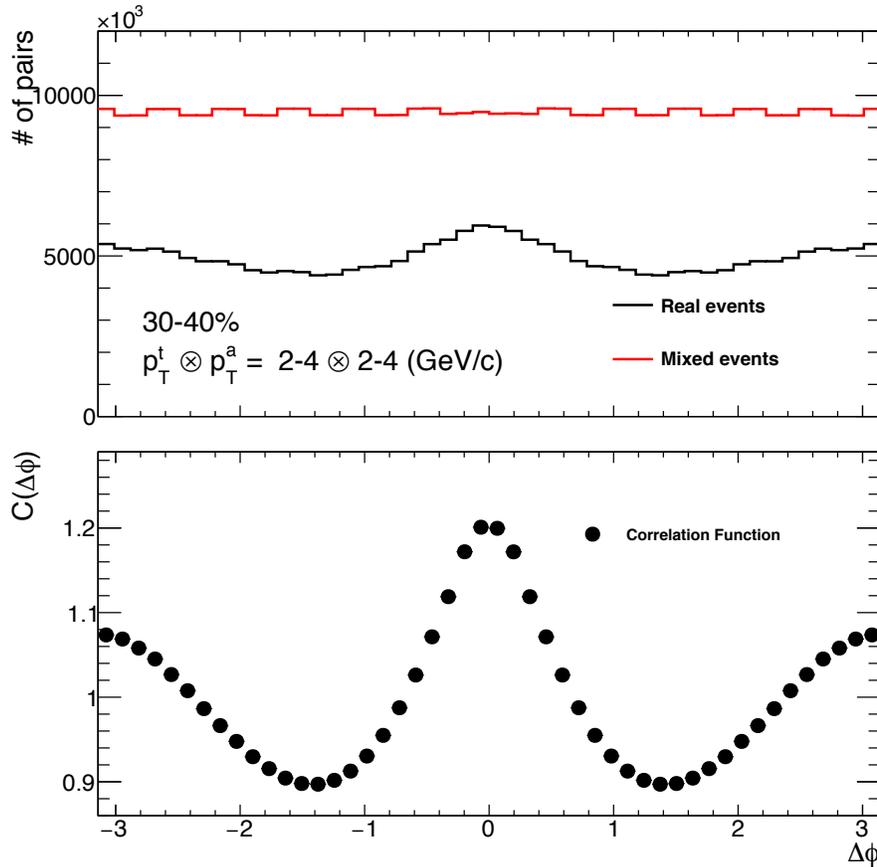
Figure 3.10: (Top) azimuthal distributions of real (black) and mixed events (red). (Bottom) Correlation function $C(\Delta\phi)$ after divided by mixed pairs.

3.5.1   Rejection of merged and split tracks

In this subsection, how to reject inefficiency of pair reconstructions.

Two track resolution

In the real experiment, sometimes very close two tracks can be reconstructed as a single track (track merging) and single track can be reconstructed as two tracks (track splitting). The signal of two-particle correlations around $\Delta\phi = 0$ and $\Delta\eta = 0$ are smeared due to track merging and splitting effect. As seen in Fig.3.11, track merging effect can observed when two tracks share the same pads in one track crossing the other track, and track splitting effect can observed when two tracks which have very similar momentum run in parallel.
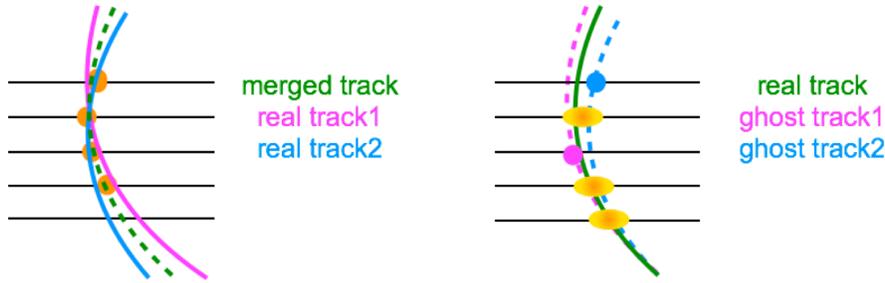
Figure 3.11: Image of track merging (left) and splitting (right).

Fig.3.12 shows unlike-sign($trig \otimes asso = + \otimes -$ and $+ \otimes -$) and like-sign($trig \otimes asso = + \otimes +$ and $- \otimes -$) correlation functions. As seen in Fig.3.12, dips are observed due to track-merging effect and the region depends on charge combination of two tracks.   The dip region also depends on a
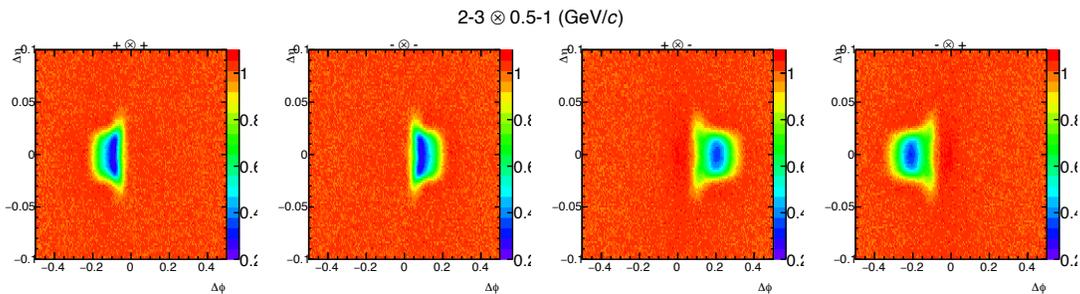
Figure 3.12:   2D correlation functions around $(\Delta\phi, \Delta\eta)=(0,0)$ with positive⊗positive, negative⊗negative, positive⊗negative and negative⊗positive. Momentum ranges are 2-3 (GeV/c) for trigger particles and 0.5-1 (GeV/c) for associate particles.

magnetic field and momenta of two tracks because the orbit and curvature depend on the vector of Lorentz force and curvature of the particles, respectively.

Rejection of merged and split tracks

In this subsection, how to reject merged and split tracks is introduced. In a magnetic field B, charged particles move by being subject to Lorentz force as Fig.3.13. Let V be a primary vertex
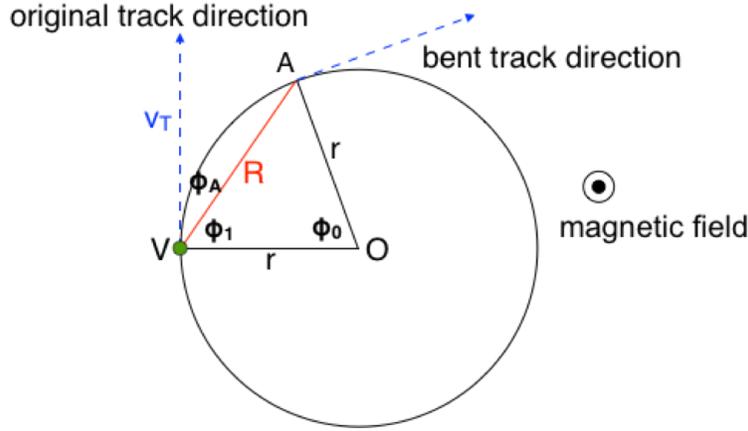
Figure 3.13: Image of movement of a charged particle in a magnetic field.

of the collision, O be a centre of the circular motion of the particle and let A be a position of the charged particle t second after. Equation of motion of the charged particle can be written as follows,

$$qv_T B = \frac{mv_T^2}{r}, \tag{3.59}$$

where q is the charge of the particle, v_T is the velocity of the particle, B is a magnitude of magnetic field, m is a mass of the particle, r is the radius of a circular motion. If you solve the equation for r,

$$r = \frac{qB}{p_T} \quad (\because mv_T = p_T)(\mathrm{CT/(J/(m/s))}) \tag{3.60}$$

$$= \frac{1}{0.3} \cdot \frac{qB}{p_T} \quad (\mathrm{eT/(GeV}/c)). \tag{3.61}$$

Because $\triangle$OVA in Fig.3.13 is a isosceles triangle, the relative angle ϕ_A between initial vector of the particle and the line segment VA can be written as follows,

$$\phi_1 = (\pi - \phi_0)/2 \tag{3.62}$$
$$\phi_A + \phi_1 = \pi/2 \tag{3.63}$$
$$\therefore \phi_A = \phi_0/2, \tag{3.64}$$

where ϕ_0 is $\angle$ AOV and ϕ_1 is $\angle$ OVA. If you apply the Cosine theorem to $\triangle$OVA, the length of the line segment VA, R, can be written as

$$R^2 = r^2 + r^2 + 2r^2 \cos(\phi_0) \tag{3.65}$$

$$\cos(\phi_0) = 1 - \frac{R^2}{2r^2} \tag{3.66}$$

$$\cos(2\phi_A) = 1 - \frac{R^2}{2r^2} \tag{3.67}$$

$$1 - 2\sin^2(\phi_A) = 1 - \frac{R^2}{2r^2} \tag{3.68}$$

$$\sin(\phi_A) = \frac{R}{2r} \tag{3.69}$$

$$\therefore \phi_A = sin^{-1}\left(\frac{R}{2r}\right) \tag{3.70}$$

Therefore, moving direction of the charged particle in a transverse plane at a certain distance from the primary vertex can be expressed with Eq.(3.61) and Eq.(3.70) as,

$$\phi^* = \phi - \sin^{-1}\left(\frac{0.3 \cdot q \cdot B \cdot R}{2p_T}\right). \tag{3.71}$$

When transverse momenta of two tracks (p_T^t and p_T^a) are different, two close tracks cross at a different radius in the TPC. In this study, in order not to reject truly identified pair, a relative
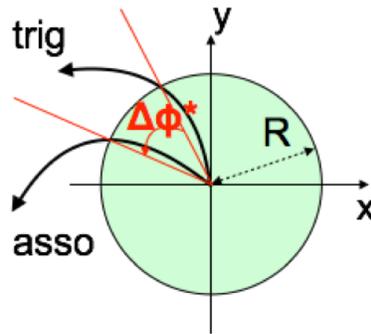
Figure 3.14: Schematic view of $\Delta\phi^*$ between two particles at certain radius R.

moving direction $\Delta\phi^*$ (image is shown in Fig.3.14) is calculated at the several radii (r = 0.60, 0.75, 0.90, 1.05, 1.20, 1.35, 1.50, 1.65, 1.80, 1.95 (m)). When track merging and splitting is observed, two tracks cross or their distance become very close. The minimum value $\Delta\phi^*_{min}$ is estimated with $\Delta\phi^*$ in several radii as seen in Fig.3.16. As seen in Fig.3.16, the dip is gathered into $\Delta\phi^*_{min} = 0$. The two-dimensional distributions are projected to $\Delta\phi^*_{min}$ and $\Delta\eta$ within $|\Delta\eta| < 0.05$ and $|\Delta\phi^*_{min}| < 0.05$ respectively and fitted by Gaussian functions Fig.3.17. The cut regions are determined by 3σ of fitting parameter which is shown in Fig.3.18.
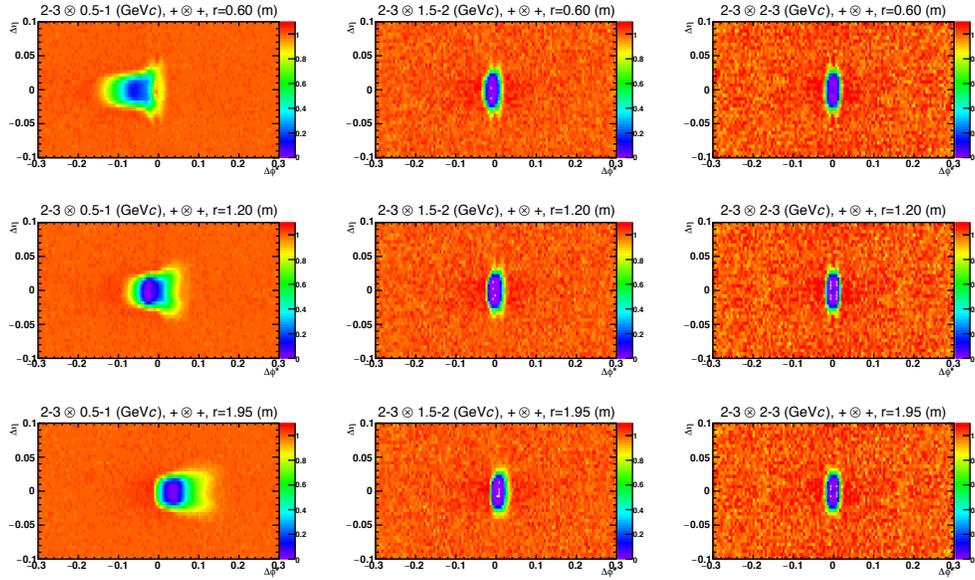
Figure 3.15: 2D $\Delta\phi^*$-$\Delta\eta$ correlations with 2-3 (GeV/c) positively charged trigger particles and 0.5-1 (left column), 1.5-2 (middle column) and 2-3 (right column) positively charged associate particles in $r = 0.60$ (top row), $r = 1.20$ (middle row) and $r = 1.95$ (m) (bottom row).
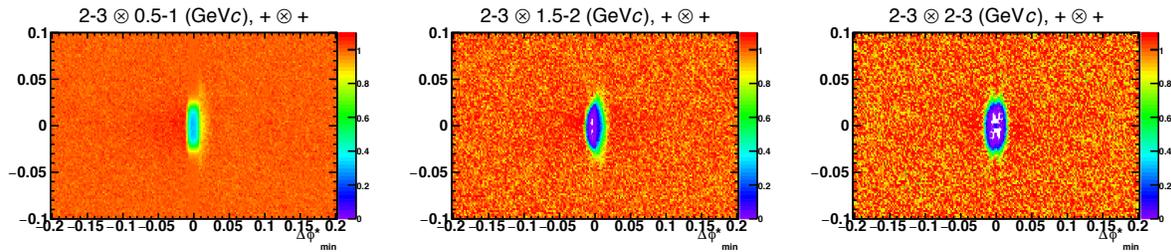
Figure 3.16: 2D $\Delta\phi^*_{min}$-$\Delta\eta$ correlations with 2-3 (GeV/c) positively charged trigger particles and 0.5-1 (left column), 1.5-2 (middle column) and 2-3 (right column) positively charged associate particles.
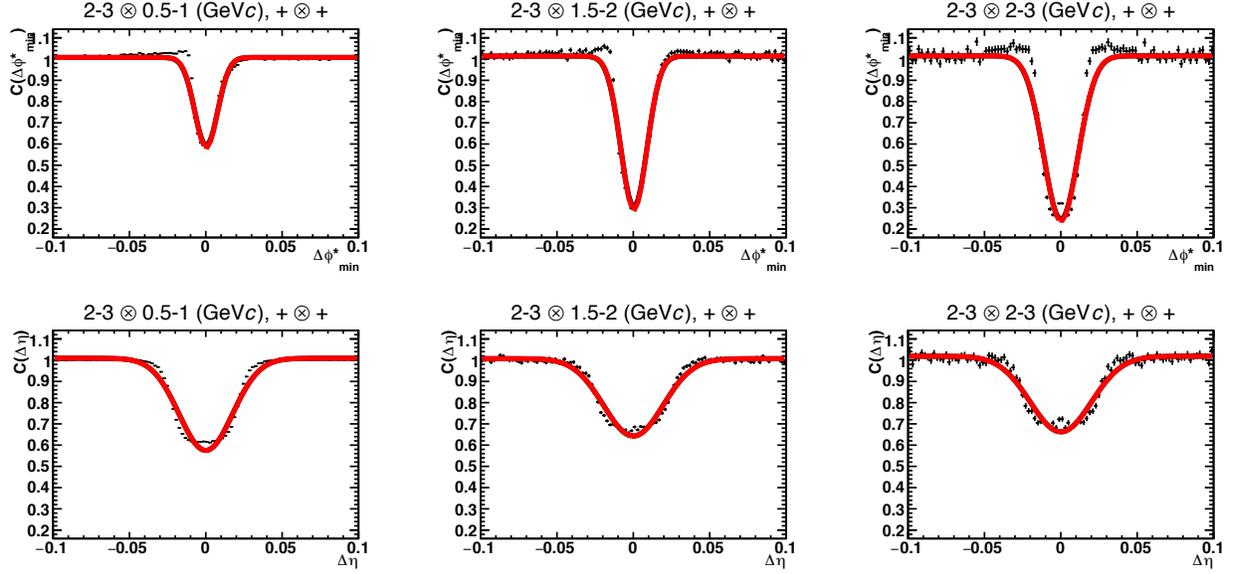
Figure 3.17: Projected $\Delta\phi^*_{min}$ and $\Delta\eta$ correlations fitted by Gaussian functions. Projected regions are $|\Delta\eta| < 0.05$ for projection to $\Delta\phi^*_{min}$ and $|\Delta\phi^*_{min}| < 0.05$ for projection to $\Delta\eta$.

3.5.2   Two-particle correlations with respect to the event plane

Event plane is measured in $\eta < -0.5 (\eta > 0.5)$, and correlations with respect to event plane is analyzed in $\eta > 0$ ($\eta < 0$) in order to reduce auto-correlation effect for reconstruction of event plane as shown in Fig.3.19.   Relative angle of trigger particle with respect to event plane is defined as $\phi_s = \phi^{trig} - \Psi_2$ as shown in Fig.3.20.

3.6   Subtraction of flow background

In heavy-ion collisions, a large number of combinatorial background exist as an underlying event. In order to extract jet-correlated yield, uncorrelated background contributions from higher-order-harmonic collective flow should be subtracted from measured correlations. In this section, the method of determination of a background shape and how to subtract it are presented.
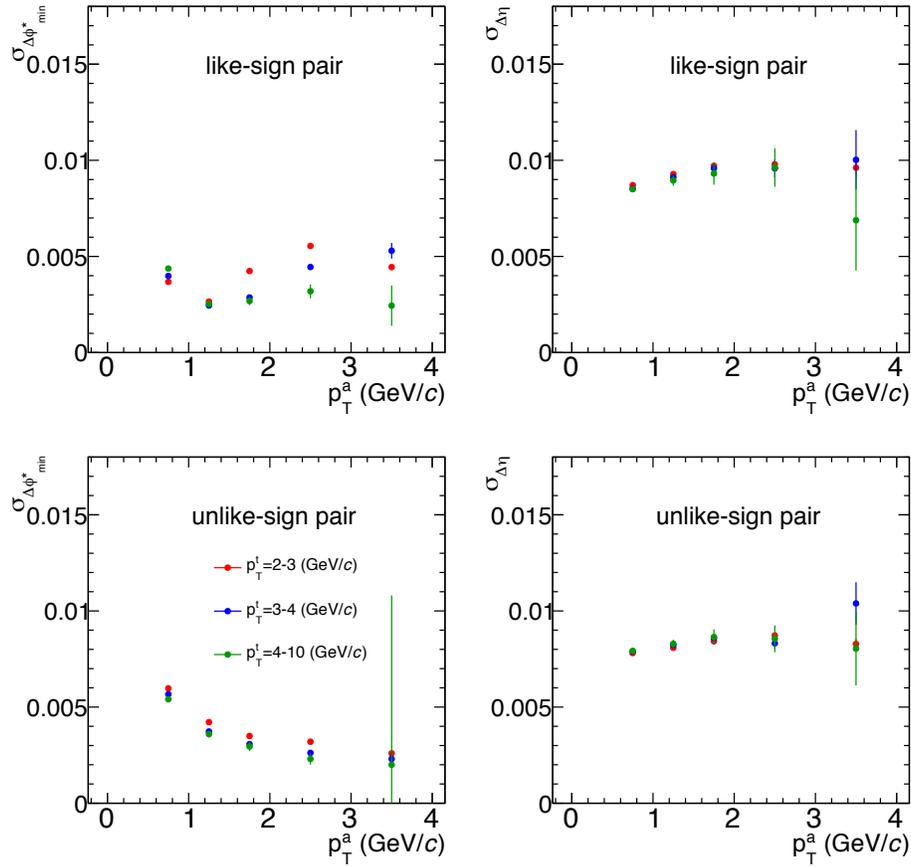
Figure 3.18: Gaussian width of $\Delta\phi^*_{min}$ (top) and $\Delta\eta$ (bottom) as a function of p^a_T with 2-3 (red), 3-4 (blue) and 4-10 (GeV/c) trigger particles.
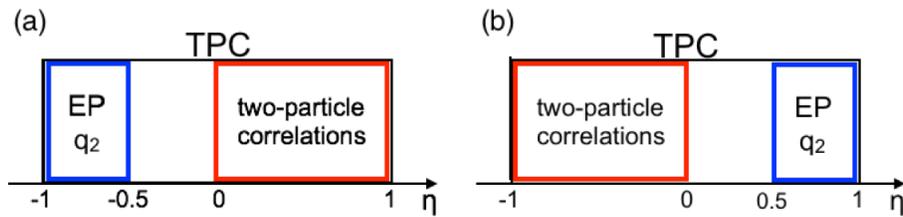
Figure 3.19: Subevent division for event plane reconstructions and measurements of two-particle correlations. Pseudorapidity gap between subevents are 0.5 in order to reduce auto-correlation. Case (a) and case (b) are averaged after checking their consistency.
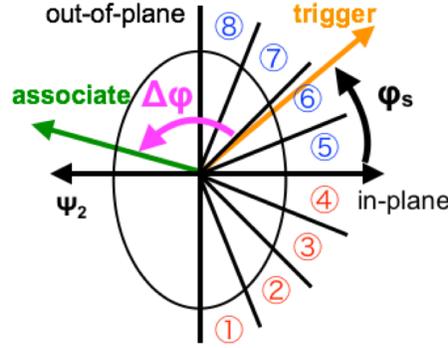
Figure 3.20: Schematic picture of trigger angle binning with respect to the second-order event plane. $\Delta\phi = \phi^a - \phi^t$ is the relative angle of associate particle with respect to the trigger particle. $\phi_s = \phi^t - \Psi_2$ represents the relative angle of trigger particle with respect to the second order event plane.

3.6.1 Flow distributions of azimuthal pair correlations

In case of single-particle flow is written as Eq.(3.1), and then in the case of two-particle correlation, flow distributions can be written as,

$$\frac{dN^{ta}}{d(\Delta\phi)} = \int_0^{2\pi} d\phi^t \frac{dN^t}{d\phi^t} \frac{dN^a}{d\phi^a} \tag{3.72}$$

$$\propto \int d\phi^t \left\{ 1 + 2\sum_k v_k^t \cos k(\phi^t - \Psi_k) \right\} \left\{ 1 + 2\sum_l v_l^a \cos l(\phi^a - \Psi_l) \right\}. \tag{3.73}$$

where N^{ta} is the number of pairs, $\Delta\phi = \phi^a - \phi^t$ is a relative angle between trigger and associate particles, N^t and N^a are the number of trigger and associated particles, ϕ^t and ϕ^a are azimuthal angle of the trigger and associate particles, v_k^t and v_l^a are the amplitude of azimuthal anisotropy,

respectively. Eq:3.73 can be written without ϕ^a by substituting as $\phi^a = \Delta\phi + \phi^t$,

$$
\begin{aligned}
\frac{dN^{ta}}{d(\Delta\phi)} \quad &\propto \quad \int d\phi^t \left\{ 1 + 2\sum_k v_k^t \cos k(\phi^t - \Psi_k) \right\} \left\{ 1 + 2\sum_l v_l^a \cos l(\phi^t + \Delta\phi - \Psi_l) \right\} \quad (3.74) \\
&= \quad \int d\phi^t \left\{ 1 + 2\sum_k v_k^t \cos k(\phi^t - \Psi_k) + 2\sum_l v_l^a \cos l(\phi^t + \Delta\phi - \Psi_l) \right. \\
&\qquad \left. + 4\sum_k \sum_l v_k^t v_l^a \cos k(\phi^t - \Psi_k) \cos l(\phi^t + \Delta\phi - \Psi_l) \right\} \\
&= \quad \int d\phi^t \left\{ 1 + 2\sum_k v_k^t \cos k(\phi^t - \Psi_k) + 2\sum_l v_l^a \cos l(\phi^t + \Delta\phi - \Psi_l) \right. \\
&\qquad + 2\sum_k \sum_l v_k^t v_l^a \left\{ \left[(k+l)\phi^t - k\Psi_k - l\Psi_l + l\Delta\phi \right] \right. \\
&\qquad \left. \left. + \left[(k-l)\phi^t - k\Psi_k + l\Psi_l - l\Delta\phi \right] \right\} \right\} \\
&= \quad \int d\phi^t \left\{ 1 + 2\sum_k v_k^t v_k^a \cos(k\Delta\phi) \right\} \quad (3.75) \\
&\qquad (\because \int d\phi \cos n\phi = 0). \quad (3.76)
\end{aligned}
$$

where b_0 is a normalization factor. Therefore, distribution of two-particle correlations ($F(\Delta\phi)$) can be written as follows

$$
F(\Delta\phi) = b_0 \left\{ 1 + \sum_{n=1} \left[2v_n^t \cdot v_n^a \cos n(\Delta\phi) \right] \right\} \quad (3.77)
$$

3.6.2 Determination of Flow-Background shape via Data-Driven Monte-Carlo simulation

In this study, the real-event pair distributions are normalized by mixed-event ones with event plane aligned. In this case, the analytical formula is difficult to describe but reconstruction via Monte-Carlo simulation is not difficult because it can be analyzed as same way as experimental way. Additionally, we can easily input non-linear correlation terms such as correlation between different-order flow harmonics and Ψ_n aligned mixing into flow simulation by the Monte-Carlo method. The following is analysis procedure of flow Monte-Carlo simulations.

1. Generation of Event Plane

The 2nd (Ψ_2) and the 3rd (Ψ_3) order event plane is generated at first at random because Ψ_2 and Ψ_3 do not correlated with each other. It is found that the fourth-order event plane Ψ_4 is correlated with Ψ_2 [reference]. So Ψ_4 is smeared from Ψ_2 as following to the ratio of $v_4\{\Psi_2\}$

to $v_4\{\Psi_4\}$.

$$
\begin{aligned}
v_4\{\Psi_2\} &= \langle\cos 4[(\phi - \Psi_2)]\rangle && (3.78)\\
&= \langle\cos 4[(\phi - \Psi_4) + (\Psi_4 - \Psi_2)]\rangle && (3.79)\\
&= v_4\{\Psi_4\}\langle\cos 4[(\Psi_4 - \Psi_2)]\rangle && (3.80)\\
\therefore \langle\cos 4[(\Psi_4 - \Psi_2)]\rangle &= v_4\{\Psi_2\}/v_4\{\Psi_4\}. && (3.81)
\end{aligned}
$$

The amplitude of correlation $\langle\cos 4[(\Psi_4 - \Psi_2)]\rangle$ is converted into χ_{42} parameter by Eq.(3.82) as,

$$
\left\langle\cos[4(\Psi_4^{real} - \Psi_2^{real})]\right\rangle = \frac{\sqrt{\pi}}{2\sqrt{2}}\chi_{42}e^{-\chi_{42}^2/4}\left[I_{(k-1)/2}\left(\frac{\chi_{42}^2}{4}\right) + I_{(k+1)/2}\left(\frac{\chi_{42}^2}{4}\right)\right]. \quad (3.82)
$$

Fig.3.21 is centrality dependence of the ratio $v_4\{\Psi_2\}/v_4\{\Psi_4\}$. Therefore, Ψ_4^{real} is determined by $\Psi_4^{real} = \Psi_2^{real} + \Delta\Psi_{42}$ and the angle Ψ_4^{obs} is determined as

$$
\begin{aligned}
\Psi_4^{obs} &= \Psi_4^{real} + \Delta\Psi_4 && (3.83)\\
&= \Psi_2^{real} + \Delta\Psi_{42} + \Delta\Psi_4. && (3.84)
\end{aligned}
$$

2. Determination of single-particle distributions

Azimuthal distributions of single particle can be determined because event planes are generated in 1st step and amplitude of v_n in each p_T bins are already known.

3. Generation particles

Particles are generated from the distributions at random.

4. Calculation of a relative angle between two particles

Two-particle correlations are calculated by particles generated as a 3rd step.

Analytical formula is difficult to describe in event plane dependent correlations because the resolution of event plane is not ideal value. However, in Monte-Carlo simulations, calculations of flow background are not so difficult. Flow Monte carlo simulation is done as follows.

1. Generation of particles

From the 1st to 3rd step of upper description are the same as upper description.

2. Smearing of event plane

Event-plane angle is smeared from real event plane Ψ_2^{real} along to the probability distribution function of $\Psi_2^{smeared}$ with respect to Ψ_2^{real} shown by Fig.3.22.

3. Calculation of a relative angle between two particles

two-particle correlations are analyzed by particles generated at the 3rd step with trigger selecting trigger particle's angle with respect to smeared event plane $\Psi_n^{smeared}$.
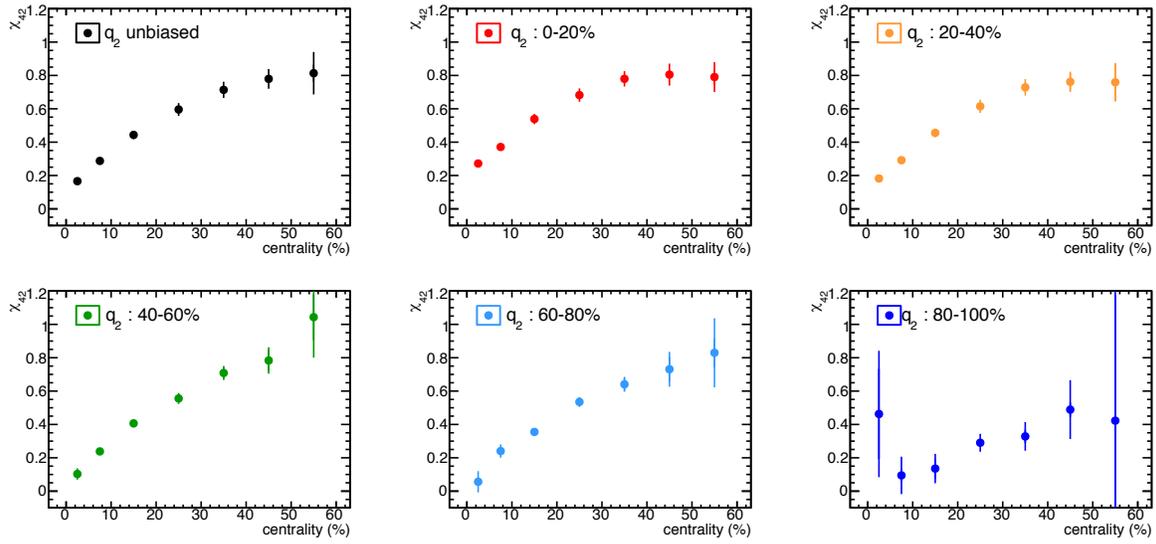
Figure 3.21: $\langle \cos 4[(\Psi_4 - \Psi_2)] \rangle$ as a function of centrality in each q_2 bin.
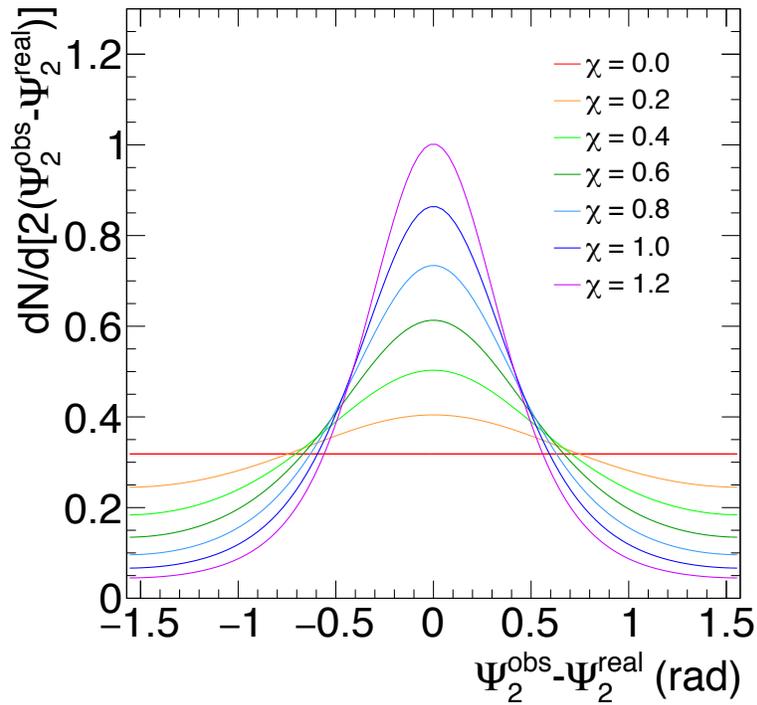
Figure 3.22: Probability distributions of observed event plane with respect to the real event plane in some typical χ values.

3.6.3   Zero Yield At Minimum (ZYAM)

Measured correlation function $C(\Delta\phi)$ is assumed to compose of two component, jet-like yield signal $J(\Delta\phi)$ and flow background $F(\Delta\phi)$. In addition, the signal $J(\Delta\phi)$ on the near side and away side is assumed to be completely separated. With those assumption, the determined flow backgrounds are subtracted with Zero Yield At Minimum (ZYAM) assumption: the yield should be zero at the smallest yield point. Therefore, flow subtracted jet distribution ($J(\Delta\phi)$) can be written as

$$J(\Delta\phi) = C(\Delta\phi) - F(\Delta\phi), \tag{3.85}$$

here, b_0 correspond to a background level which is explained in the following section.

Fig.3.23 shows inclusive-trigger correlations with background fitted to the experimental data. Fig.3.24 shows event-plane dependent correlations with respect to the event plane shown with fitted background distributions. The background distributions reproduce the shape without around $\Delta\phi = 0$ and $\Delta\phi = \pi$ where remaining jet-correlated yield can be observed.
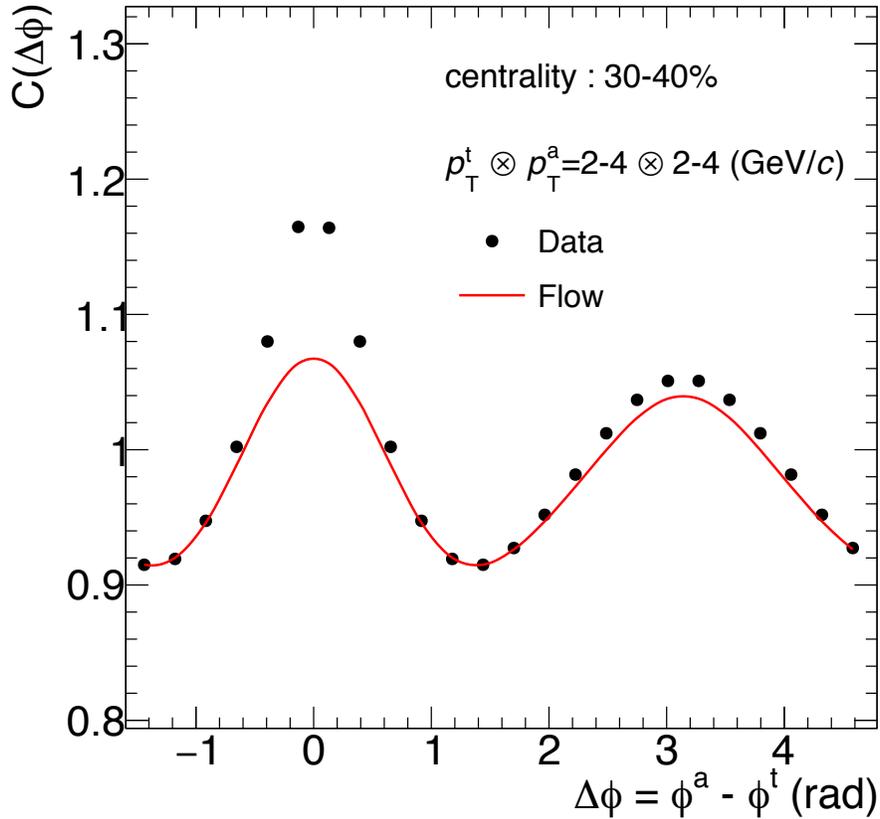
Figure 3.23: Inclusive-triggered correlation function with background fitted by ZYAM assumption.
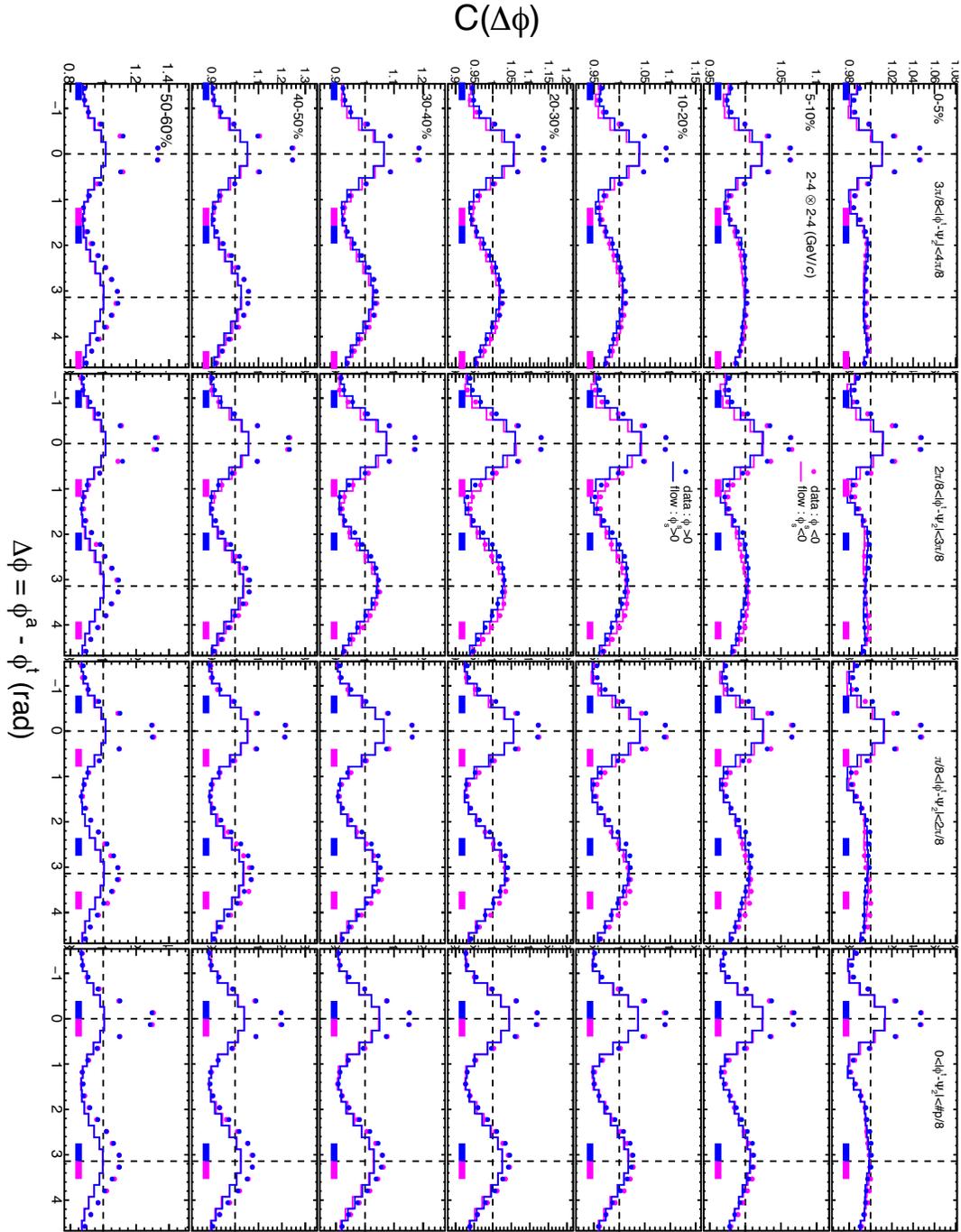
Figure 3.24: Correlation functions and simulated background distributions with trigger angle selections with respect to the second-order event plane with 2-4⊗2-4 (GeV/c) in each centrality bin.

3.7   Azimuthal distribution of pair yield per trigger particles

Azimuthal distribution of pair yield per trigger particle ($Y(\Delta\phi)$) is calculated as follows,

$$Y(\Delta\phi) = \frac{1}{N^t}\frac{dN^{ta}}{d\Delta\phi} = \frac{1}{2\pi\varepsilon^a} \cdot \frac{N^{ta}}{N^t} J(\Delta\phi) \tag{3.86}$$

where ε^a is efficiency of associated particles, N^{ta} is the number of pairs in the acceptance where correlations are projected, and N^t is the number of trigger particles. The reason why only associated particles are corrected by efficiencies is the factor of efficiency of trigger particles is cancelled out. Fig.3.25 shows correlated yield distribution after background subtraction, normalization and efficiency correction. As seen in Fig.3.25, the minimum value is zero. Fig.3.26 shows jet-correlated yield with trigger angle selections with respect to the second-order event plane in each centrality bin. Large peak is observed in the near side and some residual yield is observed in the away side. Left-right symmetry with respect to the dashed-line at $\Delta\phi = 0$ and $\Delta\phi = \pi$ is observed for $\phi_s < 0$ and $\phi_s > 0$. Therefore, the correlations with $\phi_s > 0$ are averaged into those with $\phi_s < 0$ thereafter.
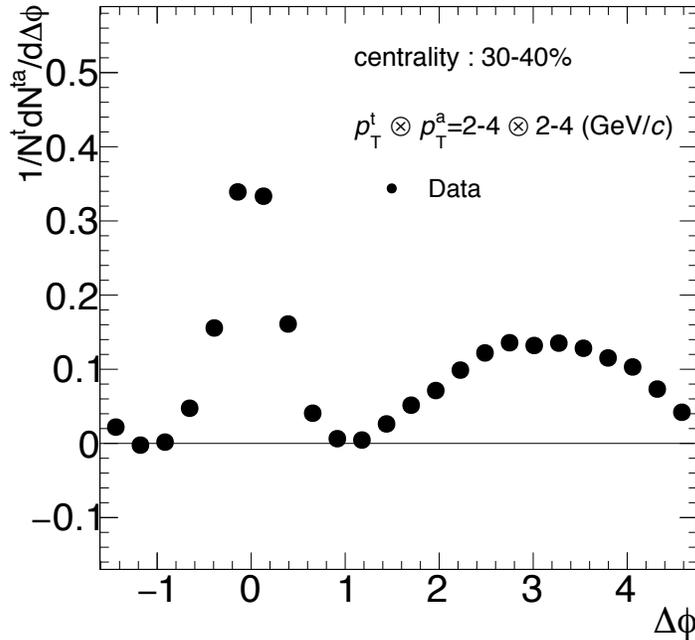
Figure 3.25:   Azimuthal distribution of correlated yield after background subtraction (using Fig.3.23), normalization and efficiency correction.
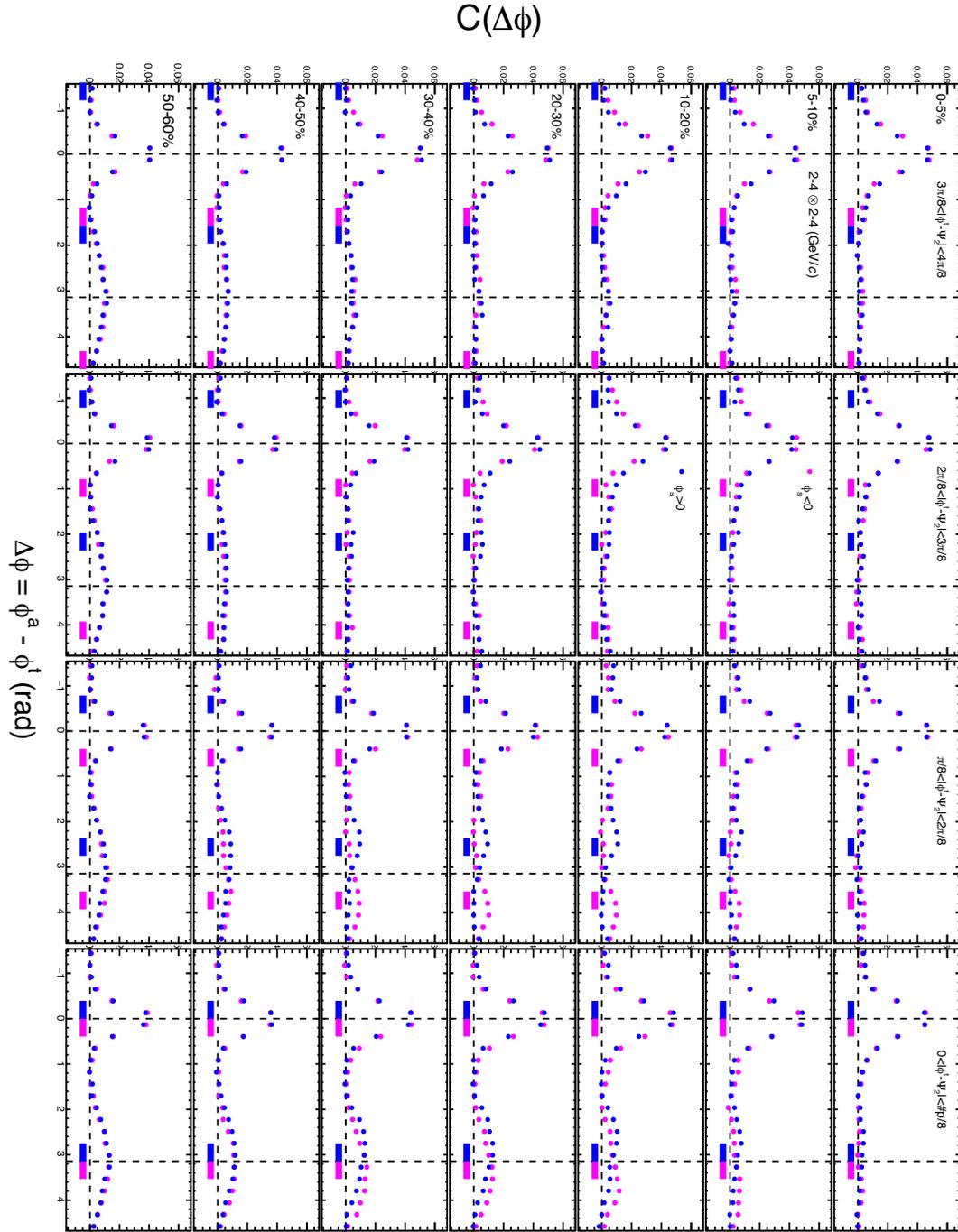
Figure 3.26: Jet-correlated yield distributions with trigger angle selections with respect to the second-order event plane with 2-4⊗2-4 (GeV/c) in each centrality bin.

3.7.1   Estimation of tracking efficiency

Tracking efficiency of charged particles reconstructed with TPC is estimated with p_T spectra and embedding simulation. Embedding method is a Monte-Carlo simulation : we embed a 'known' particles which is generated by event generator (e.g. PYTHIA, HIJING or UrQMD) is embedded to the real experimental data through the simulated detector and measure whether the particle can be reconstructed or not. After applying as same cut to the embedded tracks as that for experimental data, single-track efficiency is estimated. Fig.3.27 shows the TPC tracking efficiency of pions, kaons, proton, and anti-proton as a function of p_T and centrality.
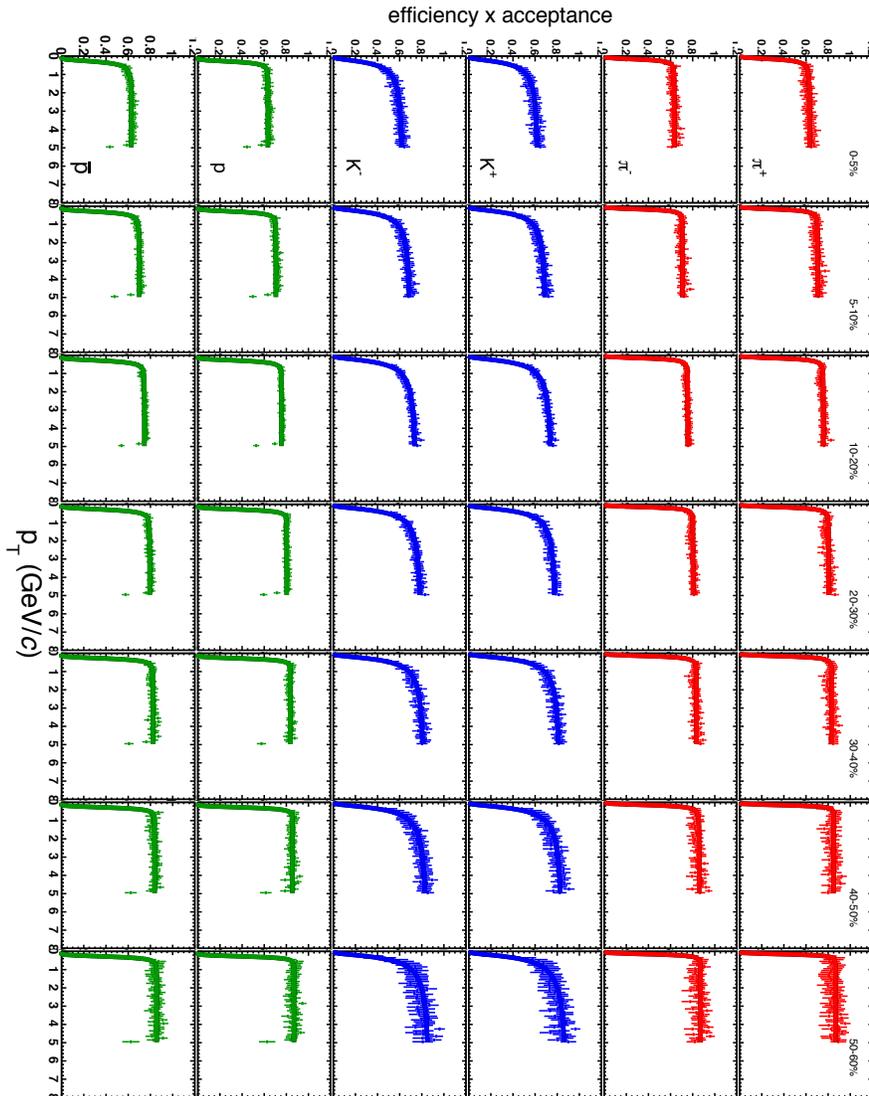
Figure 3.27: The single particle efficiencies of pions, kaons, protons and anti-protons as a function of p_T in each centrality estimated by embedding simulation.

Tracking efficiency of charged hadrons can be obtained by integrating the efficiency of each particle with being weighted by corrected p_T spectra. But the spectra are limited up to 0.8 (GeV/c) for Kaons and 3 (GeV/c) for pions and proton and anti-proton. Therefore, the spectra are extended to 4 (GeV/c) via Blast-wave fit with Tsallis statistics [69] as shown in Fig.3.28. Finally, the tracking efficiency is obtained as shown in Table.3.2.
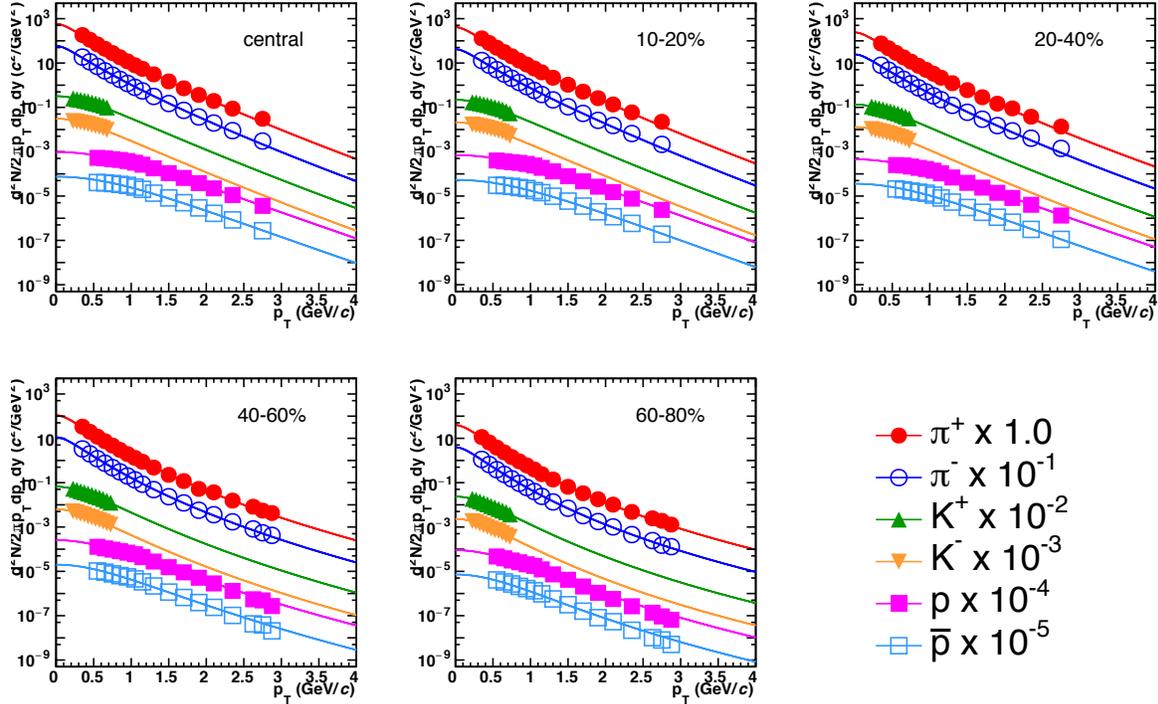
Figure 3.28: p_T spectra of pions, kaons, protons and anti-protons with fitted by Blast-wave function with Tsallis statistics [69].

3.8 Correction of trigger-smearing effect

If the resolution of event plane is ideal, trigger particles can be selected truly with respect to the event plane. However, the resolution of event plane is $0 < Res\Psi_n < 1$, and then, trigger particles can be selected as different ϕ_s bins. Pair yield per trigger particle with respect to the event plane is smeared neighboring trigger angle bins because of the finite resolution of event plane. This trigger smearing effect must be corrected in order to measure real event plane dependence. Two independent correction method is applied in this study. Fitting method is established PHENIX [41] and expanded to correction of the fourth-order term by Dr. T. Todoroki's thesis ([40]) and iterative unfolding method is established by Dr. T. Todoroki's thesis [40]. The detail is described in this section.

Table 3.2: Summary of tracking efficiency

centrality (%)	p_T (GeV/c)	efficiency (%)
0-5	0.5-1.0	0.587
	1.0-2.0	0.613
	2.0-4.0	0.625
5-10	0.5-1.0	0.663
	1.0-2.0	0.686
	2.0-4.0	0.697
10-20	0.5-1.0	0.709
	1.0-2.0	0.733
	2.0-4.0	0.745
20-30	0.5-1.0	0.758
	1.0-2.0	0.781
	2.0-4.0	0.792
30-40	0.5-1.0	0.789
	1.0-2.0	0.810
	2.0-4.0	0.822
40-50	0.5-1.0	0.807
	1.0-2.0	0.827
	2.0-4.0	0.840
50-60	0.5-1.0	0.824
	1.0-2.0	0.842
	2.0-4.0	0.856

3.8.1   Fitting method

Assuming the pair yield per trigger particles are distributed with respect to the event plane, the effect of trigger smearing effect due to limited event-plane resolution can be corrected in analogous to the resolution correction in the single-particle flow measurement via event-plane method. The azimuthal angle of pair yield with respect to Ψ_2 at given $\Delta\phi$ can be written as

$$\frac{dN^{1+Y}}{d(\phi^a - \Psi_2)} = 1 + Y((\phi^a - \Psi_2)) \tag{3.87}$$

$$= 1 + Y(\phi_s + \Delta\phi) \tag{3.88}$$

$$= 1 + 2v_2^Y \cos(\phi_s + \Delta\phi) + 2v_4^Y \cos(\phi_s + \Delta\phi), \tag{3.89}$$

where $Y(\phi_s, \Delta\phi)$ is azimuthal distribution of pair yield before correction, ϕ_s is the relative angle of trigger particles with respect to the Ψ_2 $\phi_s = \phi^t - \Psi_2$, $\Delta\phi = \phi^a - \phi^t$ and $v_{2,4}^Y$ is an azimuthal anisotropy of pair yield. Here, the relation expression $\phi^a - \Psi_2 = (\phi^t - \Psi_2) + (\phi^a - \phi^t) = \phi_s + \Delta\phi$ is applied to Eq.(3.87). The distribution is fitted by the Fourier fitting to $1 + Y(\phi_s, \Delta\phi)$ as a function of ϕ_s with a phase shift $\Delta\phi$. Then, the anisotropy parameter $v_{2,4}^Y$ can be obtained and the azimuthal

distributions using v_n^Y can be corrected by the event plane resolution as

$$\frac{dN^{1+PTY}}{d(\phi^a - \Psi_2)} = 1 + 2\frac{v_2^Y}{\sigma_2}\cos 2(\phi_s + \Delta\phi) + 2\frac{v_4^Y}{\sigma_{42}}\cos 4(\phi_s + \Delta\phi). \qquad (3.90)$$

The corrected distribution can be obtained by taking a ratio of uncorrected and corrected function as,

$$1 + Y^{cor}(\phi_s + \Delta\phi) = \frac{1 + 2\frac{v_2^Y}{\sigma_2}\cos 2(\phi_s + \Delta\phi) + 2\frac{v_4^Y}{\sigma_{42}}\cos 4(\phi_s + \Delta\phi)}{1 + 2v_2^Y\cos 2(\phi_s + \Delta\phi) + 2v_4^Y\cos 4(\phi_s + \Delta\phi)} \times (1 + Y^{raw}(\phi_s + \Delta\phi)) \quad (3.91)$$

$$Y^{cor}(\phi_s + \Delta\phi) = \frac{1 + 2\frac{v_2^Y}{\sigma_2}\cos 2(\phi_s + \Delta\phi) + 2\frac{v_4^Y}{\sigma_{42}}\cos 4(\phi_s + \Delta\phi)}{1 + 2v_2^Y\cos 2(\phi_s + \Delta\phi) + 2v_4^Y\cos 4(\phi_s + \Delta\phi)} \times (1 + Y^{raw}(\phi_s + \Delta\phi)) - 1. \quad (3.92)$$

Fig.3.29 shows an example of the unfolding by the fitting method and the Fig.3.29 is the all the ϕ_s distribution in one centrality bin and one p_T combination.

3.8.2 Iteration method

The smearing effect is unfolded by iterative calculation. Firstly, pair yield distribution is defined as $Y(\phi_s, \Delta\phi)$ as a function of trigger direction $\phi_s = \phi^t - \Psi_2$ and azimuthal angle $\Delta\phi = \phi^a - \phi^t$. Constant offset $O = 1$ to the pair yield as $A(\phi_s + \Delta\phi) = Y(\phi_s + \Delta\phi) + O$ in order to avoid divergence of calculations in the unfolding by treating small value around 0. Now, the trigger bin ϕ_s is divided into 8 bins, and those width are $\pi/8$ (rad) from $-\pi/2$ (rad) to $\pi/2$ (rad) in Ψ_2 dependent correlations, and the relative angle between trigger and associate particle $\Delta\phi$ is divided into 24 bins. For simplicity, trigger bin ϕ_s and relative angle bin $\Delta\phi$ is rewritten by indexes i ($=0$ - 7) and k ($=0$ - 23), respectively. Pair yield distribution is named as $A(i, k)$ and summarized into a vector $\mathbf{A}(k)$ at a given k as follows,

$$\mathbf{A}(k) = \begin{pmatrix} A(0, k) \\ A(1, k) \\ A(2, k) \\ A(3, k) \\ A(4, k) \\ A(5, k) \\ A(6, k) \\ A(7, k) \end{pmatrix}. \qquad (3.93)$$

Probability distribution function of Ψ_2^{obs} with respect to Ψ_2^{real} is given by Eq.(3.43). The contamination from other trigger bins can be estimated by the probability distribution function and the width of trigger bin. Now, the smearing matrix $\mathbf{S}(k)$ is introduced with considering cyclic boundary
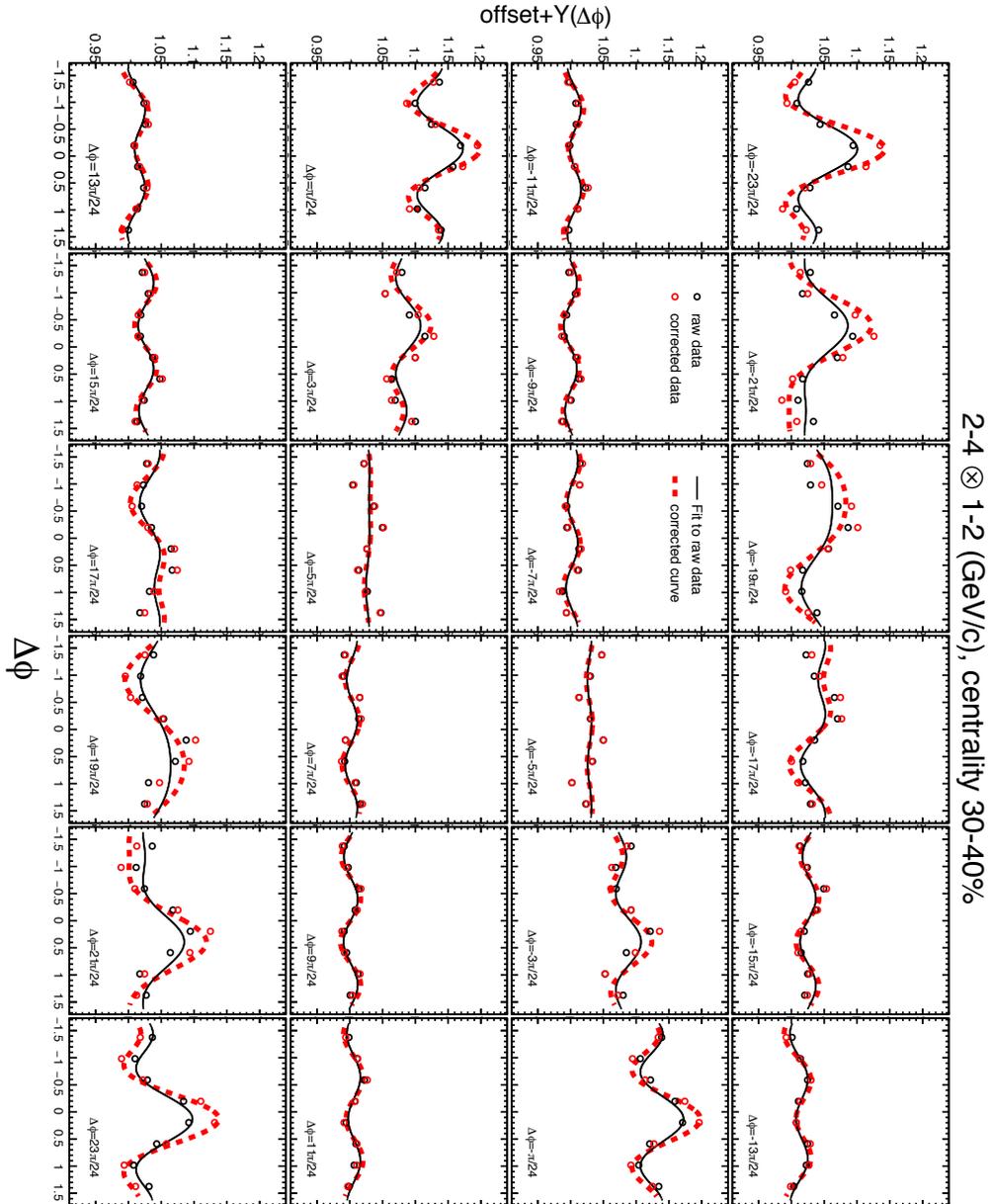
Figure 3.29: Offset added correlated yield as a function of ϕ_s fitted by Fourier function (black) and resolution corrected data and curve (red) in each $\Delta\phi$ window.

condition and symmetry of even function as,

$$
S = \begin{pmatrix}
s_0 & s_1 & s_2 & s_3 & s_4 & s_3 & s_2 & s_1 \\
s_1 & s_0 & s_1 & s_2 & s_3 & s_4 & s_3 & s_2 \\
s_2 & s_1 & s_0 & s_1 & s_2 & s_3 & s_4 & s_3 \\
s_3 & s_2 & s_1 & s_0 & s_1 & s_2 & s_3 & s_4 \\
s_4 & s_3 & s_2 & s_1 & s_0 & s_1 & s_2 & s_3 \\
s_3 & s_4 & s_3 & s_2 & s_1 & s_0 & s_1 & s_2 \\
s_2 & s_3 & s_4 & s_3 & s_2 & s_1 & s_0 & s_1 \\
s_1 & s_2 & s_3 & s_4 & s_3 & s_2 & s_1 & s_0
\end{pmatrix} ,
\tag{3.94}
$$

where s_m is a contamination probability from m trigger bin away from selected bin, and s_0 is true signal in a selected bin and the sum of the elements is normalized to unity as $\sum s_m = 1$. The smeared correlation matrix $\mathbf{B}(k)$ can be determined by the multiplying the smearing matrix from left to the pair yield distribution as

$$
\mathbf{B}(k) = \mathbf{S}(k)\mathbf{A}(k).
\tag{3.95}
$$

The diagonal element c_{ii} of effective correction matrix $\mathbf{C}(k)$ is defined as

$$
c_{ii} = A(i,k)/B(i,k),
\tag{3.96}
$$

here, the off-diagonal elements c_{ij} ($i \neq j$) are ignored because trigger smearing is assumed to smear only by resolution effect (smearing matrix) in this study. Then, corrected correlation vector $\mathbf{A}^{\mathbf{corr}}(k)$ can be obtained as

$$
\mathbf{A}^{\mathbf{corr}}(k) = \mathbf{C}(k)\mathbf{A}(k).
\tag{3.97}
$$

However, the first correlation vector $\mathbf{A}(k)$ is not real distribution, smeared by the limited event-plane resolution in this method. Therefore, the procedure above is iterated until correction matrix converges. The Matrixes $\mathbf{A}(k)$, $\mathbf{B}(k)$ and $\mathbf{C}(k)$ are re-defined as $\mathbf{A}^{(\mathbf{n})}(k)$, $\mathbf{B}^{(\mathbf{n})}(k)$ and $\mathbf{C}^{(\mathbf{n})}(k)$ ($n \geq 1$) to describe a iteration procedure which is summarized in Fig.3.30.

Here, the correlation matrix for $n = 1$, $\mathbf{A}^{(\mathbf{1})}(k)$, correspond to the uncorrected correlation. Those matrixes in n-th loop is defined as,

$$
\mathbf{B}^{(\mathbf{n})}(k) = \mathbf{S}(k)\mathbf{A}^{(\mathbf{n})}(k)
\tag{3.98}
$$

$$
\mathbf{A}^{(\mathbf{n})}(k) = \mathbf{C}^{(\mathbf{n-1})}(k)\mathbf{A}^{(\mathbf{1})}(k)
\tag{3.99}
$$

where the elements of correction matrix $\mathbf{C}^{(\mathbf{n})}(k)$ is defined as,

$$
c_{ii}^{(n)} = A^{(n)}(i,k)/B^{(n)}(i,k)
\tag{3.100}
$$

$$
c_{ij}^{(n)} = 0 \text{ (for } i \neq j).
\tag{3.101}
$$

In this method, correction matrix directly affected by statistical fluctuations. When making the correction matrix, smoothing parameters with neighboring bins are needed in order to avoid divergence of the matrix. Therefore, the smoothing parameters are introduced both for i and k indexes
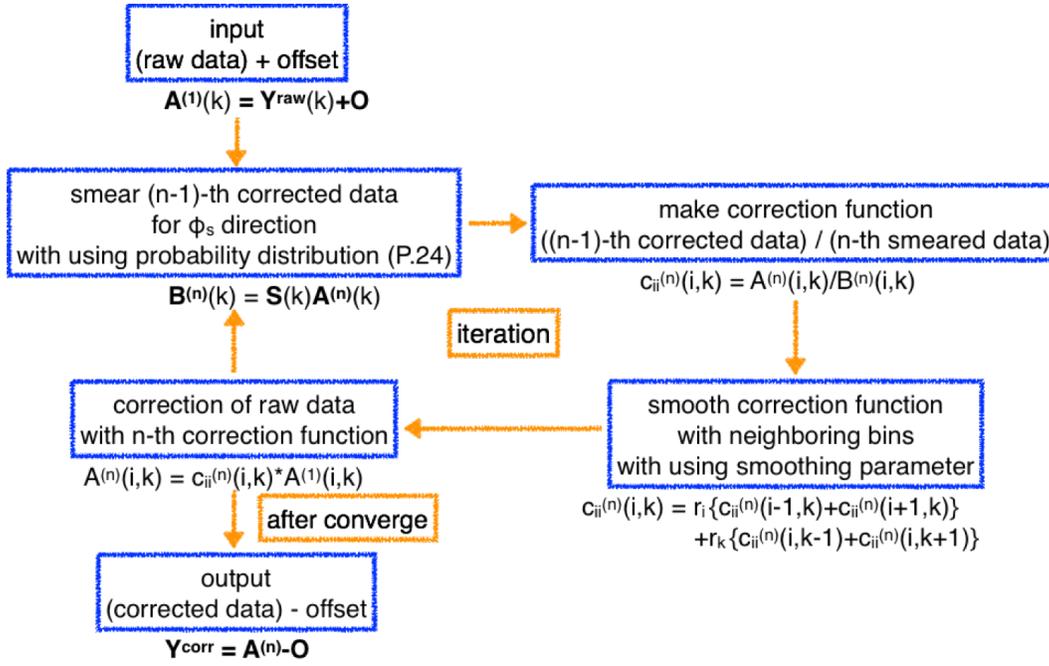
Figure 3.30: Summary of unfolding loop procedure.

as,

$$
\begin{aligned}
c_{ii}^{(n)}(i,k) &= (1 - 2r_i - 2r_k)c_{ii}^{(n)}(i,k) + r_i c_{ii}^{(n)}(i-1,k) + r_i c_{ii}^{(n)}(i+1,k) \\
&\quad + r_k c_{ii}^{(n)}(i,k-1) + r_k c_{ii}^{(n)}(i,k+1)
\end{aligned}
\tag{3.102}
$$

The chi-squared value of correction matrix χ_C^2 is calculated in the every loop and evaluate the difference with the once previous matrix as

$$
\chi_C^2 = \sum_i \sum_k \frac{\left\{ c_{ii}^{(n)}(i,k) - c_{ii}^{(n-1)}(i,k) \right\}^2}{\sqrt{\left\{ \delta c_{ii}^{(n)}(i,k) \right\}^2 + \left\{ \delta c_{ii}^{(n-1)}(i,k) \right\}^2}},
\tag{3.103}
$$

where $\delta c_{ii}^{(n)}(i,k)$ is statistical error of the element of correction matrix. The iteration ends when χ_C^2 have a local minimum value. Fig.3.31 shows example of iterative unfolding procedure upto 50 loops.

3.9   Systematic uncertainties

In this section, systematic uncertainties in flow measurements and two-particle correlations are presented.
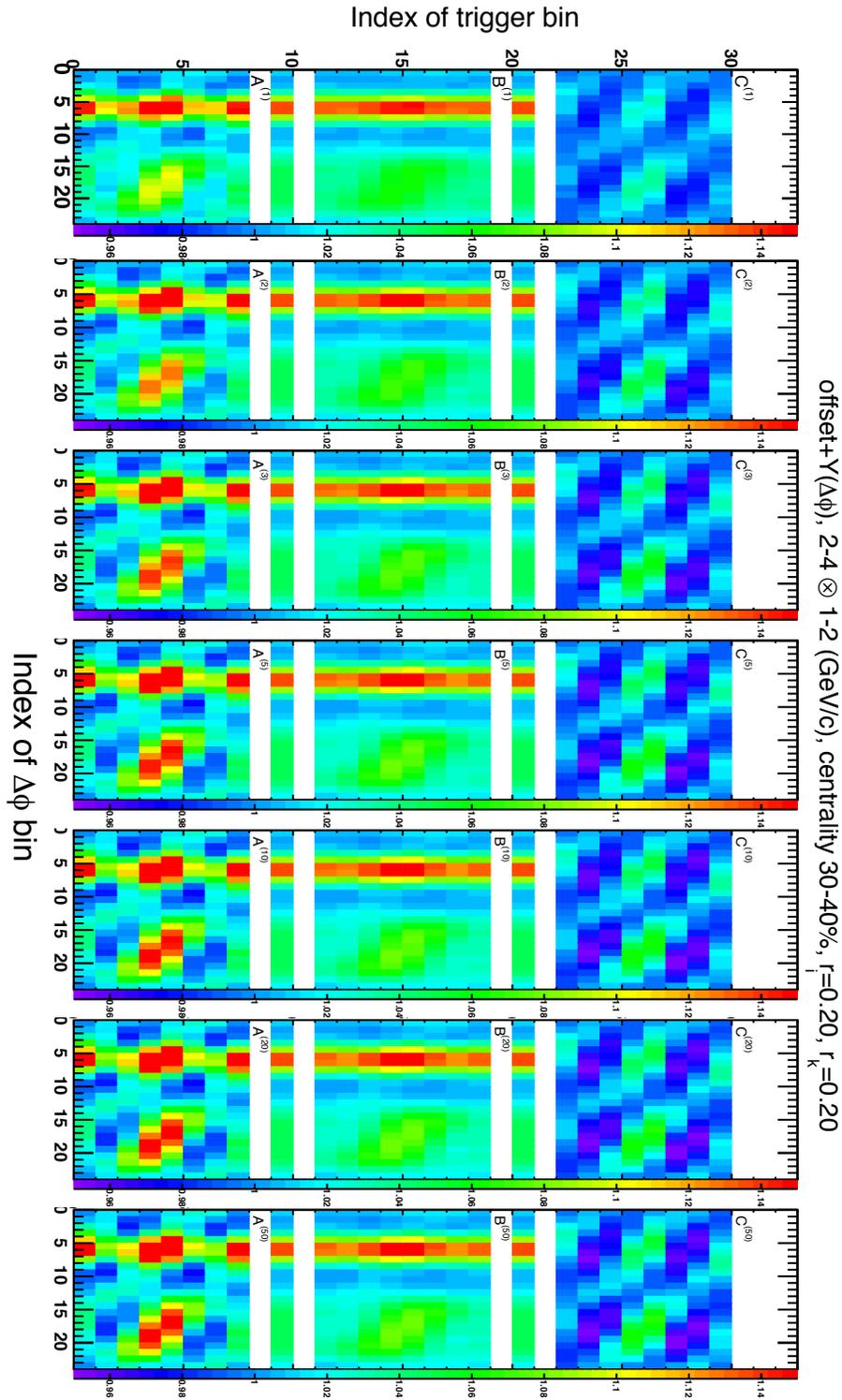
Figure 3.31: Corrected correlations (A), smeared correlations (B) and correction function (C) in selected loops (1, 2, 3, 5, 10, 20, 50th). Smoothing parameters are $r_i = r_k = 0.20$.

3.9.1   Systematic uncertainties in flow measurements

The sources of systematic uncertainties on flow measurements considered in this study are listed as follows,

- differences of track cut parameters and z-vertex V_z,

- difference of East/West event plane

- difference of analysis method between two-particle-correlation method and event-plane method.

DCA, NHitsFit and V_z are changed to loose or tight cut in order to change contamination of secondary particles, track quality and effective acceptance of the TPC. The azimuthal anisotropy v_n was measured by different cut parameter combinations as shown in Table.3.3. When changing

Table 3.3: Track and event selections for estimation of systematic uncertainties

variables	cuts		
	loose	default	tight
DCA	< 2 cm	< 1 cm	< 0.5 cm
NHitsFit	> 15	> 20	< 25
$|V_z|$		< 30 cm	< 20 cm

one parameter to tight or loose cut, the other parameters are fixed to default parameters. Here, cut parameters are assumed to have no systematic correlations. Therefore, six different combinations have been considered to estimate systematic uncertainties from track and event selections as shown in Fig.3.32. The systematic uncertainties of track and V_z selections σ_{cut} are defined as

$$\sigma_{cut} = \sqrt{\sum_i^6 |v_{n,i} - v_{n,ave}|^2}, \tag{3.104}$$

where the index i corresponds to the difference of track and z-vertex cuts. Fig.3.33 shows the flow measured at the east side with respect to west side event plane and the west side with respect to east side event plane. The systematic uncertainties on the difference between east side and west side σ_{EW} are defined by the absolute value of its difference,

$$\sigma_{EW} = |v_{n,east} - v_{n,west}|. \tag{3.105}$$

Fig.3.34 shows the flow measured via event plane method and two-particle correlation method. The systematic uncertainties on the difference between event plane method and two-particle correlation method σ_{met} are defined by the absolute value of its difference,

$$\sigma_{met} = |v_{n,EP} - v_{n,2PC}|. \tag{3.106}$$

The total systematic uncertainties can be written as square root quadratic sum of these errors as,

$$\sigma_{total} = \sqrt{\sigma_{cut}^2 + \sigma_{EP}^2 + \sigma_{met}^2}. \tag{3.107}$$

Fig.3.35 shows the linear sum of systematic uncertainties (histograms) of each component and the quadratic sum of them (data point).
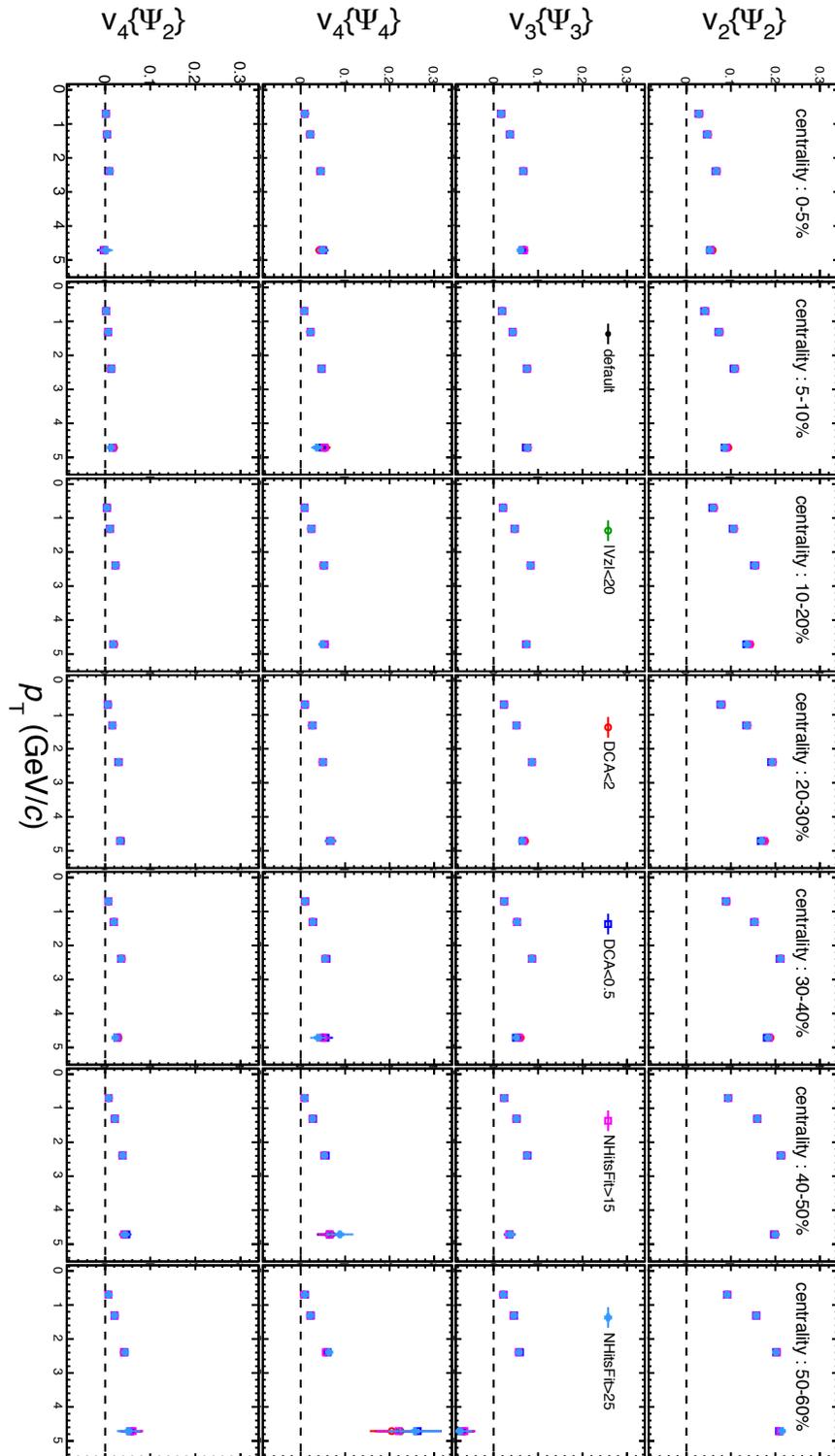
Figure 3.32: p_T dependence of azimuthal anisotropy with various track and event selections : (black) all default cuts, (green) $|V_z| < 20$ cm, (red) DCA < 2cm, (blue) DCA < 0.5 cm, NHitsFit > 15, NHitsFit > 25.
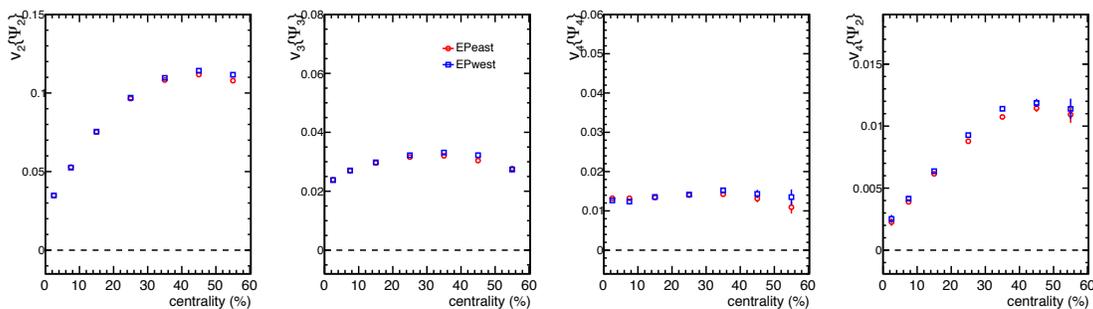
Figure 3.33: Azimuthal anisotropy with east/west difference with inclusive p_T : (red) EPeast, (blue) EPwest.

3.9.2   Systematic uncertainties in two-particle correlations

The sources of systematic uncertainties on flow measurements considered in this study are listed as follows,

- propagation of systematic uncertainties of v_n,

- propagation of systematic uncertainties of Ψ_2-Ψ_4 correlation,

- difference of mixing binning,

- tracking efficiency,

- range of pair cut,

- difference of correction method for trigger smearing effect,

- differences of smoothing parameters.

For measurement of two-particle correlations, systematic uncertainties from v_n, σ_{v_n} can be propagated after subtraction of flow. The systematic uncertainties from flow parameters σ_{v_n} can be defined by RMS of yield per trigger particle with $v_n \pm 1\sigma (n = 2, 3, 4)$ with respect to the average value,

$$\sigma_{v_n}(\Delta\phi) = \sqrt{\sum_k (Y_{v_k^+}(\Delta\phi) - Y_{default}(\Delta\phi))^2/6 + (Y_{v_k^-}(\Delta\phi) - Y_{default}(\Delta\phi))^2/6,} \qquad (3.108)$$

where $Y_{v_k^\pm}(\Delta\phi)$ represent the correlated yield with flow subtraction with $v_k \pm 1\sigma$ and $Y_{default}(\Delta\phi)$ are the correlated yield with flow subtraction with default flow parameters. The same background level as default flow parameters is applied for estimation of systematic uncertainties. Fig.3.36-3.38 show correlation functions with $p_T^t \otimes p_T^a = $ 2-4$\otimes$1-2 (GeV/c) with v_2, v_3 and v_4 systematics, respectively. The other p_T selections are shown in AppendixB.
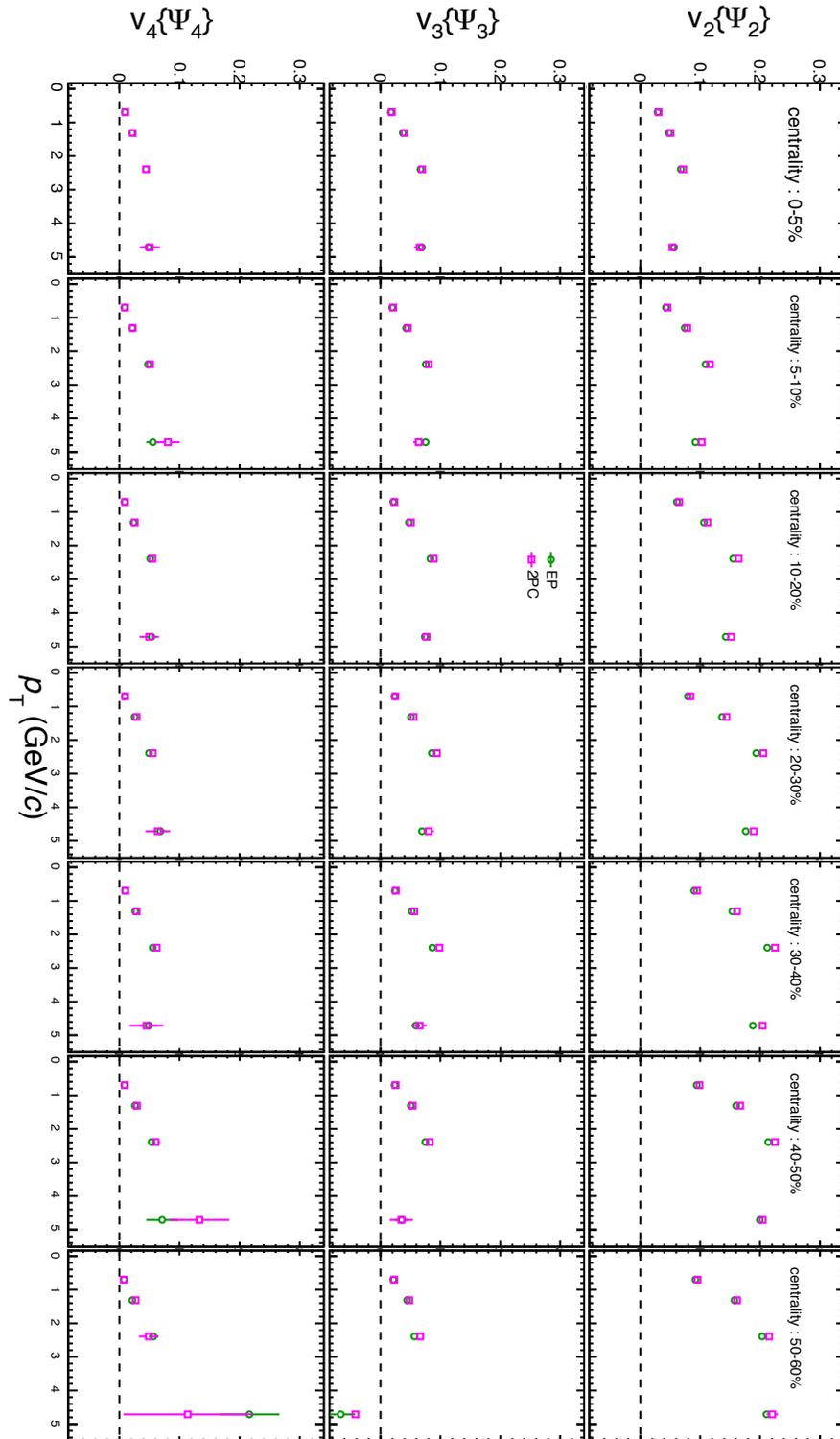
Figure 3.34: Azimuthal anisotropy with event plane method and two-particle correlations : (green) event plane method, (magenta) two-particle correlation method.
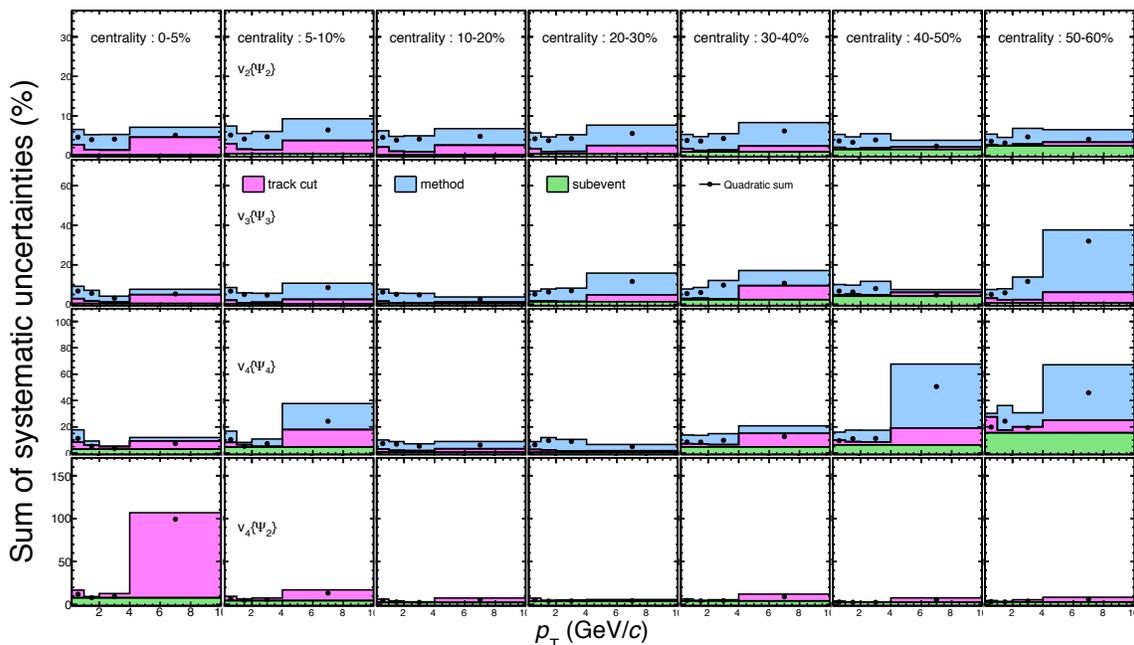
Figure 3.35: Total systematic uncertainties of azimuthal anisotropy v_n with linear sum and quadratic sum of each component.

The systematic uncertainties of the parameter χ_{42} in the event plane correlation $\sigma_{\chi_{42}}$ are defined as,

$$\sigma_{\chi_{42}}(\Delta\phi) = \sqrt{(Y_{\chi_{42}^+}(\Delta\phi) - Y_{ave}(\Delta\phi))^2/2 + (Y_{\chi_{42}^-}(\Delta\phi) - Y_{ave}(\Delta\phi))^2/2}. \qquad (3.109)$$

Fig.3.39 shows correlation functions with $p_T^t \otimes p_T^a = 2\text{-}4\otimes 1\text{-}2$ (GeV/c) with χ_{42} systematics, respectively. The other p_T selections are shown in AppendixB.

The systematic uncertainties of pair cut σ_{pair} around $(\Delta\phi, \Delta\eta) = (0, 0)$ are calculated with cut parameter in $\Delta\phi^*$ and $\Delta\eta$ by changing the cut range from 3σ to 2.5σ as,

$$\sigma_{paircut}(\Delta\phi) = |Y_{2.5\sigma}(\Delta\phi) - Y_{3\sigma}(\Delta\phi)|. \qquad (3.110)$$

The relative uncertainties are listed in Table.3.4.

The background level of correlations is determined by inclusive-trigger correlations or trigger-angle selected correlations. The absolute difference between them, $Y_{inclusive}$ and $Y_{trigbin}$, is defined as systematic uncertainties of ZYAM as,

$$\sigma_{ZYAM}(\Delta\phi) = |Y_{inclusive}(\Delta\phi) - Y_{tirgbin}(\Delta\phi)|. \qquad (3.111)$$

Fig.3.40 shows correlation functions with $p_T^t \otimes p_T^a = 2\text{-}4\otimes 1\text{-}2$ (GeV/c) with χ_{42} systematics, respectively. The other p_T selections are shown in AppendixB.

The systematic uncertainty of tracking efficiency is 5 % [70], and therefore 5 % uncertainty σ_{eff} is added for all the data points.
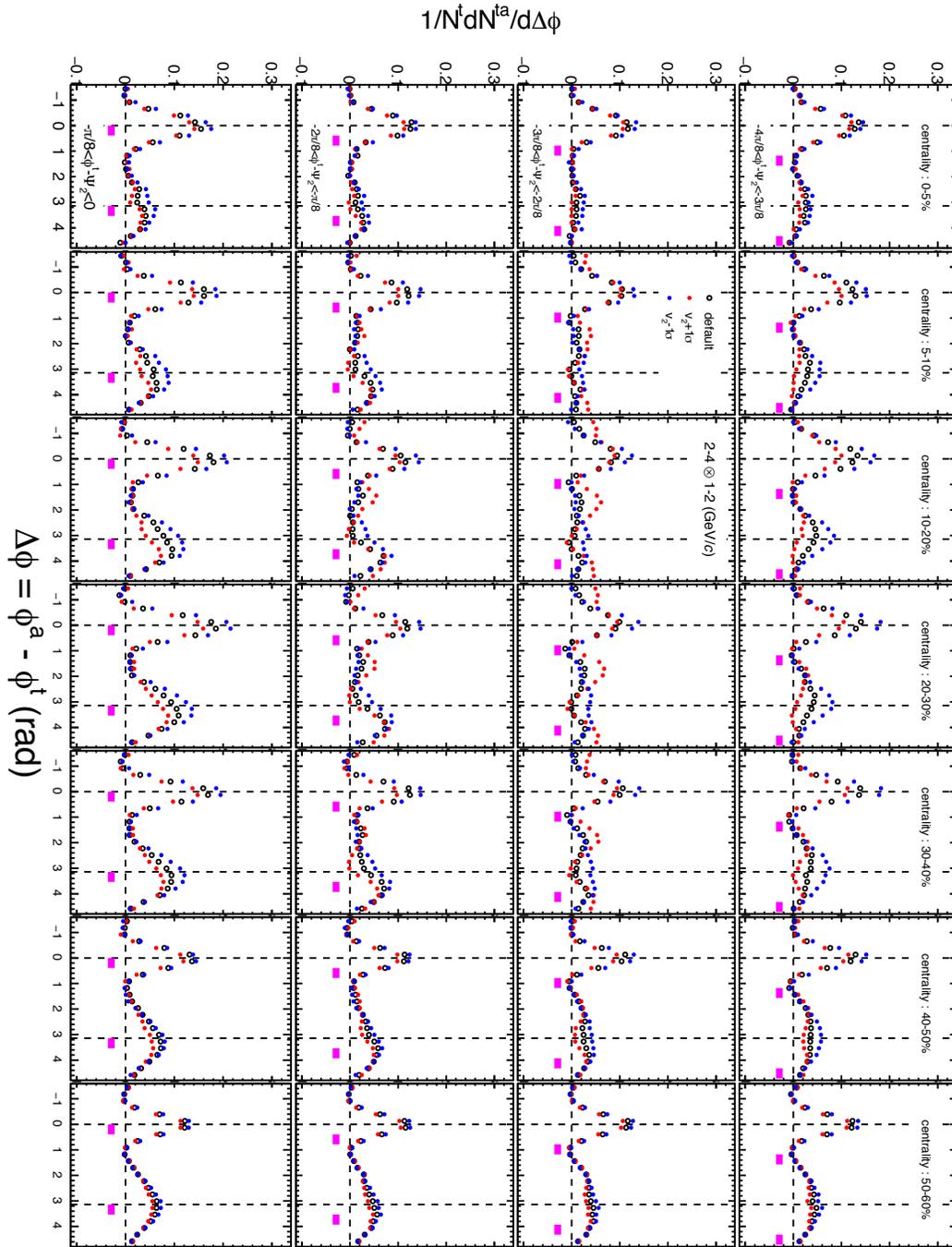
Figure 3.36: Azimuthal distributions of correlated yield with subtracting $v_2 \pm 1\sigma$ with $p_T^t \otimes p_T^a = $ 2-4⊗1-2 (GeV/c).
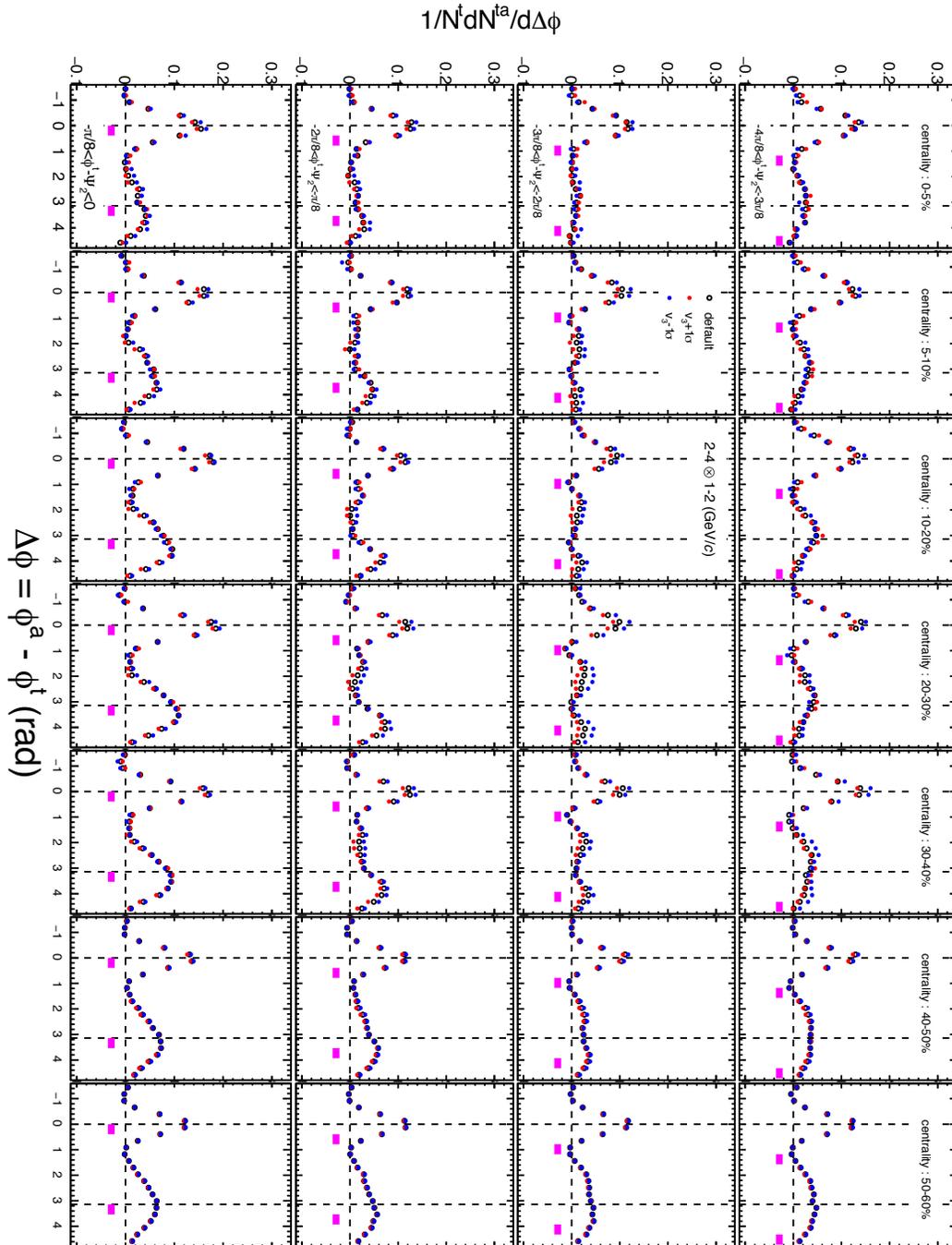
Figure 3.37: Azimuthal distributions of correlated yield with subtracting $v_3 \pm 1\sigma$ with $p_T^t \otimes p_T^a =$ 2-4⊗1-2 (GeV/c).
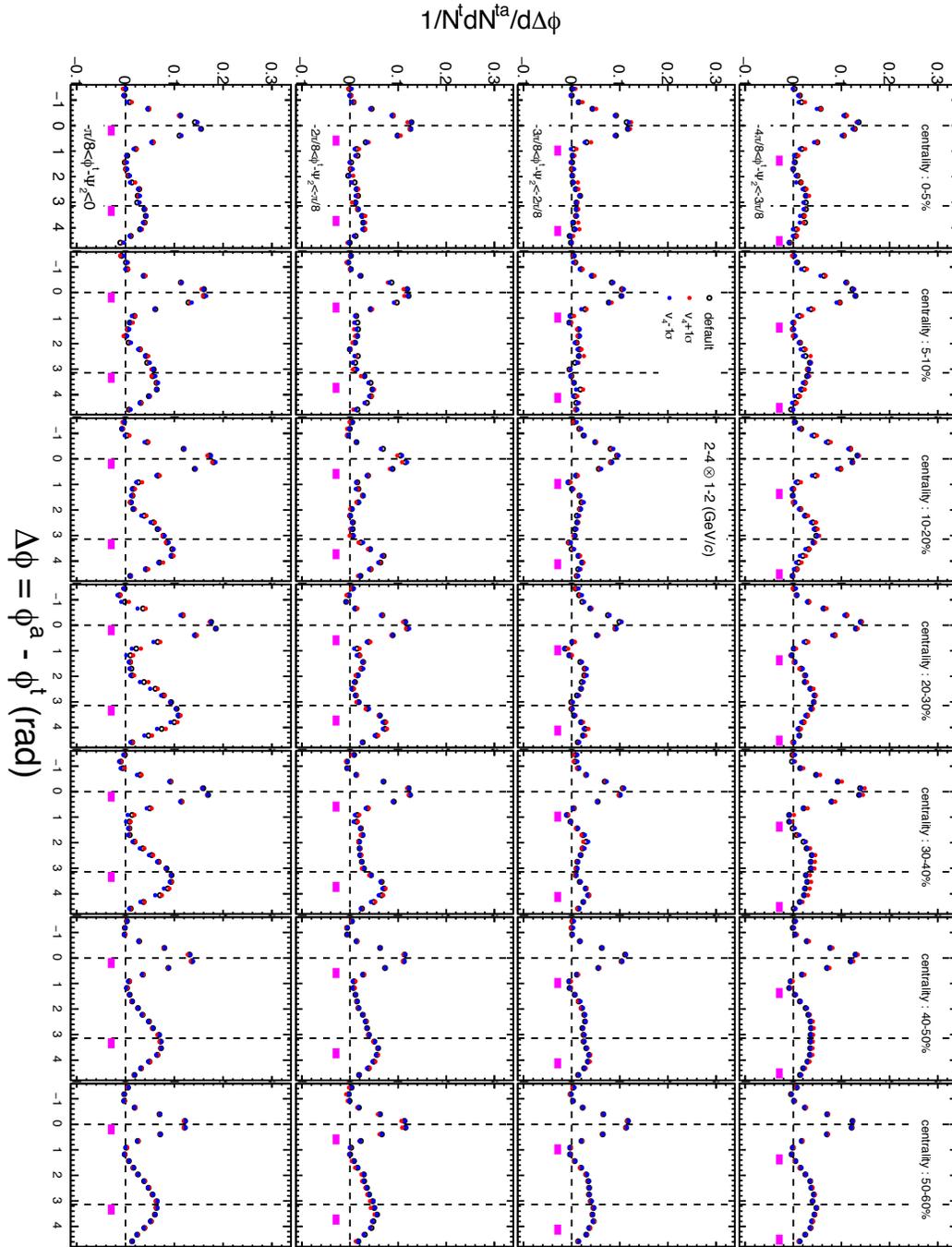
Figure 3.38: Azimuthal distributions of correlated yield with subtracting $v_4 \pm 1\sigma$ with $p_T^t \otimes p_T^a = $ 2-4⊗1-2 (GeV/c).
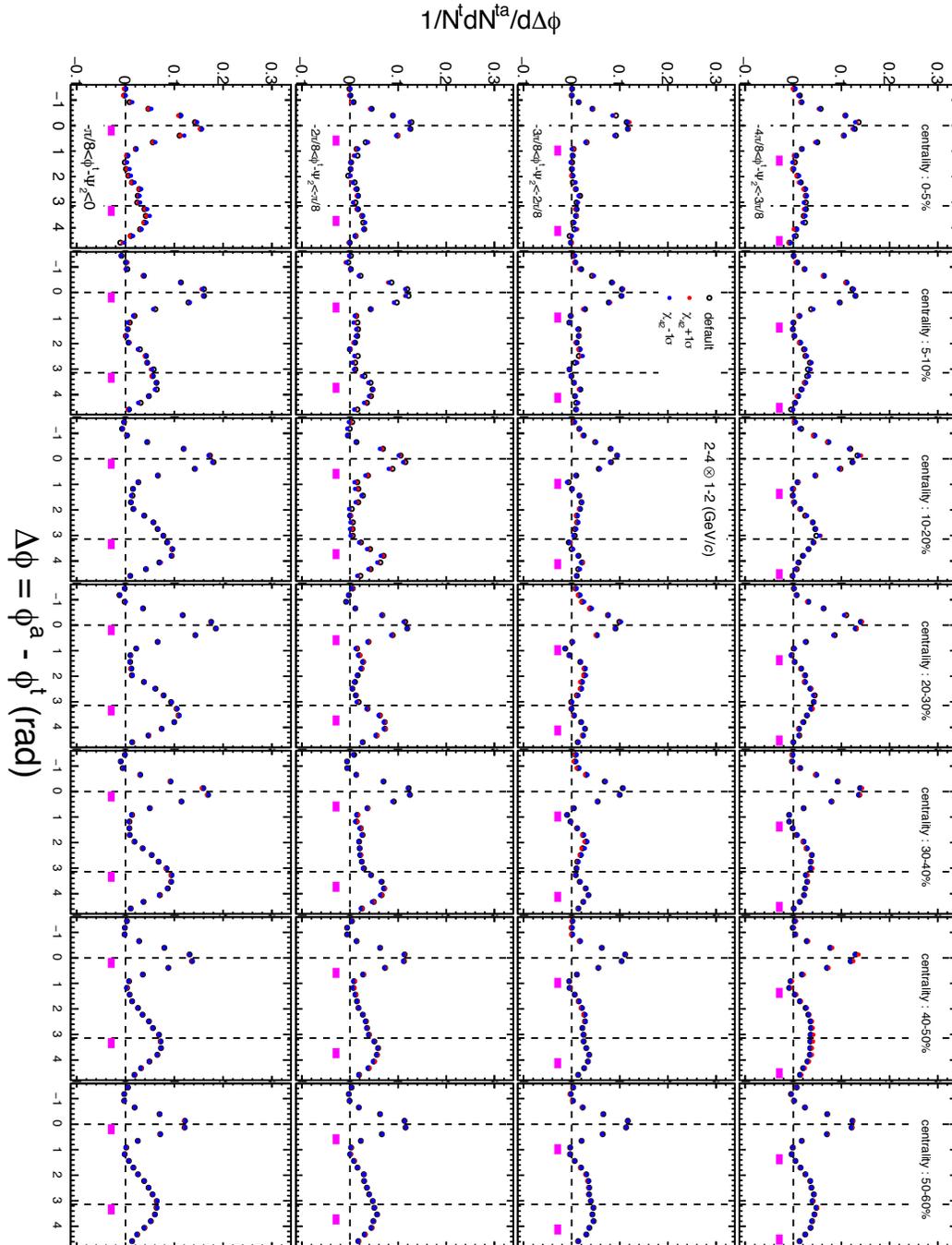
Figure 3.39: Azimuthal distributions of correlated yield with subtracting $\chi_{42} \pm 1\sigma$ with $p_T^t \otimes p_T^a =$ 2-4⊗1-2 (GeV/c).
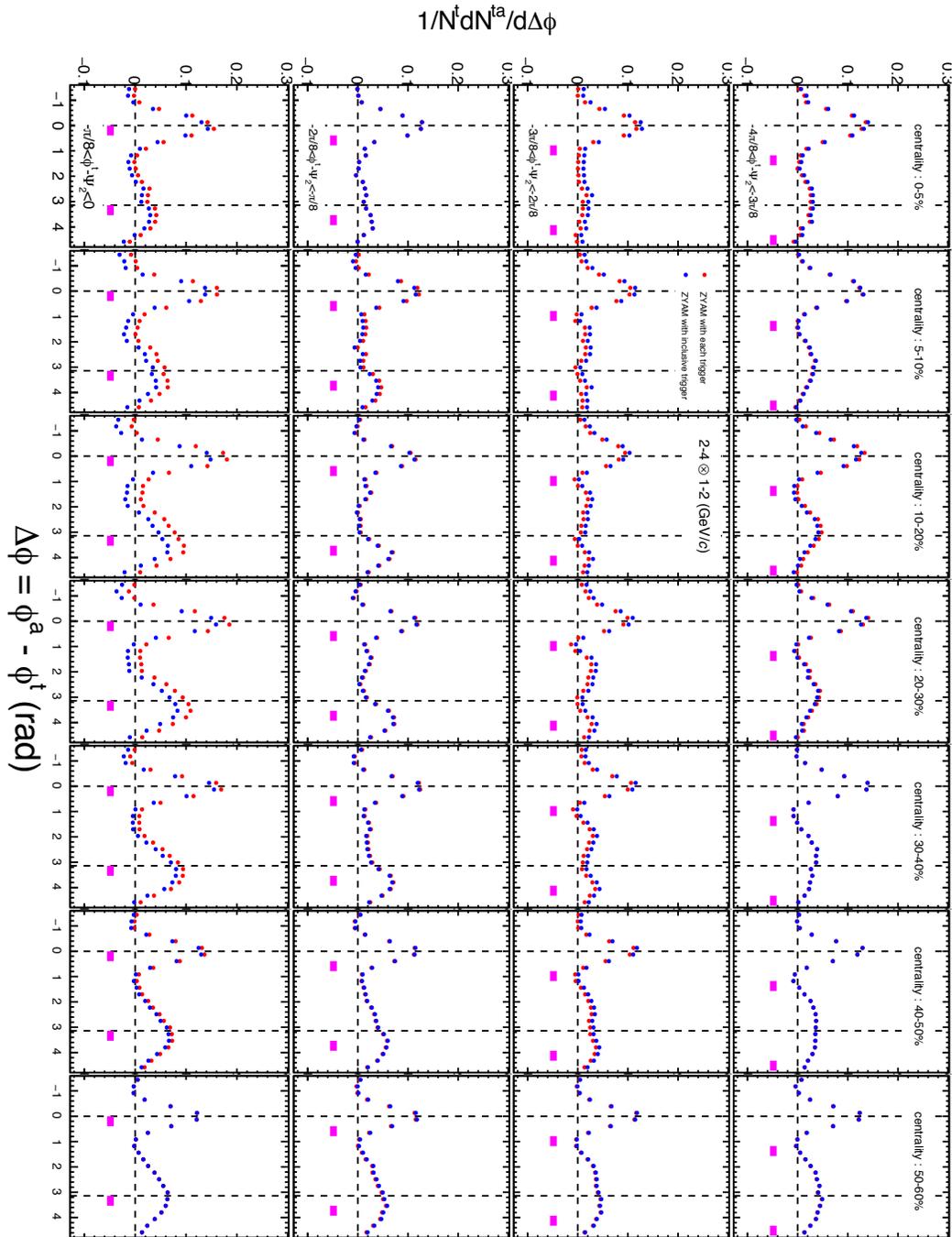
Figure 3.40: Azimuthal distributions of correlated yield with ZYAM determined with trigger-angle selected correlation (red) and inclusive-trigger correlation (blue) $p_T^t \otimes p_T^a = 2\text{-}4\otimes 1\text{-}2$ (GeV/c).

Table 3.4: Relative uncertainties of pair cut (%)

p_T^t (GeV/c)		2 - 4			4 - 10		
p_T^a (GeV/c)		0.5 - 1	1 - 2	2 - 4	0.5 - 1	1 - 2	2 - 4
0-5 %	$0 < |\Delta\phi| < \pi/12$	6.7	6.4	6.8	6.3	6.3	6.9
	$\pi/12 < |\Delta\phi| < 2\pi/12$	3.3	2.4	0	4.5	4.2	0
5-10 %	$0 < |\Delta\phi| < \pi/12$	6.3	6.3	6.7	6.2	6.2	6.9
	$\pi/12 < |\Delta\phi| < 2\pi/12$	4.5	4.2	0	4.4	4.0	0
10-20 %	$0 < |\Delta\phi| < \pi/12$	5.9	5.9	6.5	5.8	5.9	6.7
	$\pi/12 < |\Delta\phi| < 2\pi/12$	2.8	2.8	0	4.2	3.8	0
20-30 %	$0 < |\Delta\phi| < \pi/12$	5.4	5.5	6.3	5.6	5.5	6.2
	$\pi/12 < |\Delta\phi| < 2\pi/12$	2.5	2.0	0	4.0	3.6	0
30-40 %	$0 < |\Delta\phi| < \pi/12$	5.0	5.1	6.1	5.2	5.2	5.9
	$\pi/12 < |\Delta\phi| < 2\pi/12$	2.3	1.8	0	3.8	3.5	0
40-50 %	$0 < |\Delta\phi| < \pi/12$	4.9	4.9	5.9	5.0	5.1	5.8
	$\pi/12 < |\Delta\phi| < 2\pi/12$	2.2	1.7	0	3.7	3.5	0
50-60 %	$0 < |\Delta\phi| < \pi/12$	4.7	4.7	5.6	4.9	5.1	5.6
	$\pi/12 < |\Delta\phi| < 2\pi/12$	2.0	1.5	0	3.5	3.0	0

For the systematic study, the mixing class is not divided by the second-order event plane because event mixing has been performed without event plane alignment in previous event-plane dependent correlations [40, 41, 42]. The absolute difference between correlations with event-plane aligned mixing $Y_{EPaligned}$ and those with event-plane not aligned mixing $Y_{noEPalignment}$ are treated as systematic uncertainties of event mixing σ_{mix} as,

$$\sigma_{mix}(\Delta\phi) = |Y_{noEPalignment}(\Delta\phi) - Y_{EPalignment}(\Delta\phi)|. \tag{3.112}$$

Fig.3.41 shows correlation functions with $p_T^t \otimes p_T^a =$ 2-4⊗1-2 (GeV/c) with mixing systematics. The other p_T selections are shown in AppendixB.

The total systematic uncertainties without event-plane resolution correction $\sigma_{no-EPcorrection}$ are defined as,

$$\sigma_{no-EPcorrection}(\Delta\phi) = \sqrt{\sigma_{v_n}^2(\Delta\phi) + \sigma_{\chi 42}^2(\Delta\phi) + \sigma_{paircut}^2(\Delta\phi) + \sigma_{ZYAM}^2(\Delta\phi) + \sigma_{eff}^2(\Delta\phi)}. \tag{3.113}$$

For the correction of trigger smearing effect, two methods are tested, fitting method and iteration method. The systematic uncertainties of the difference between fitting method Y_{fit} and iteration method Y_{iter}, σ_{method} are calculated as,

$$\sigma_{method}(\Delta\phi) = |Y_{fit}(\Delta\phi) - Y_{iter}(\Delta\phi)|. \tag{3.114}$$

Fig.3.42 shows correlation functions with $p_T^t \otimes p_T^a =$ 2-4⊗1-2 (GeV/c) corrected by iteration method and fitting method, respectively. The other p_T selections are shown in AppendixB.
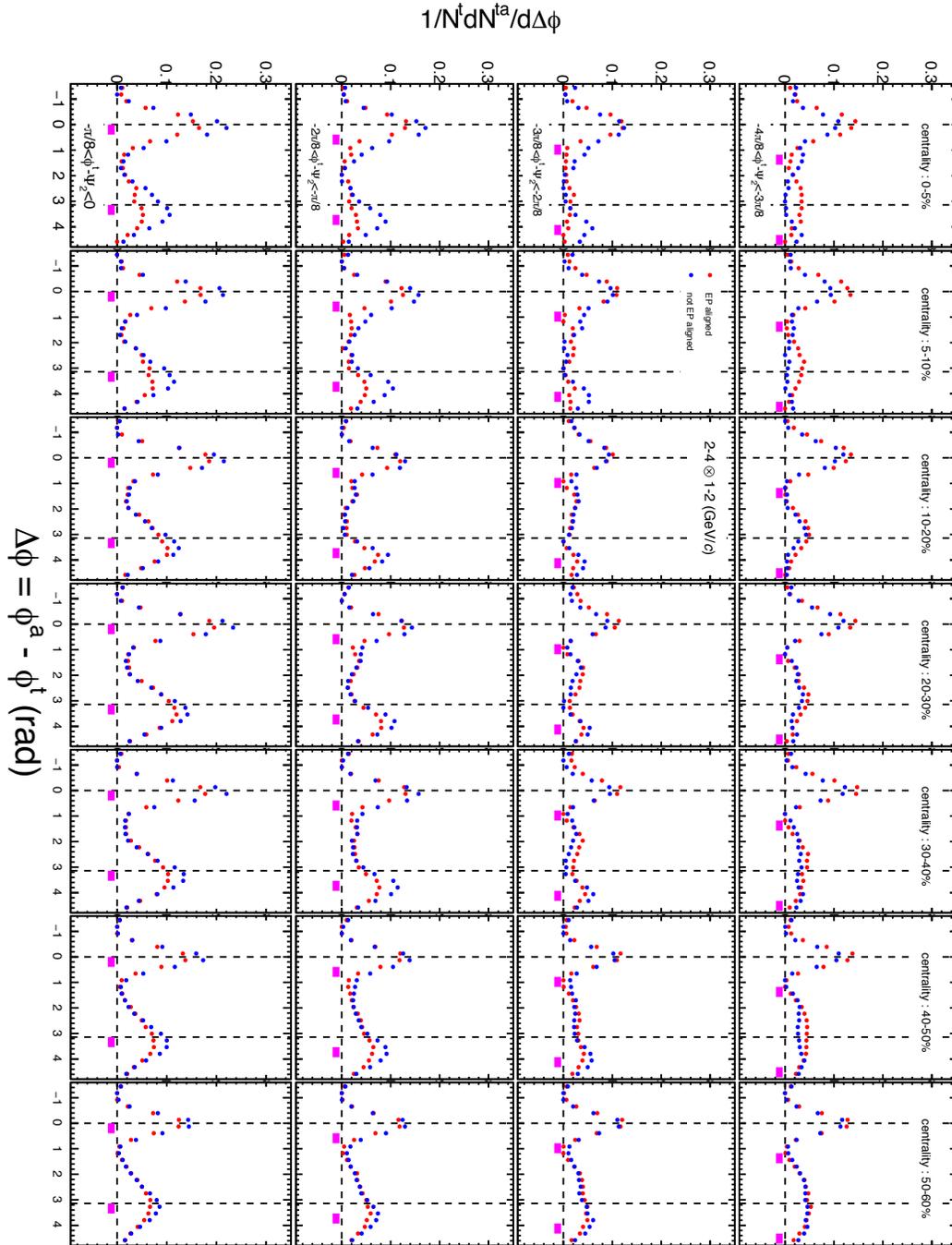
Figure 3.41: Azimuthal distributions of correlated yield with and without alignment of the second-order event plane (red) and inclusive-trigger correlation (blue), respectively, with $p_T^t \otimes p_T^a = 2\text{-}4 \otimes 1\text{-}2$ (GeV/c).
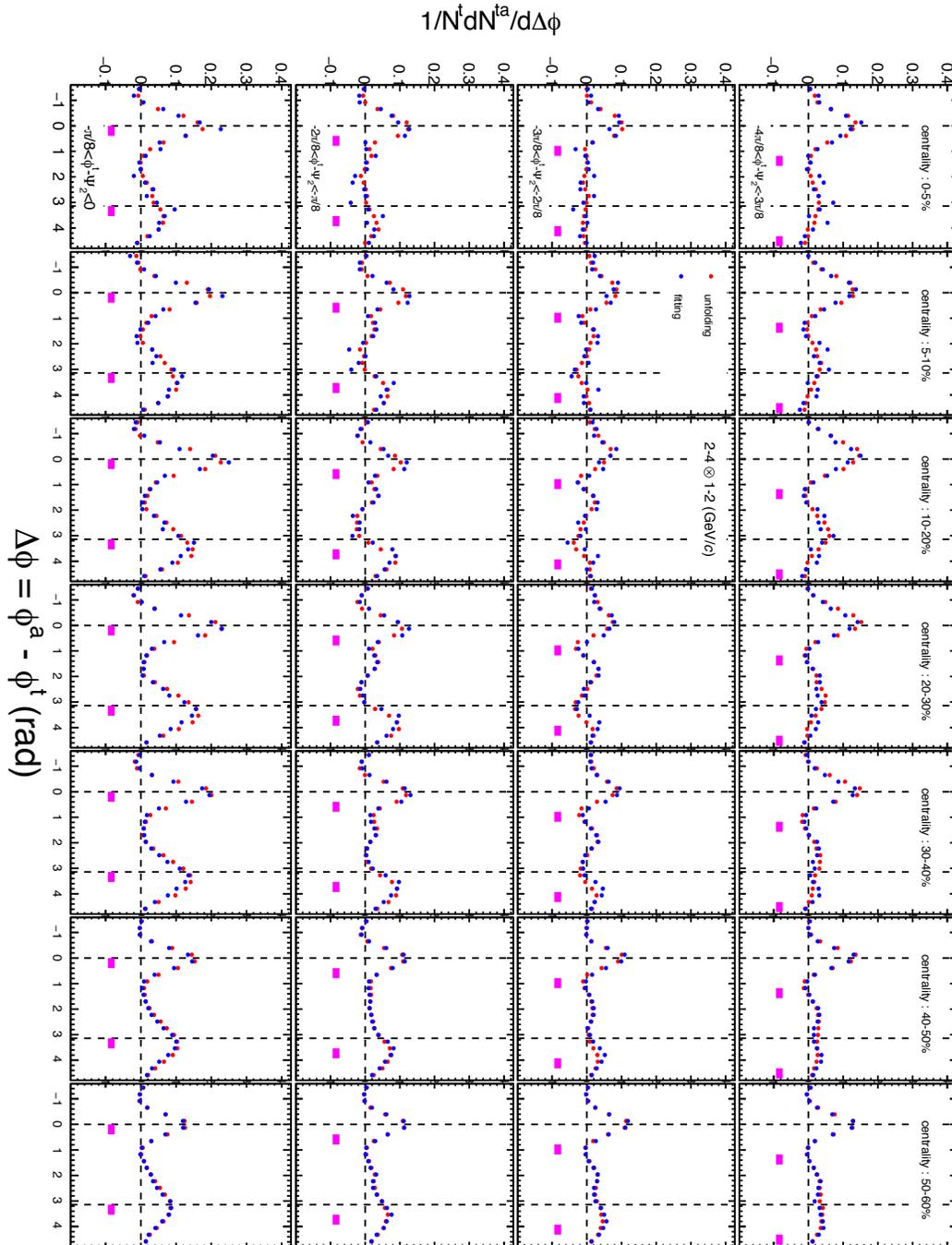
Figure 3.42: Azimuthal distributions of correlated yield corrected by iteration method (red) and fitting method (blue), respectively, with $p_T^t \otimes p_T^a = $ 2-4$\otimes$1-2 (GeV/c).

For iteration method, five smoothing parameters are tested and the systematic uncertainties of the difference between them σ_{smooth} is defined as follows,

$$\sigma_{smooth}(\Delta\phi) = \sqrt{\sum_i (Y_i(\Delta\phi) - Y_{ave}(\Delta\phi))^2/5}, \tag{3.115}$$

where $Y_i(\Delta\phi)$ is the yield with the smoothing parameter $p_{\Delta\phi=0.20}$, $p_{\phi_s=0.20}$, $p_{\Delta\phi=0.30}$, $p_{\phi_s=0.20}$, $p_{\Delta\phi=0.20}$, $p_{\phi_s=0.30}$, $p_{\Delta\phi=0.10}$, $p_{\phi_s=0.20}$ and $p_{\Delta\phi=0.20}$, $p_{\phi_s=0.10}$. Fig.3.43 shows correlation functions with $p_T^t \otimes p_T^a = 2\text{-}4 \otimes 1\text{-}2$ (GeV/c) corrected by iteration method with various smoothing parameters, respectively. The other p_T selections are shown in AppendixB.

The total systematic uncertainties of the unfolding $\sigma_{EPcorrection}$ are defined as,

$$\sigma_{EPcorrection}(\Delta\phi) = \sqrt{\sigma_{smooth}^2(\Delta\phi) + \sigma_{iteration}^2(\Delta\phi) + \sigma_{method}^2(\Delta\phi)}. \tag{3.116}$$

The total systematic uncertainties in two-particle correlations are defined as,

$$\sigma_{total}(\Delta\phi) = \sqrt{[\sigma_{no-EPcorrection}(\Delta\phi)]_{EPpropagated}^2 + \sigma_{EPcorrection}^2(\Delta\phi)}, \tag{3.117}$$

where the systematic uncertainties without event-plane resolution correction $\sigma_{no-EPcorrection}$ are propagated by correction by iteration method. Fig.3.44 shows the fraction of square of systematic uncertainty σ_i (i is the uncertainty of each source) to the square total systematic uncertainty. The uncertainty of Monte-Carlo (mainly from v_2), the effect of smearing correction and the difference of event mixing are major components.
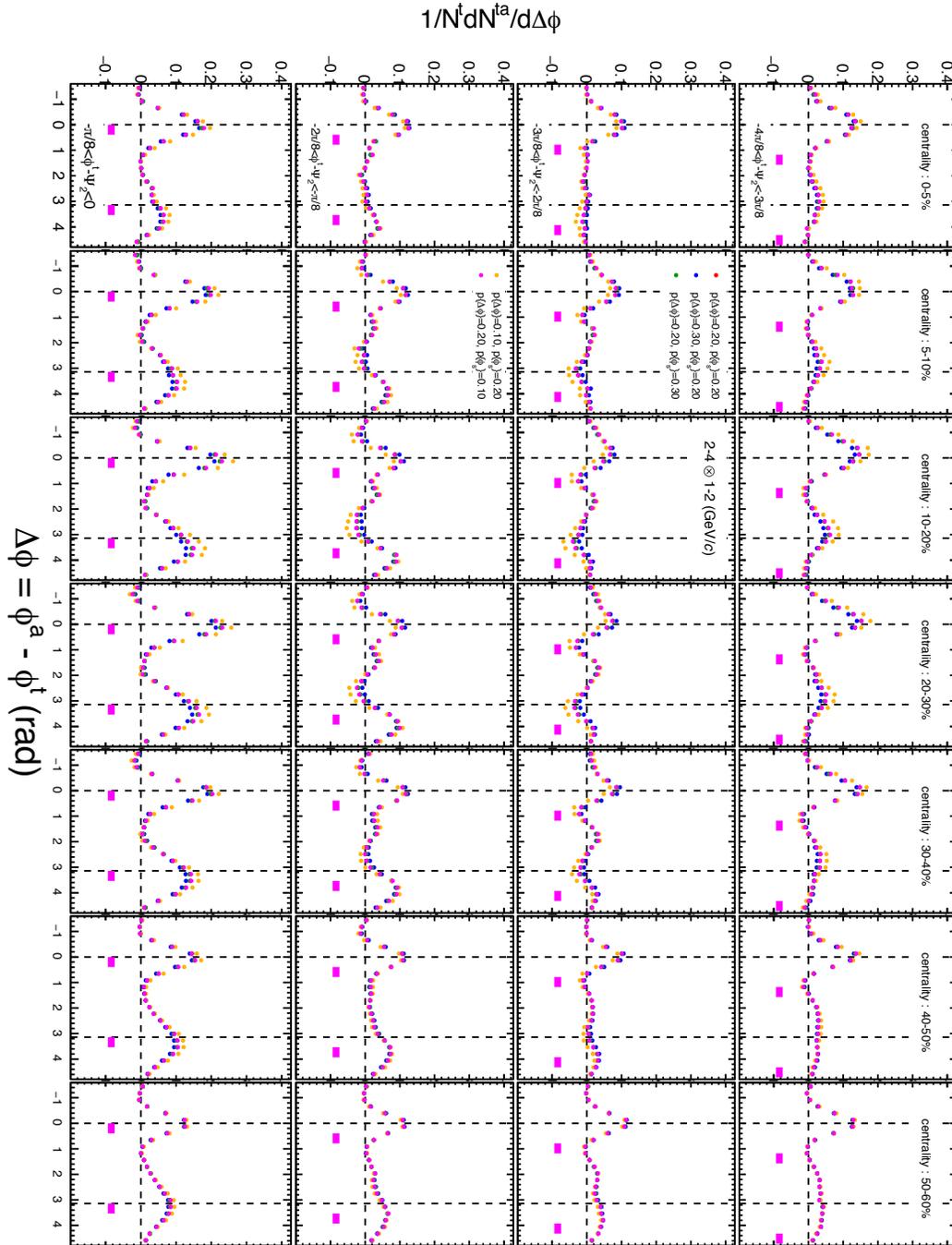
Figure 3.43: Azimuthal distributions of correlated yield corrected by iteration method with various smoothing parameters with $p_T^t \otimes p_T^a$ = 2-4$\otimes$1-2 (GeV/c).
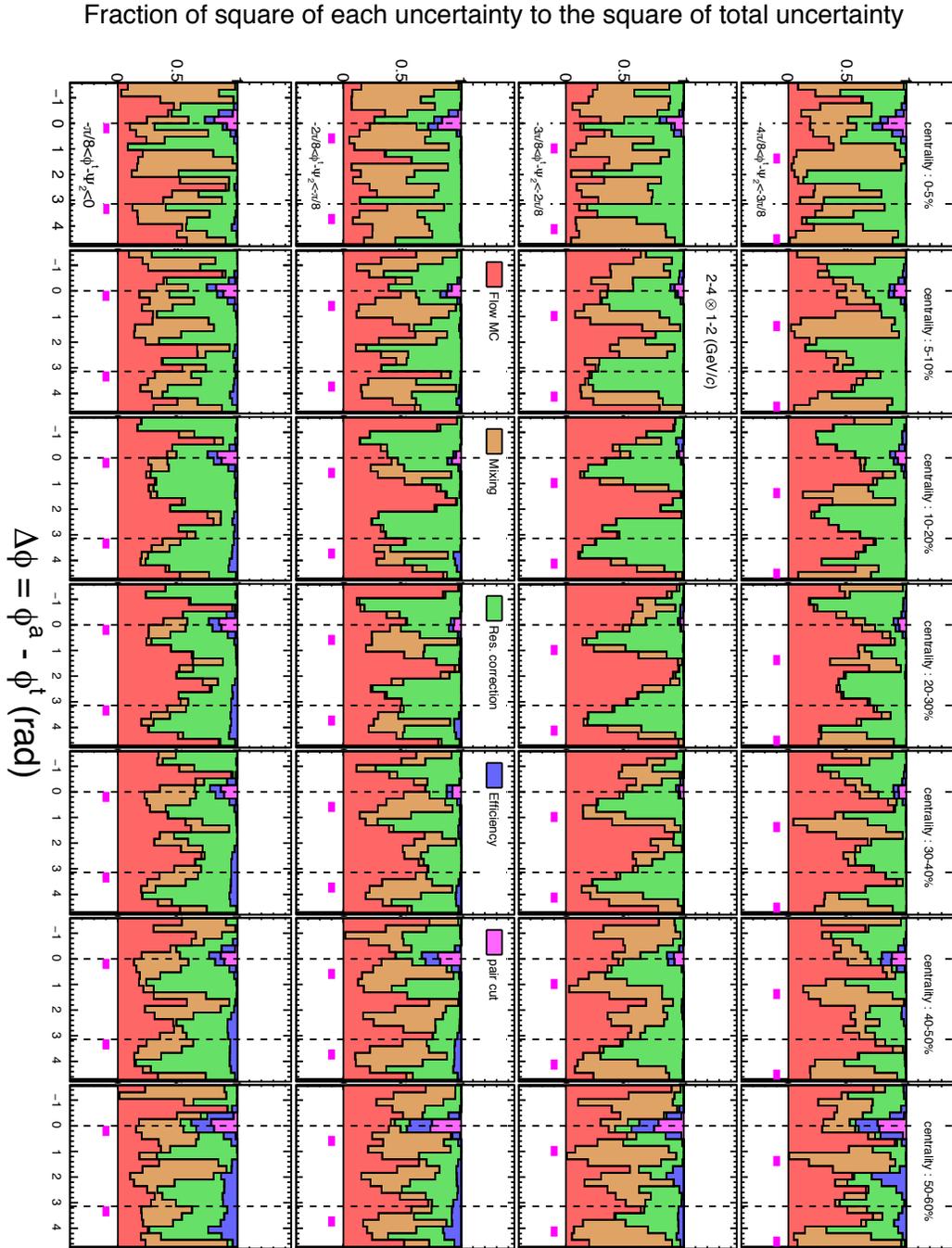
Figure 3.44: Azimuthal angle dependence of fraction of square of each systematic source to the square of total systematic uncertainty with $p_T^t \otimes p_T^a =$ 2-4⊗1-2 (GeV/c).

3.10   A Multi-Phase Transport (AMPT) model

In this section, AMPT model is introduced.

3.10.1   AMPT

A Multi-Phase Transport (AMPT) model is an event generator which describes the evolution of the QGP step-by-step [71]. Heavy Ion Jet Interaction Generator (HIJING) is used for generating the initial conditions : hard process (minijets) and soft process (soft strings). Excited strings are converted into partons with string melting. Zhang ' s Parton Cascade (ZPC) is introduced for modeling elastic partonic scatterings. For modeling hadronization, the Lund string fragmentation model or a quark coalescence model are used. Finally, A Relativistic Transport (ART) model is used to describe hadron scatterings. Structure of AMPT model with quark coalescence model is summarized in Fig.3.45.

Figure 3.45: Illustration of the structure of the AMPT model with string melting.

3.10.2   AMPT analysis

AMPT model is calculated to study interplay between jet and bulk through parton-parton itneraction. Table.3.5 is the setup of AMPT simulation. In this study, charged hadrons, $\pi^{\pm}$, $K^{\pm}$, p and $\bar{\text{p}}$, whose tracks can be reconstructed by the TPC are used for the analysis. Unlike the real experiment, initial eccentricity and reaction plane can be obtained in the simulation. Thus, the following cases are tested :

- two-particle correlations with trigger angle selections with respect to the second-order event plane with flow vector q_2 selections,

- two-particle correlations with trigger angle selections with respect to the second-order event plane with participant eccentricity ε_2 selections,

The acceptance used for the analysis is restricted within $|\eta| < 1$ in order to compare directly with the real experiment.

Table 3.5: AMPT setup

Variable	value
$\sqrt{s_{NN}}$	200 GeV
collision system	Au+Au
impact parameter	$0 < b < 25.60$ (minimum bias)
string melting	ON
number of time-steps for hadron cascade (NTMAX)	150 (fm/c)
flag for popcorn mechanism(netbaryon stopping)	ON
shadowing flag	ON
quenching flag	ON
quenching parameter $-dE/dx$	2.0 (GeV/fm)
parton cross section	3 mb
initial and final state radiation	ON
k_T kick	ON
HIJING shadowing	default

The eccentricity ε_2 and the length of flow vector q_2 is selected as shown in Fig.3.46 and Fig.3.47.
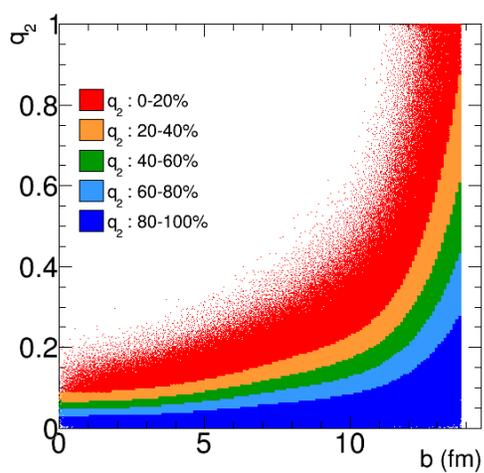
Figure 3.46: 20 % events selected based on q_2 in AMPT model.
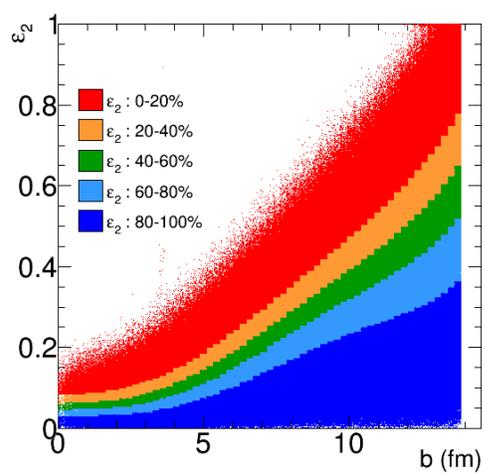
Figure 3.47: 20 % events selected based on ε_2 in AMPT model.

Chapter 4

Results

In this chapter, higher-order harmonic flow parameters v_n used for background subtraction in two-particle correlations and azimuthal distribution of correlated yield after background subtraction are presented.

4.1 Azimuthal anisotropy

Fig.4.1 shows the results of higher-order harmonic flow measured via event-plane method with taking 1.0 η gap between event plane and particles to be interested in.
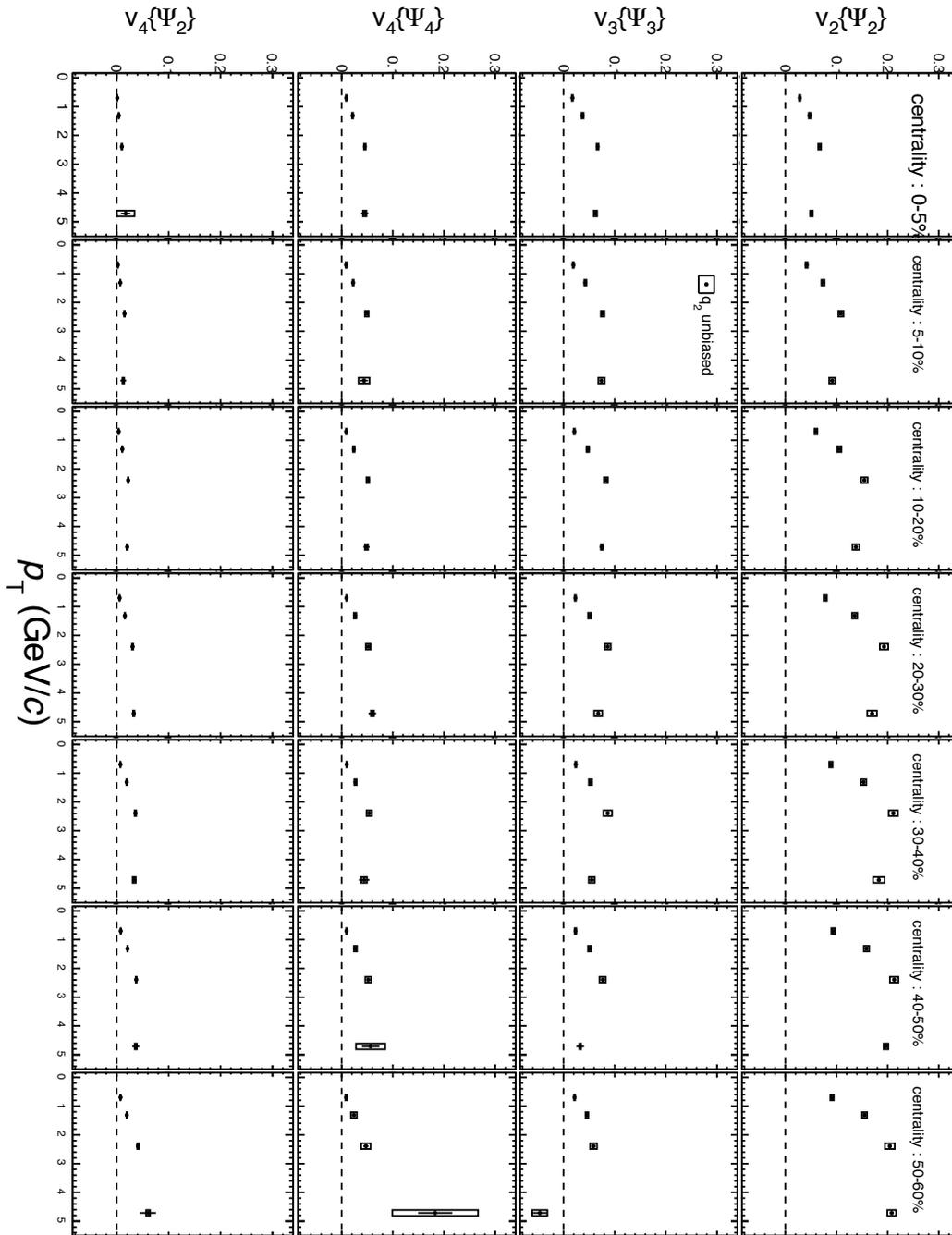
Figure 4.1: Higher-order-harmonic flow v_n measured in this analysis.

4.2 Two-particle correlations

In this section, the results of two-particle correlations after background subtraction are presented with trigger angle selections with respect to the second-order event plane. Trigger particle's p_T ranges are 2-4 and 4-10 (GeV/c) and associate particle's p_T ranges are 0.5-1 ,1-2 and 2-4 (GeV/c).

4.2.1 Second-order event-plane dependent two-particle correlations

Difference of event mixing

Fig.4.2 shows comparison of correlation functions before background subtractions (top) and azimuthal distributions of correlated yield (bottom) with p_T : 2-4⊗2-4 (GeV/c) in 20-30 % centrality. In the previous studies [40][41][42][72], event-plane dependent two-particle correlations have been measured without Psi_2 alignment in event mixing. Systematic differences exist between two mixing method after background subtraction, but those differences are small although correlation shapes before background subtraction are quite different. In the event-plane (Psi_n) dependent two-particle correlations, systematic uncertainty from v_n is major component because the uncertainties from other flow harmonics are treated as square of their systematics but uncertainty from v_n is treated as first power. Thus, systematic uncertainties of event-plane dependent correlations are larger than uncertainties in correlations without trigger angle selections. However, when mixed event pairs are calculated with Psi_n alignment, uncertainty from v_n can be reduced because mixed event also have v_n oscillation. Therefore, it is possible to reduce systematic uncertainties by calculating mixed event pairs with Psi_n alignment. In this study, correlations before background subtractions without Psi_2 alignment in event mixing have v_2 oscillation because of collectivity of two particles, while those with Psi_2 alignment in event mixing have less v_2 oscillation because most of v_2 component is canceled out by dividing mixed pairs with v_2 oscillation.
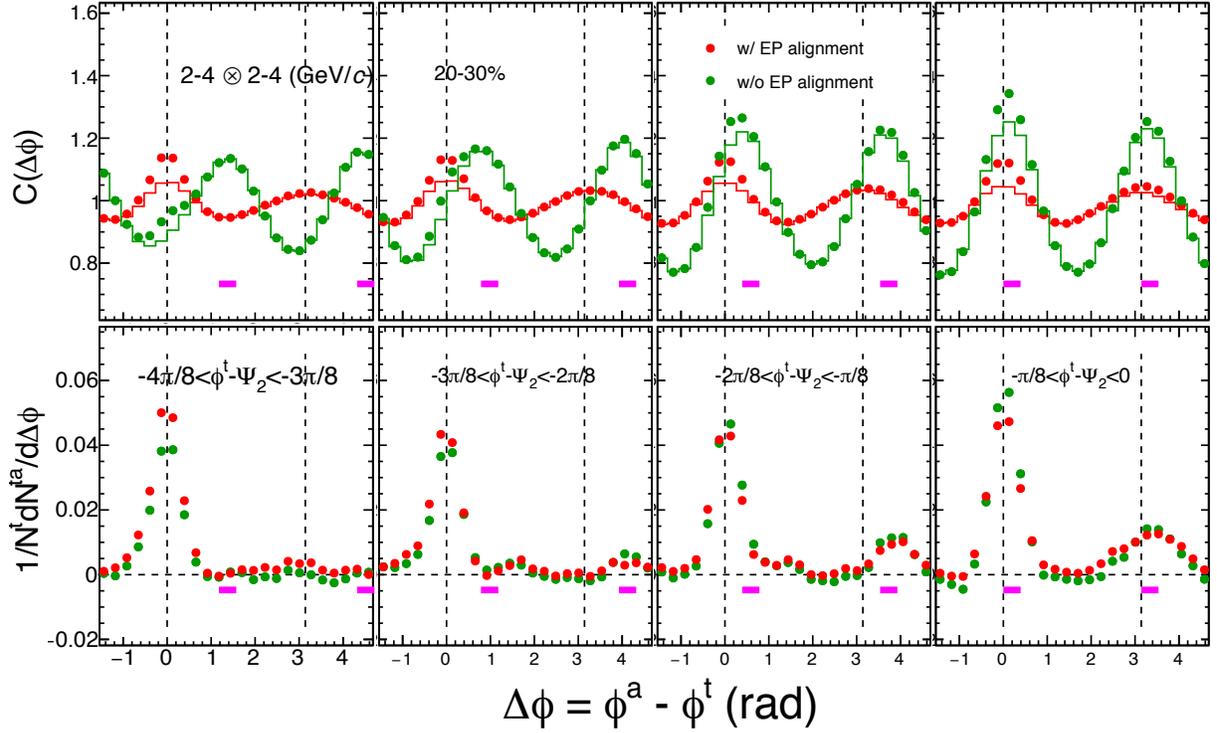
Figure 4.2: Comparison of correlation functions before background subtractions (top) and azimuthal distributions of correlated yield (bottom) with p_T : 2-4⊗2-4 (GeV/c) in 20-30 % centrality. The directions of trigger particles change from out-of-plane (left) to in-plane (right). The color difference correspond to the difference of mixing binning on Ψ_2. The underlines indicate event-plane directions.

Selected results are shown in Fig.4.3 and Fig.4.4. The other results are shown in AppendixA. Fig.4.3 shows difference of out-of-plane and in-plane trigger of azimuthal distributions of correlated yield with p_T : 2-4⊗2-4 (GeV/c) in 0-5, 20-30, 50-60 % centrality bins. In 0-5 % centrality (right), both out-of-plane triggered and that with in-plane triggered correlations are fully suppressed on the away side due to partonic energy loss in the medium. In 20-30 % (middle) and 50-60 % (right) centrality, away-side yield of out-of-plane triggered correlations are suppressed, but that of in-plane triggered correlations are not suppressed. The suppression of away-side yield in out-of-plane triggered correlations is smaller in more peripheral collisions. According to energy-loss model, the probability of penetration of hadrons is expected to be higher in the direction with shorter path-length. In the most central collision, the ellipticity of participant region is small and the system size is larger, and thus difference of path length between out-of-plane and in-plane is small, which results in no difference between out-of-plane and in-plane triggered correlations. From mid-central to peripheral collisions, the ellipticity is large enough to make a difference of in-medium path length, which results in the difference of correlated yield on the away side. The observed trends in the away side do not contradict the energy loss model. The away side peak of in-plane triggered correlation in 20-30 % collisions has an asymmetry with respect to $\Delta\phi = \pi$. That shift can be caused by trigger selections separately in the left and right side of the event plane [73].
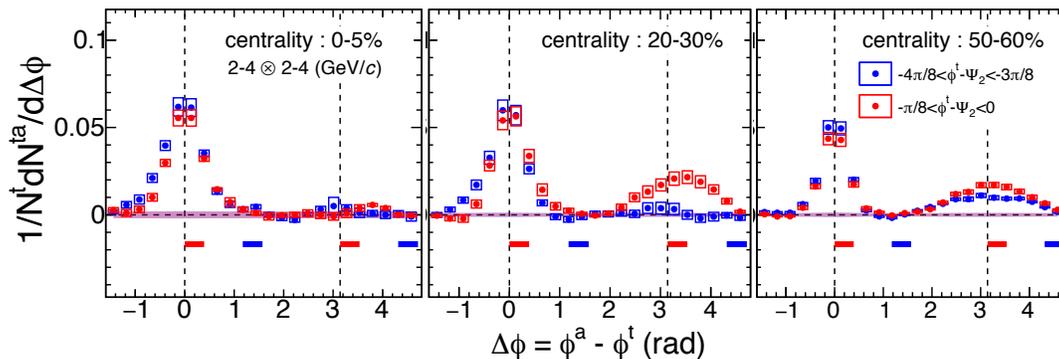
Figure 4.3: Azimuthal distributions of correlated yield with p_T : 2-4⊗2-4 (GeV/c) in 0-5 (left), 20-30 (middle) and 50-60 % (right) centrality bins. The directions of trigger particles are out-of-plane : $-4\pi/8 < \phi_s < -3\pi/8$ (blue) and in-plane : $-\pi/8 < \phi_s < 0$ (red). The underlines indicate event-plane directions.

Fig.4.4 shows polar representation of azimuthal correlations with 2-4⊗1-2 (GeV/c) in 0-5, 20-30, 50-60 % centrality in order to see how correlation shapes are modified. Second-order event-plane Ψ_2 direction is set to horizontal axis and trigger directions are analogous to Fig.3.20. Relative angle of associate particle with respect to trigger particle circles counter-clock-wise direction. Residual correlated yields are observed in the same direction with trigger particles (near side). In particular, apparent back-to-back yields appear in correlations with in-plane and out-of-plane trigger bins and the yield is larger with in-plane trigger bin because of shorter path-length of initial partons in the medium. Modification of correlation shapes is the strongest in 20-30 % where in-medium

path length is different enough to make difference of jet quenching effect. Correlation shapes with two mid-plane triggers are strongly modified ; away side yield is not observed in the back-to-back direction and the peak positions are shifted. Moreover, away side yield with mid-out-of-plane trigger $(-3\pi/8 < \phi_s < -2\pi/8)$ has mainly out-of-plane direction where the path length is the longest mid-in-plane trigger $(-4\pi/8 < \phi_s < -3\pi/8)$ has shifted to Ψ_2 direction where the path length is the shortest. This result can be understood by the balance of partonic energy loss and re-distribution of deposited energy from partons because of asymmetric in-medium path length even in the same centrality.
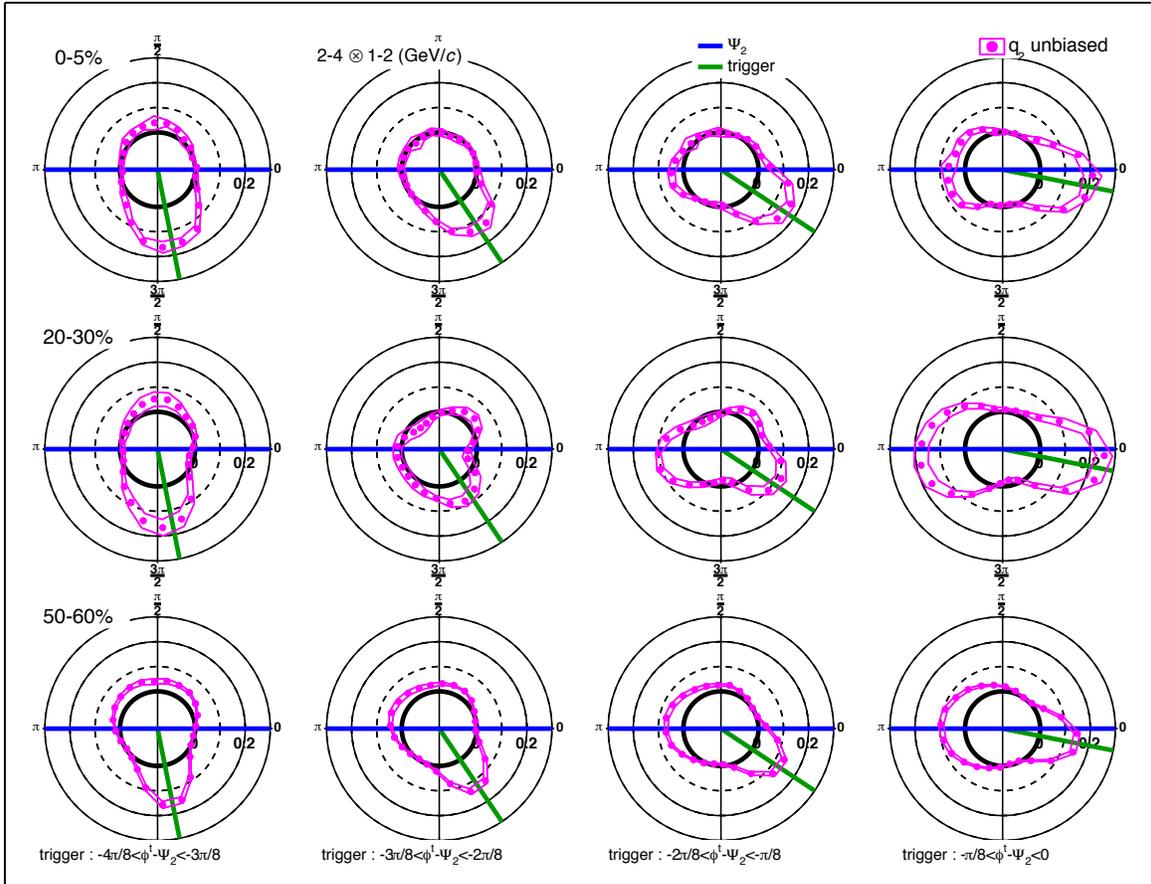
Figure 4.4: Azimuthal distributions of correlated yield with p_T : 2-4⊗2-4 (GeV/c) in 0-5 (top), 20-30 (middle) and 50-60 (bottom) % centrality bins. The directions of trigger particles change from out-of-plane : $-4\pi/8 < \phi_s < -3\pi/8$ (left) to in-plane : $-\pi/8 < \phi_s < 0$ (right). The underlines indicate event-plane directions.

4.3 Results with q_2 selections

4.3.1 Azimuthal anisotropy with q_2 selections

The flow parameters v_n are measured with the same way as q_2 unbiased case (Fig.4.1). Measured v_n before taking the ratio are shown in AppendixA. Fig.4.5 shows the ratio of v_2 measured in q_2 selected events to v_2 measured in q_2 unbiased events. At least top and bottom 20 % q_2 selected events are separated even considering the uncertainties. The ratios show almost no p_T dependence within systematic uncertainties. The results confirm the collectivity of the system and possible effect of the difference of path length because of non-zero v_2 with high-p_T ranges.
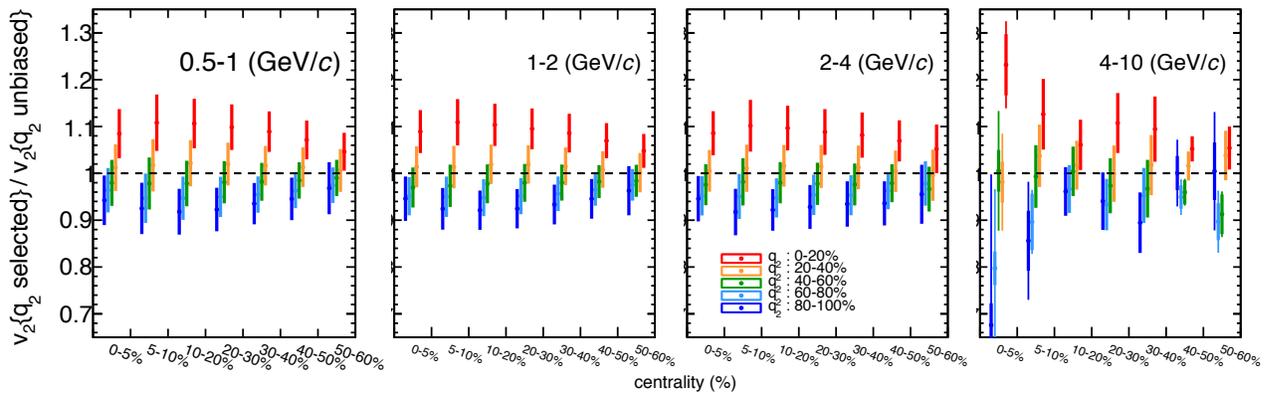
Figure 4.5: The ratio of v_2 measured in q_2 selected events to v_2 measured in q_2 unbiased events in p_T slice from 0.5-1 GeV/c(left) to 4-10 GeV/c(right).

4.3.2   Second-order event plane dependent two-particle correlations with q_2 selections

In this subsection, selected correlations with q_2 selections are presented. The other results are shown in AppendixA. Fig.4.6 shows polar representations of correlated yield with p_T : 2-4⊗1-2 (GeV/c) with top and bottom q_2 20 % (q_2 : 0-20 and 80-100 %, respectively) selection in 0-5, 20-30 and 50-60 % centrality. Separation of top-q_2 and bottom-q_2 event selections is observed for in-plane and out-of-plane trigger bins in 0-5 and 20-30 % centrality, where the largest path length difference is expected between large-q_2 and small-q_2 events. In 50-60 % centrality, q_2 dependence is small or nothing because average participant shape is elliptic enough to make no difference with q_2 selections. Longer (shorter) path length is expected in the in-plane direction with small-q_2 (large-q_2) events and shorter (longer) path length is expected in the out-of-plane direction with small-q_2 (large-q_2) events due to the difference of the initial participant eccentricity. Larger yield is observed in the large-q_2 events in the away side, which is expected to have shorter path length than in the small-q_2 events. In the out-of-plane triggers, the yield in the small-q_2 events is smaller than in large-q_2 events even for its shorter path length. That could be the effect of energy re-distribution with larger path length in the statical medium direction. Fig.4.7 shows polar representations of correlated yield with p_T : 2-4⊗1-2 (GeV/c) with q_2 selections in 20 % steps in 2-30 % centrality. Trigger angle dependence is observed in all q_2 bins ; the trend is similar as q_2 unbiased events (Fig.4.4). Correlation shapes are slightly modified by q_2 selections. In particular, away-side yield of out-of-plane triggered correlations increase with larger q_2. These difference comes from difference of initial participant shape or effect of collective flow.
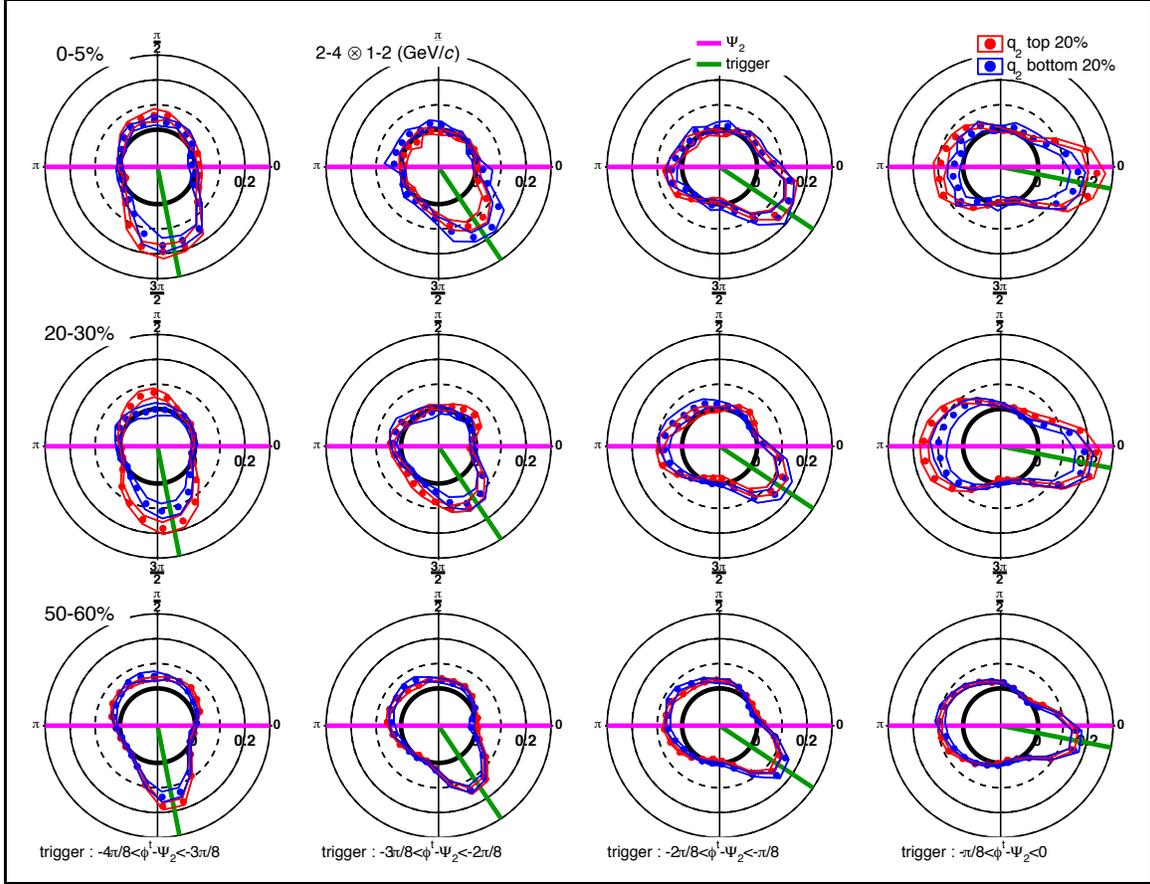
Figure 4.6: Azimuthal distribution of correlated yield with p_T : 2-4⊗1-2 (GeV/c) in 0-5 (top), 20-30 (middle) and 50-60 % (bottom) with top and bottom 20 % q_2 selections with trigger angle selection with respect to the second-order event plane.
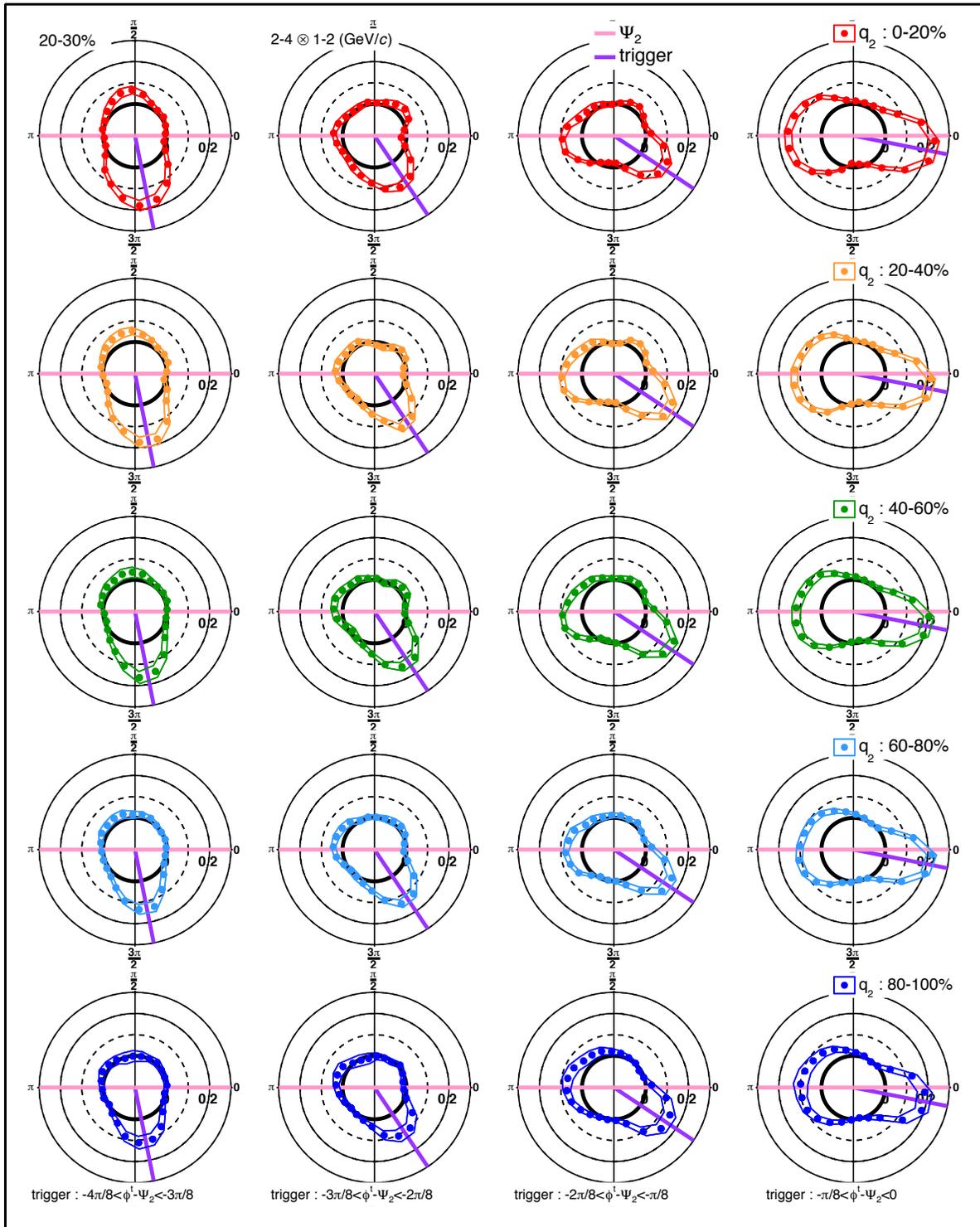
Figure 4.7: Azimuthal distribution of correlated yield with p_T : 2-4⊗1-2 (GeV/c) in 20-30 % with 20 % q_2 selections from top to bottom with trigger angle selection with respect to the second-order event plane.

Chapter 5

Discussions

We discuss what is observed for azimuthal distributions of correlated yield after background subtraction in this chapter.

5.1 Event-plane dependent two-particle correlations

In this section, results of event-plane dependent correlations will be disucussed.

5.1.1 Comparison with AMPT model

In this subsection, the experimental results are compared with AMPT model in order to study the effect of the interplay between jets and flow. Fig.5.1 shows azimuthal anisotropy in AMPT model compared with experimental data which is measured in this study in 0-50 % centrality. Analysis method is the same way as experimental data. The other results are shown in AppendixC. v_2 in AMPT model tested in this setup is smaller than experimental data at $p_T \geq 1$, while v_3 and v_4 are almost consistent. One possible reason is that parton cross section (3 mb) is small to reproduce elliptic flow.

Fig.5.2 shows azimuthal distribution of correlated yield after v_2, v_3 and v_4 contribution subtraction in 0-50 % centrality. In AMPT model Psi_2-Psi_4 correlation is not considered because that contribution on correlation shape is trivial. In 0-20 % centrality, AMPT does not reproduce the experimental data. In 20-50 % centrality, AMPT reproduces the away-side shape experimental data. Near-side peaks are smaller in AMPT model than the experimental data.

Fig.5.3 shows trigger-angle dependence of two-particle correlations with 2-4 GeV/$c$triggers and 2-4 GeV/$c$associates in 0-50 % centrality. The other p_T combinations are shown in AppendixC. AMPT model partially reproduces the trend of experimental data. Away-side yield with in-plane trigger is larger than those with out-of-plane trigger, and peak-position are shifted to the direction of Ψ_2. However, the amplitude of away-side yields are overestimated. Near-side yields also have trigger angle dependence ; the near-side yields are suppressed with changing to out-of-plane trigger. It could be the effect of jet-quenching effect or role of collective flow.
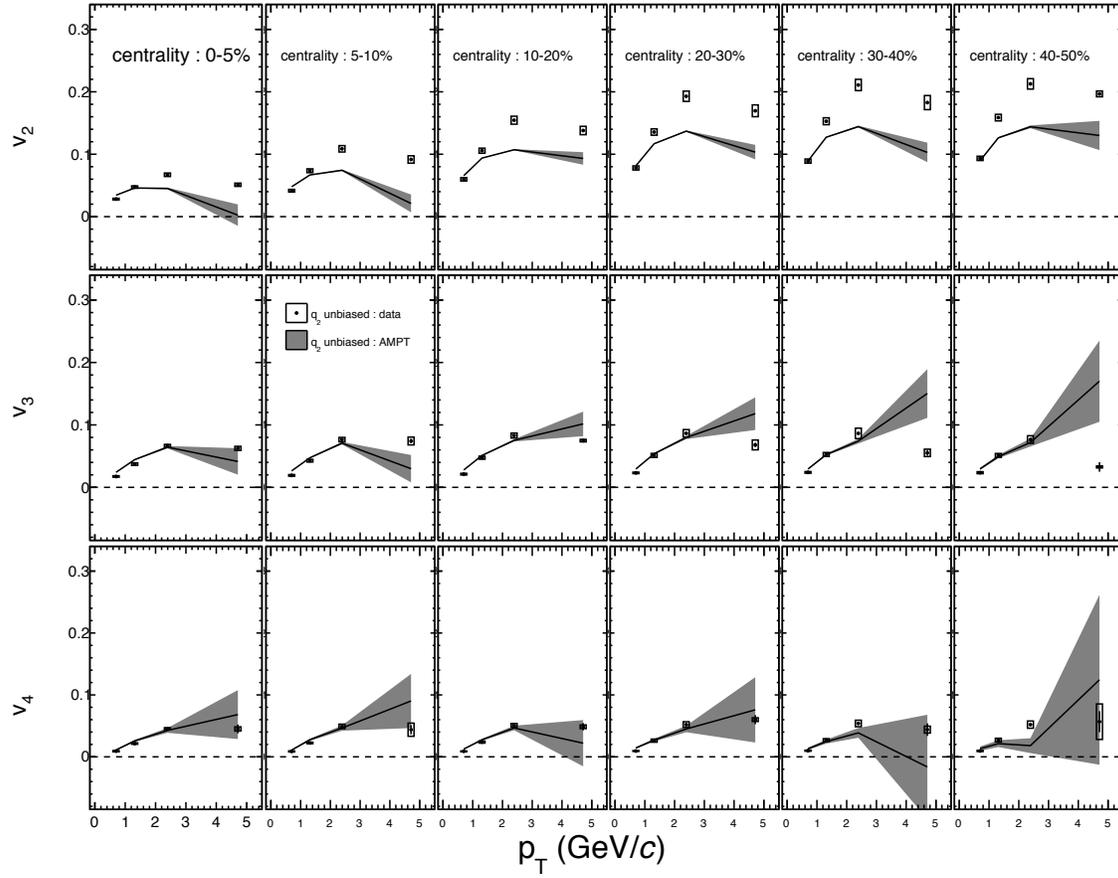
Figure 5.1: Azimuthal anisotropy in AMPT model compared with experimental data which is measured in this study in 0-50 % centrality. Analysis method is the same way as experimental data.
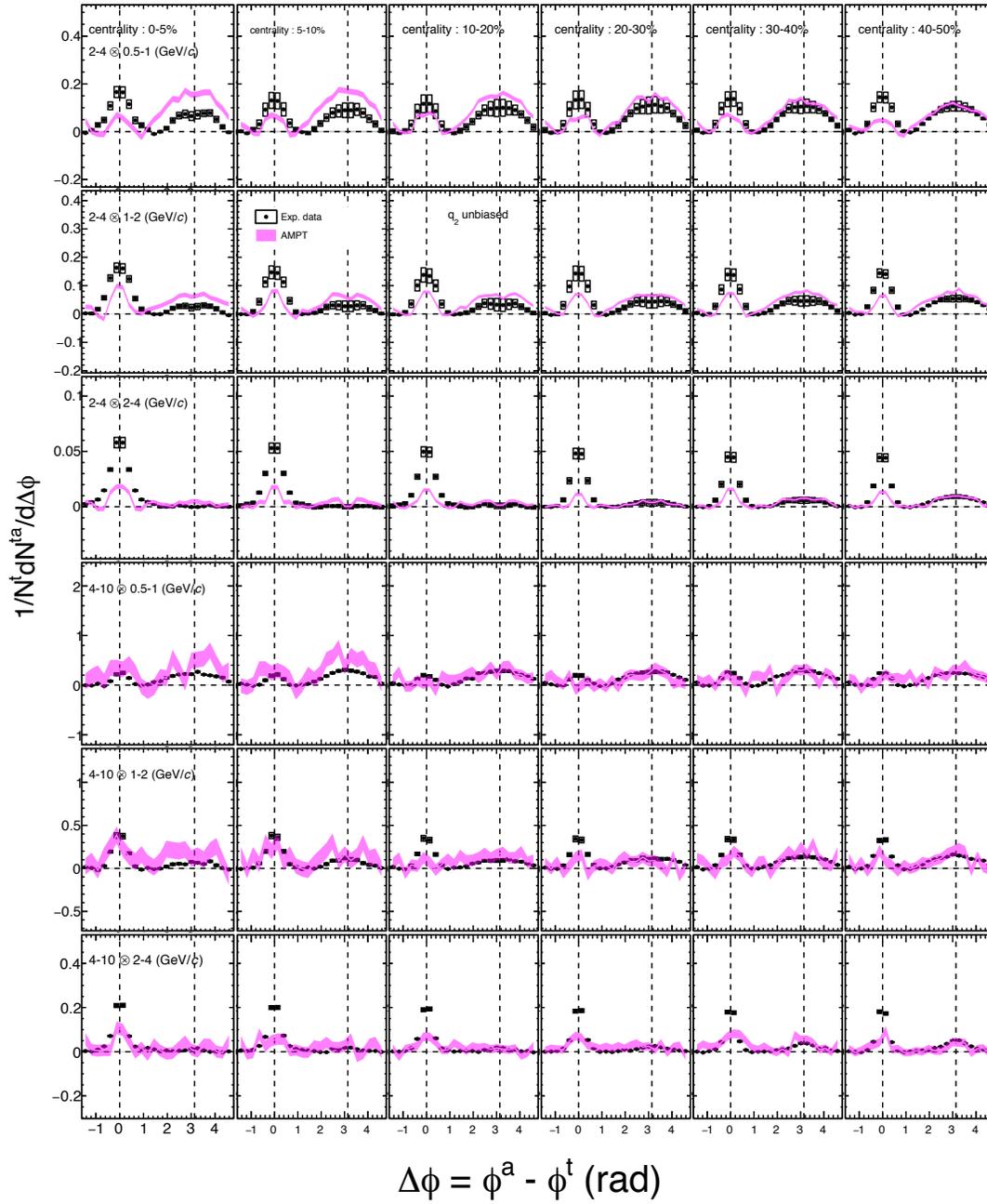
Figure 5.2: Azimuthal distribution of correlated yield after v_2, v_3 and v_4 contribution subtraction in 0-50 % centrality. In AMPT model Ψ_2-Ψ_4 correlation is not considered because that contribution is trivial.
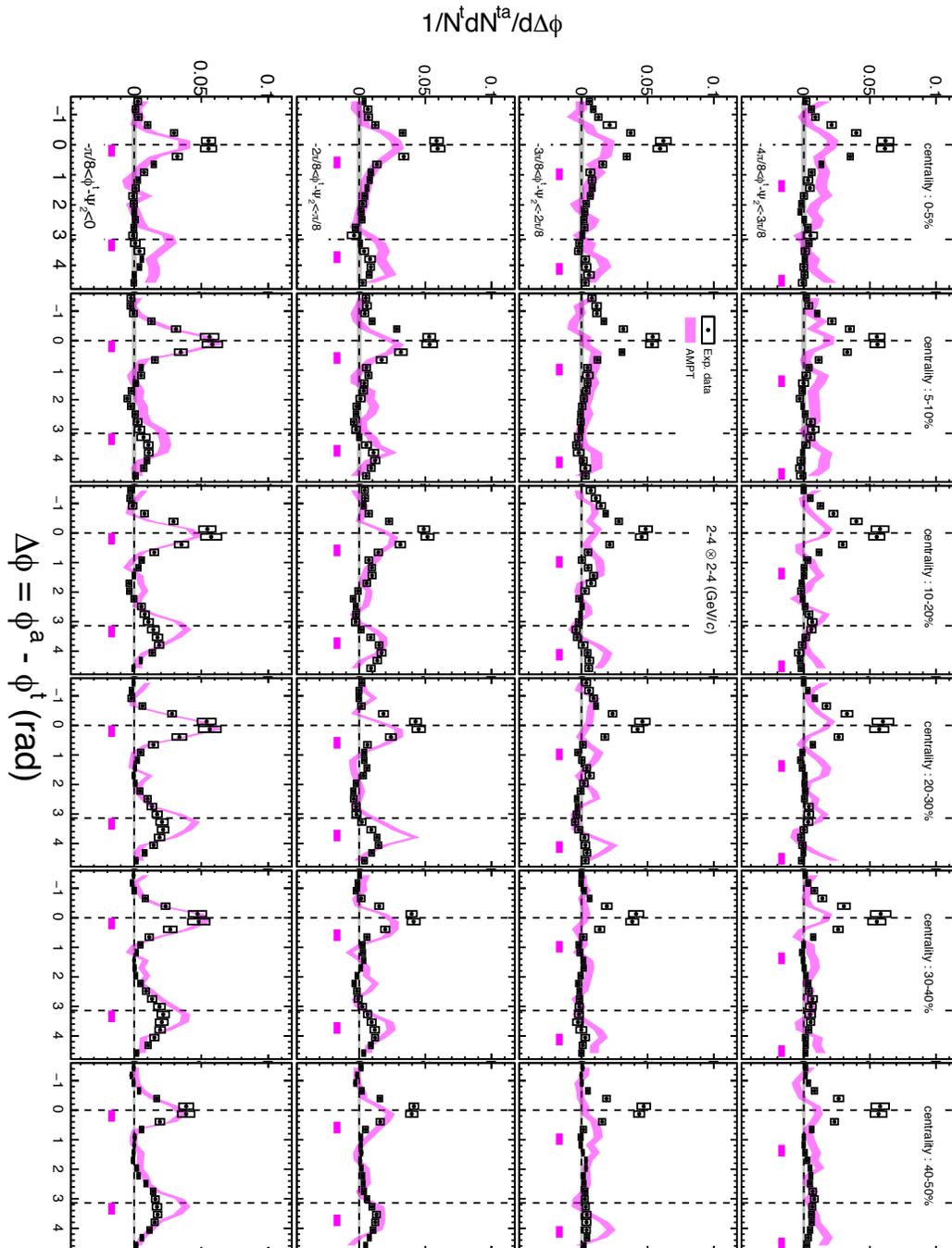
Figure 5.3: Trigger angle ϕ_s dependence of azimuthal distribution of correlated yield after v_2, v_3 and v_4 contribution subtraction in 0-50 % centrality. In AMPT model Ψ_2-Ψ_4 correlation is not considered because that contribution is trivial.

5.1.2　Integrated yield

Integrated yield is calculated for a quantitative discussion of trigger-angle dependent correlated yield. Fig.5.4 shows integrated yield as a function of ϕ_s, where the region for integration is $|\Delta\phi| < \pi/3$ for near side and $|\Delta\phi| < 2\pi/3$ for away side. Integrated yields with 2-4 (GeV/c) for trigger particles and 0.5-1 and 1-2 (GeV/c) for associate particles have similar trend on both near side and away side in all centrality bins : the integrated yield is the largest with the in-plane trigger bin and is gradually suppressed with out-of-plane trigger and become larger with the out-of-plane trigger bin in all centrality bins. The trend on the near side, the suppression of the yield with increasing ϕ_s, is similar with centrality dependence of near side peak [30],[74], which means that near-side yield are suppressed with more peripheral collisions. This can be interpreted as near-side yield is larger in dynamical direction. The enhancement of integrated yield at the out-of-plane bin where the longest path length is expected can be a possible effect of energy re-distribution of the lost energy of high-energy partons. The integrated yields with both trigger p_T range and 2-4 (GeV/c) associates have different trigger angle dependence from lower associate p_T ranges. On the near side, little trigger angle dependence is observed in 0-10 % , the similar trend at lower associate p_T ranges is observed in 10-40 % and the enhancement of integrated yield with changing to out-of-plane trigger. This could be the effect of energy re-distribution of deposited energy to the bulk. On the away side, the integrated yields are suppressed in the out-of-plane direction due to the path-length dependence of energy loss. The integrated yield with 4-10 (GeV/c) triggers, 0.5-1 and 1-2 (GeV/c) associates on both near side and away side have similar trend with each other. In 5-50 %, the trend is similar with lower trigger p_T both on near side and away side. In 0-5 %, the integrated yield is the largest at the mid-in-plane trigger bin but the trend that the yield is larger with in-plane trigger is the same. In 50-60 %, the integrated yield is enhanced in the out-of-plane direction both on the near side and away side.

Scaling with path length

Directions of particles and centrality can be translated into path length and global scaling of energy loss can be studied. Centrality dependence of nuclear modification R_{AA} is usually measured to investigate path-length dependence of high energy partons. But the measurements of particle direction and centrality dependence are converted into the dimension of path length and energy loss of single particle is studied by the PHENIX collaboration [75]. Path length is determined by calculating effective length with transverse distribution of participant density by simulating standard Glauber Monte-Carlo. Fig.5.5 shows path length L_ε dependence of R_{AA} of p_T : 1.0-10.0 (GeV/c) with in 10-60 % centrality bins. The universal scaling holds at higher p_T region ($p_T \geq 4.0$ GeV/c).

In this study, scaling with path length is tested to investigate how the path length dependence of correlated yield can be understood in each trigger bin. Path length is calculated with standard Glauber Monte-Carlo with selecting particles direction with respect to the second-order participant plane which is assumed to correspond to the second-order event plane. It is assumed that hard scattering can occur anywhere in the participant region and no p_T dependence exists for both trigger and associate particles. As shown in Ref.[75], the behavior of single particle R_{AA} is different
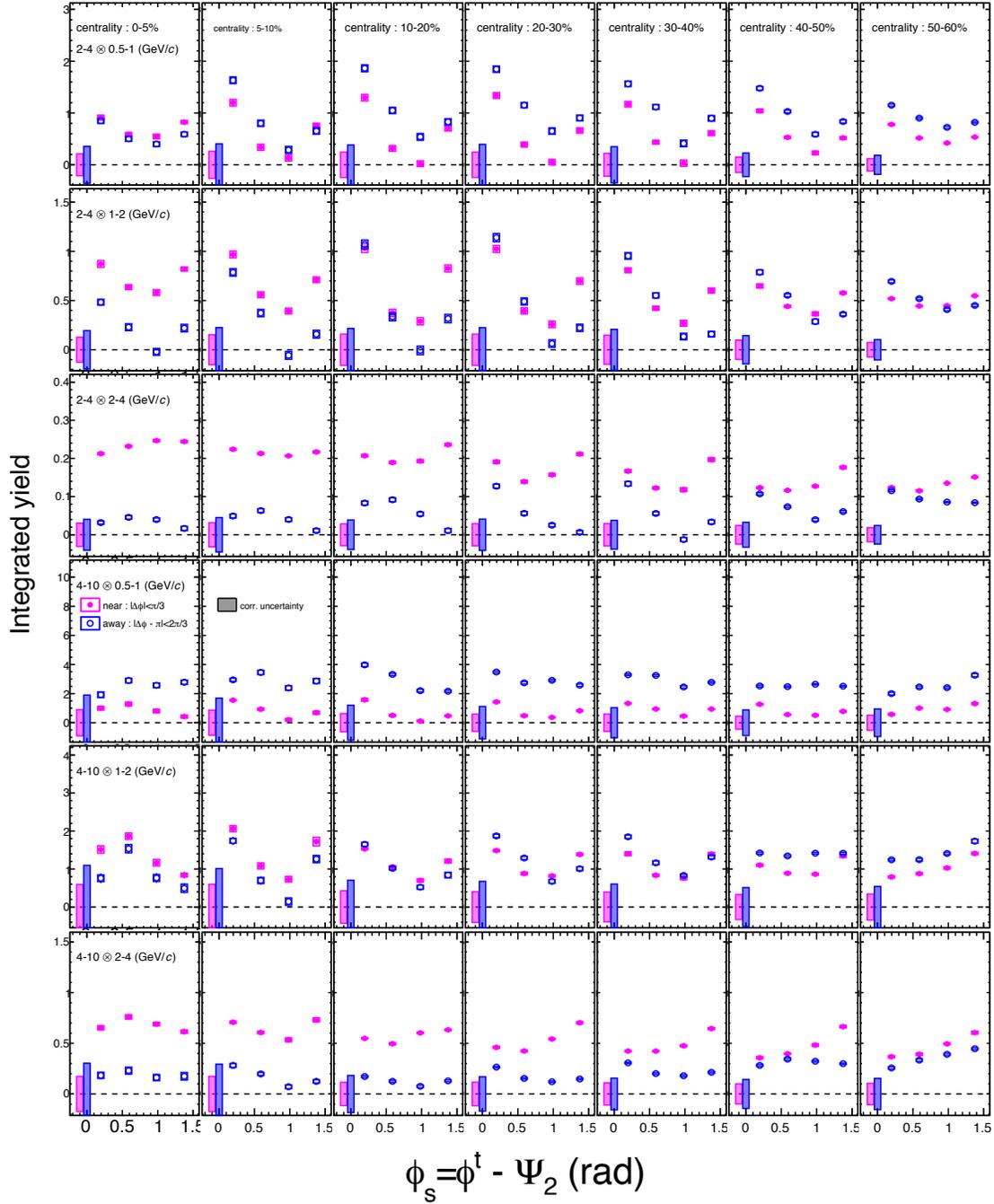
Figure 5.4: Trigger angle ϕ_s dependence of integrated yield with 2-4, 4-10 (GeV/c) for trigger particles and 0.5-1, 1-2 and 2-4 (GeV/c) for associate particles in each centrality.
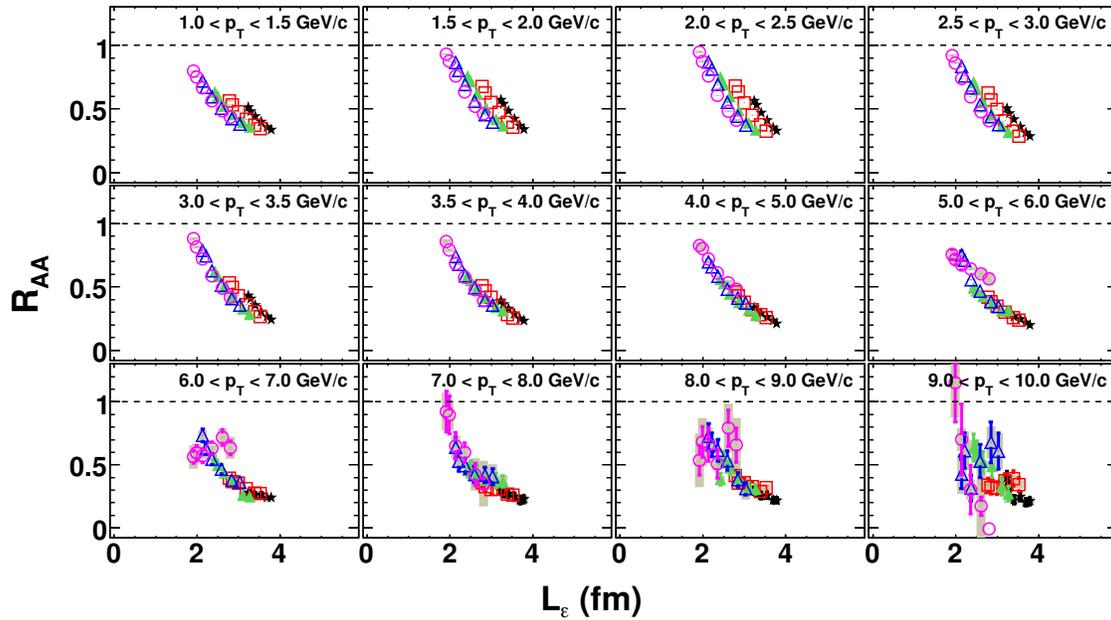
Figure 5.5: R_{AA} of π^0 as a function of path length L_ε based on the hard sphere calculation : (black) stars, 10-20%; open (red) squares, 20-30%; (green) triangles, 30-40%, open (blue) triangles, 40-50%; open (magenta) circles, 50-60% [75].

below 8 GeV/c. Therefore, path length dependence is shown by each trigger bin. Fig.5.6 and Fig.5.7 show integrated yield as a function of path length L in the near side and away side, respectively. Correlated yield in the near side is enhanced with L and that in the away side are suppressed with L. These rough trends means that energy re-distribution of deposited energy from jets is dominant in the near side and partonic energy loss is dominant in the away side. Behavior of path length (centrality) dependence is different between trigger particles directions. For example in $p_T^t \otimes p_T^a = $ 4-10⊗2-4 (GeV/c), path length dependence is flat in the out-of-plane trigger bin but integrated yield are enhanced with increasing L in the other three trigger bins. Thus, correlated yield of two-particle correlations is not scaled with simple path length calculation among each trigger bin because the balance of jet penetration and energy re-distribution cannot be described.
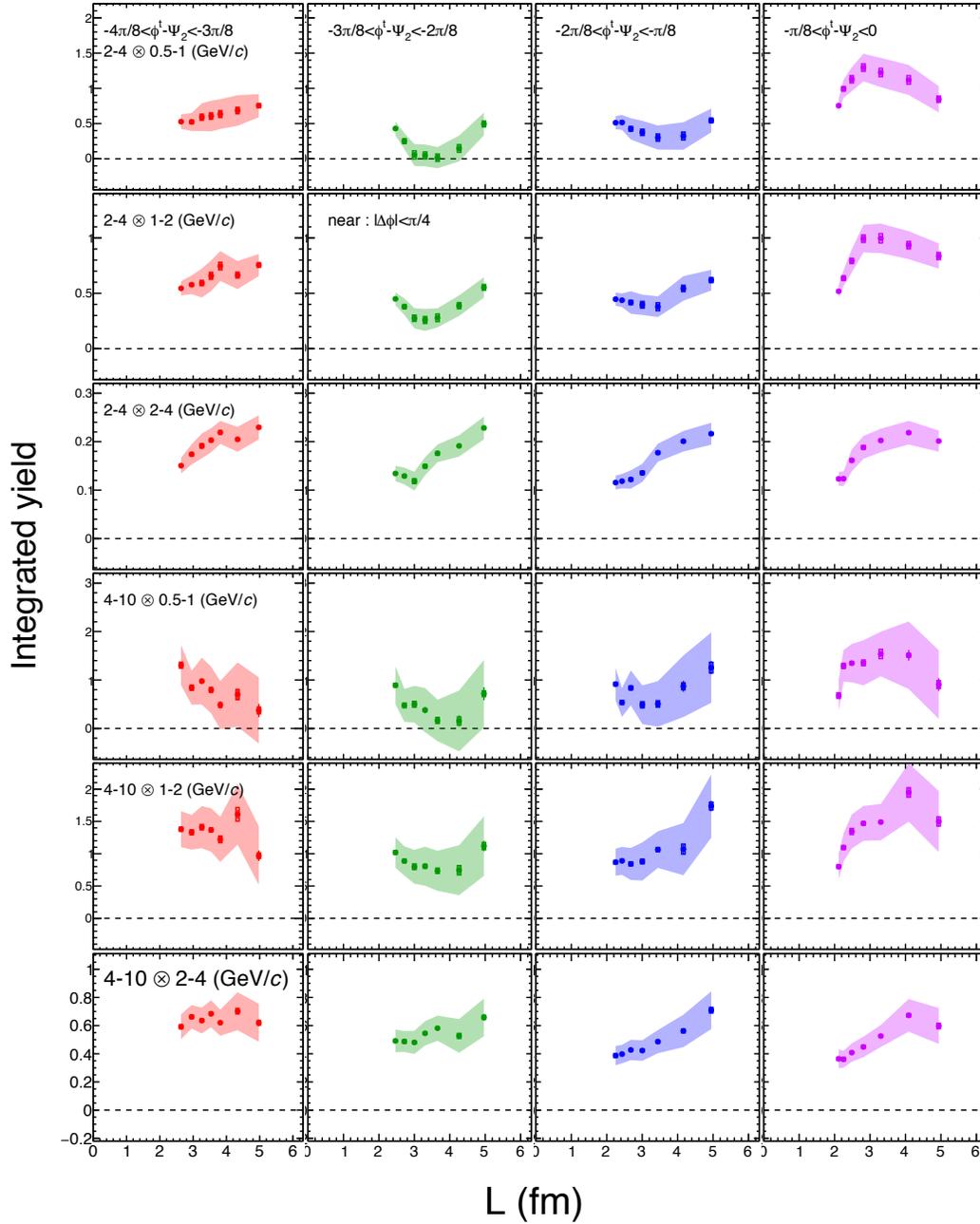
Figure 5.6: Integrated yield of the near side as a function of path length L in 0-60 % centrality.
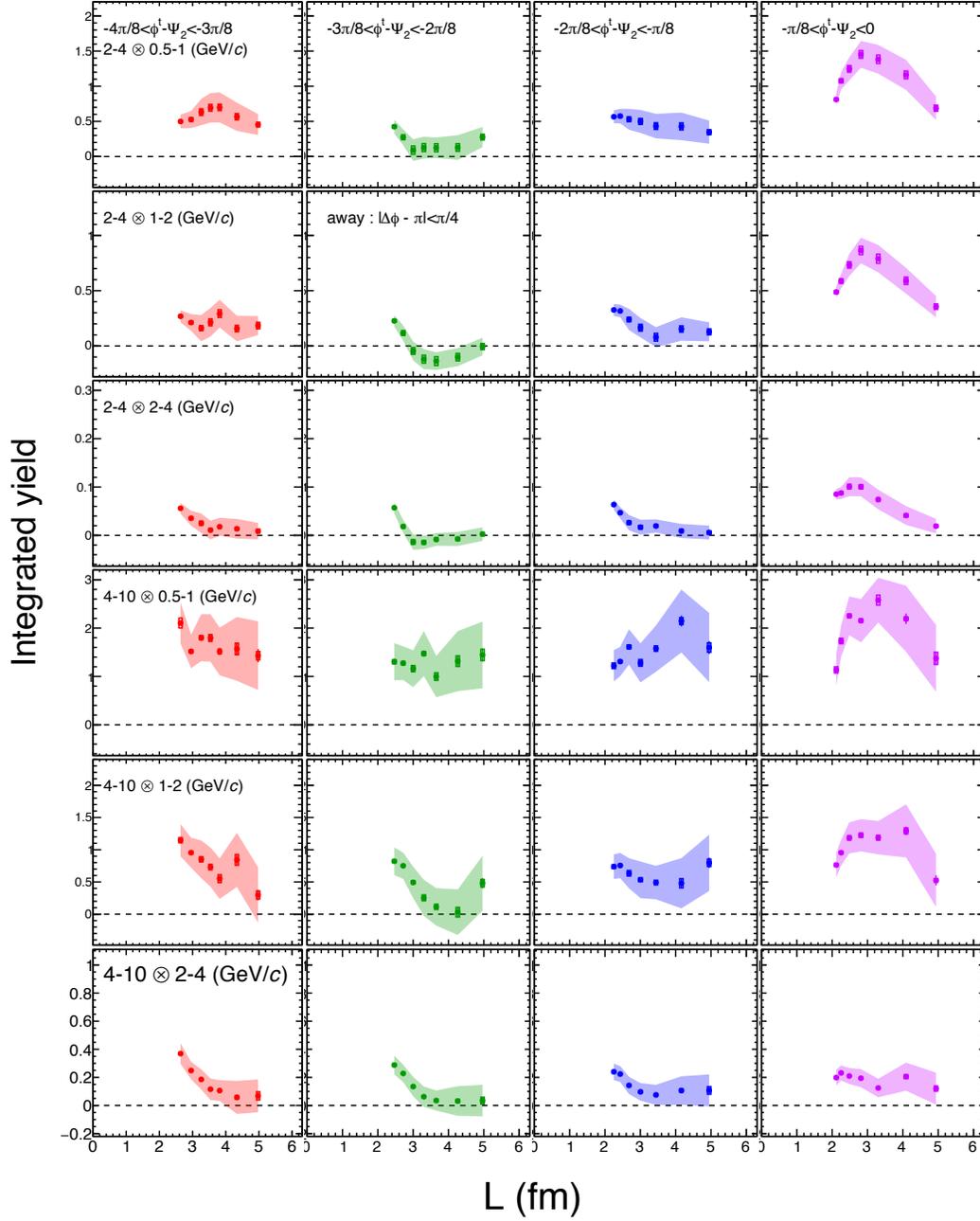
Figure 5.7: Integrated yield of the away side as a function of path length L in 0-60 % centrality.

Azimuthal anisotropy of correlated yield

Trigger angle dependence of integrated yield are fitted by Fourier function and extract the oscillation parameters v_2^Y and v_4^Y as

$$F(\phi_s) \quad = \quad a\{1 + 2v_2^Y \cos(2\phi_s) + 2v_4^Y \cos(4\phi_s)\}, \tag{5.1}$$

where a is the mean and ϕ_s can be written as $\phi_s = \phi^t - \Psi_2$. In order to convert the equation Eq.(5.1) the function of relative angle of associate particle to the event plane, ϕ_s in refeqyieldvn is replaced by $\phi_s + \Delta\phi$ ($\Delta\phi = \phi^a - \phi^t$). The parameter v_n^Y indicates that anisotropy per one trigger particle which is assumed to distribute uniformly in full azimuth. However, trigger particles have non-zero anisotropy as shown in Fig.4.1. Therefore real azimuthal distribution can be expressed by superposition of them as

$$\{1 + 2v_n^Y \cos n(\phi^a - \Psi_2)\} \times \{1 + 2v_n^t \cos n(\phi^t - \Psi_2)\} \tag{5.2}$$

$$= \{1 + 2v_n^Y \cos n(\phi^a - \Psi_2)\} \times \{1 + 2v_n^t \cos n[(\phi^a - \phi^t) + (\phi^a - \Psi_2)]\} \tag{5.3}$$

$$= \{1 + 2v_n^Y \cos n(\phi^a - \Psi_2)\} \times \{1 + 2v_n^t \cos n(\phi^a - \phi^t)\cos n(\phi^a - \Psi_2)\} \tag{5.4}$$

$$= 1 + 2\{v_n^Y + v_n^t \cos n(\phi^a - \phi^t)\}\cos n(\Delta\phi) + \mathcal{O} \tag{5.5}$$

$$\simeq 1 + 2\{v_n^Y + v_n^t \cos n(\Delta\phi)\}\cos n(\phi^a - \Psi_2) \tag{5.6}$$

$$= 1 + 2v_n^{Y,corr} \cos n(\phi^a - \Psi_2), \tag{5.7}$$

where v_n^t is azimuthal anisotropy of trigger particles. Here, v_n^Y and v_n^t are assumed to be sufficiently small and their product is ignored. Thus, the corrected azimuthal anisotropy of integrated yield can be obtained as $v_n^{Y,corr} = v_n^Y + v_n^t \cos n(\Delta\phi)$. Fig.5.8 and Fig.5.9 show azimuthal anisotropy of correlated yield $v_n^{Y,corr}$ and single particle v_n in the near side ($|\Delta\phi| < \pi/4$). In the near side Fig.5.8, except for higher trigger p_T in 0-5 %, $v_2^{Y,corr}$ shows positive value. There is centrality and associate p_T dependence for $v_2^{Y,corr}$ and $v_4^{Y,corr}$: they are the largest in mid-central collisions and decrease with increasing associate p_T while single particle $v_n\{\Psi_2\}$ increases with p_T and centrality. For 2-4 (GeV/c) associate p_T, $v_2^{Y,corr}$ is smaller than single particle v_2. If $v_2^{Y,corr}$ is larger than single particle v_2, ellipticity formed by correlated yield is stronger than that by hydrodynamics but the jet-like yield component is very small compared with the collective flow. Moreover, if $v_2^{Y,corr}$ is larger than single particle v_2 and $v_4^{Y,corr}$ is larger than single particle $v_4\{\Psi_2\}$, coexistence of path length dependent energy loss and re-distribution. The result confirms that the contribution of path-length energy loss is dominant with lower associate p_T and re-distribution is dominant with higher associate p_T. In the away side Fig.5.9, v_n with lower trigger p_T is larger than that with higher one. In 0-40 % centrality, opposite associate p_T dependence is observed : $v_2^{Y,corr}$ increases with associate p_T with 2-4 (GeV/c) triggers. This is because high-p_T particles are not emitted from back-to-back direction to high-p_T triggers due to path-length dependent partonic energy loss. At the same time, $v_4^{Y,corr}$ also have the same trend as $v_2^{Y,corr}$. This observation means that the yield is suppressed with mid-plane triggers and the contribution of re-distribution of the deposited energy from high-p_T particles also appear and quadrangularity with respect to the second-order event plane.
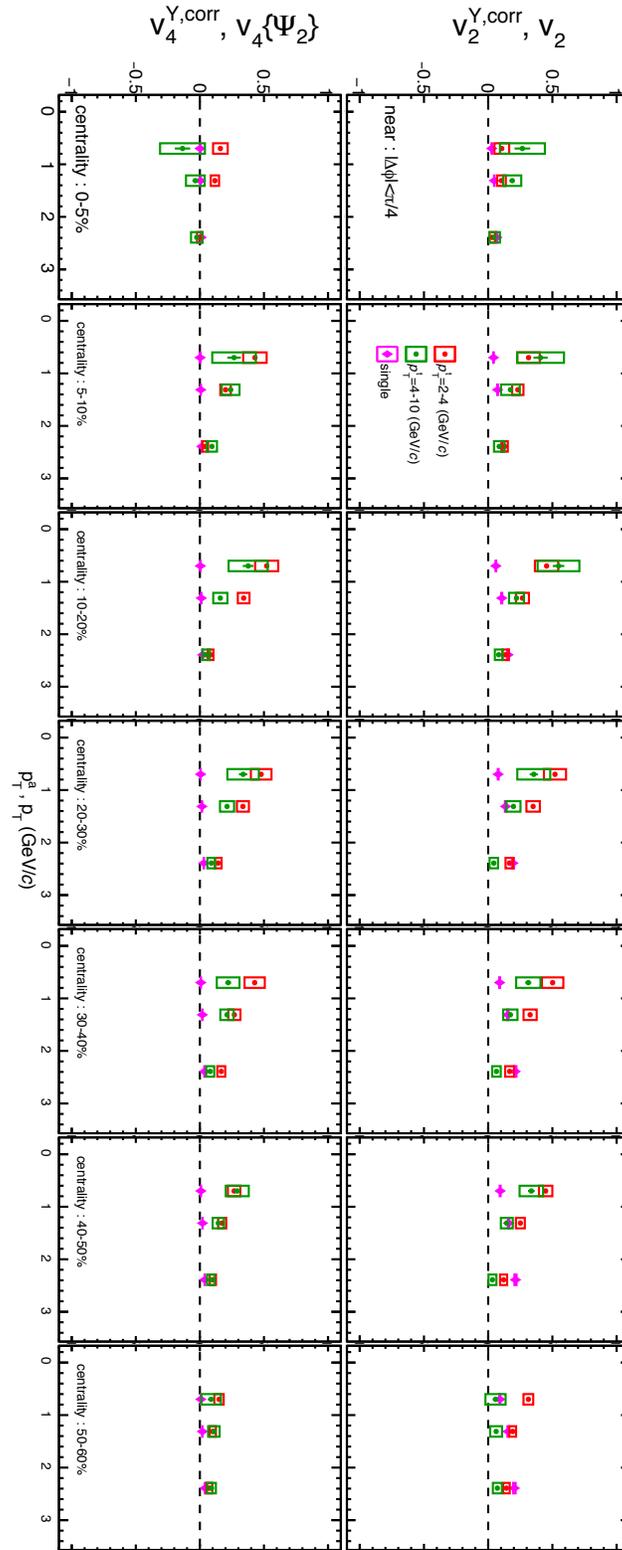
Figure 5.8: Azimuthal anisotropy of correlated yield $v_n^{Y,corr}$ in the near side and that of single particle.
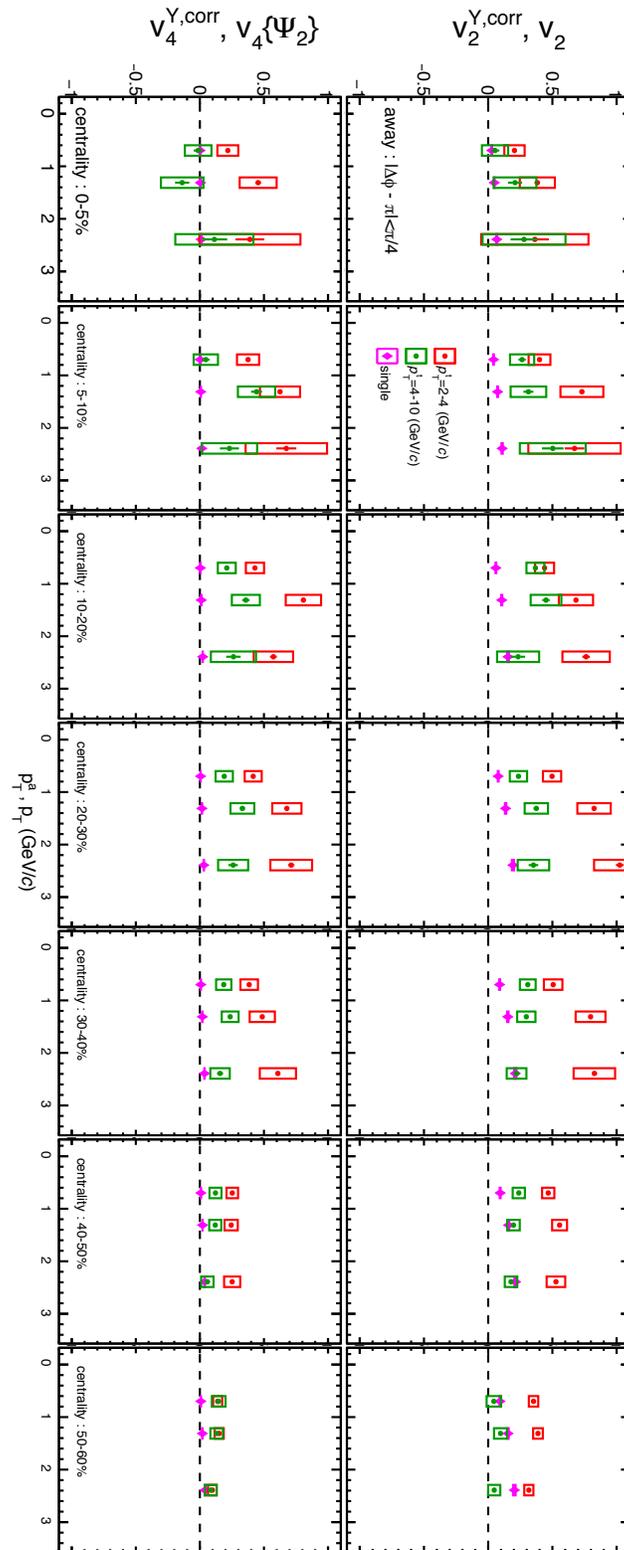
Figure 5.9: Azimuthal anisotropy of correlated yield $v_n^{Y,corr}$ in the away side and that of single particle.

5.1.3 Asymmetry of the near-side and away-side structure

As seen in 20-30 % centrality in Fig.4.3, the asymmetry is observed due to the difference of in-medium path length on the left side and right side. In order to evaluate the asymmetry on each side, the asymmetry parameter A_{LR} is calculated as

$$A_{LR} = \frac{\int_0^a d\Delta\phi Y(\Delta\phi) - \int_{-a}^0 d\Delta\phi Y(\Delta\phi)}{\int_{-a}^a d\Delta\phi Y^{inclusive}(\Delta\phi)}, \tag{5.8}$$

where a is the limit of integrated range, $a = \pi/3$ and $2\pi/3$ for the near and away side, respectively. The first term of numerator corresponds to the right side of the peak and the second term corresponds to the left, and therefore in the definition of this thesis, more yield is obtained in the in-plane (out-of-plane) direction for $A_{LR} > 0$ ($A_{LR} < 0$). The existence of asymmetric yield structure do not contradict Mach-Cone Model. The effect of mach-cone shock wave could be observed asymmetrically with asymmetric trigger angle selection with respect to the event plane because of the limited system size created in the heavy-ion collisions. Fig.5.10 shows asymmetry on the near side and away side as a function of ϕ_s. Asymmetry with 2-4 (GeV/c) triggers have the same trend in all centrality bins and with all associate p_T ranges : asymmetries of two in-plane trigger bins have positive value and those of two out-of-plane trigger bins have negative value. This observation indicates that more correlated particles are emitted in the in-plane direction with in-plane trigger and emitted in the out-of-plane direction with out-of-plane trigger. The asymmetry is enhanced in the mid-central collisions where the trigger angle dependence of integrated yield is also enhanced. Asymmetries with 4-10 (GeV/c) triggers and 0.5-1 and 1-2 (GeV/c) associates have positive value at almost all the point. Asymmetries with 4-10 (GeV/c) triggers and 2-4 (GeV/c) associates on both near side and away side fluctuate around zero and have no systematic trend. In the away side, asymmetries with 2-4 (GeV/c) triggers have the similar trend as near side in 0-40 % and at least in the in-plane trigger in 40-60 %. Asymmetries with 4-10 (GeV/c) triggers and 0.5-1 and 1-2 (GeV/c) associates have similar trend with near side for two in-plane triggers.
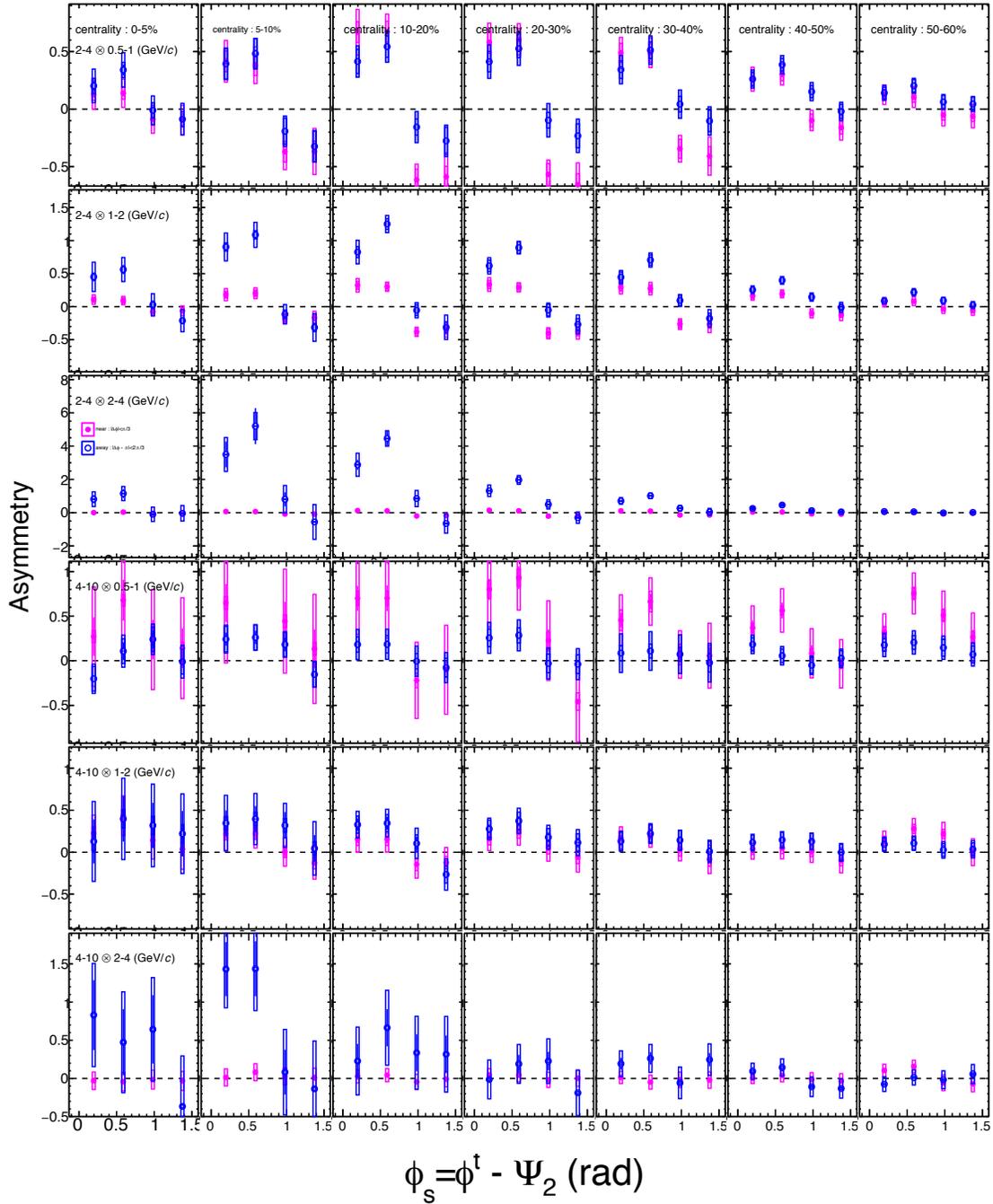
Figure 5.10: Trigger angle ϕ_s dependence of near-side (magenta) and away-side (blue) asymmetry with 2-4, 4-10 (GeV/c) trigger particles and 0.5-1, 1-2 and 2-4 (GeV/c) associate particles in each centrality from 0-5 % (left) to 50-60 % (right).

5.2 Event plane and q_2 dependent two-particle correlations

In this section, event-plane dependent two-particle correlations with q_2 selections are discussed.

5.2.1 Comparison with AMPT model

Fig.5.11 shows the ratio of elliptic flow v_2 with flow vector q_2 or initial participant eccentricity ε_2 selections in AMPT model compared with experimental data. Measured v_n with q_2 and ε_2 selections are shown in AppendixC. The effect of q_2 selections is almost the same as experimental data and that of ε_2 selections is stronger than q_2 selections at $0.5 < |\eta| < 1$. q_2 selections have been done with the information of finally emitted particles and directly correlated with v_2, but the the fraction of the number of particles for q_2 calculation to the whole particles generated in an event is limited in this analysis. v_2 is correlated with initial eccentricity ε_2 but the correlations are modified due to collective flow, but the whole participant nuclei are used to calculate ε_2. Hence, the effect of event shape engineering is stronger with ε_2 selections.
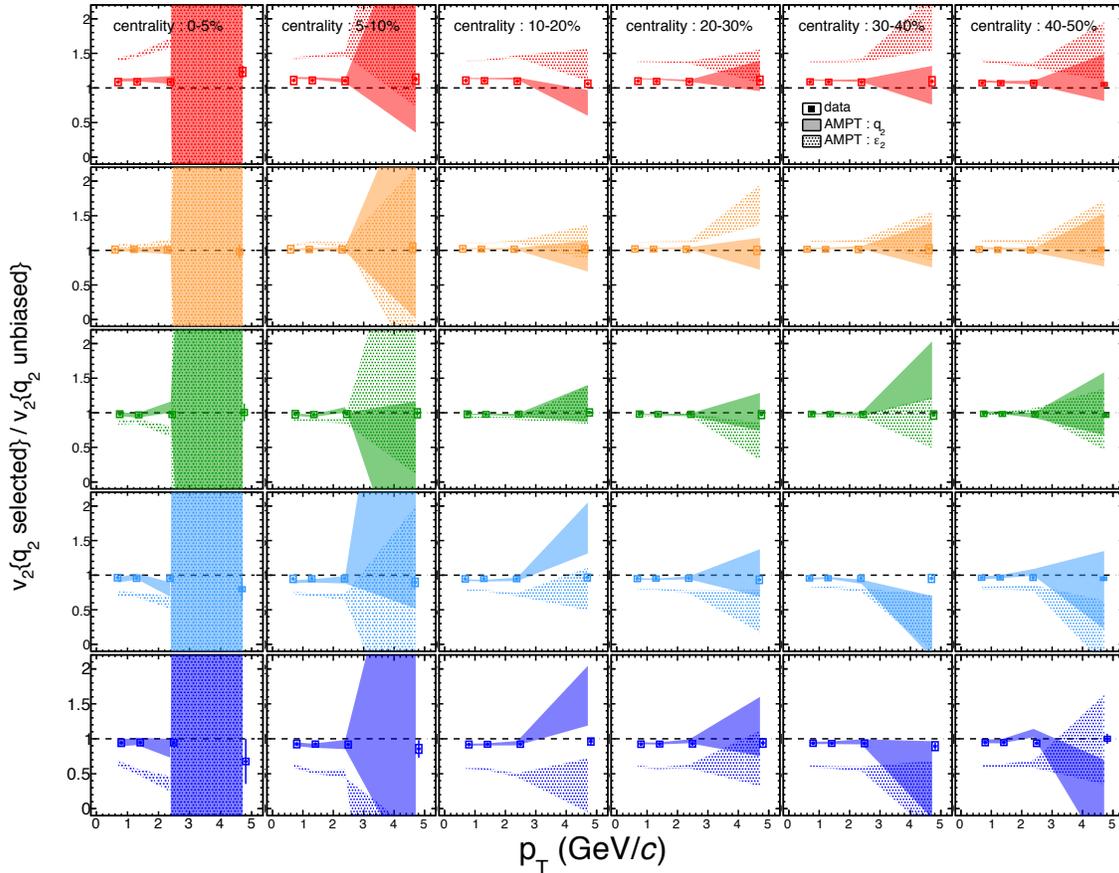
Figure 5.11: Ratio of v_2 with q_2 or ε_2 selections to that without selections in AMPT model compared with experimental data with q_2 selections in 0-50 % centrality.

Fig.5.12 and Fig.5.13 show correlations with trigger angle selections with respect to the event plane with top and bottom q_2 20 % selections. The trend of trigger angle dependence is the same as q_2 unbiased events. For correlations in mid-central collisions with top q_2 selections in AMPT, small peak is observed around $\Delta\phi = \pi/2$ which is perpendicular to the event plane. Apparent q_2 dependence cannot be observed for AMPT model with this statistics. Fig.5.14 shows comparison of correlations with top and bottom q_2 20 % events selection. In AMPT model, trigger angle dependence of is stronger in top q_2 events, which we expect. Away-side peak with top q_2 events in the in-plane triggered correlations are larger than that with bottom q_2 events. In the in-plane and out-of-plane trigger bins, yields are larger with top q_2 selections, which is not conflict with what is observed for experimental data. Fourth-order oscillations are observed in top q_2 events while v_4 is subtracted. The other correlations in AMPT is shown appendixC. Fig.5.15 and Fig.5.16 show comparison of correlations with q_2 and ε_2 selections with top and bottom 20 % selections, respectively. In both top and bottom event selections, correlations with q_2 selections and ε_2 selections are almost consistent. That fact means that q_2 selections lead to the same effect as ε_2 selections in AMPT model.
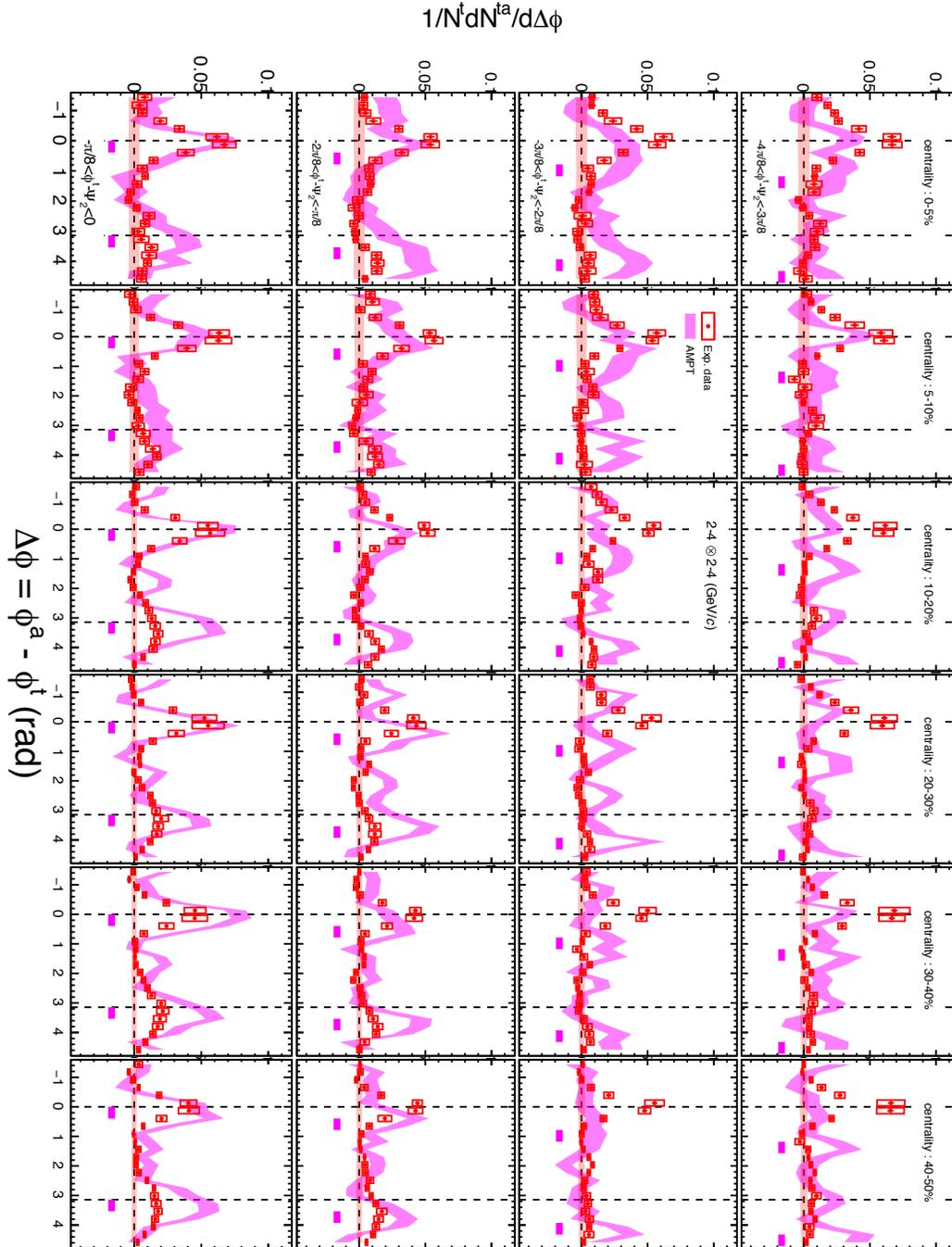
Figure 5.12: Comparison of experimental data and AMPT. Trigger angle ϕ_s dependence of azimuthal distribution of correlated yield after v_2, v_3 and v_4 contribution subtraction with top q_2 20 % selections in 0-50 % centrality. Trigger and associate p_T combination is $p_T^t \otimes p_T^a = 2\text{-}4 \otimes 2\text{-}4$ (GeV/c).
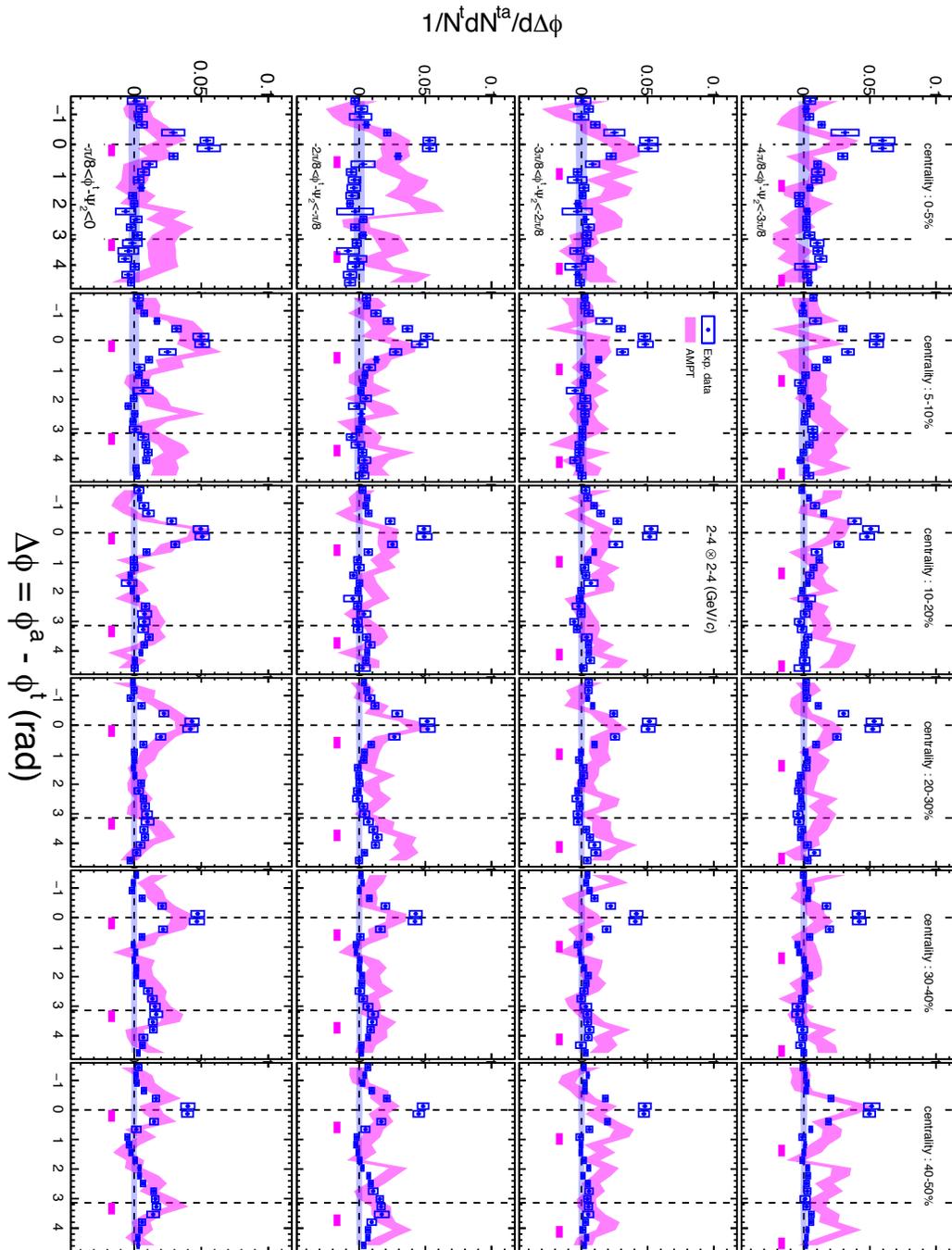
Figure 5.13: Comparison of experimental data and AMPT. Trigger angle ϕ_s dependence of azimuthal distribution of correlated yield after v_2, v_3 and v_4 contribution subtraction with bottom q_2 20 % selections in 0-50 % centrality. Trigger and associate p_T combination is $p_T^t \otimes p_T^a$ = 2-4$\otimes$2-4 (GeV/c).
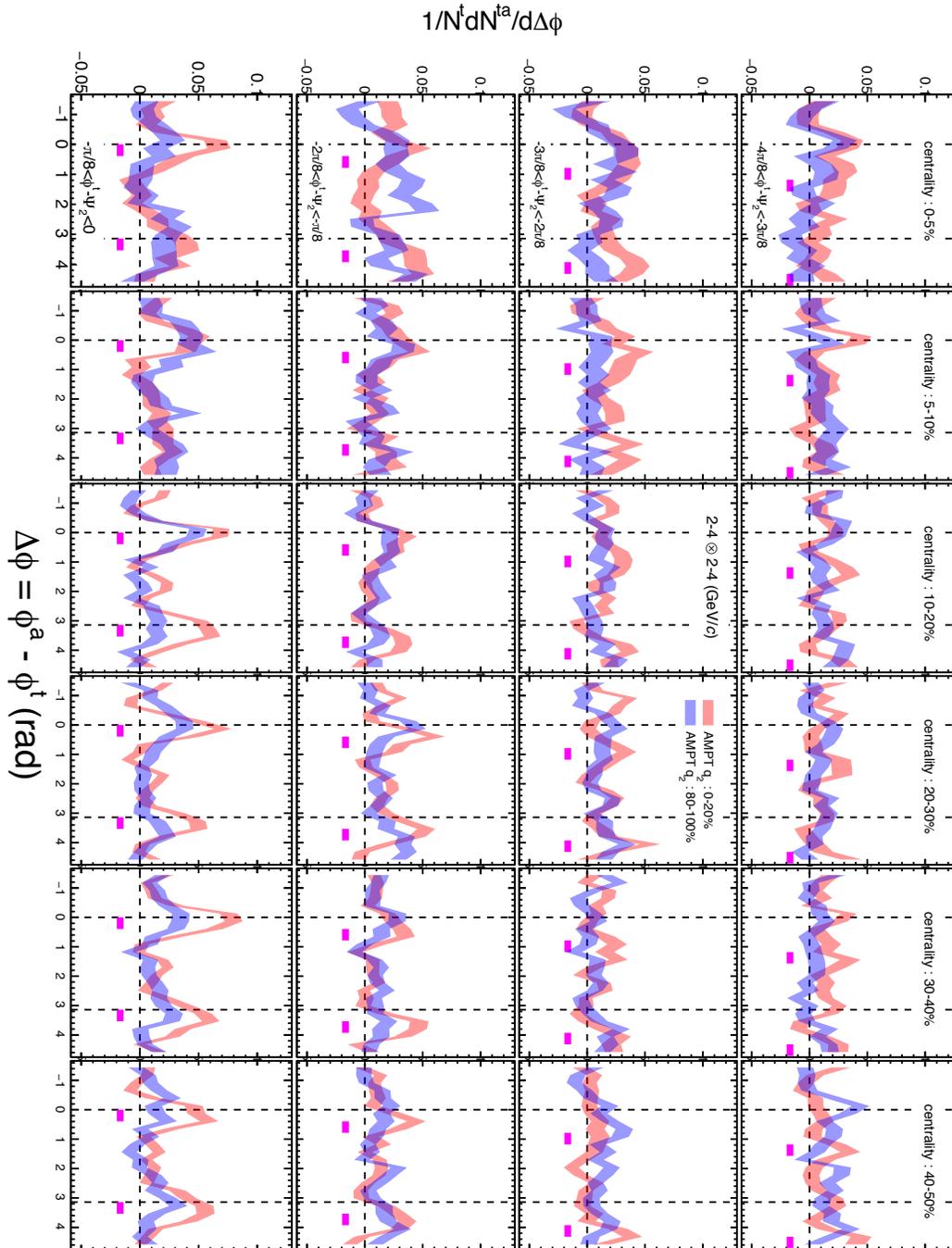
Figure 5.14: Trigger angle ϕ_s dependence of azimuthal distribution of correlated yield after v_2, v_3 and v_4 contribution subtraction with top and bottom q_2 20 % selections in 0-50 % centrality. Trigger and associate p_T combination is $p_T^t \otimes p_T^a = $ 2-4⊗1-2 (GeV/c).
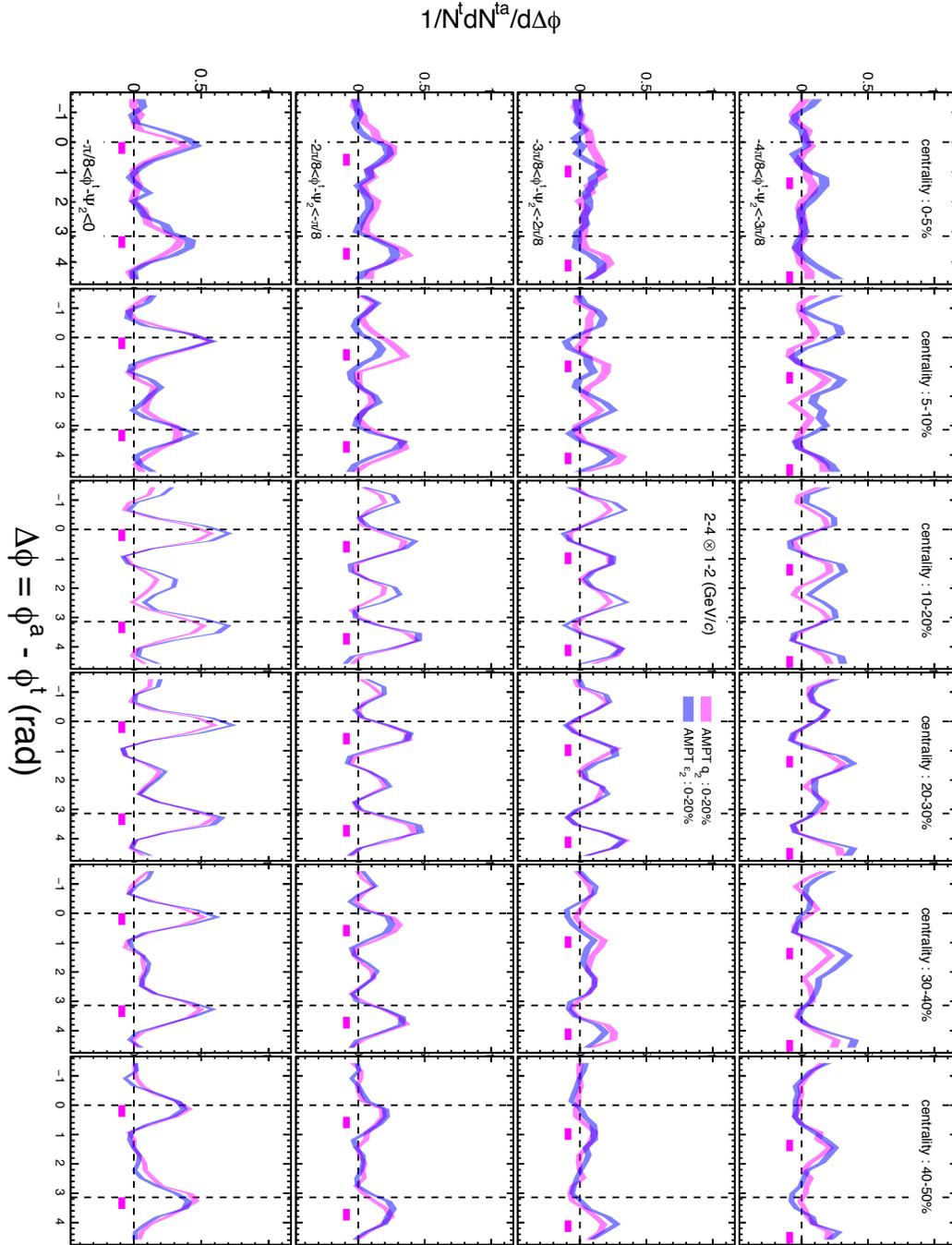
Figure 5.15: Trigger angle ϕ_s dependence of azimuthal distribution of correlated yield after v_2, v_3 and v_4 contribution subtraction with top q_2 20 % and top ε_2 20 % selections in 0-50 % centrality. Trigger and associate p_T combination is $p_T^t \otimes p_T^a = $ 2-4⊗1-2 (GeV/c).
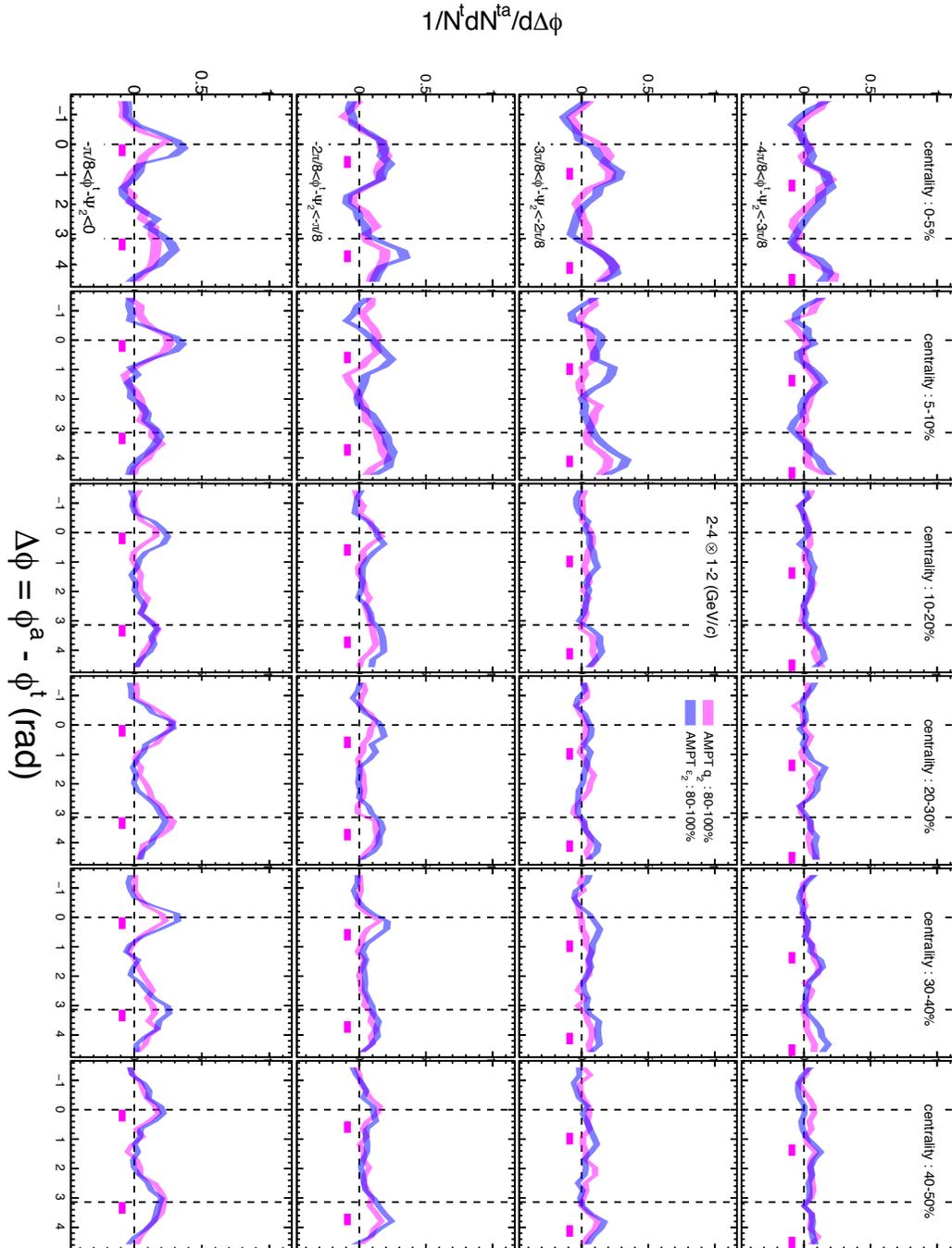
Figure 5.16: Trigger angle ϕ_s dependence of azimuthal distribution of correlated yield after v_2, v_3 and v_4 contribution subtraction with bottom q_2 20 % and bottom ε_2 20 % selections in 0-50 % centrality. Trigger and associate p_T combination is $p_T^t \otimes p_T^a = $ 2-4⊗1-2 (GeV/c).

5.2.2   Integrated yield

Fig.5.17 shows integrated yield as a function of ϕ_s, where the region for integration is $|\Delta\phi| < \pi/3$ for near side and $|\Delta\phi| < 2\pi/3$ for away side. The results of the other momentum ranges are shown in AppendixA. For the in-plane trigger bin, especially for mid-central collisions 10-30 %, the integrated yields are larger with larger q_2 events in the in-plane trigger $0 < \phi_s < \pi/8$, which means that the yields get larger with shorter path length. For the two mid-plane triggers, the yields in large q_2 events are systematically smallest in 0-40 % but q_2 dependence is not clearly observed in all centrality bins. For the out-of-plane trigger bin, the integrated yields are larger with larger q_2 events in the in-plane trigger $3\pi/8 < \phi_s < 4\pi/8$, which means that the yields get larger with longer path length. Thus, the same trend is observed for q_2 dependence with in-plane and out-of-plane trigger but the meaning is opposite. The results suggests that the effect of quark coalescence and that of penetration are dominant with in-plane triggers and the effect of energy re-distribution is dominant with out-of-plane trigger for q_2 dependence.

Scaling with path length

Fig.5.18 and Fig.A.47 show integrated yield as a function of path length L with $p_T^t \otimes p_T^a = $ 2-4⊗1-2 and 2-4⊗2-4 (GeV/c).Here, q_2 is assumed to be one-to-one correspond to ε_2, and the initial shape is selected by participant eccentricity in Glauber Monte-Carlo. Integrated yield are enhanced (suppressed) in the near (away) side. Centrality and q_2 bins are roughly on the same line in each trigger bin, which implies that integrated yield of each trigger angle direction can be explained by difference of path length. However, the trend of path length dependence between each trigger angle are different. Role of elliptic flow could make a difference of path length dependence of integrated yield. If energy re-distributed particles are pushed toward in-plane direction, integrated yield may not scale path length.

Azimuthal anisotropy of correlated yield

Fig.5.20 and Fig.5.21 show azimuthal anisotropy of correlated yield $v_n^{Y,corr}$ as a function of p_T^a with 2-4 (GeV/c) triggers in the near side and away side, respectively. The results with 4-10 (GeV/c) triggers are shown in AppendixA. The trend of p_T dependence, $v_2^{Y,corr}$ decreasing with increasing p_T, is observed in 5-60 % centrality in the near side. However, no clear q_2 dependence is observed for $v_2^{Y,corr}$. On the other hand, $v_4^{Y,corr}$ shows q_2 dependence ; v_4 decreases with increasing p_T both in near side and away side. More elliptic shape will be expected for large q_2 events and more peripheral events. However, the trend of $v_4^{Y,corr}$ from mid-central to peripheral collisions is opposite to that from small q_2 to large q_2. The effect of energy loss is not strongly changes by q_2 selections but the re-distribution can changes with q_2 selections. Therefore, the contribution of energy re-distribution cannot be explained simply by difference of in-medium path length.
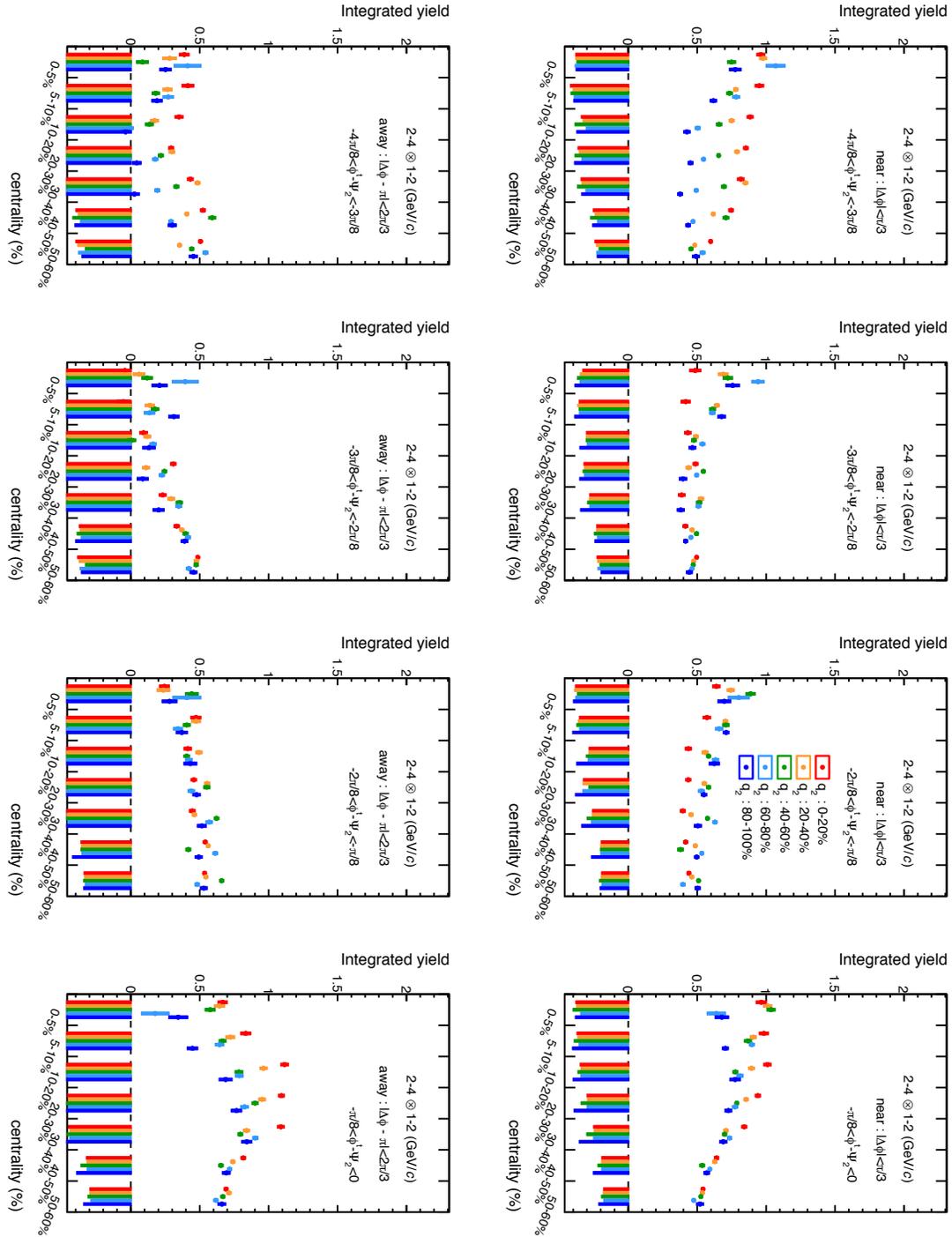
Figure 5.17: Centrality and q_2 dependence of integrated yield with $p_T : 2 - 4 \otimes$ 1-2 (GeV/c). (Top row) near side $|\Delta\phi| < \pi/3$, (bottom row) away side $|\Delta\phi| < 2\pi/3$. Trigger angle is from out-of-plane (left) to in-plane (right).
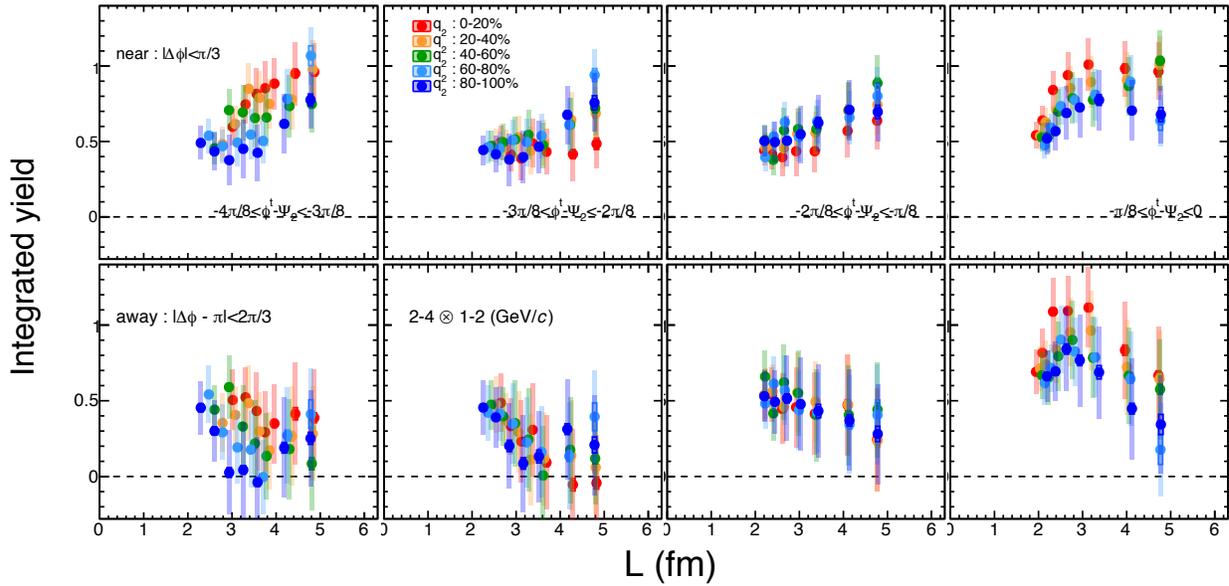
Figure 5.18: Integrated yield as a function of path length L with $p_T : 2\text{-}4 \otimes 1\text{-}2$ (GeV/c) in the near side (top) and away side (bottom).
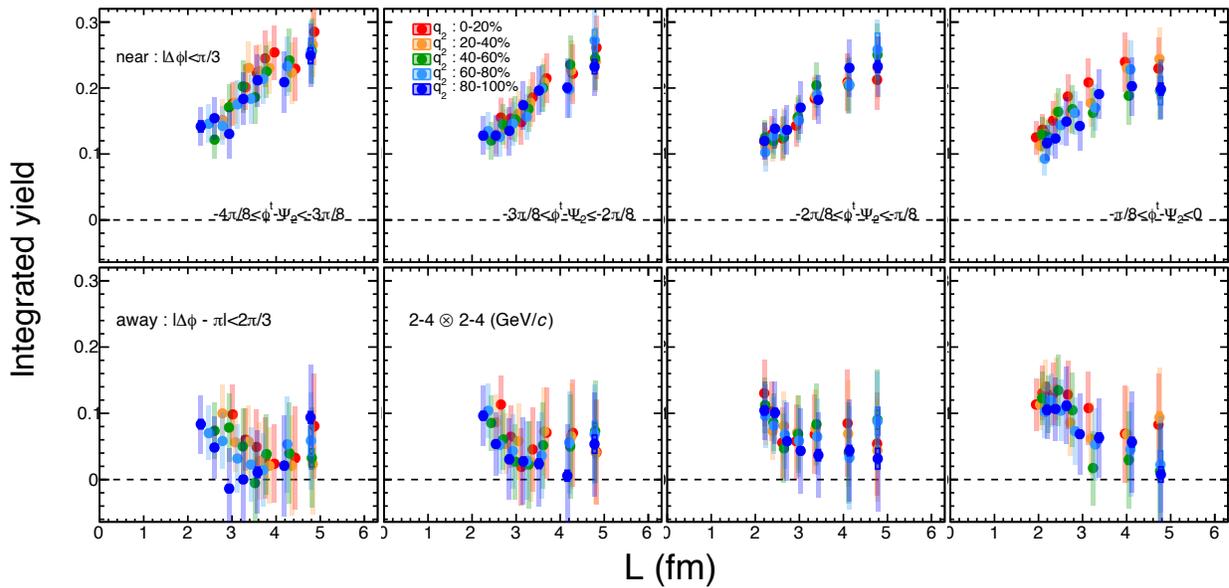
Figure 5.19: Integrated yield as a function of path length L with $p_T : 2\text{-}4 \otimes 2\text{-}4$ (GeV/c) in the near side (top) and away side (bottom).
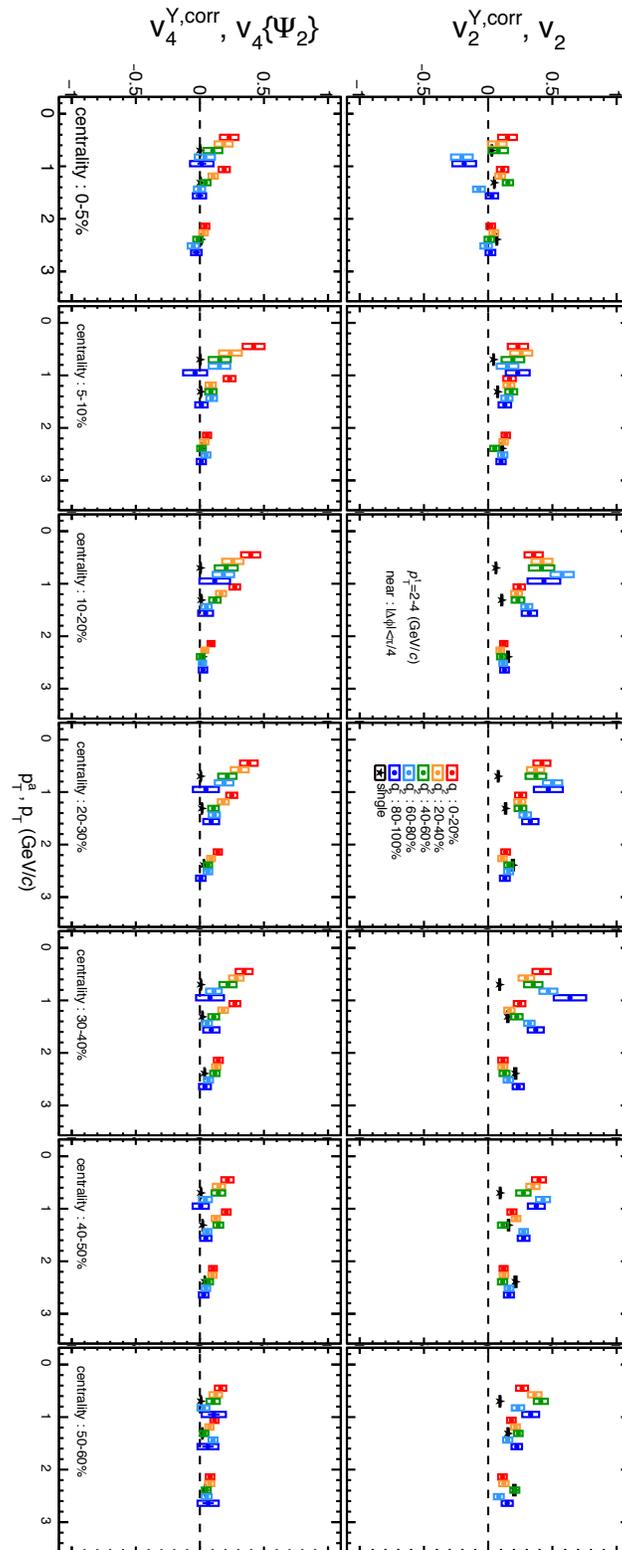
Figure 5.20: Azimuthal anisotropy of correlated yield with p_T : 2-4 (GeV/c) in the near side with q_2 selections.
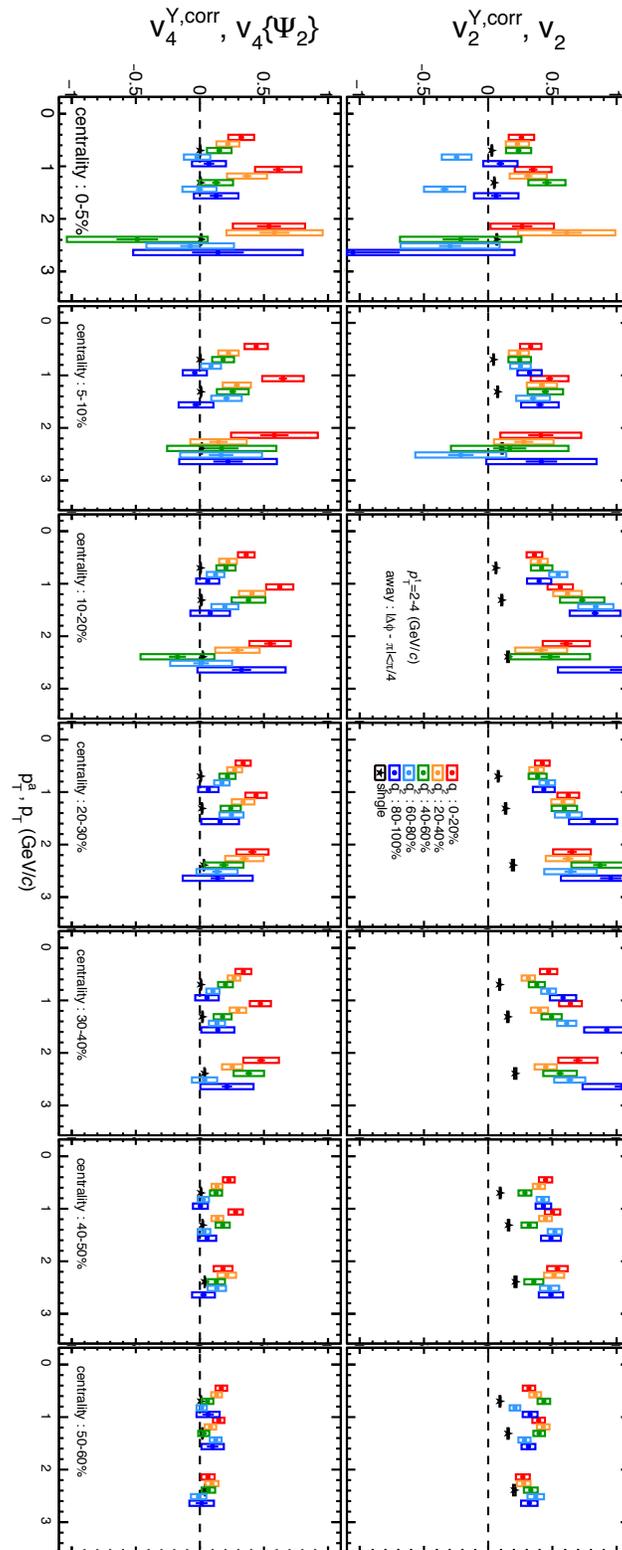
Figure 5.21: Azimuthal anisotropy of correlated yield with p_T : 2-4 (GeV/c) in the away side with q_2 selections.

5.2.3 Asymmetry of the near-side and away-side structure

Fig.5.22 show the asymmetry on the near side and away side with 2-4⊗1-2 GeV/c. The results of the other momentum ranges are shown in AppendixA. Near-side asymmetry with 0-60 % q_2 selections two in-plane trigger bins have positive value and two out-of-plane trigger bins have negative value and that with 60-100 % q_2 selections is almost zero. Absolute value of asymmetry in the away side is larger than that in the near side, which can be thought by medium effect. In 0-20 % centrality, two in-plane trigger bins have similar trend as near side in q_2 top 20 % events. On the other hand, asymmetry in the away side with q_2 60-100 % selections is positive or zero. This observation indicates that asymmetry can be caused by the ellipticity of initial shape and do not contradict the existence of mach-cone shock wave by considering with the results of integrated yield. Left/right asymmetry is enhanced by selecting large-q_2 events but no conclusion can be obtained due to large uncertainties.
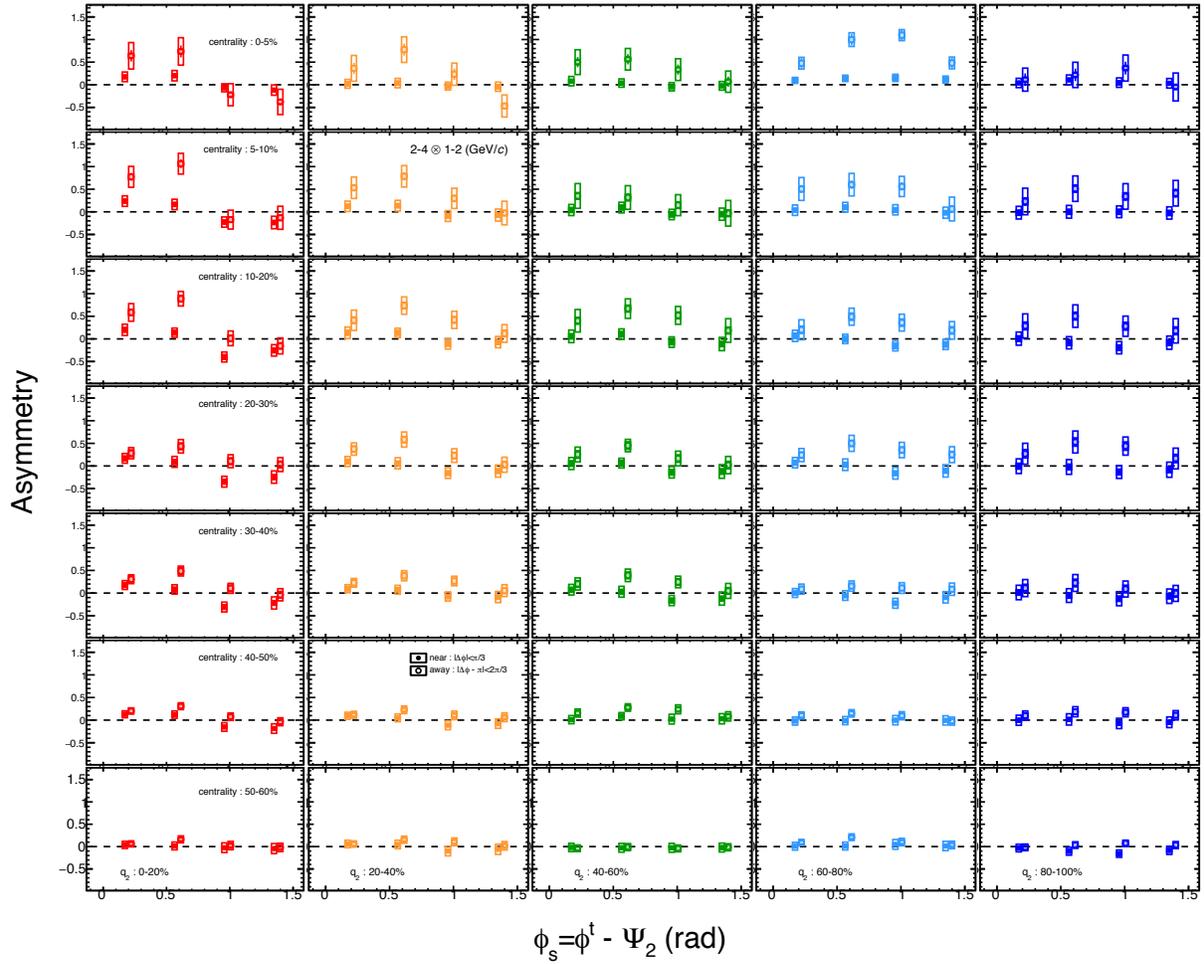
Figure 5.22: Trigger angle ϕ_s dependence of near-side and away-side asymmetry with p_T : 2-4$\otimes$1-2 (GeV/c) with q_2 selections from q_2 :0-20 % (left) to q_2 :80-100 % (right) in each centrality bin from 0-5 % (top) to 50-60 % (bottom).

Chapter 6

Conclusion

The measurement of two-particle correlations with trigger angle selection with respect to the second-order event plane in Au+Au collisions at $\sqrt{s_{NN}} = 200$ GeV have been performed with the data taken in 2011 by the STAR experiment. Azimuthal distributions of correlated yield have been measured with subtracting higher-order harmonic flow (v_2, v_3 and v_4) measured with taking 1.0 η gap between tracks and event planes.

Difference of correlation shapes between in-plane (same direction as event plane) and out-of-plane (perpendicular to event plane) is enhanced in mid-central collisions compared with central and peripheral collisions where the difference of path length is large. Correlated yields in the away side yield with long path length is suppressed compared with those with short path length in mid-central collisions, which is the same trend as previous study. With differential trigger angle selections, correlation shapes are modified; correlations with in-plane trigger and out-of-plane trigger have back-to-back peak but those with mid-plane triggers have the peak shifted away from back-to-back jet axis. Azimuthal correlations are compared with AMPT model with including string melting and quenching model. v_2 in AMPT model is smaller than real data but v_3 and v_4 are almost consistent. Azimuthal correlations in AMPT model reproduce away side shape from mid-central to peripheral collisions. However, near-side peak in AMPT is much smaller than real data. Near side peaks almost disappear with out-of-plane triggers and clearer peak is observed in central collisions than peripheral collisions. Integrated yield shows some characteristic behaviors. Non-monotonic behavior is observed for 2-4 GeV/c triggers : the integrated yields are suppressed with mid-plane triggers and enhanced with out-of-plane trigger, which is observed with lower trigger and associate p_T from central to mid-central collisions. If quenched jets triggered, both partonic energy loss and energy re-distribution would be appeared. The integrated yields with selecting higher associate p_T are enhanced with long path length, which indicates the contribution of re-distribution is dominant. Integrated yields are plotted as a function of simple path length calculated by Glauber Monte-Carlo. The integrated yields do not scale well in 0.5-2 GeV/c associate p_T, while the integrated yields scale in 2-4 GeV/c associate p_T comapred with lower associate p_T. This is because path-length dependent enhancement or suppression cannot be described by simple path length in lower associate p_T. The azimuthal anisotropy of integrated yield has been calculated and compared with that of single particle. $v_2^{Y,corr}$ and $v_4^{Y,corr}$ decrease with increasing p_T^a and are larger than single

particle v_2 with 0.5-2 (GeV/c) p_T on the near side in all centrality bins and 2-4 (GeV/c) from central to mid-central collisions. $v_2^{Y,corr}$ increases with increasing p_T^a with 2-4 (GeV/c) triggers while that with 4-10 (GeV/c) triggers on the away side have no p_T dependence within systematic uncertainties in mid-central collisions. This observation indicates that p_T combination dependence for the balance of partonic energy loss and energy re-distribution exists 2-4 (GeV/c) triggers. When $v_2^{Y,corr}$ and $v_4^{Y,corr}$ are larger than single particle $v_n\{\Psi_2\}$, azimuthal anisotropy caused by path length dependent partonic energy loss is stronger than hydrodynamical expansion. Left/right asymmetry of the near side shows following features : near side peaks shifted to in-plane direction with two in-plane trigger bins and shifted to out-of-plane direction with two out-of-plane triggers with lower p_T triggers. Asymmetry of peak on the near side and away side. When relative trigger angle with respect to the event plane (ϕ_s) is negative, if asymmetry is positive (negative), the peak shifts to in-plane (out-of-plane) direction. Asymmetry of the away side with higher trigger and associate p_T is not negative because higher associate p_T particles composing jets emitted more to shorter path length direction. The results of event-plane dependent two-particle correlations can be interpreted as follows.

- Jets emitted more from the short path-length direction with less energy loss.

- Jets emitted more from the long path-length direction associated with energy re-distributed particles.

As a new approach of event selections to determine the collision geometry, q_2 selections are applied to the measurement of two-particle correlations. In the real experiment, participant eccentricity cannot be directly selected, and thus the length of flow vectors have been used to restrict the initial eccentricity. The effect of event shape engineering is observed for v_2 in all centrality bins, which indicates that q_2 selections at the forward rapidity affect the v_2 at the backward rapidity. Therefore, q_2 selections at local rapidity range works as global event characterization. In addition, no p_T dependence is observed for v_2 ratio to q_2 unbiased events within statistical and systematic uncertainties. Correlation shapes are modified by trigger angle and q_2 selections in mid-central collisions especially for in-plane and out-of-plane triggers. In the out-of-plane triggered correlations, the yield in the large-q_2 events is larger than in small-q_2 events, which can be caused by the effect of energy re-distribution with larger path length. No q_2 dependence is observed for $v_2^{Y,corr}$, but on the other hand, $v_4^{Y,corr}$ increases with increasing q_2 with 2-4 (GeV/c) triggers and 0.5-2 (GeV/c) associates from central to mid-central collisions, which may indicates that q_2 and trigger angle selections affect more path-length dependence of energy re-distribution than that of partonic energy loss. The q_2 dependence of integrated yield is observed for in-plane and out-of-plane trigger slices where the difference of path length is caused by q_2 selections; the integrated yields are enhanced with increasing q_2, which means that the integrated yield of the out-of-plane trigger is enhanced with increasing path length and the integrated yield of the in-plane trigger is enhanced with decreasing path length. This observation could be interpreted as follows: the effect of jet penetration is dominant in the in-plane direction, and the effect of energy re-distribution is dominant in the out-of-plane direction. Therefore, collective expansion could be thought to have effect on the jet-like particle productions.

We point out that correlated yield cannot scale with simple path length expected for initial hard-scattered partons. More realistic model calculation, such as two-particle path length calculation with assuming position of hard scattering of high-p_T particles because path-length dependent energy loss exists, is needed for more detail discussion for the balance of path length dependent partonic energy loss and energy re-distribution from high energy particles. We expect the results in this thesis will help to further constrain the later stage conditions on the theoretical models. Finally, if more data is taken at 200 GeV with including Event Plane Detector (EPD; pseudorapidity coverage: $2.1 < |\eta| < 5.1$), two-particle correlations with respect to the second and third order event planes is expected to be performed with taking large pseudorapidity gap between the region for two-particle correlations, that for event plane and that for q_2 selections at the STAR experiment.

Appendix A

Results of experimental data

In this chapter, correlation functions, integrated yield and asymmetry parameter are presented.

A.1   Azimuthal anisotropy with q_2 selections

Fig.A.1 show azimuthal anisotropy v_n as a function of p_T with various q_2 selections in 0-60 % centrality.

A.2   Correlation functions

In this section event-plane dependent two-particle correlations after backround subtractions and all corrections.

A.2.1   Correlation functions with inclusive q_2

Fig.A.2-A.7 show azimuthal distribution of correlated yield with various p_T combinations with trigger angle selections with respect to the second-order event plane in 0-60 % centrality.

A.2.2   Correlation functions with q_2 selections

Fig.A.8 shows azimuthal distribution of correlated yield with various p_T combinations without trigger angle selections in 0-60 % centrality. Fig.A.9-A.38 show azimuthal distribution of correlated yield with various p_T combinations with trigger angle selections with respect to the second-order event plane in 0-60 % centrality. Fig.**??**-Fig.A.13 are 2-4⊗0.5-1 (GeV/c). Fig.**??**-Fig.A.18 are 2-4⊗1-2 (GeV/c). Fig.**??**-Fig.A.23 are 2-4⊗2-4 (GeV/c). Fig.**??**-Fig.A.28 are 4-10⊗0.5-1 (GeV/c). Fig.**??**-Fig.A.33 are 4-10⊗1-2 (GeV/c). Fig.**??**-Fig.A.38 are 4-10⊗2-4 (GeV/c).

A.3   Integrated yield with q_2 selections

Fig.A.39-A.43 show integrated yield as a function of centrality and q_2.
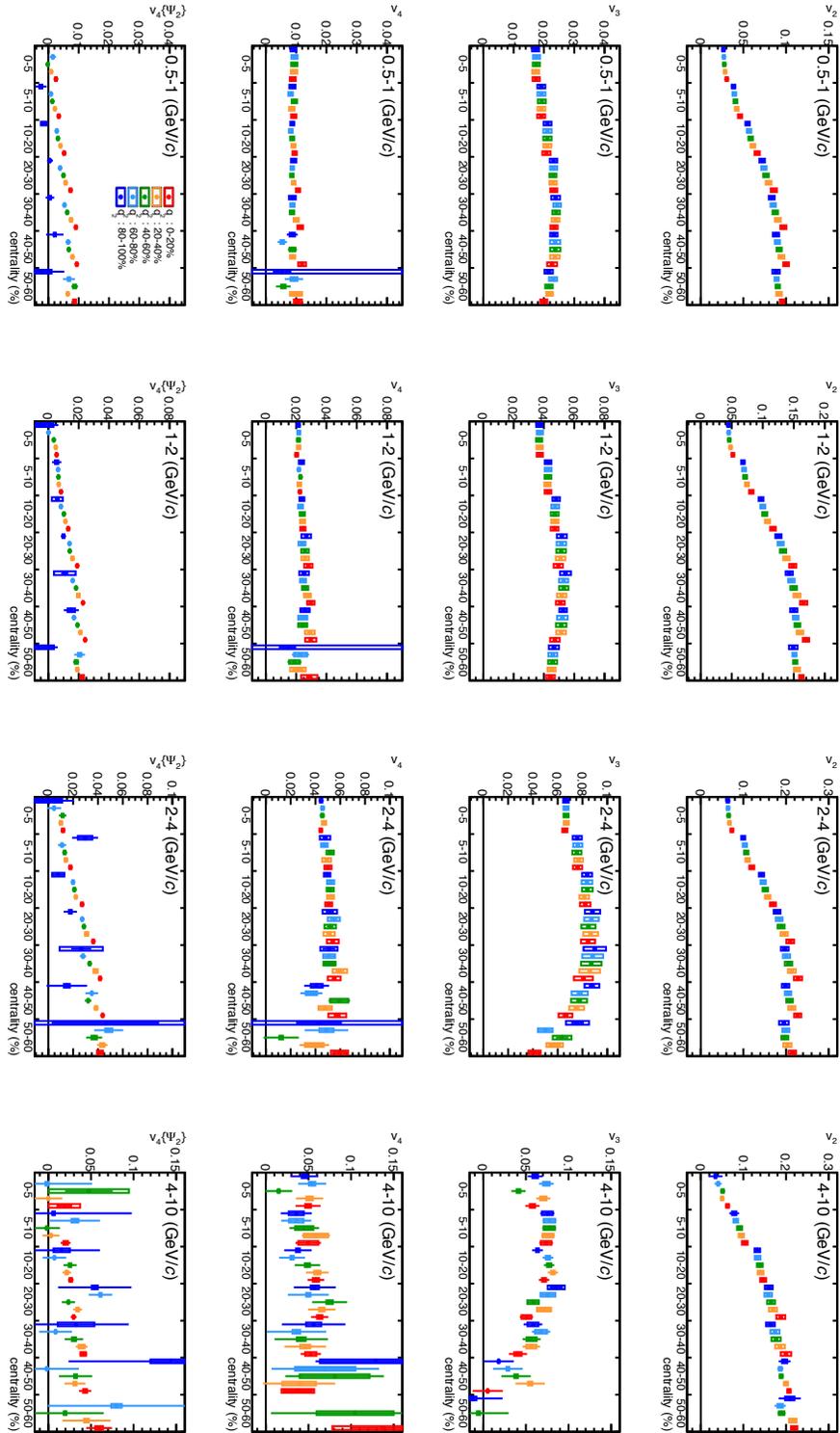
Figure A.1: Higher-order-harmonic flow v_n measured with q_2 selections in this analysis.
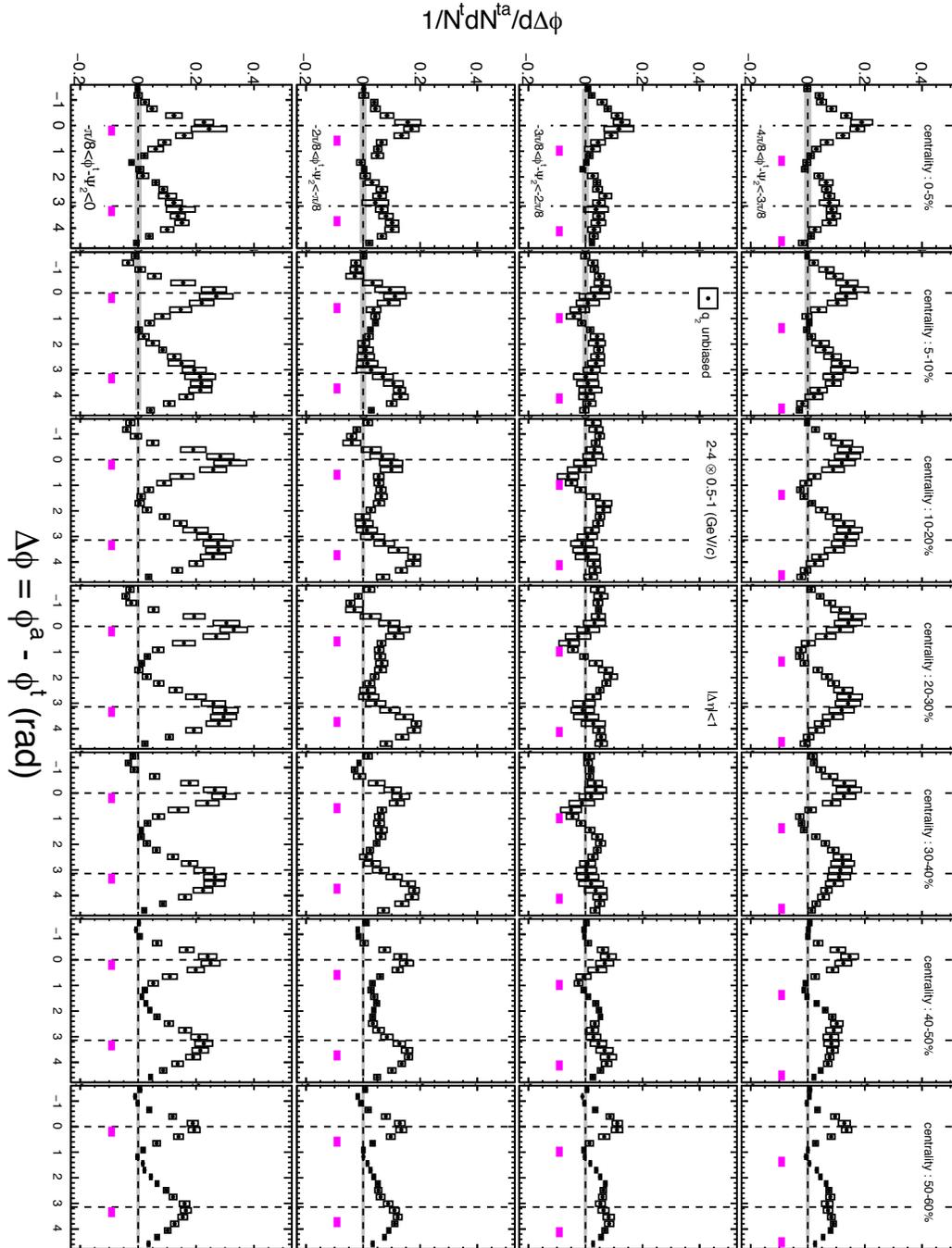
Figure A.2: Azimuthal distribution of correlated yield in p_T : 2-4⊗0.5-1 (GeV/c) with trigger angle selection with respect to the second-order event plane.
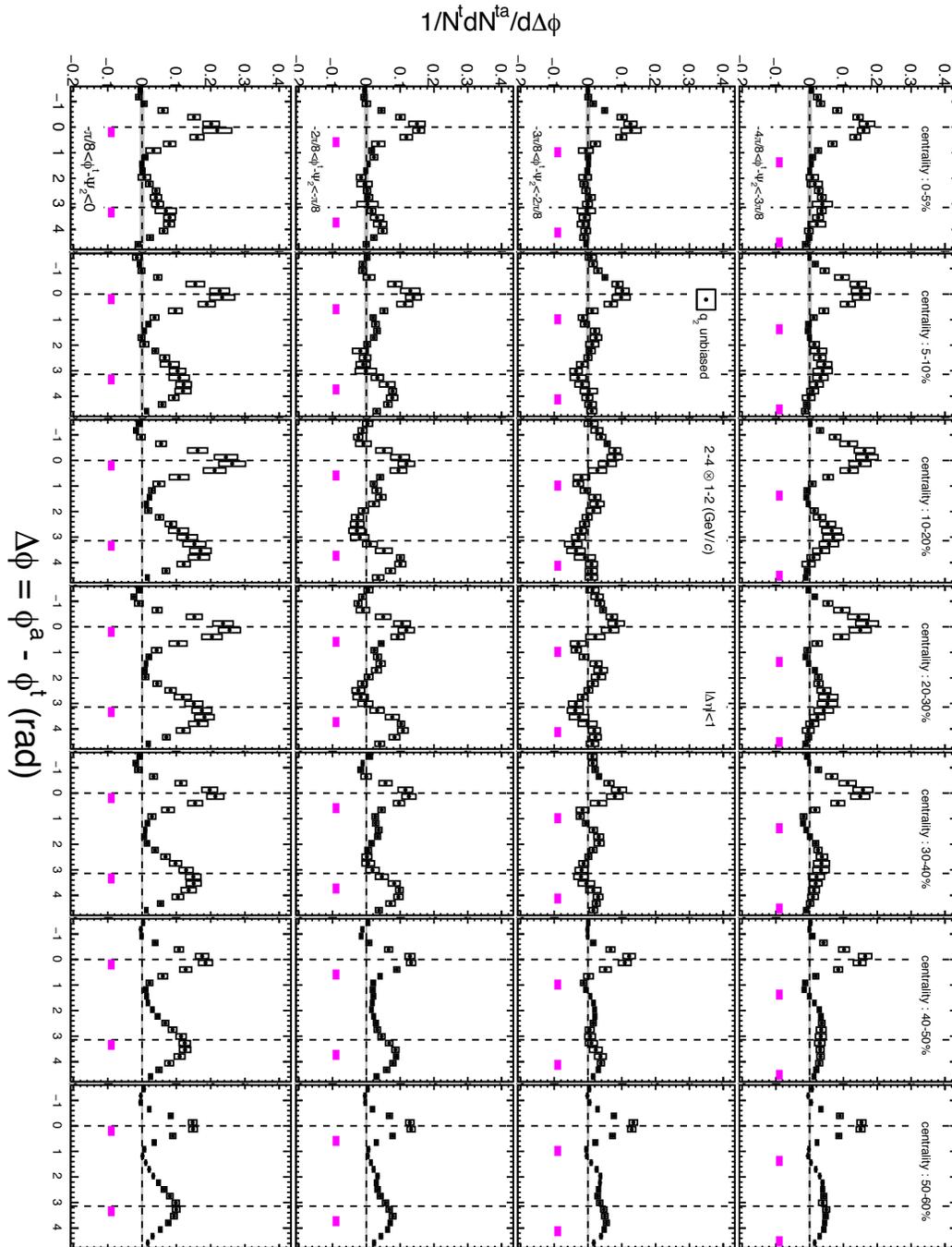
Figure A.3: Azimuthal distribution of correlated yield in p_T : 2-4⊗1-2 (GeV/c) with trigger angle selection with respect to the second-order event plane.
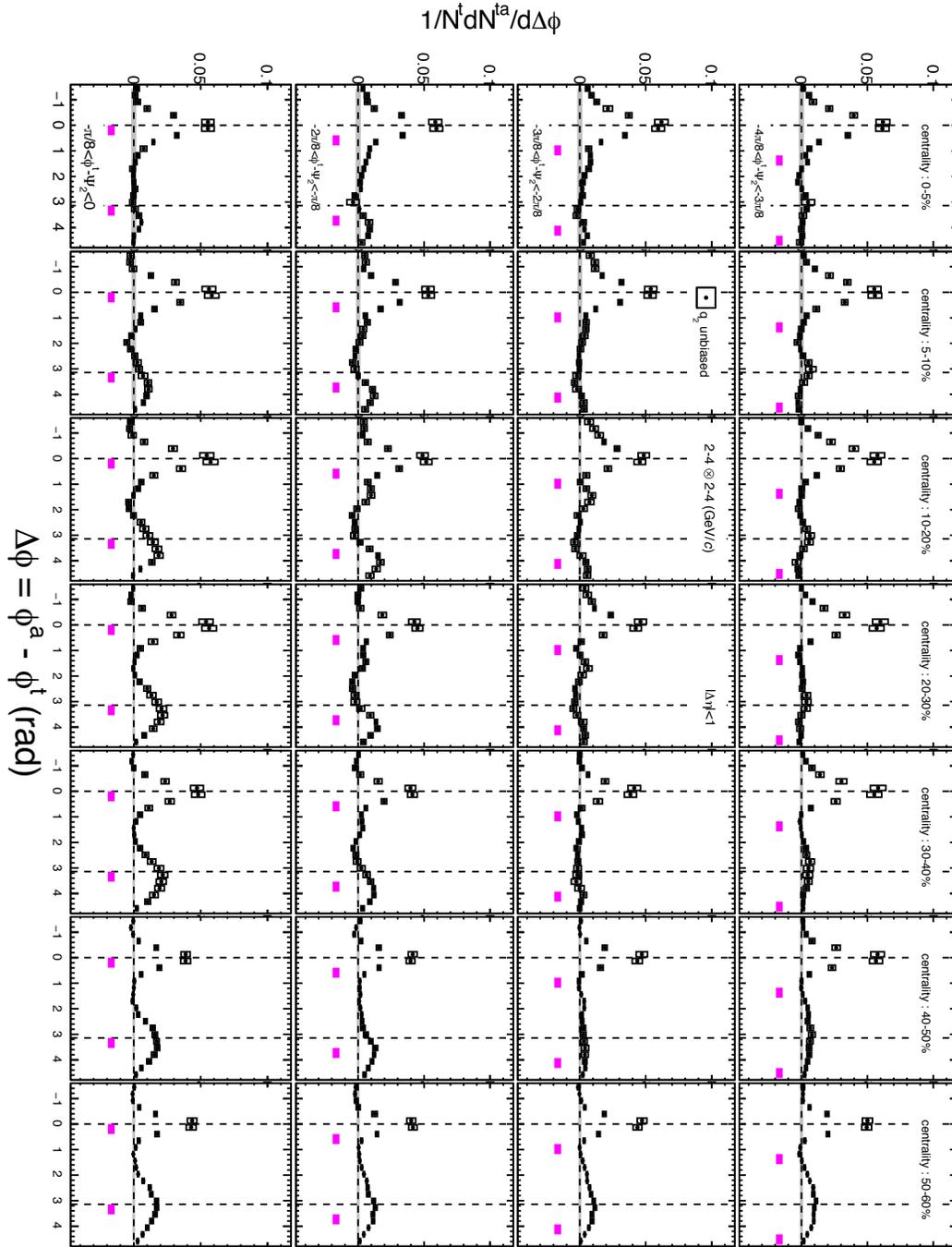
Figure A.4: Azimuthal distribution of correlated yield in p_T : 2-4⊗2-4 (GeV/c) with trigger angle selection with respect to the second-order event plane.
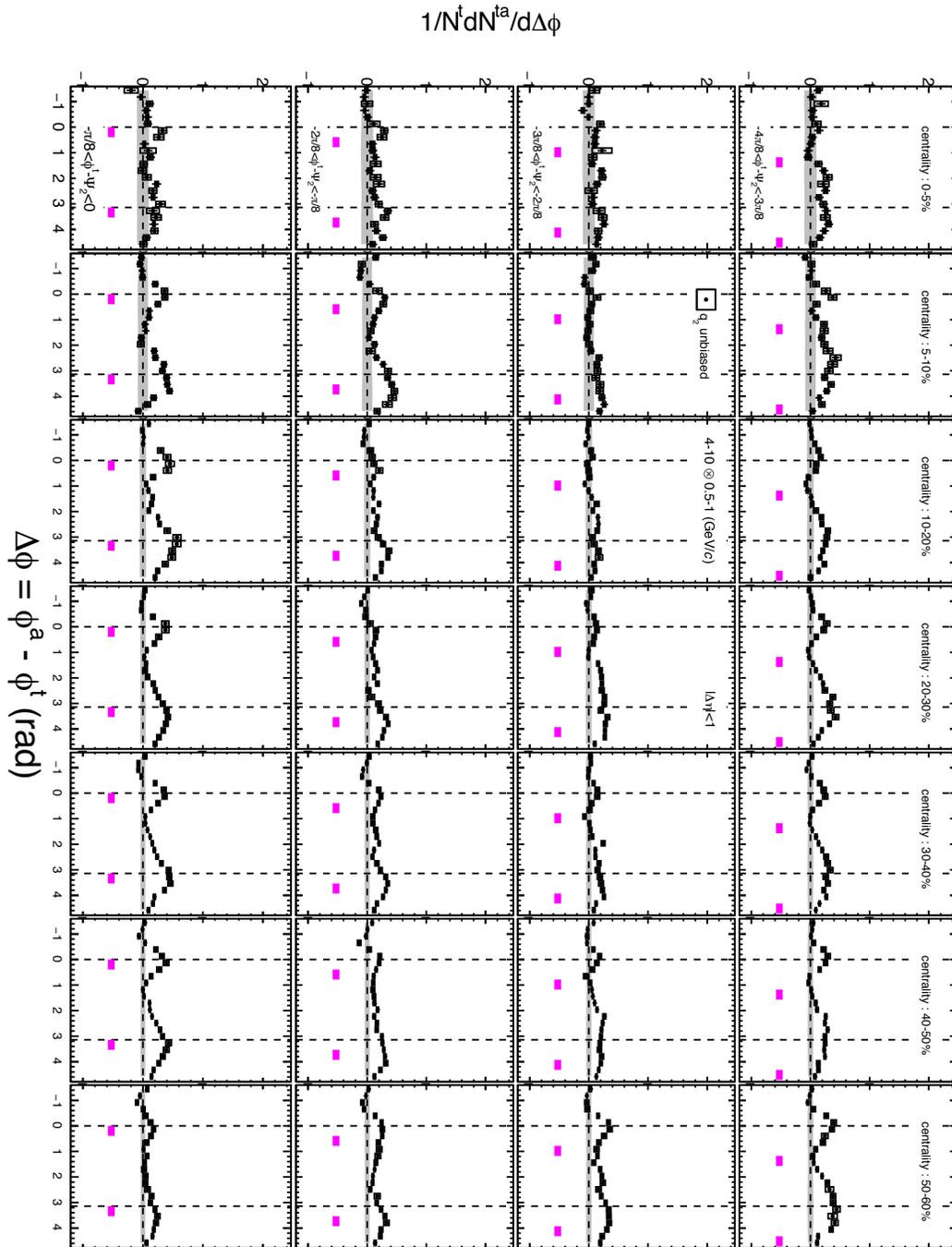
Figure A.5: Azimuthal distribution of correlated yield in p_T : 4-10$\otimes$0.5-1 (GeV/c) with trigger angle selection with respect to the second-order event plane.
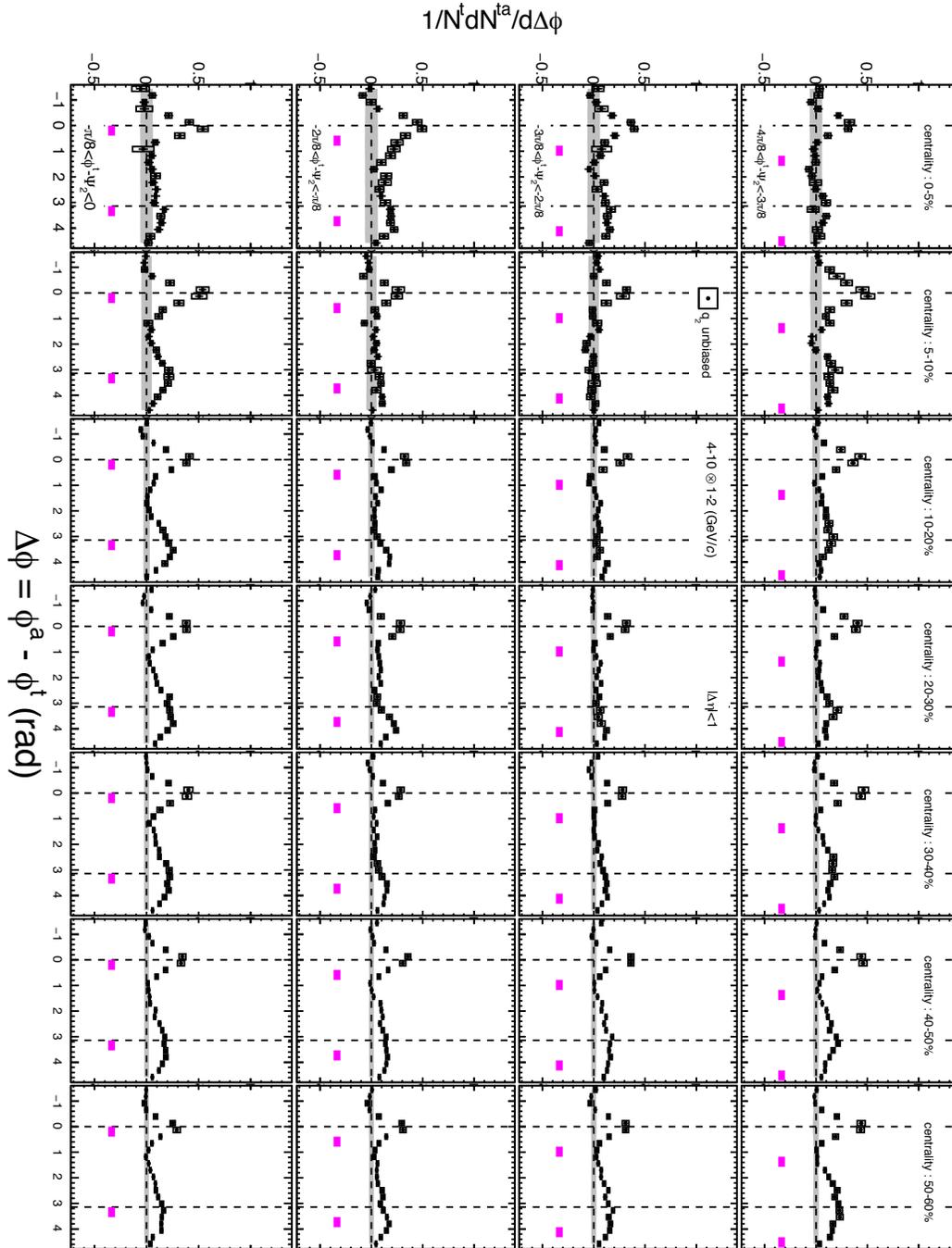
Figure A.6: Azimuthal distribution of correlated yield in $p_T : 4\text{-}10 \otimes 1\text{-}2$ (GeV/c) with trigger angle selection with respect to the second-order event plane.
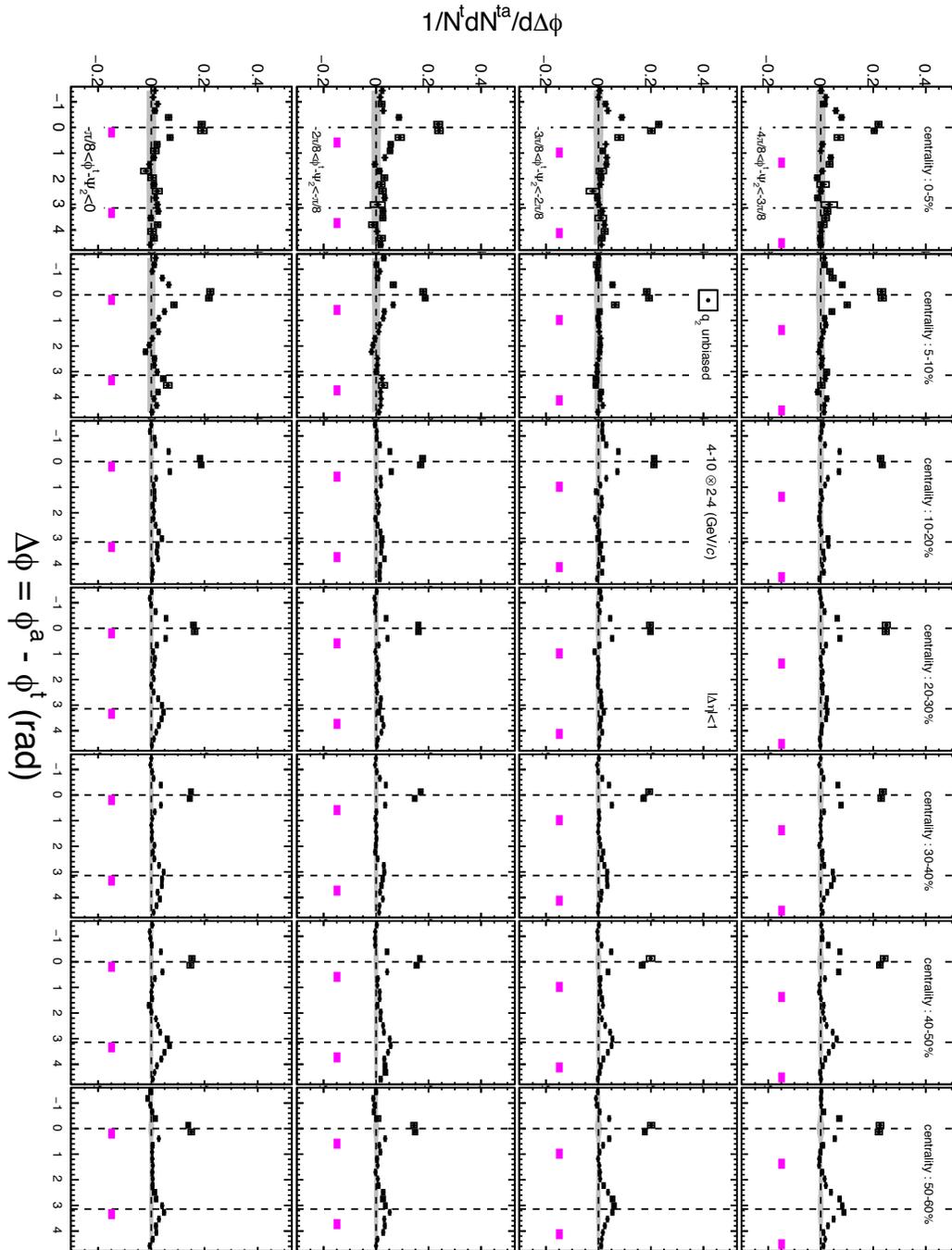
Figure A.7: Azimuthal distribution of correlated yield in $p_T : 4\text{-}10 \otimes 2\text{-}4$ (GeV/c) with trigger angle selection with respect to the second-order event plane.
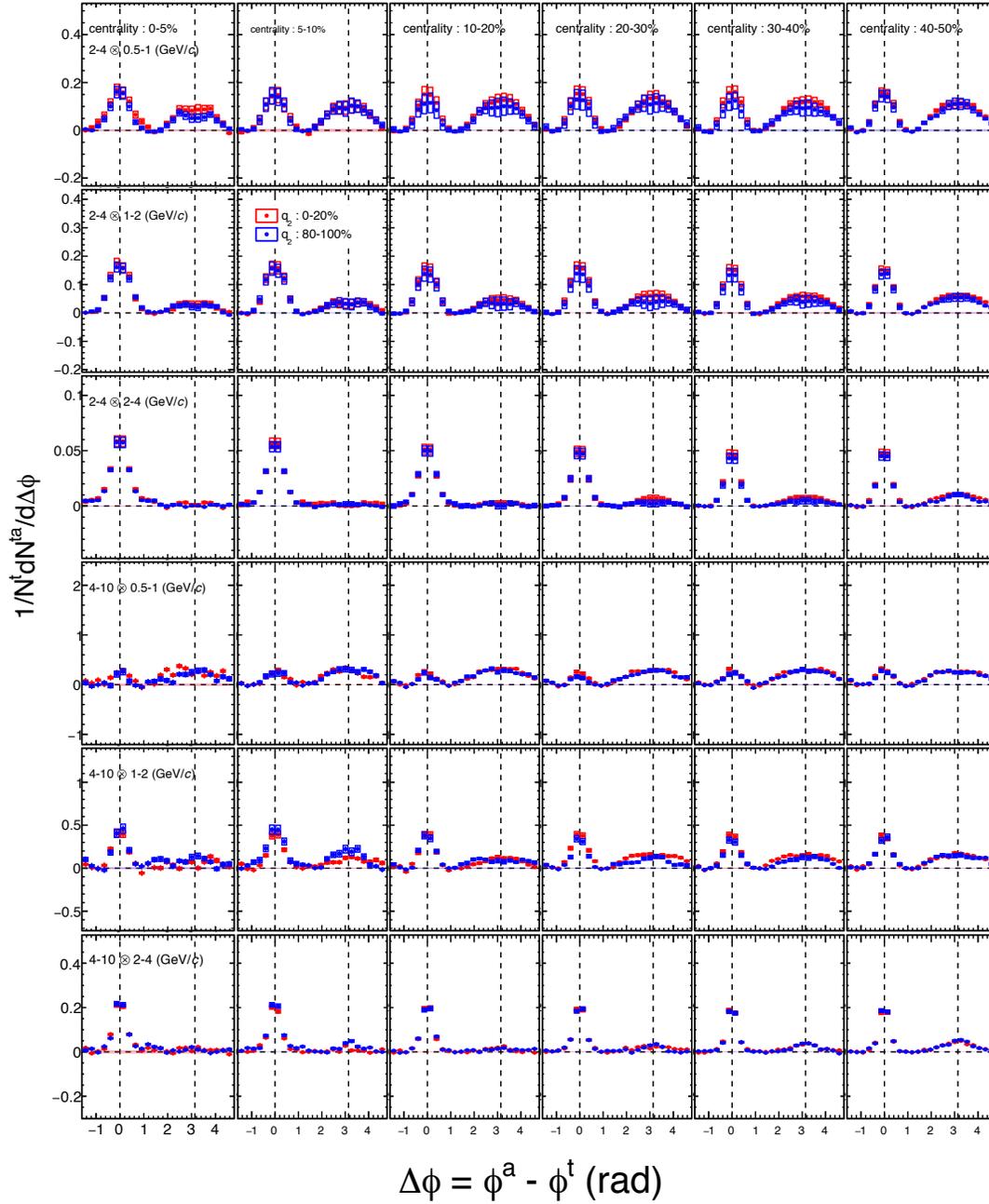
Figure A.8: Azimuthal distribution of correlated yield with various p_T combinations after v_2, v_3 and v_4 contribution subtraction in 0-50 % centrality. Trigger particle's p_T are 2-4 and 4-10 (GeV/c), and associate particle's p_T are 0.5-1, 1-2 and 2-4 (GeV/c).
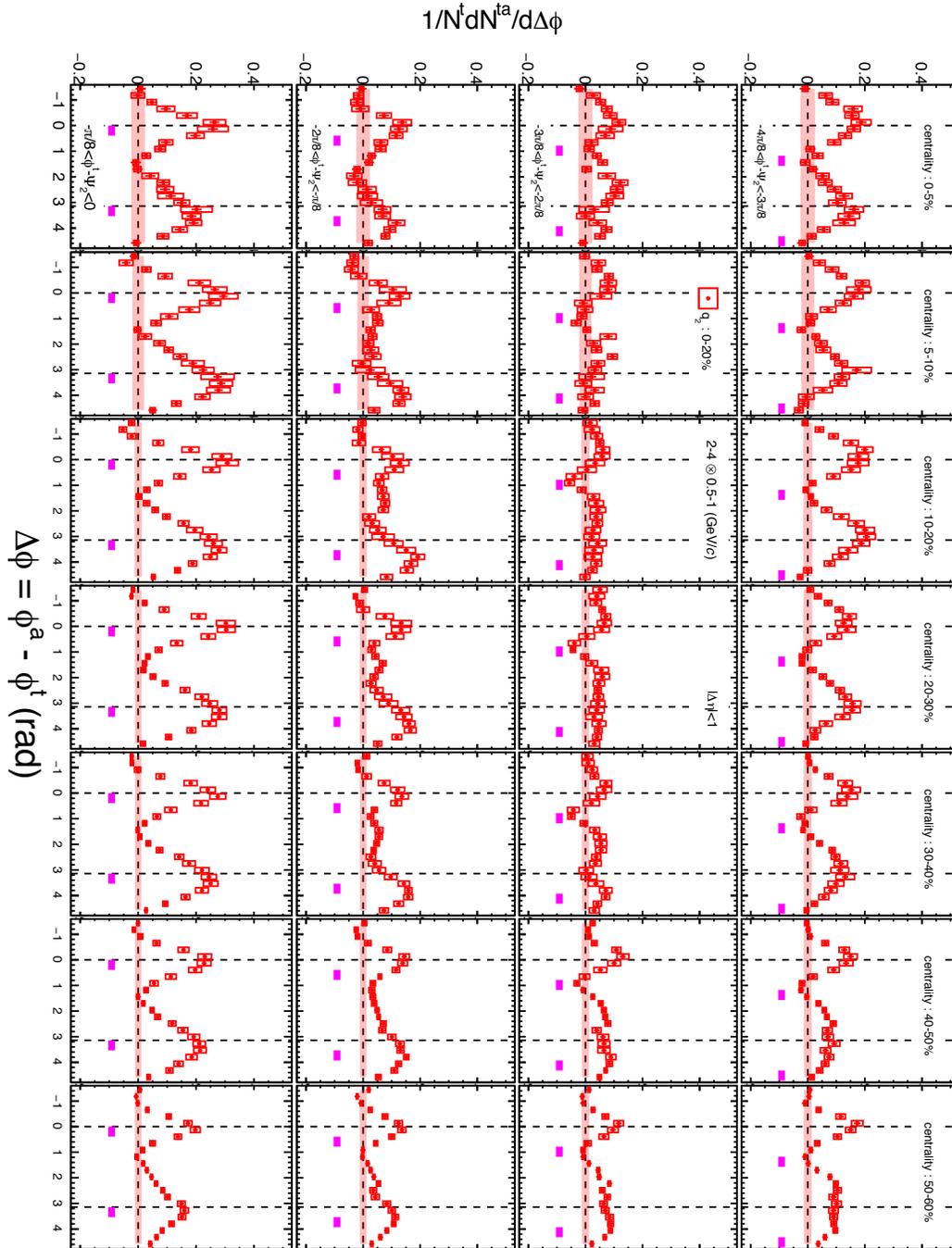
Figure A.9: Azimuthal distribution of correlated yield in $p_T : 2\text{-}4 \otimes 0.5\text{-}1$ (GeV/c) with trigger angle selection with respect to the second-order event plane in $q_2 : 0 - 20\%$ selected events.
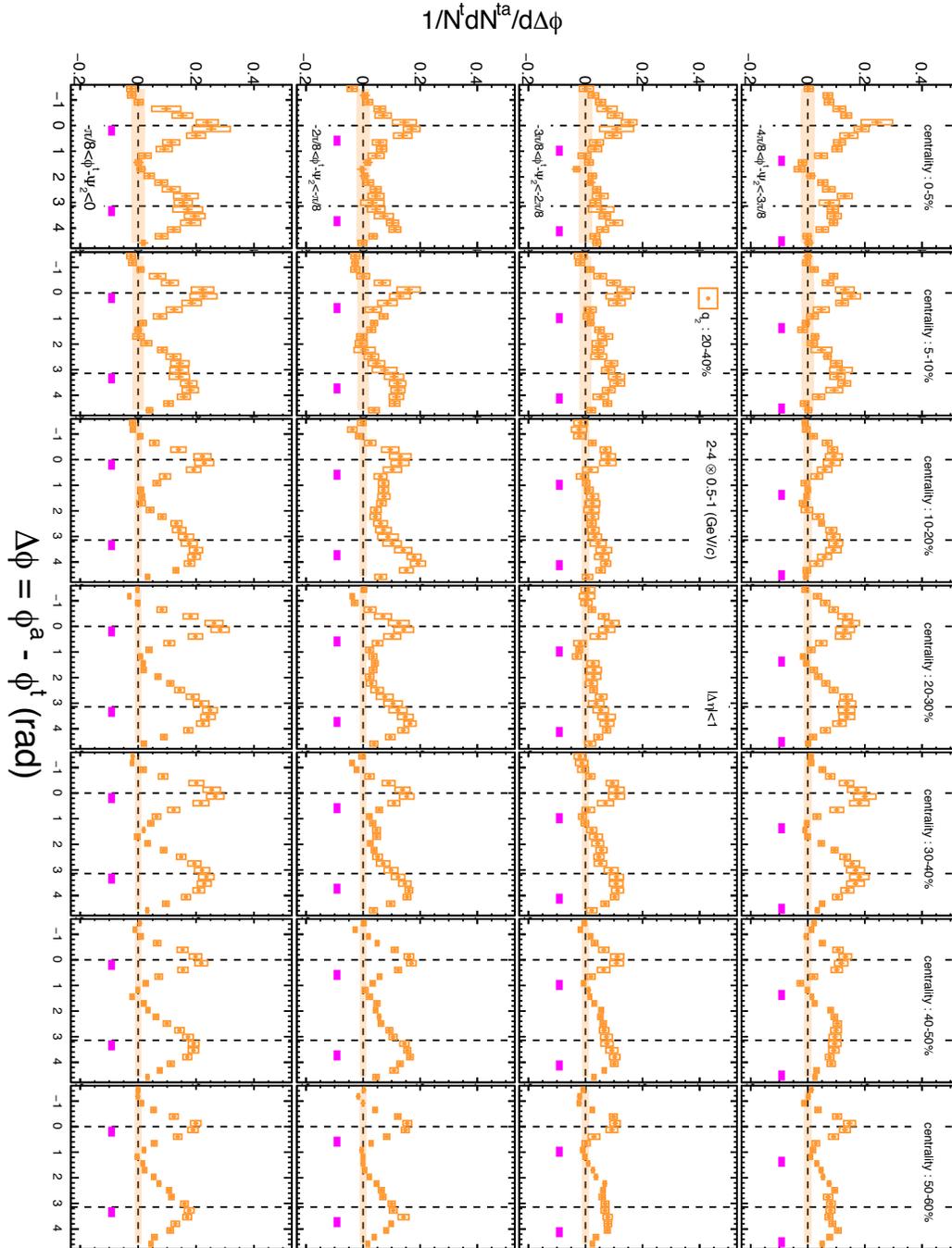
Figure A.10: Azimuthal distribution of correlated yield in p_T : 2-4⊗0.5-1 (GeV/c) with trigger angle selection with respect to the second-order event plane in q_2 : 20 − 40% selected events.
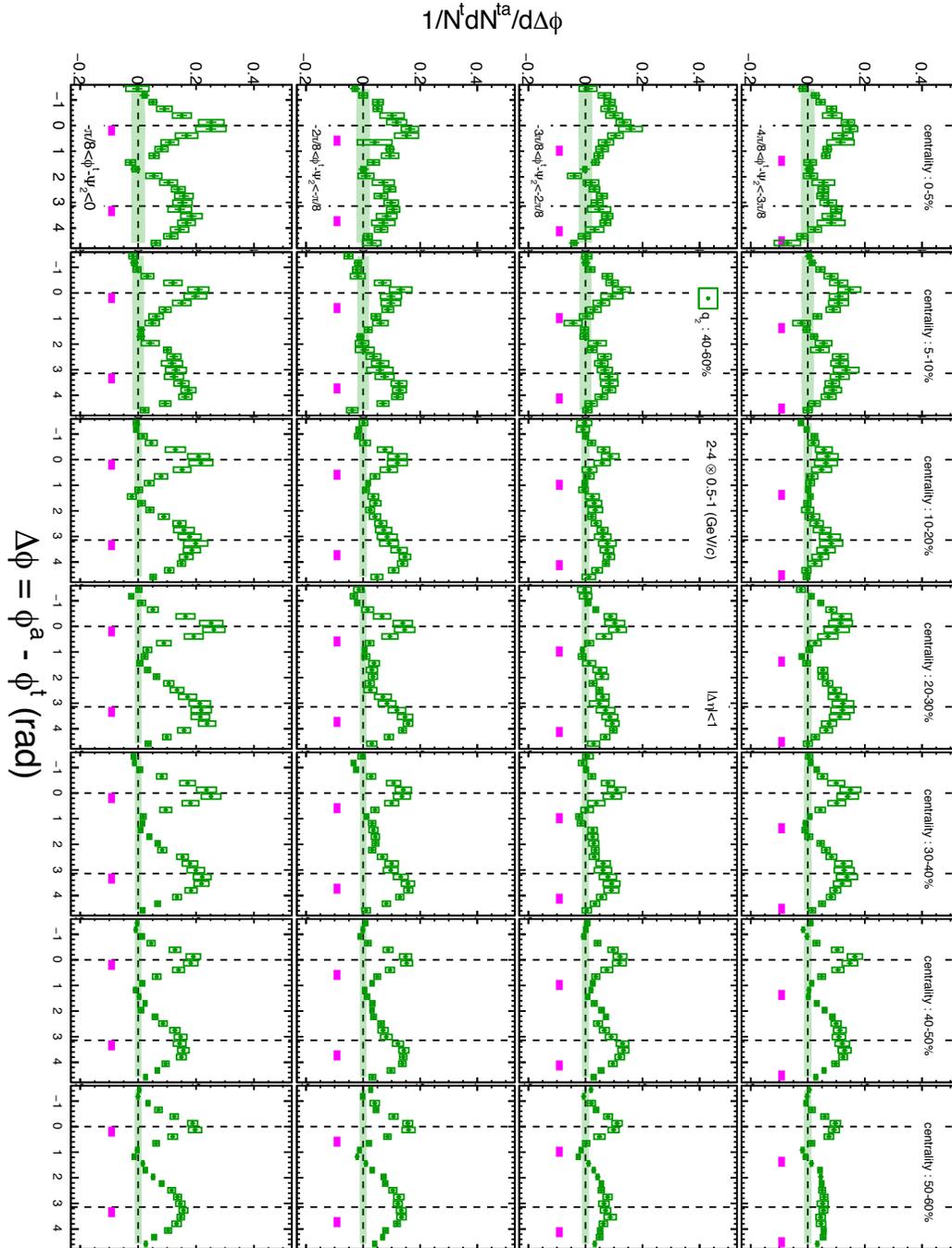
Figure A.11: Azimuthal distribution of correlated yield in p_T : 2-4⊗0.5-1 (GeV/c) with trigger angle selection with respect to the second-order event plane in q_2 : 40 − 60% selected events.
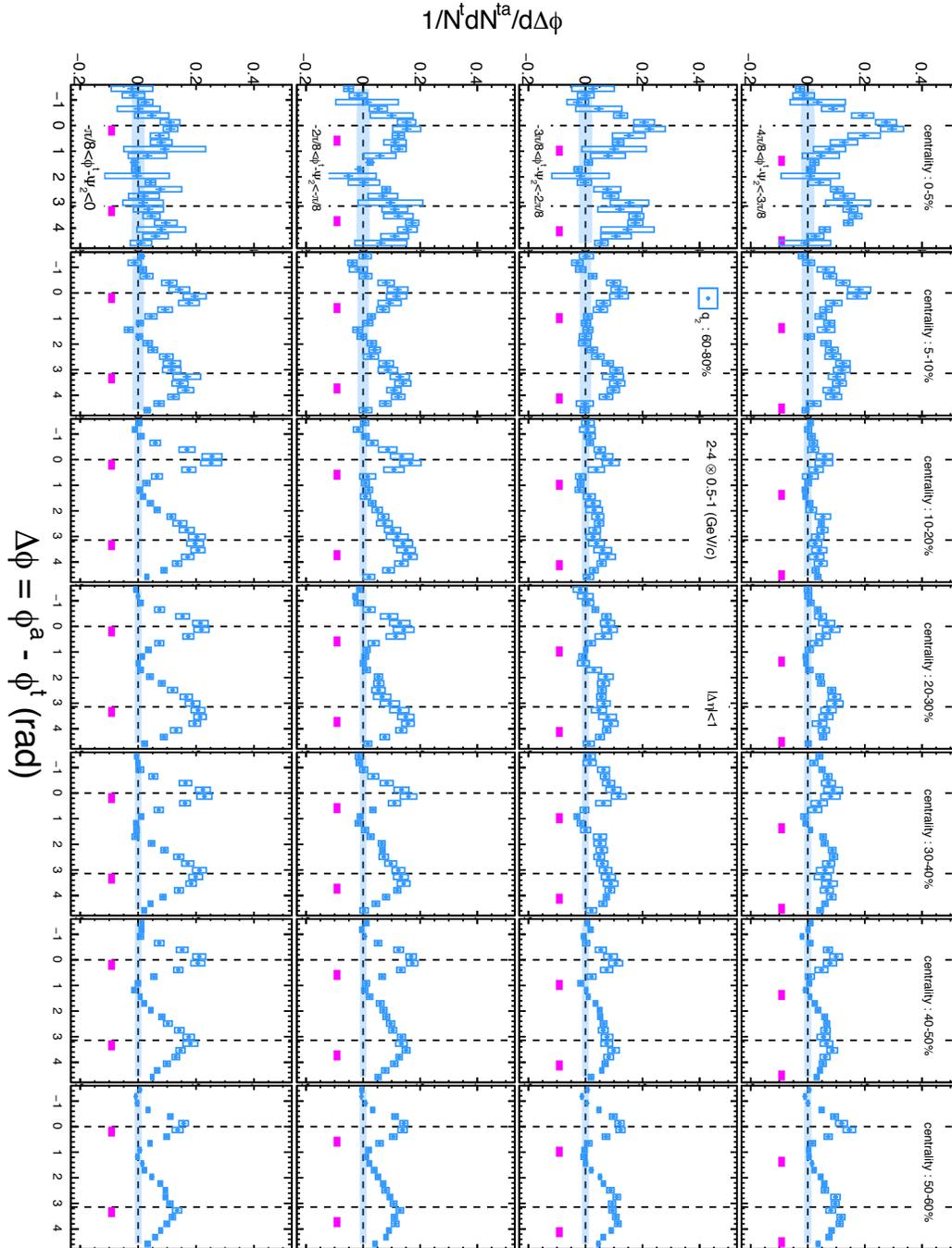
Figure A.12: Azimuthal distribution of correlated yield in p_T : 2-4⊗0.5-1 (GeV/c) with trigger angle selection with respect to the second-order event plane in q_2 : $60 - 80\%$ selected events.
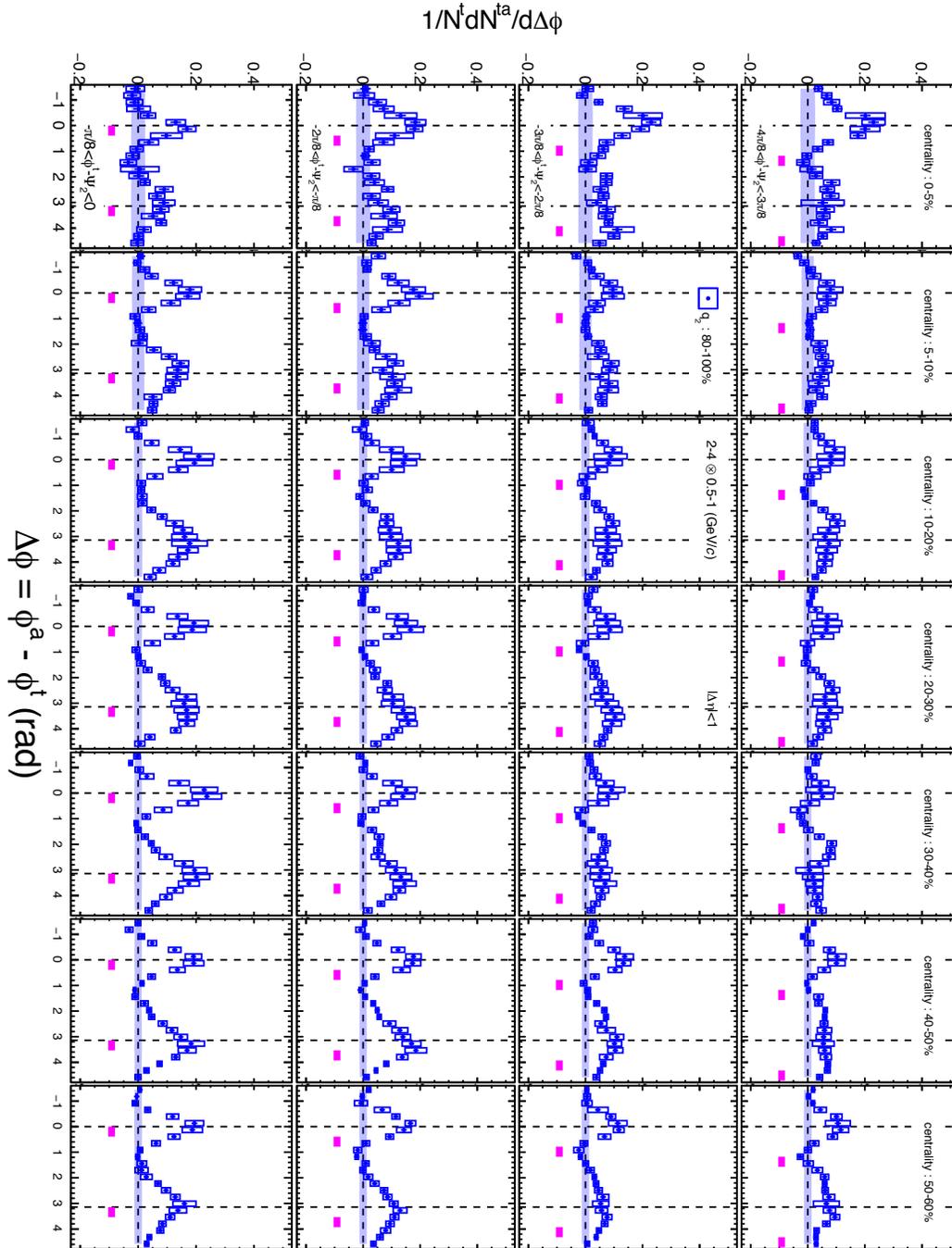
Figure A.13: Azimuthal distribution of correlated yield in p_T : 2-4$\otimes$0.5-1 (GeV/c) with trigger angle selection with respect to the second-order event plane in q_2 : $80 - 100\%$ selected events.
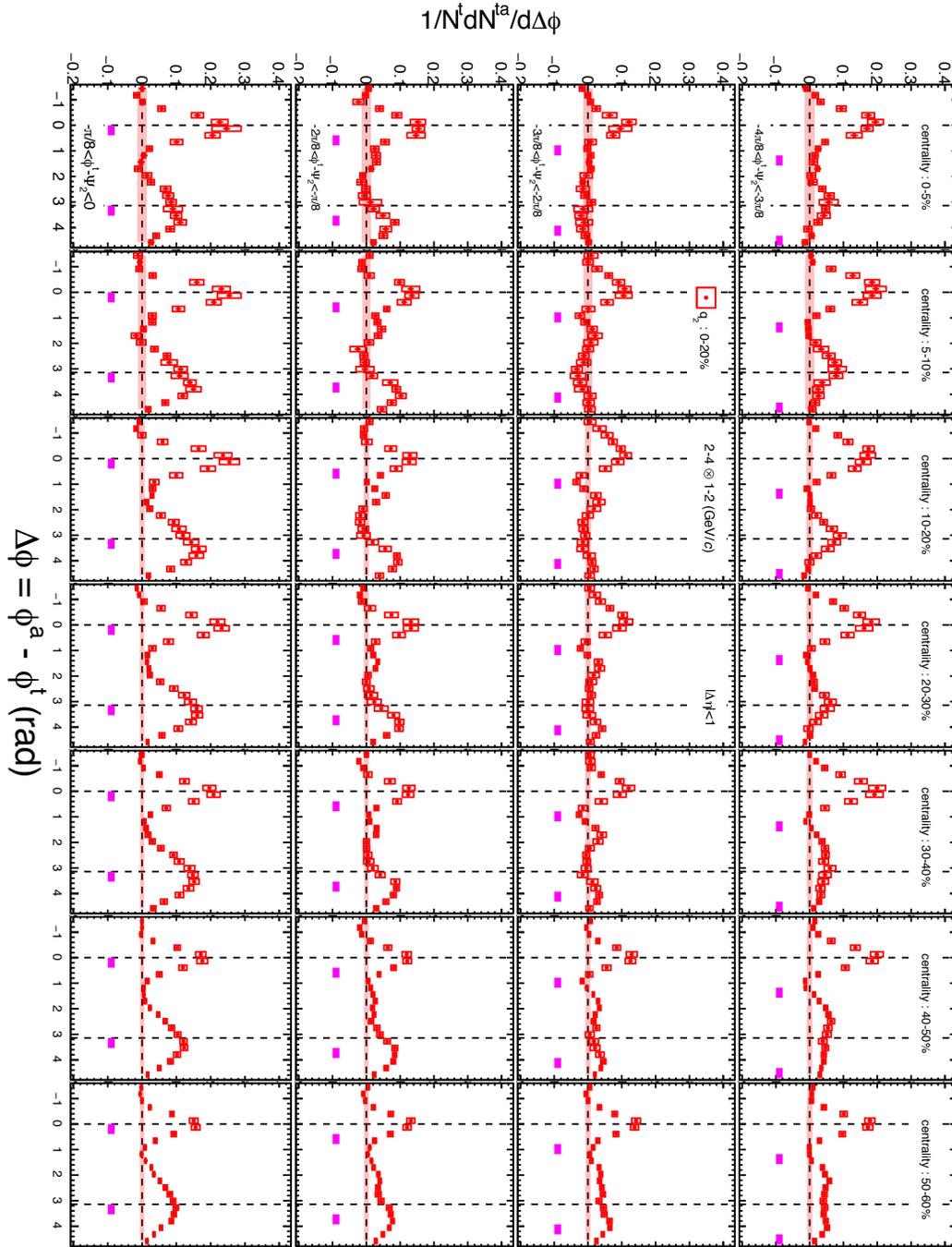
Figure A.14: Azimuthal distribution of correlated yield in p_T : 2-4⊗1-2 (GeV/c) with trigger angle selection with respect to the second-order event plane in q_2 : $0 - 20\%$ selected events.

Figure A.15: Azimuthal distribution of correlated yield in $p_T : 2$-$4 \otimes 1$-2 (GeV/c) with trigger angle selection with respect to the second-order event plane in $q_2 : 20 - 40\%$ selected events.
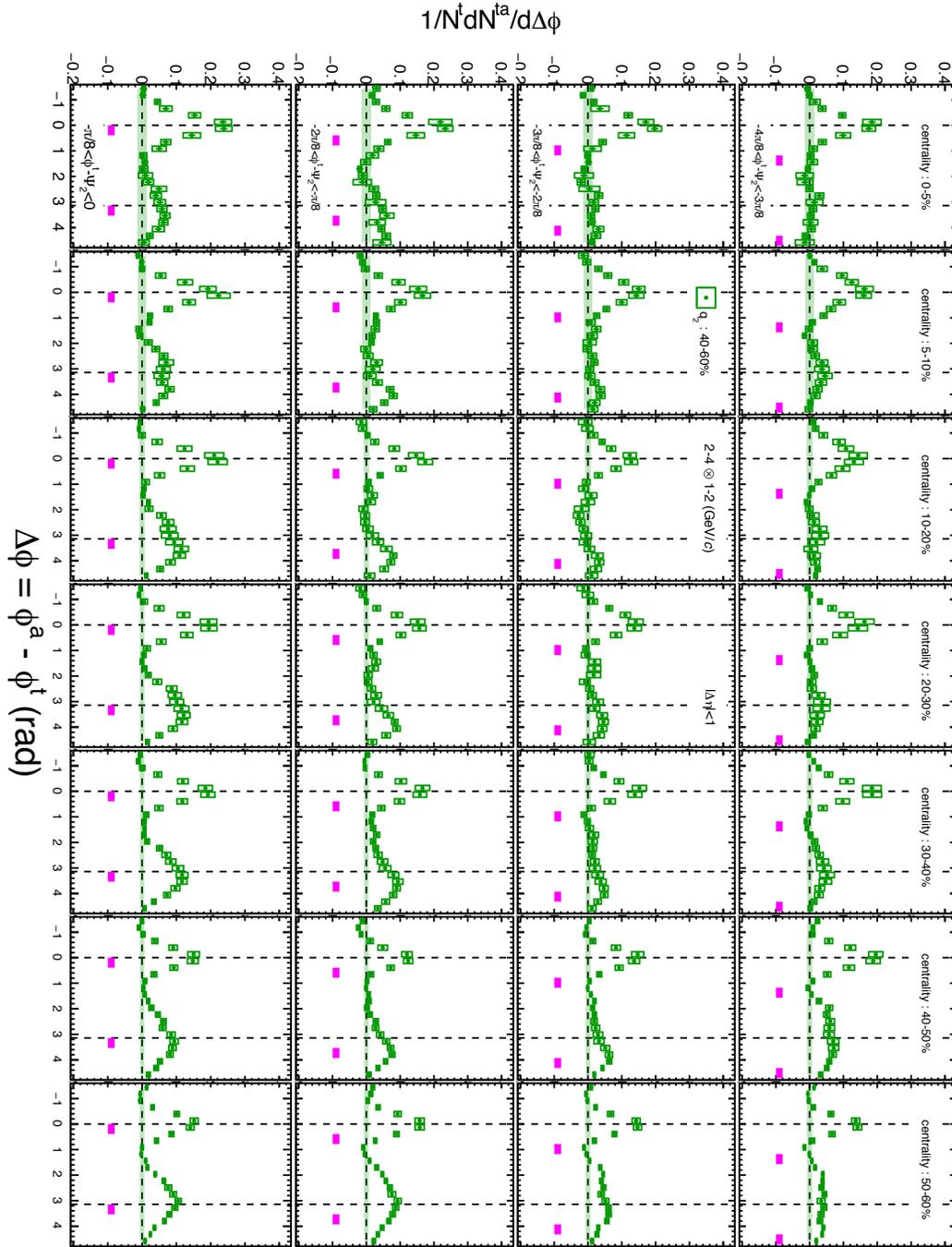
Figure A.16: Azimuthal distribution of correlated yield in p_T : 2-4⊗1-2 (GeV/c) with trigger angle selection with respect to the second-order event plane in q_2 : $40 - 60\%$ selected events.
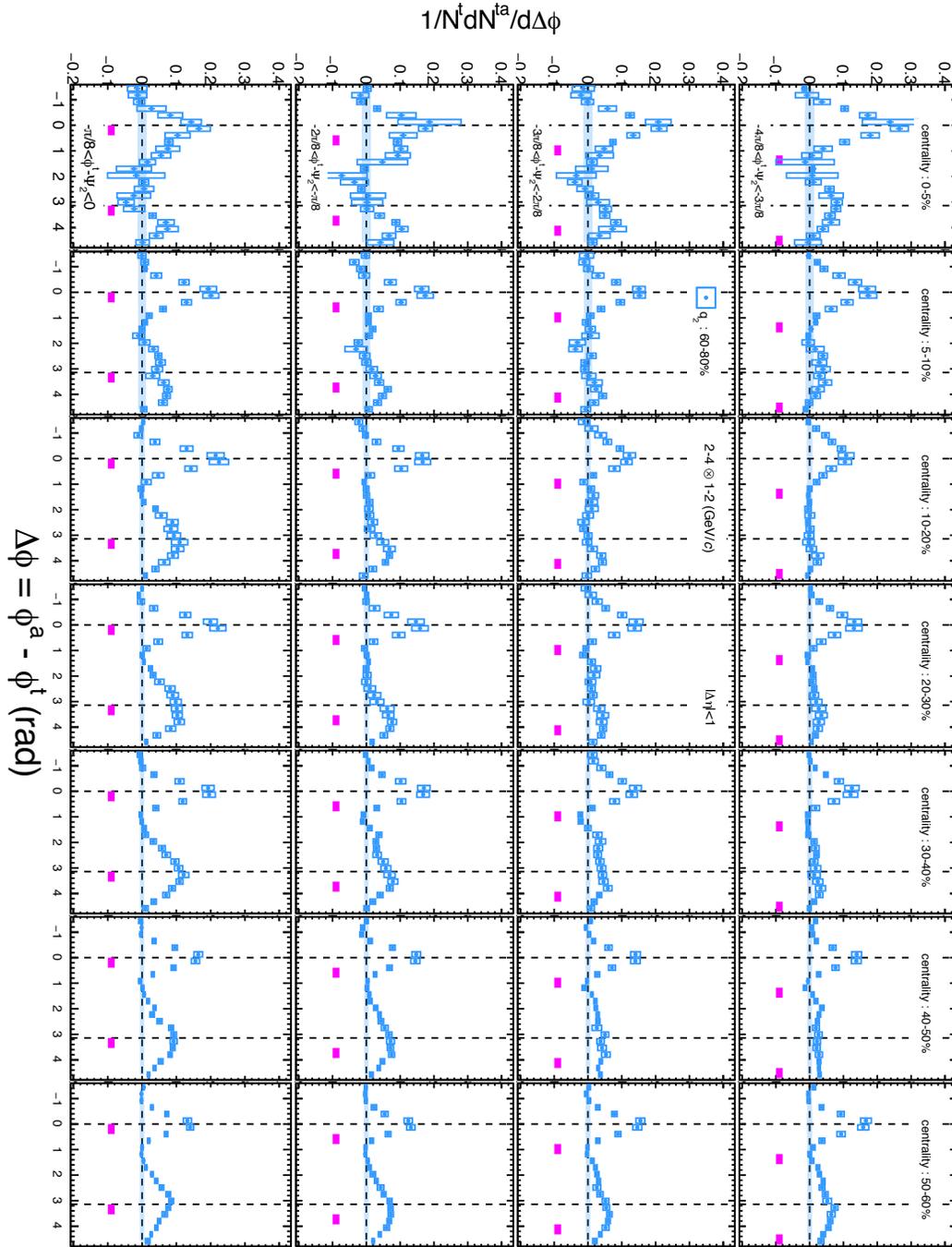
Figure A.17: Azimuthal distribution of correlated yield in $p_T : 2\text{-}4\otimes1\text{-}2$ (GeV/c) with trigger angle selection with respect to the second-order event plane in $q_2 : 60 - 80\%$ selected events.
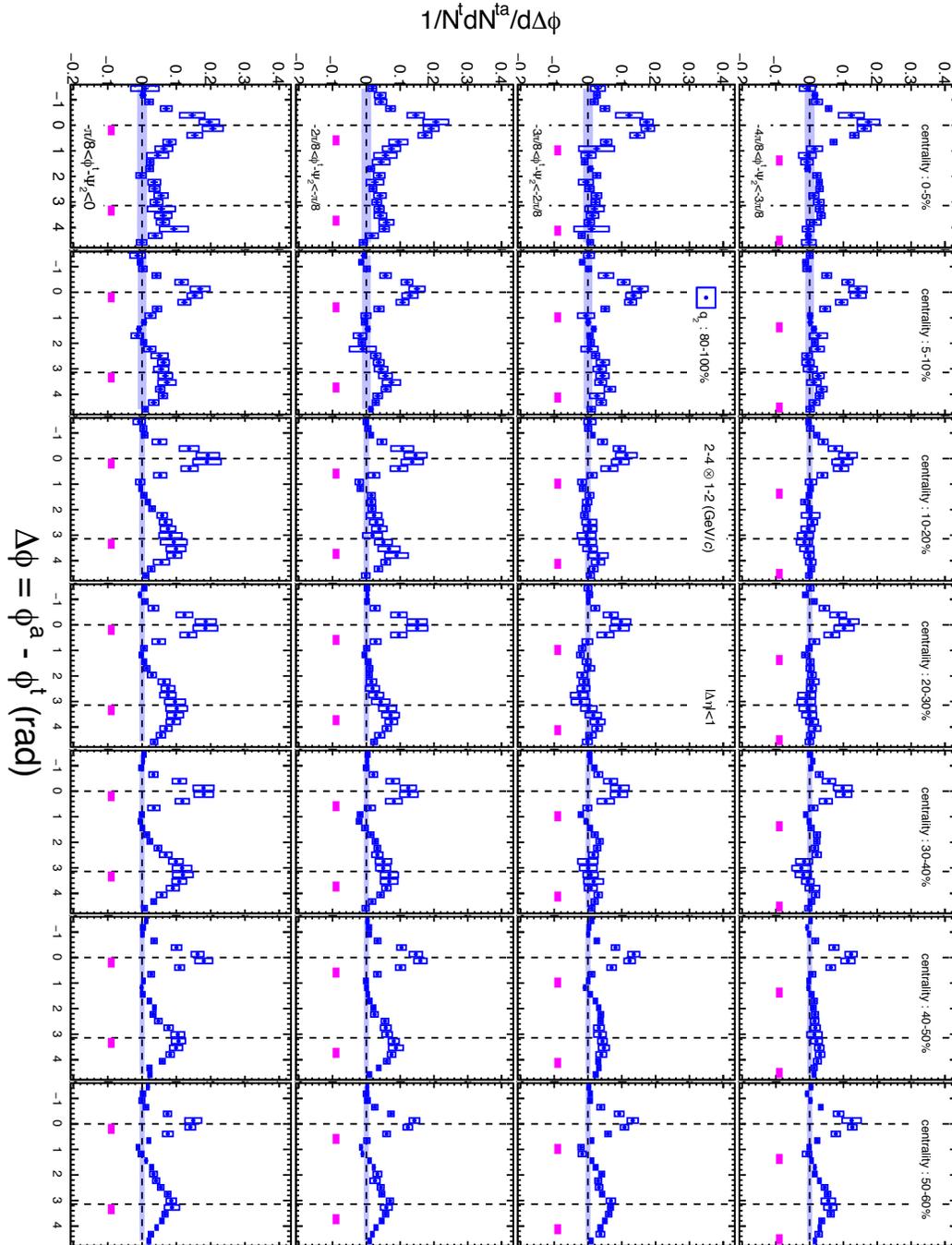
Figure A.18: Azimuthal distribution of correlated yield in p_T : 2-4⊗1-2 (GeV/c) with trigger angle selection with respect to the second-order event plane in q_2 : $80 - 100\%$ selected events.
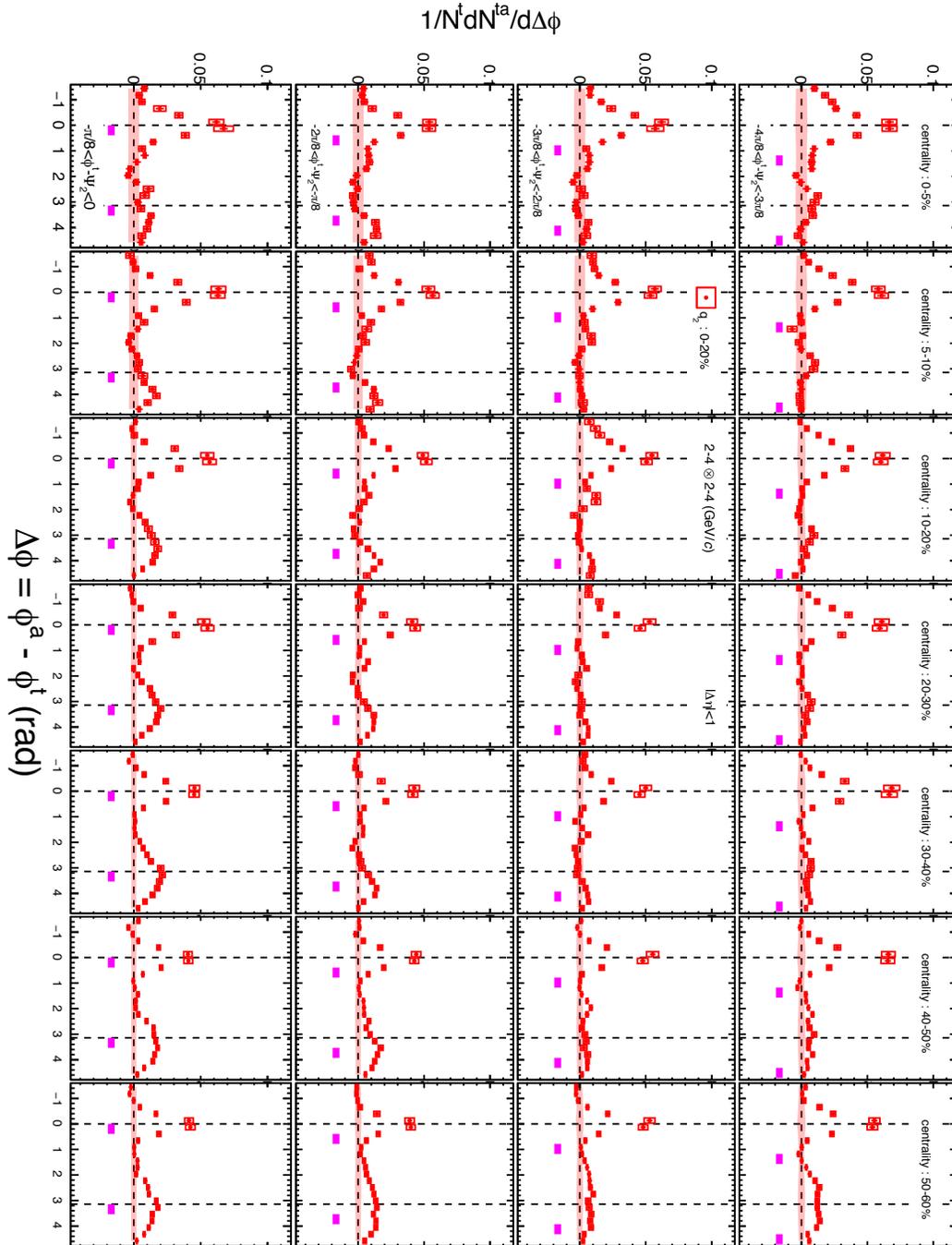
Figure A.19: Azimuthal distribution of correlated yield in p_T : 2-4⊗2-4 (GeV/c) with trigger angle selection with respect to the second-order event plane in q_2 : $0 - 20\%$ selected events.
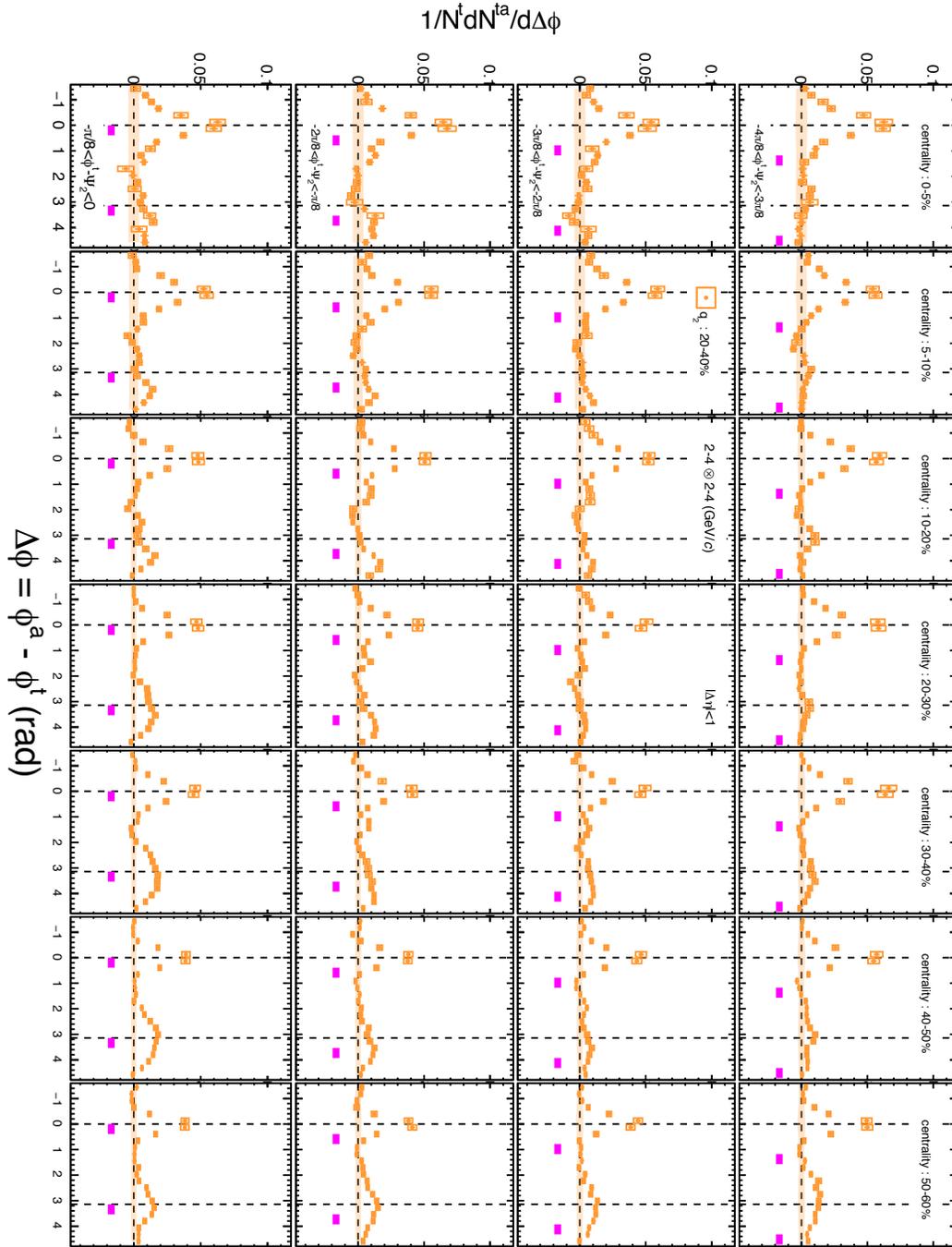
Figure A.20: Azimuthal distribution of correlated yield in p_T : 2-4⊗2-4 (GeV/c) with trigger angle selection with respect to the second-order event plane in q_2 : $20-40\%$ selected events.
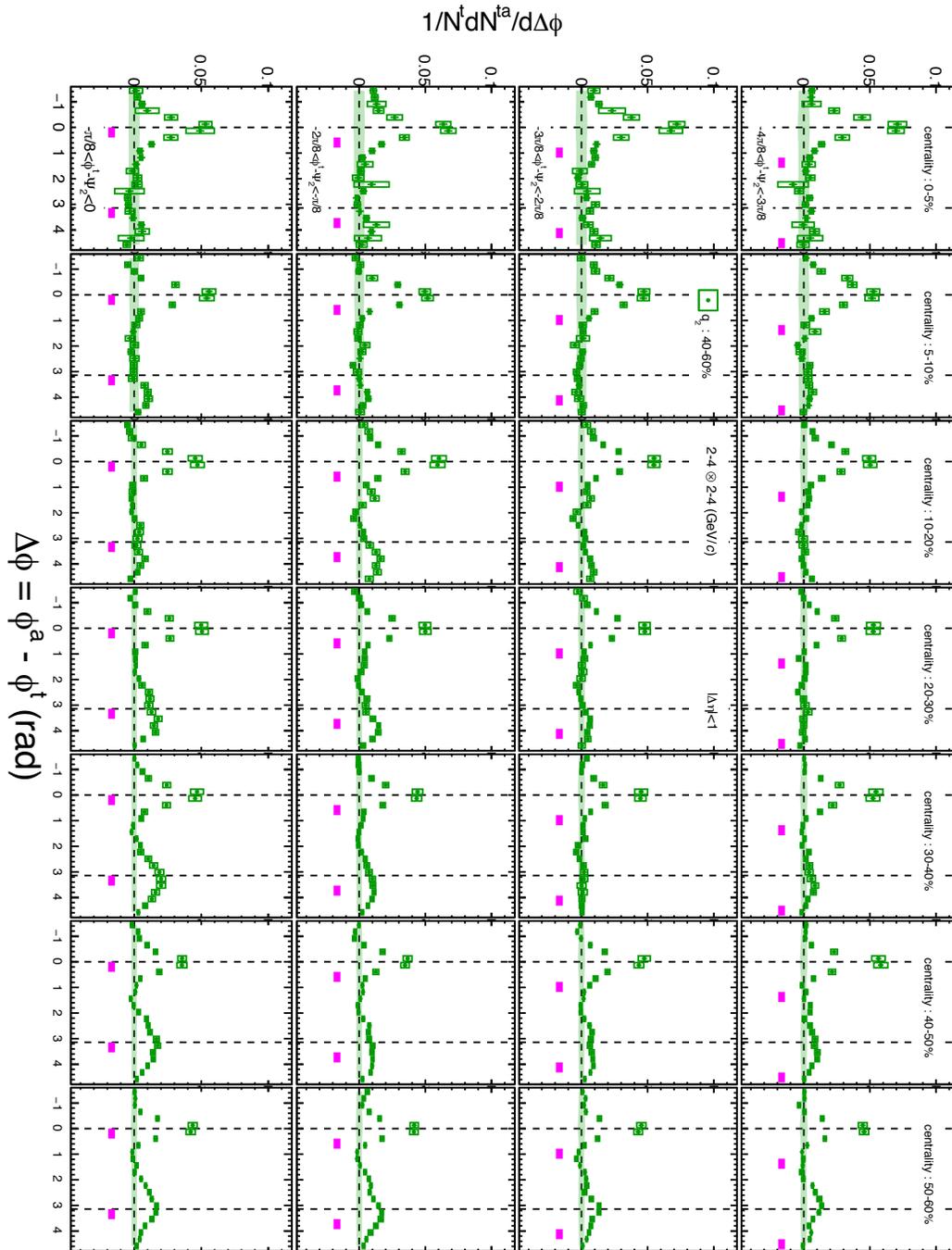
Figure A.21: Azimuthal distribution of correlated yield in $p_T : 2\text{-}4 \otimes 2\text{-}4$ (GeV/c) with trigger angle selection with respect to the second-order event plane in $q_2 : 40 - 60\%$ selected events.
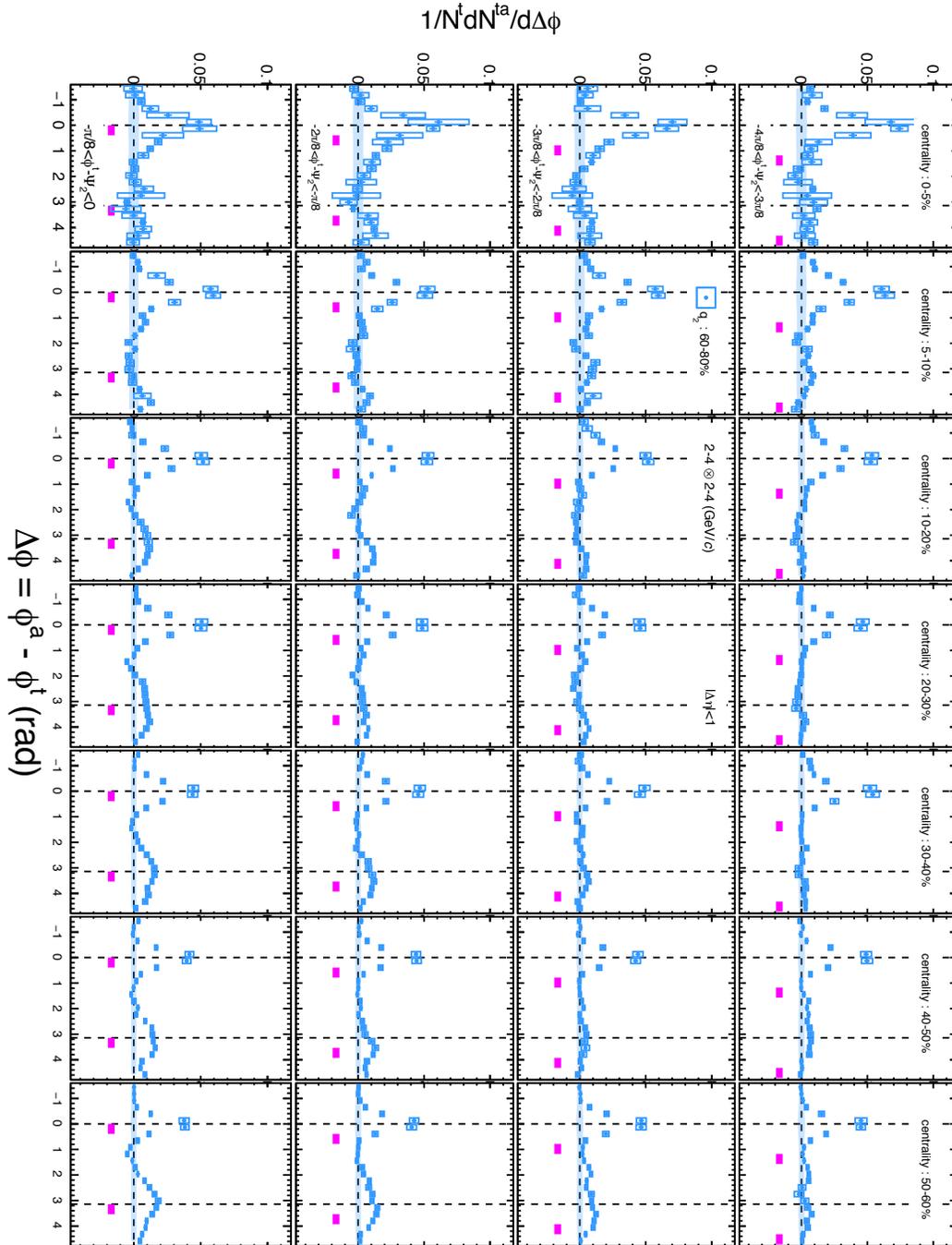
Figure A.22: Azimuthal distribution of correlated yield in $p_T : 2\text{-}4 \otimes 2\text{-}4$ (GeV/c) with trigger angle selection with respect to the second-order event plane in $q_2 : 60 - 80\%$ selected events.
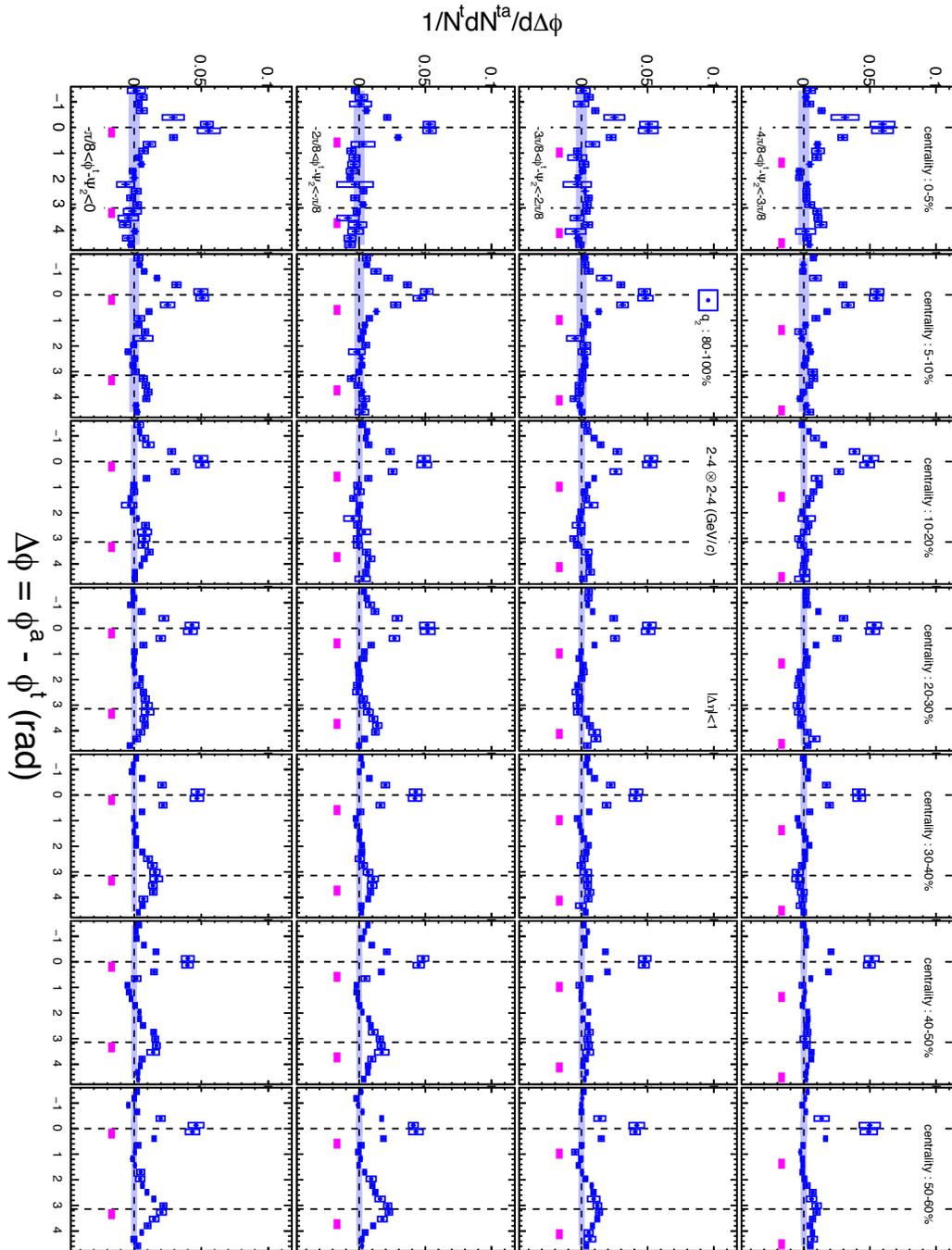
Figure A.23: Azimuthal distribution of correlated yield in p_T : 2-4$\otimes$2-4 (GeV/c) with trigger angle selection with respect to the second-order event plane in q_2 : $80 - 100\%$ selected events.
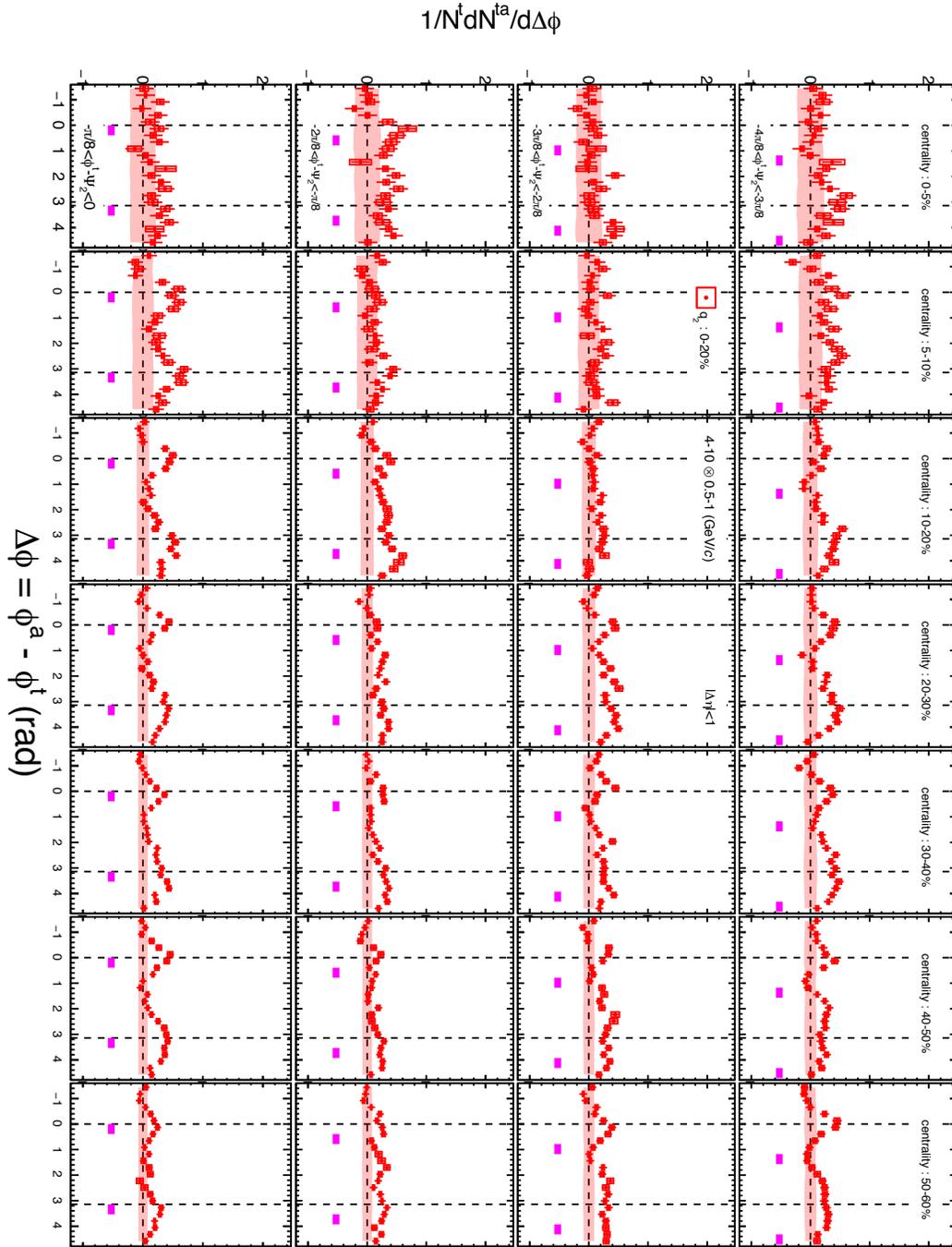
Figure A.24: Azimuthal distribution of correlated yield in p_T : 4-10⊗0.5-1 (GeV/c) with trigger angle selection with respect to the second-order event plane in q_2 : $0 - 20\%$ selected events.
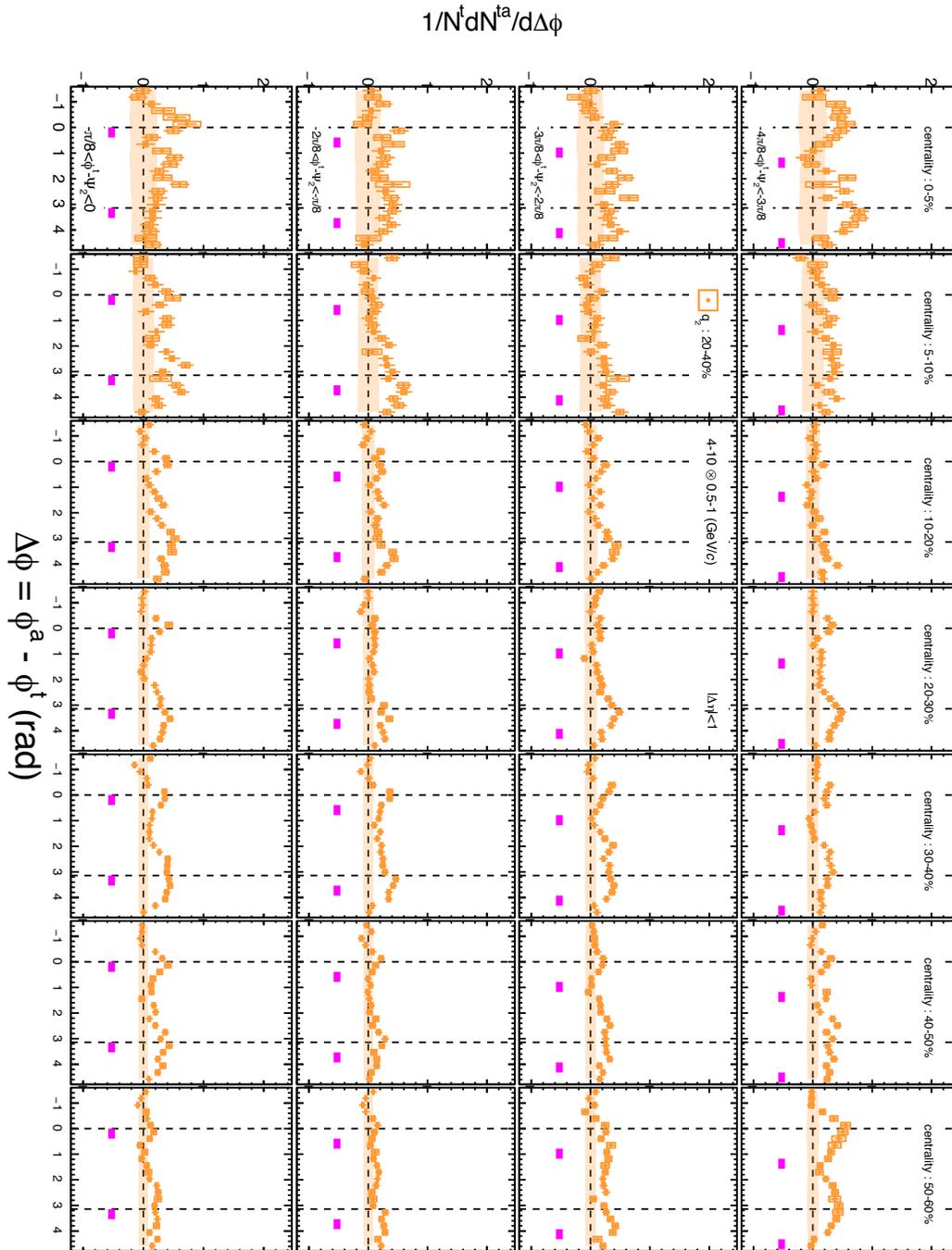
Figure A.25: Azimuthal distribution of correlated yield in p_T : 4-10⊗0.5-1 (GeV/c) with trigger angle selection with respect to the second-order event plane in q_2 : 20 − 40% selected events.
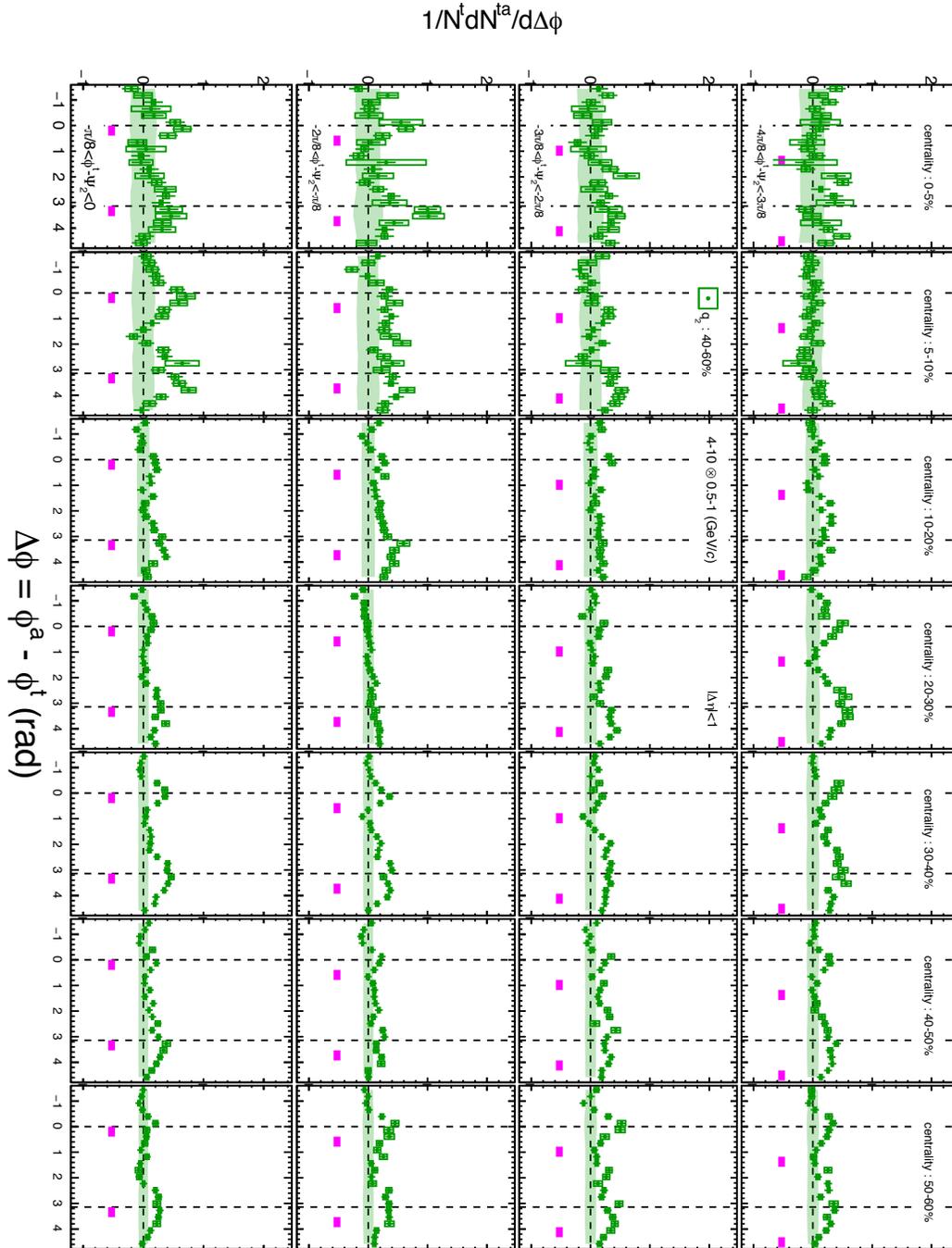
Figure A.26: Azimuthal distribution of correlated yield in p_T : 4-10⊗0.5-1 (GeV/c) with trigger angle selection with respect to the second-order event plane in q_2 : $40 - 60\%$ selected events.
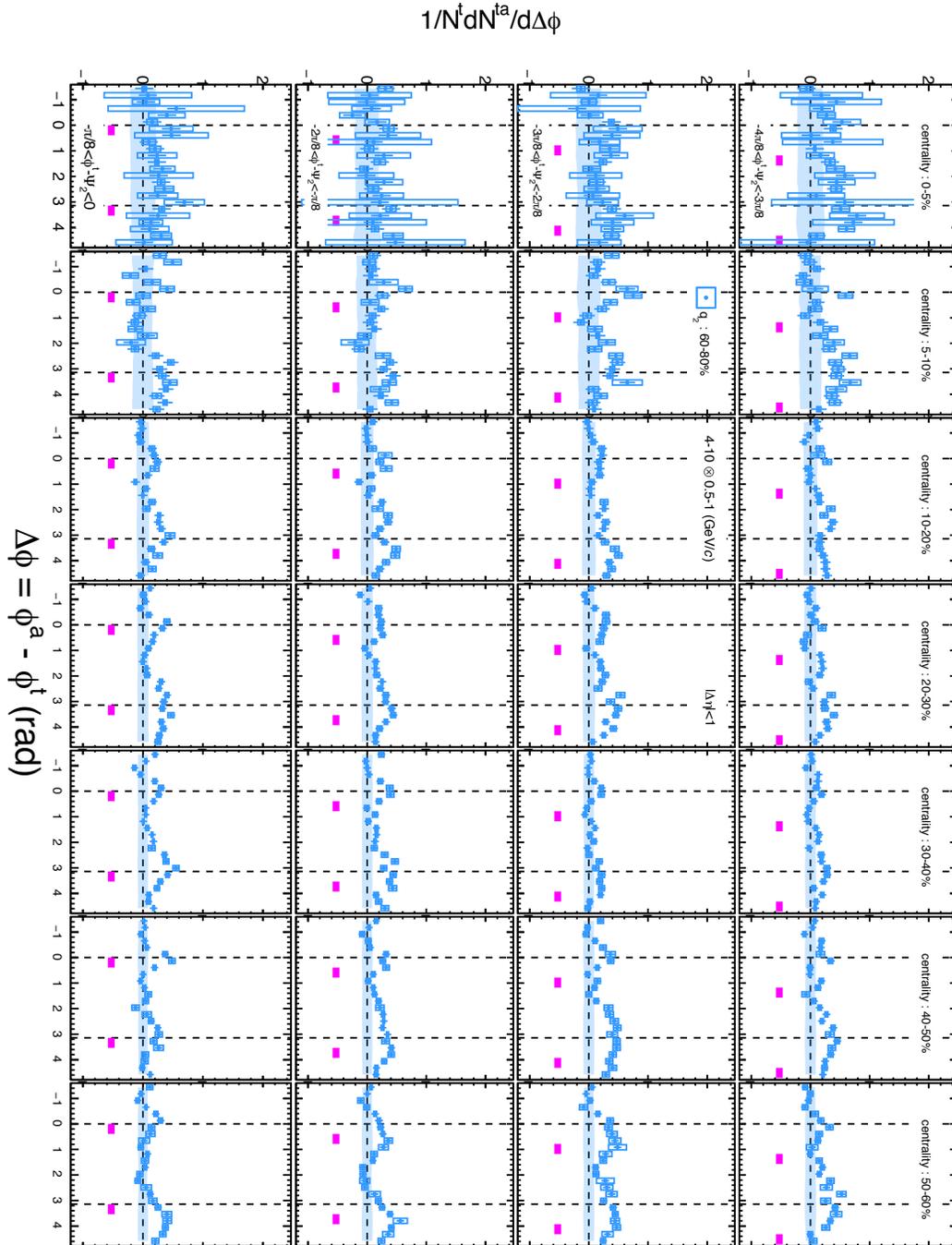
Figure A.27: Azimuthal distribution of correlated yield in p_T : 4-10⊗0.5-1 (GeV/c) with trigger angle selection with respect to the second-order event plane in q_2 : $60 - 80\%$ selected events.
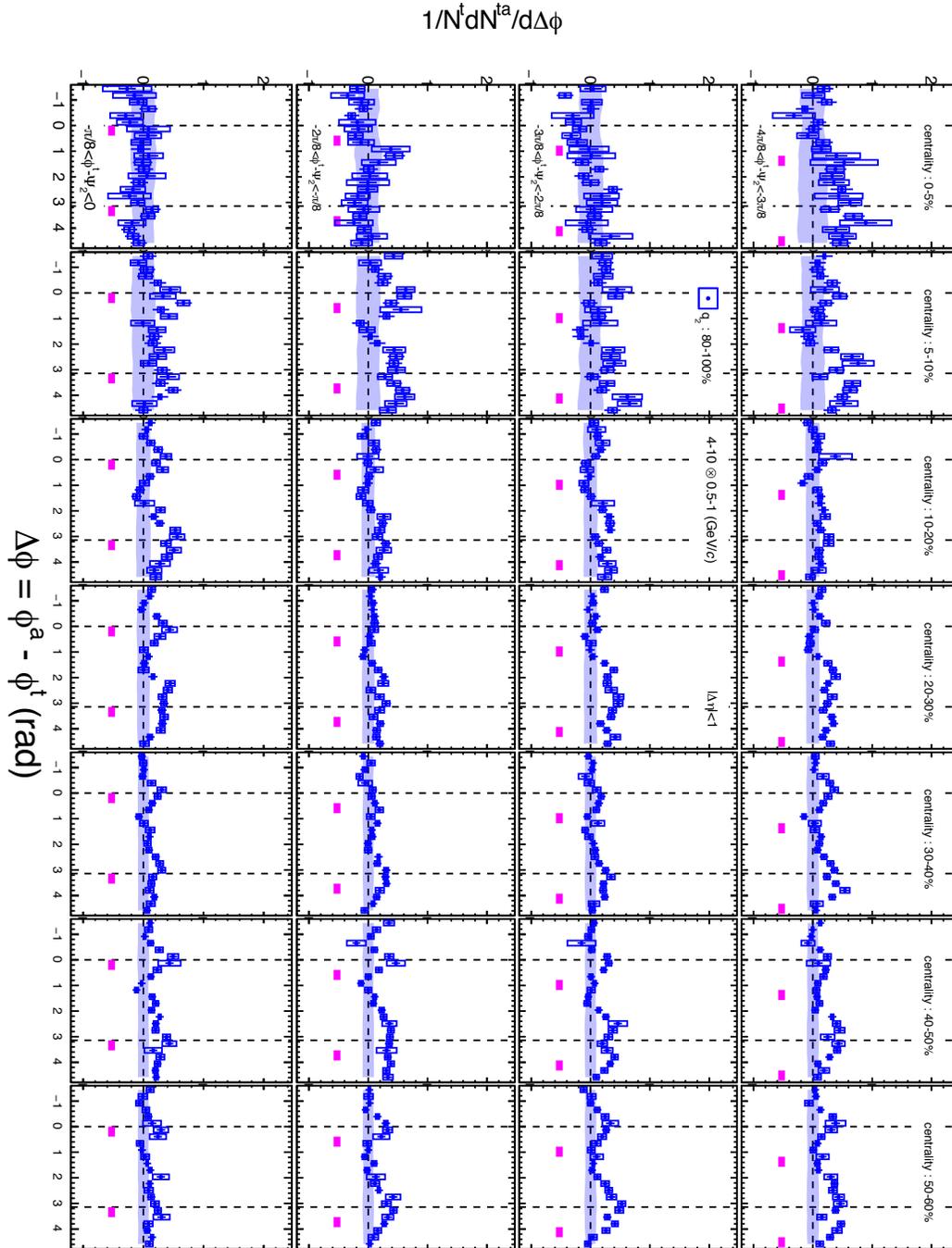
Figure A.28: Azimuthal distribution of correlated yield in p_T : 4-10⊗0.5-1 (GeV/c) with trigger angle selection with respect to the second-order event plane in q_2 : $80 - 100\%$ selected events.
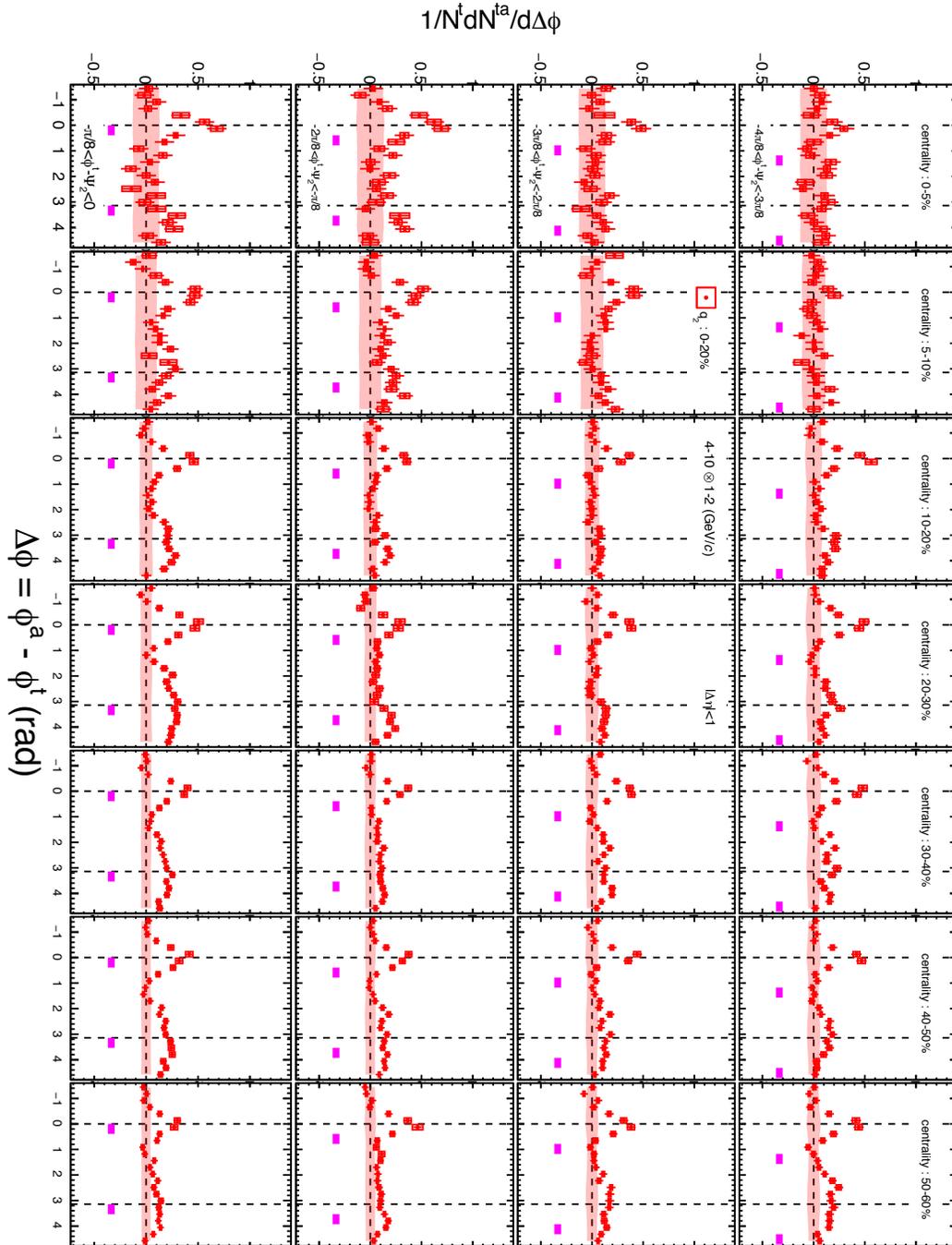
Figure A.29: Azimuthal distribution of correlated yield in $p_T : 4\text{-}10 \otimes 1\text{-}2$ (GeV/c) with trigger angle selection with respect to the second-order event plane in $q_2 : 0 - 20\%$ selected events.
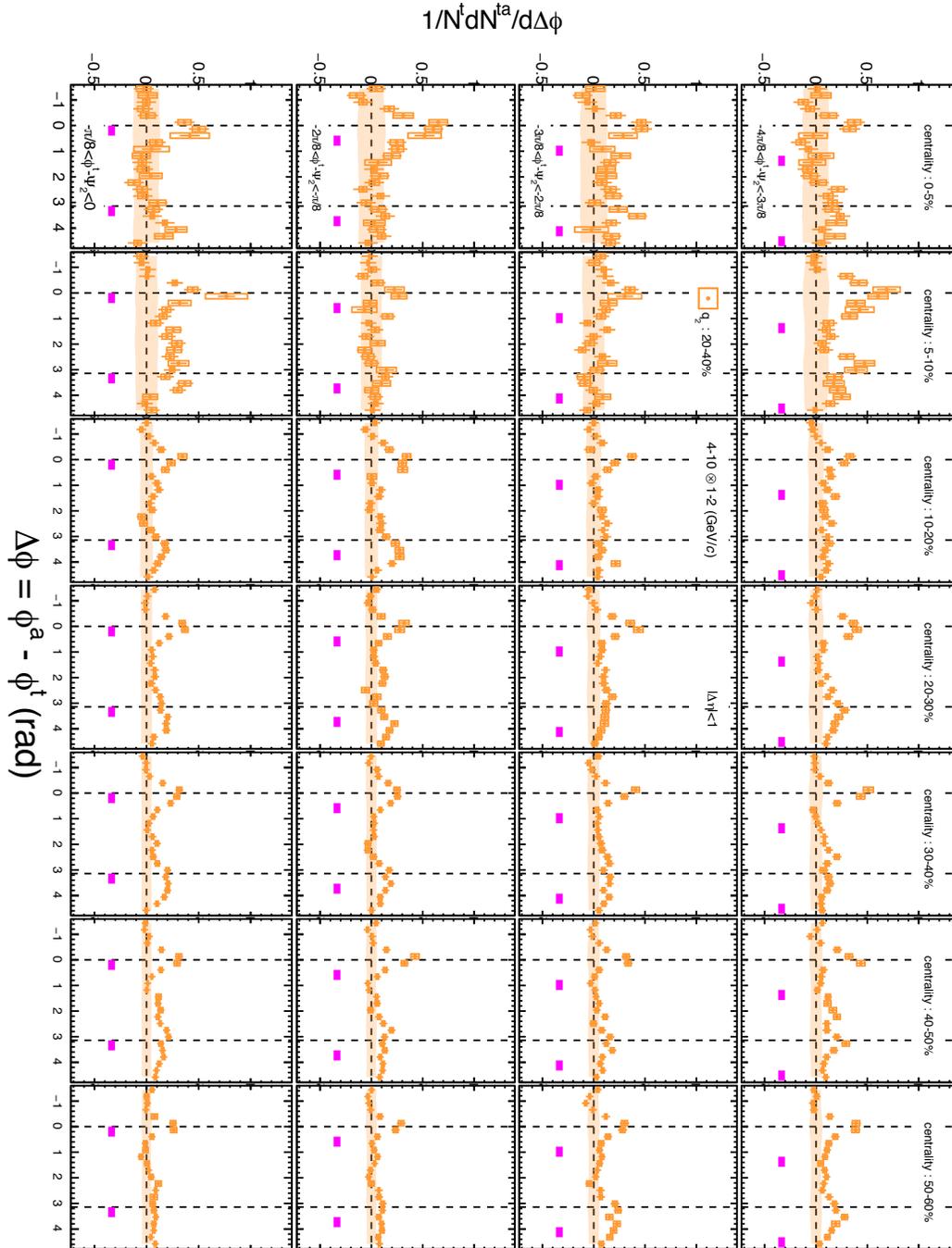
Figure A.30: Azimuthal distribution of correlated yield in p_T : 4-10⊗1-2 (GeV/c) with trigger angle selection with respect to the second-order event plane in q_2 : $20 - 40\%$ selected events.
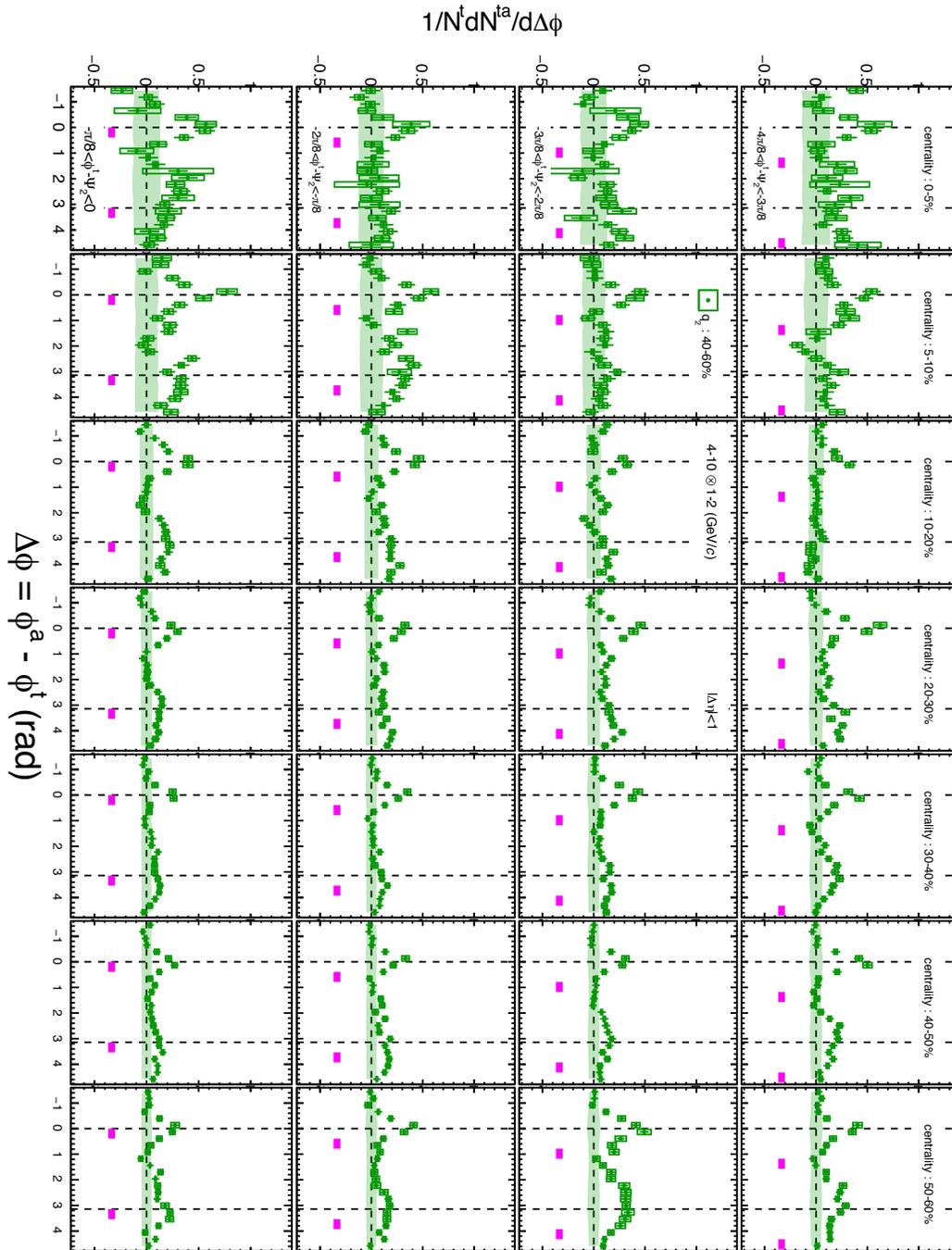
Figure A.31: Azimuthal distribution of correlated yield in $p_T : 4\text{-}10 \otimes 1\text{-}2$ (GeV/c) with trigger angle selection with respect to the second-order event plane in $q_2 : 40 - 60\%$ selected events.
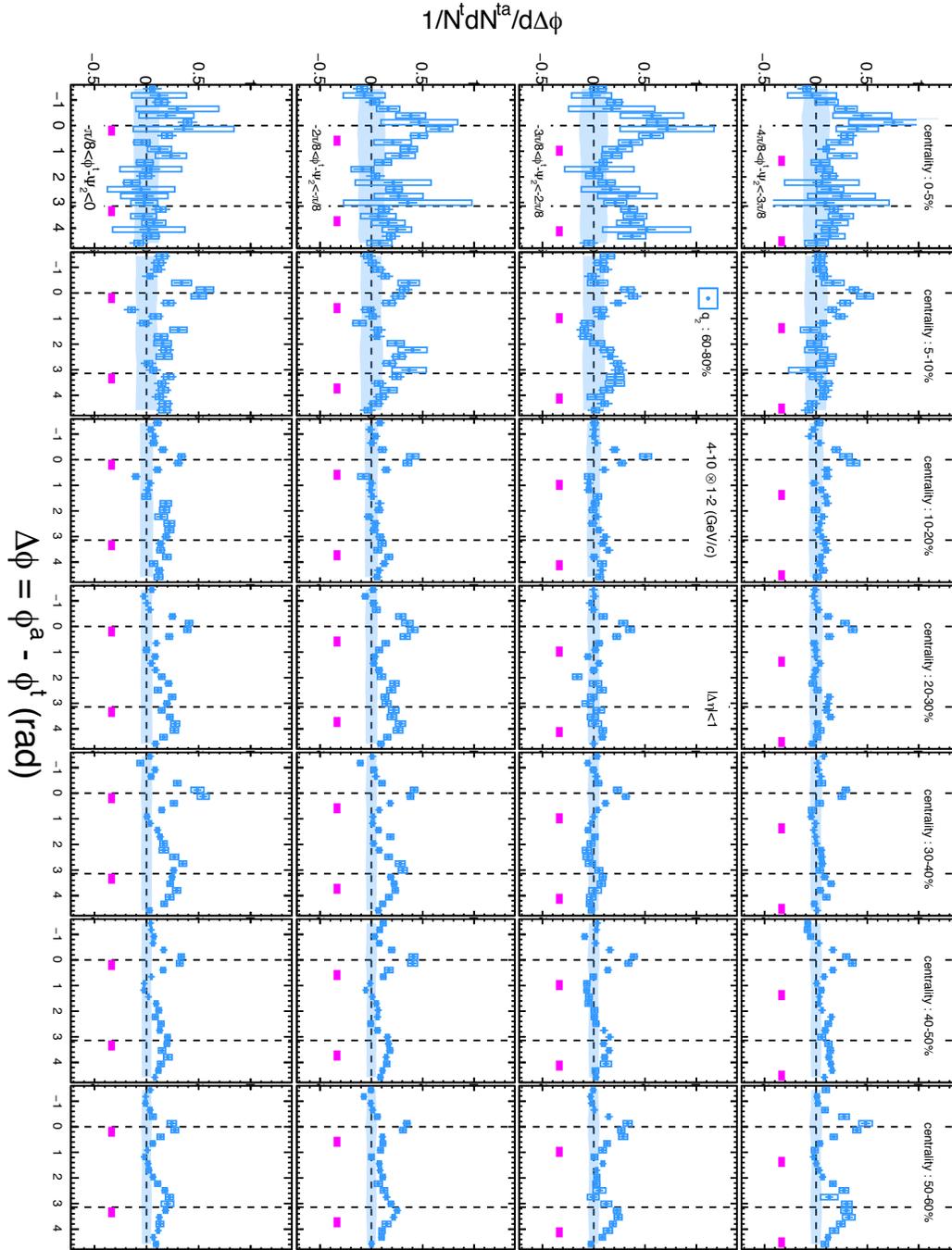
Figure A.32: Azimuthal distribution of correlated yield in $p_T : 4\text{-}10 \otimes 1\text{-}2$ (GeV/c) with trigger angle selection with respect to the second-order event plane in $q_2 : 60 - 80\%$ selected events.
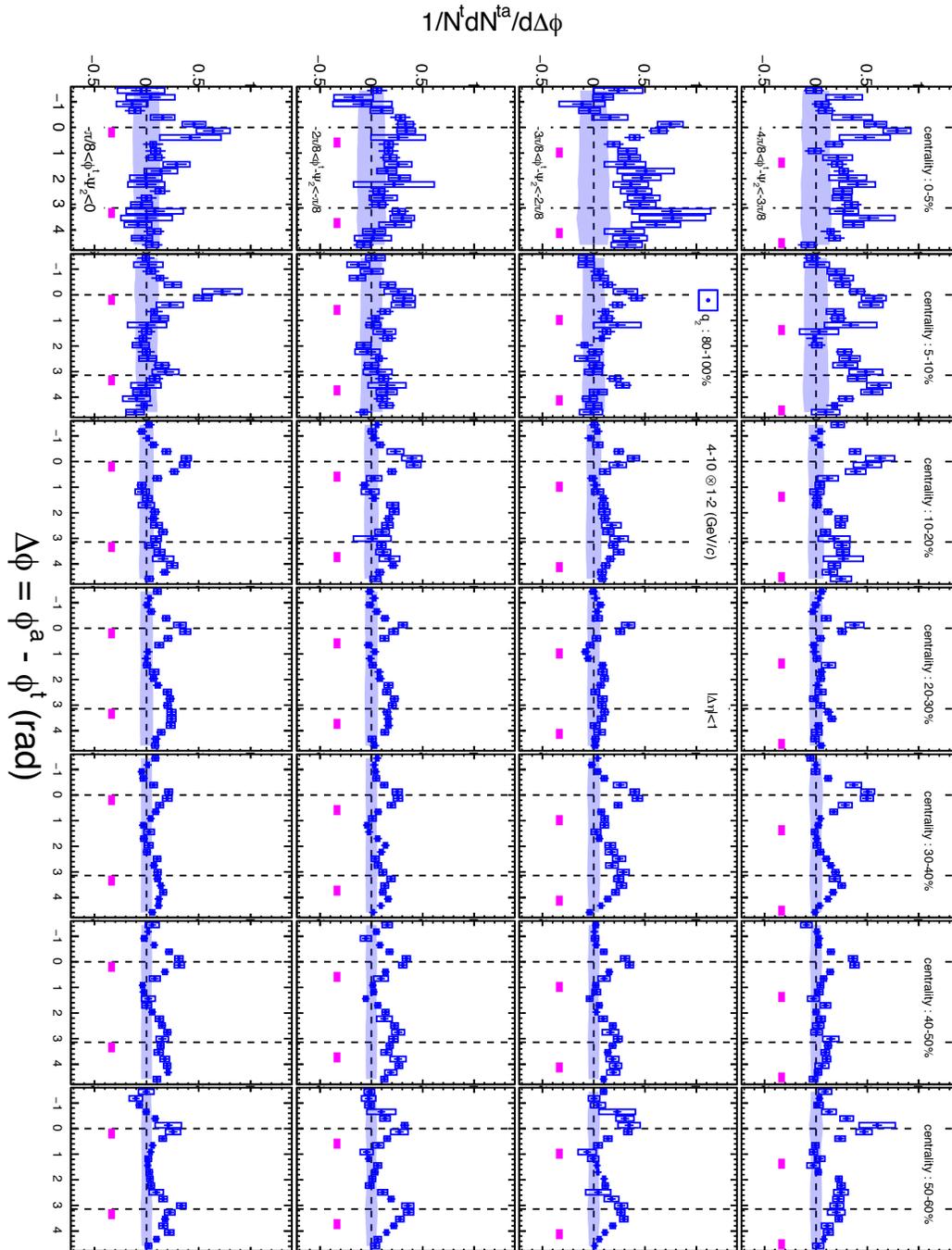
Figure A.33: Azimuthal distribution of correlated yield in $p_T : 4\text{-}10 \otimes 1\text{-}2$ (GeV/c) with trigger angle selection with respect to the second-order event plane in $q_2 : 80 - 100\%$ selected events.
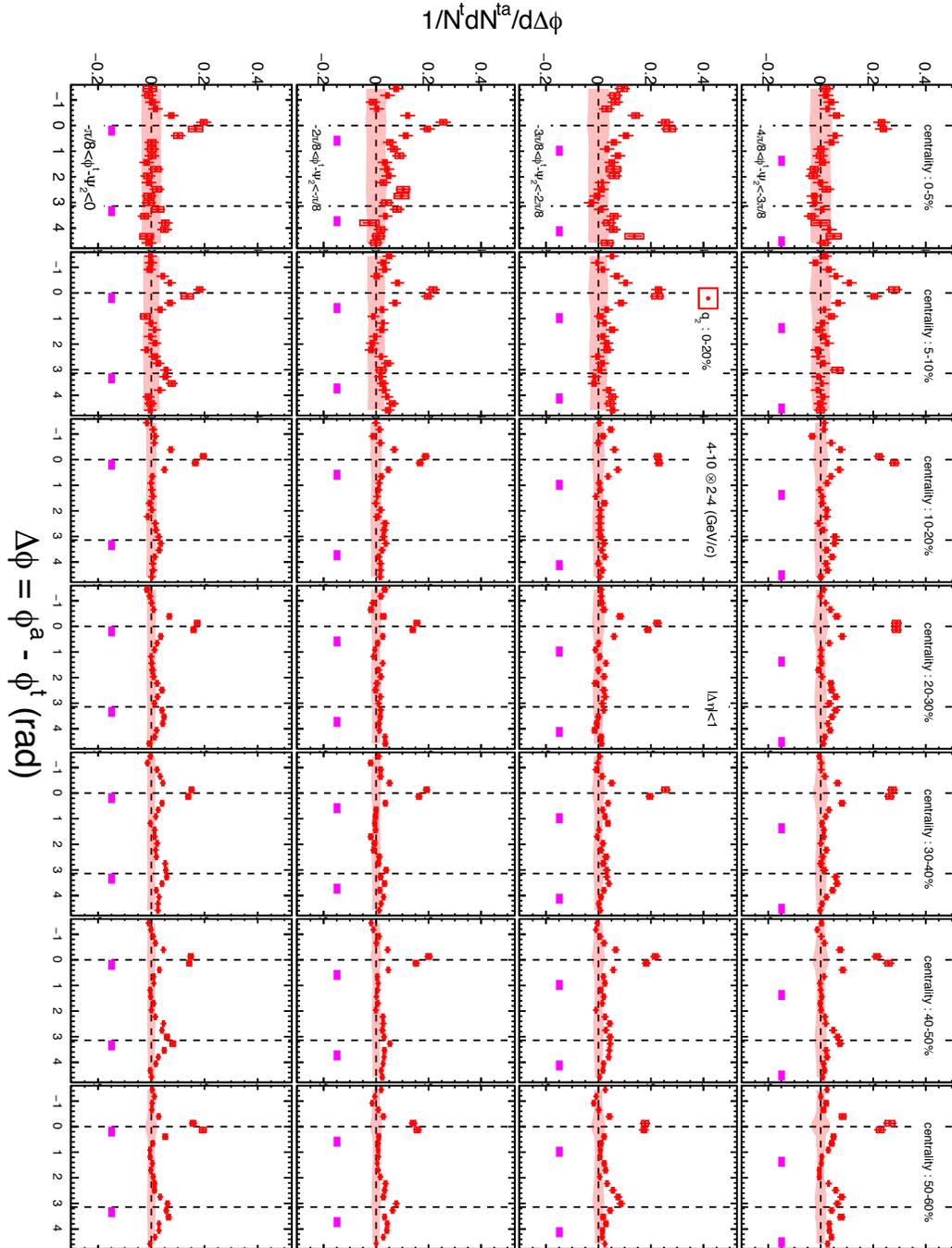
Figure A.34: Azimuthal distribution of correlated yield in $p_T : 4\text{-}10 \otimes 2\text{-}4$ (GeV/c) with trigger angle selection with respect to the second-order event plane in $q_2 : 0 - 20\%$ selected events.
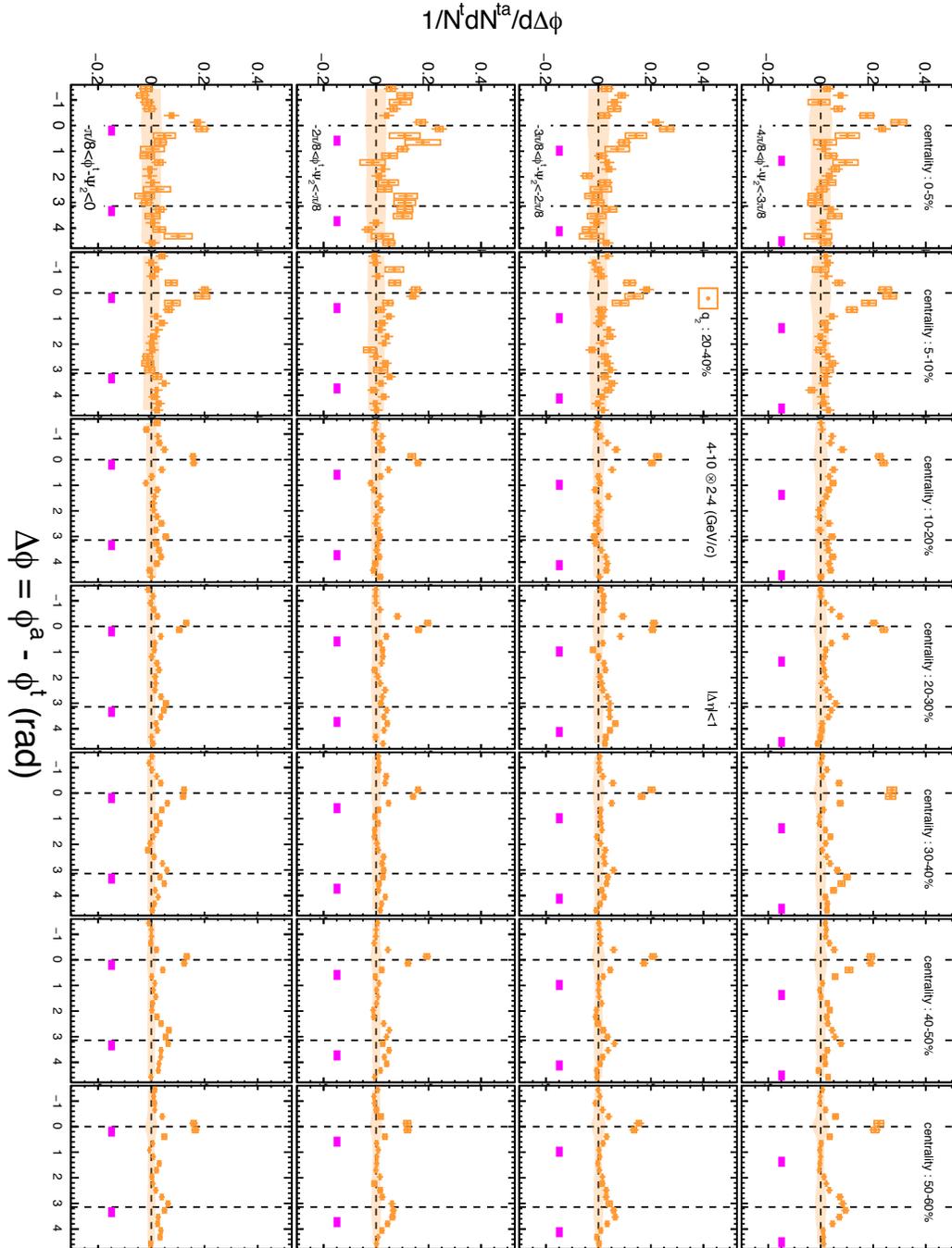
Figure A.35: Azimuthal distribution of correlated yield in $p_T : 4\text{-}10 \otimes 2\text{-}4$ (GeV/c) with trigger angle selection with respect to the second-order event plane in $q_2 : 20 - 40\%$ selected events.
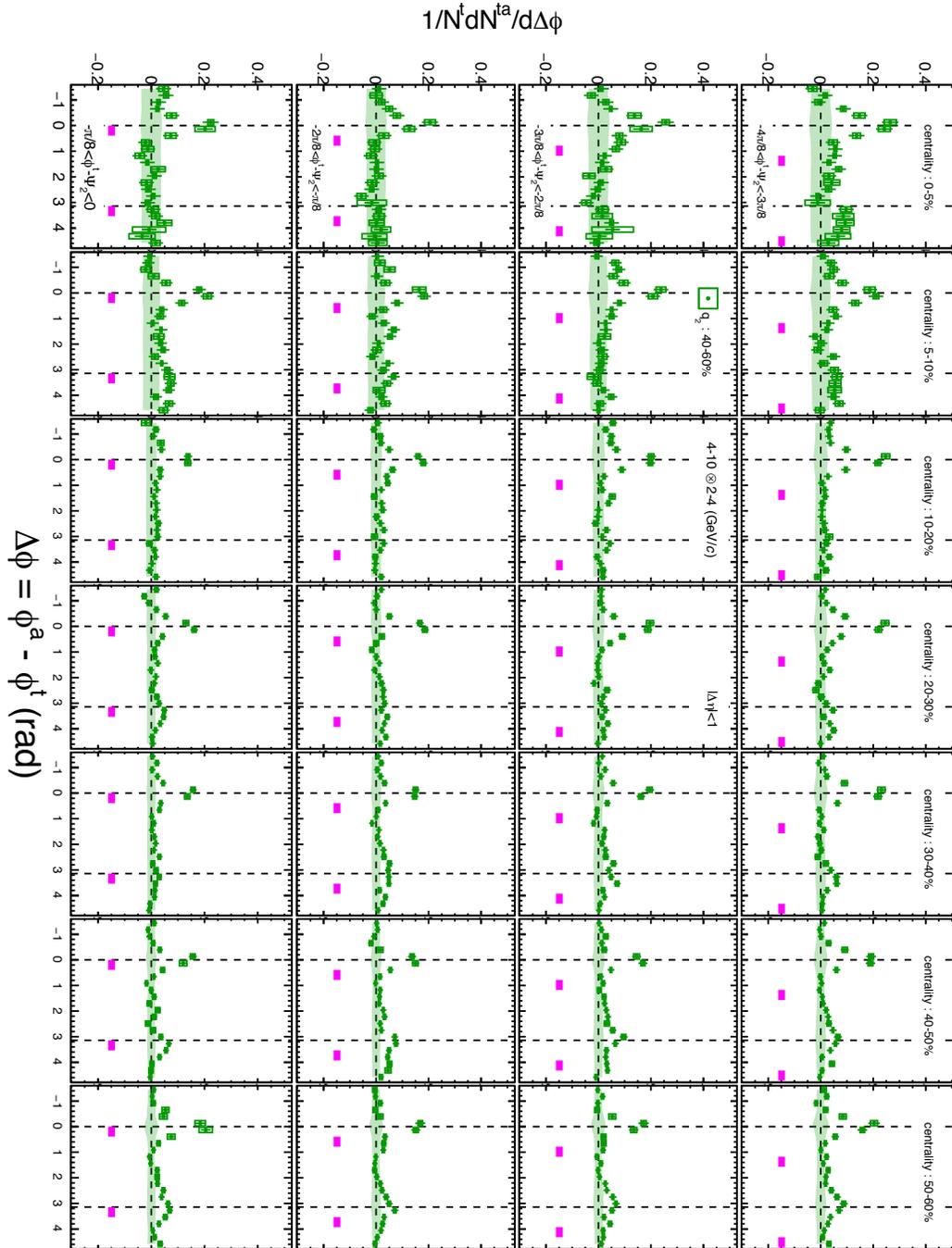
Figure A.36: Azimuthal distribution of correlated yield in p_T : 4-10⊗2-4 (GeV/c) with trigger angle selection with respect to the second-order event plane in q_2 : $40 - 60\%$ selected events.
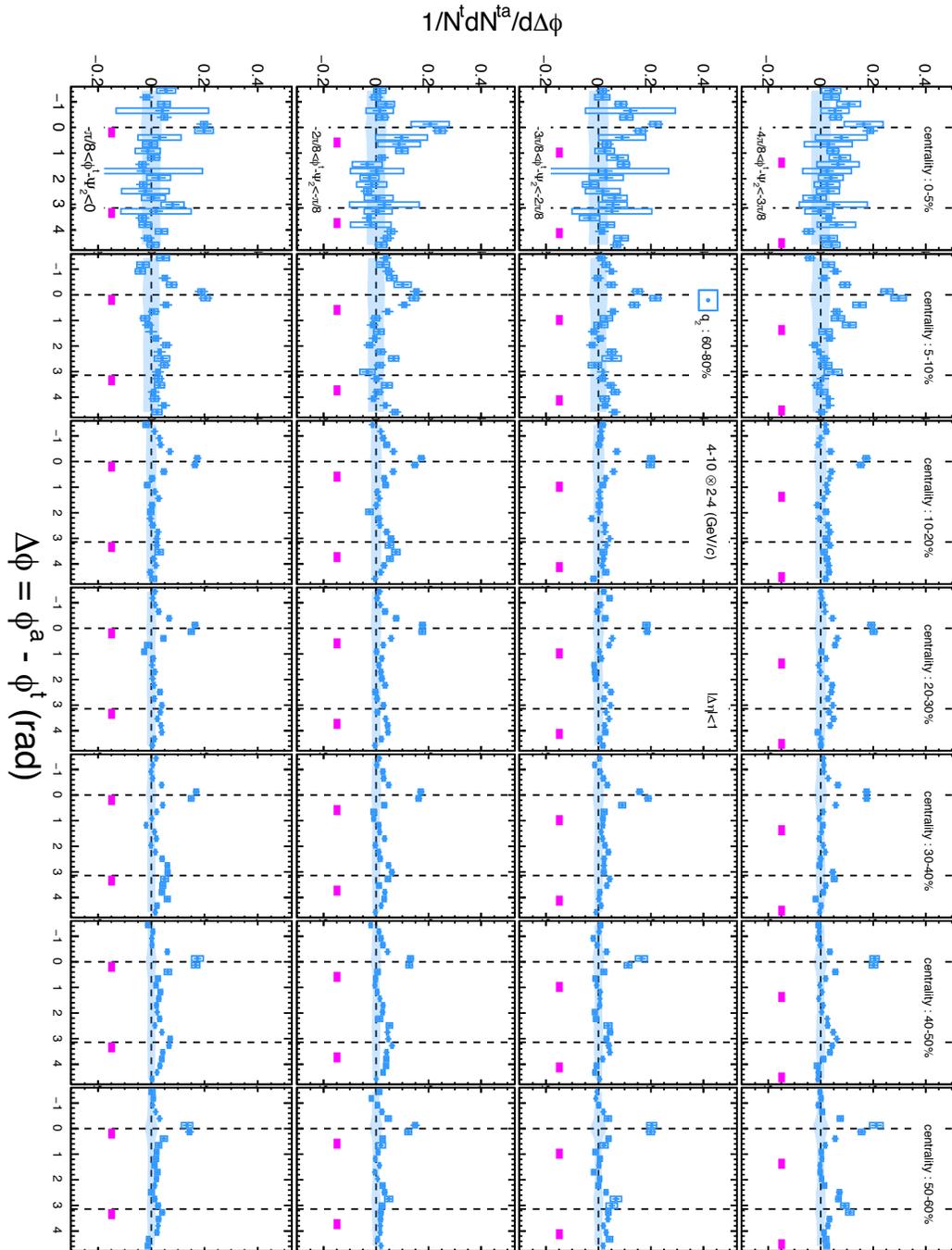
Figure A.37: Azimuthal distribution of correlated yield in $p_T : 4$-$10 \otimes 2$-4 (GeV/c) with trigger angle selection with respect to the second-order event plane in $q_2 : 60 - 80\%$ selected events.
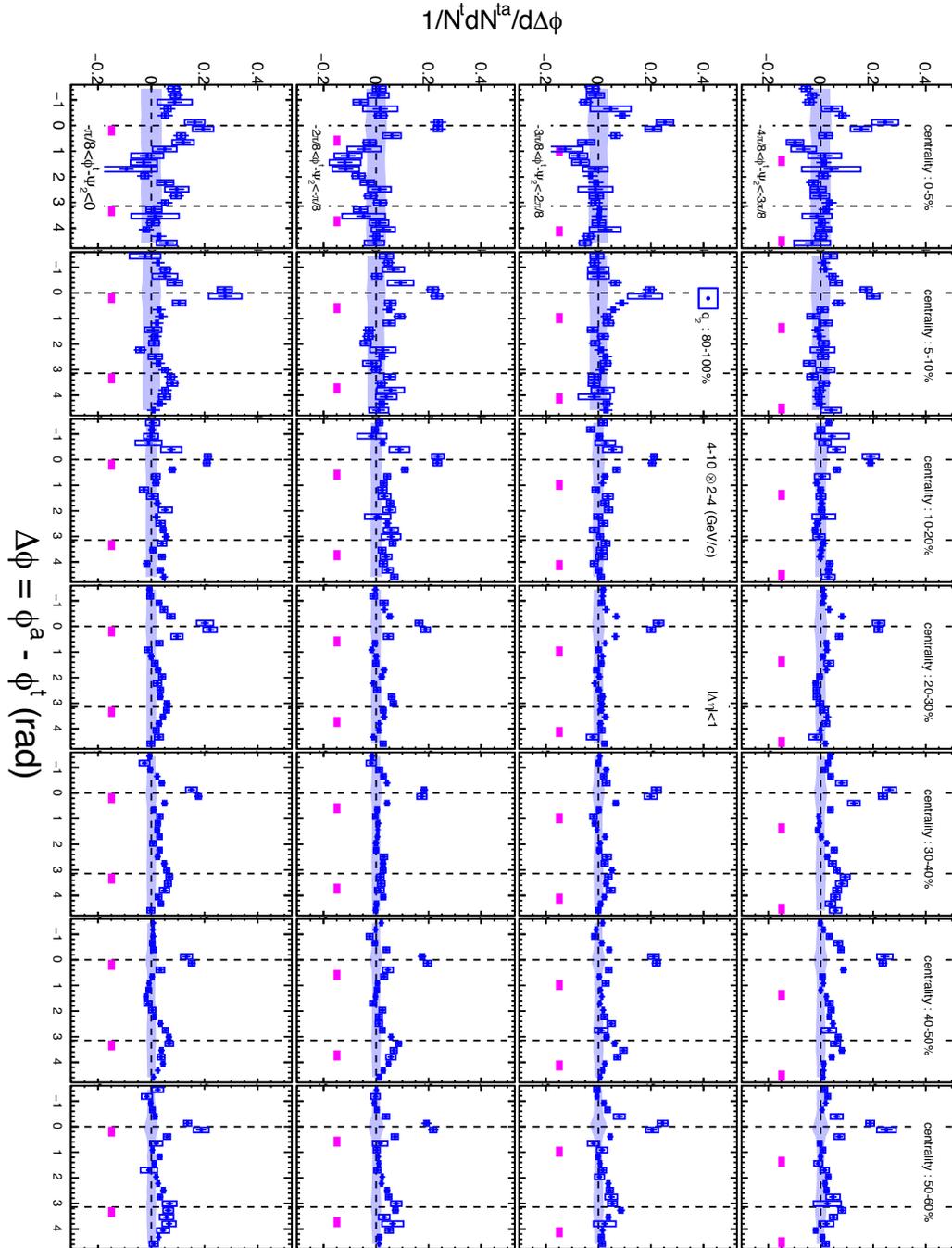
Figure A.38: Azimuthal distribution of correlated yield in $p_T : 4\text{-}10 \otimes 2\text{-}4$ (GeV/c) with trigger angle selection with respect to the second-order event plane in $q_2 : 80 - 100\%$ selected events.
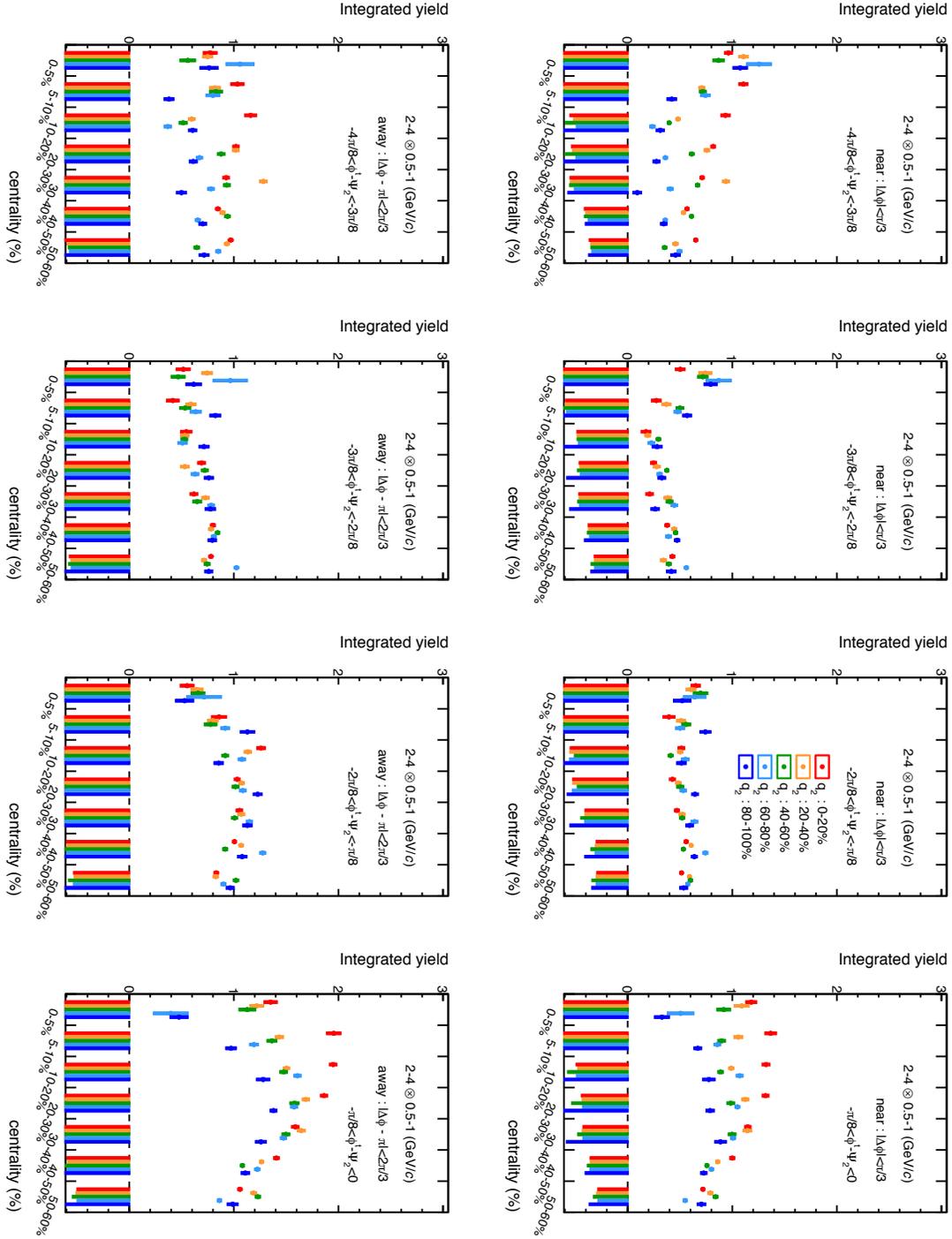
Figure A.39: Centrality and q_2 dependence of integrated yield with p_T : 2-4⊗0.5-1 (GeV/c). (Top row) near side $|\Delta\phi| < \pi/3$, (bottom row) away side $|\Delta\phi| < 2\pi/3$. Trigger angle is from out-of-plane (left) to in-plane (right).
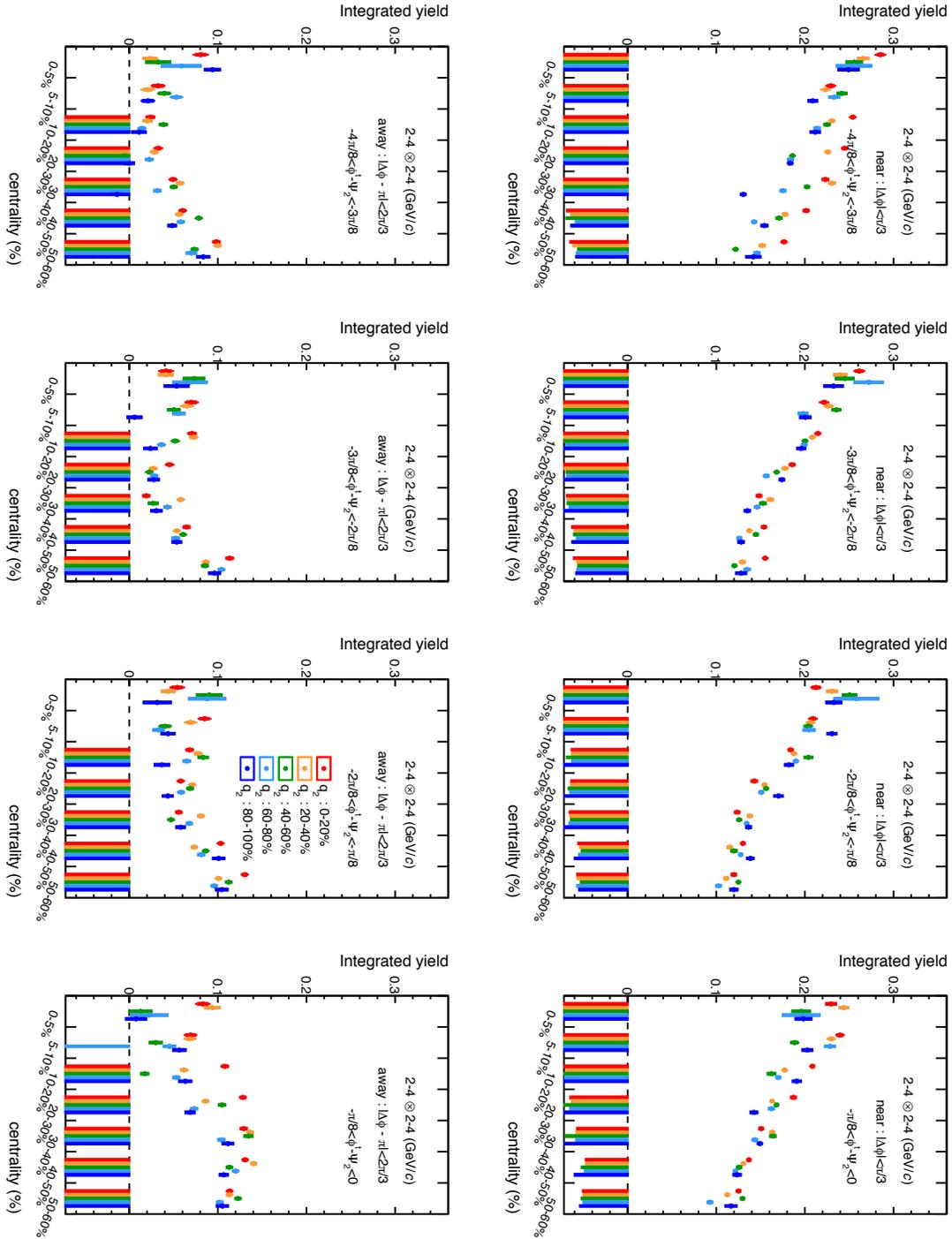
Figure A.40: Centrality and q_2 dependence of integrated yield with p_T : 2-4⊗2-4 (GeV/c). (Top row) near side $|\Delta\phi| < \pi/3$, (bottom row) away side $|\Delta\phi| < 2\pi/3$. Trigger angle is from out-of-plane (left) to in-plane (right).
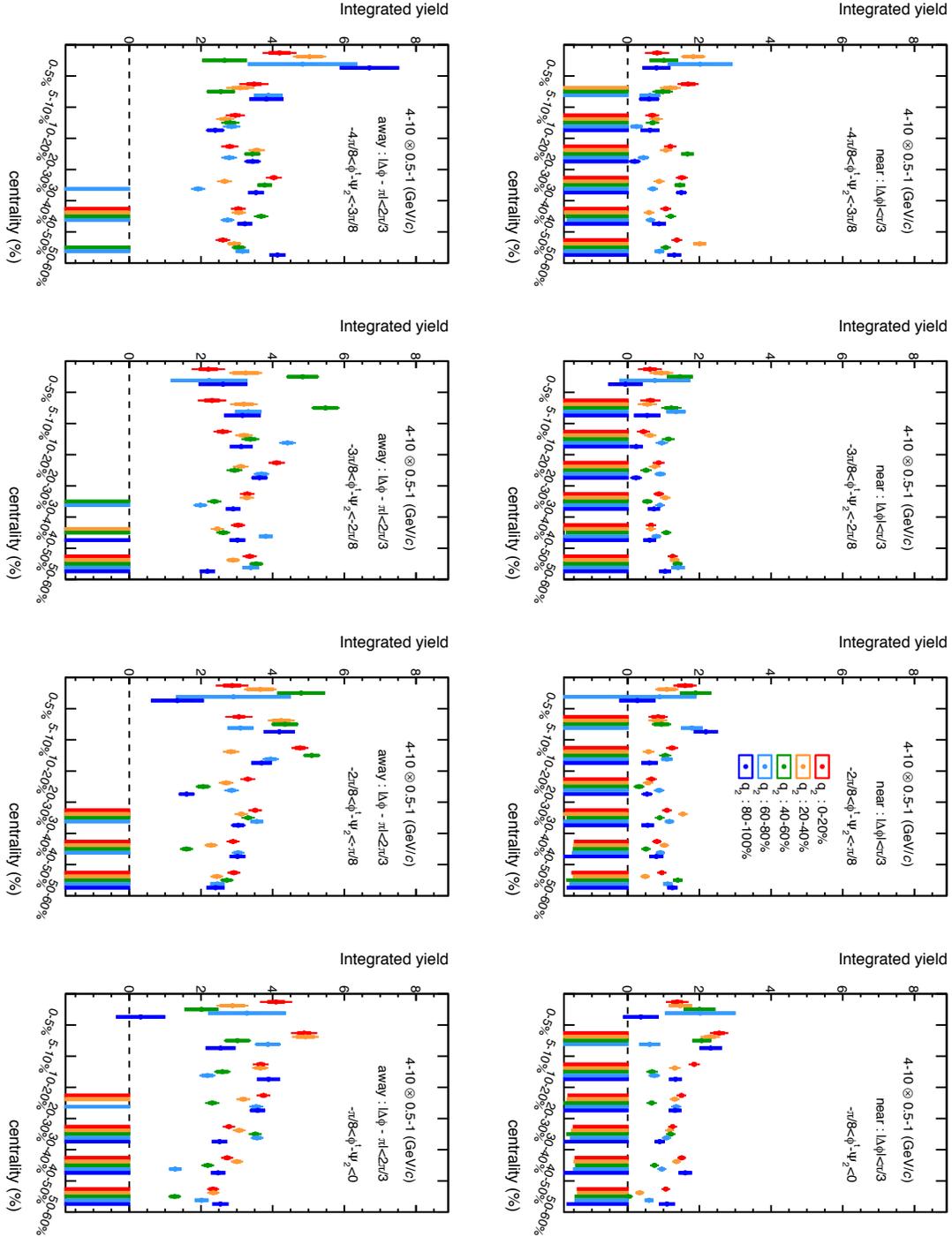
Figure A.41: Centrality and q_2 dependence of integrated yield with $p_T : 4\text{-}10\otimes0.5\text{-}1$ (GeV/c). (Top row) near side $|\Delta\phi| < \pi/3$, (bottom row) away side $|\Delta\phi| < 2\pi/3$. Trigger angle is from out-of-plane (left) to in-plane (right).
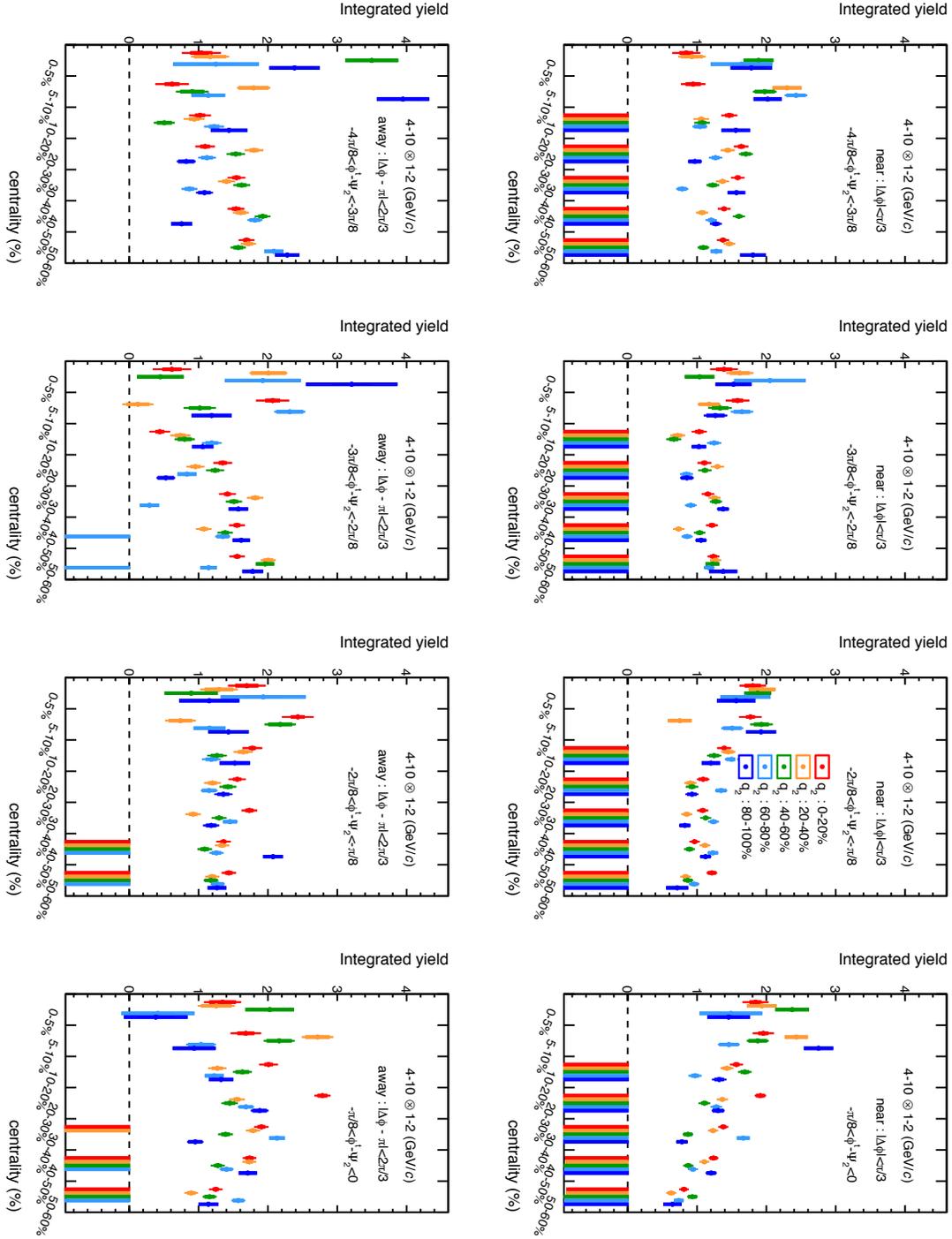
Figure A.42: Centrality and q_2 dependence of integrated yield with p_T : 4-10⊗1-2 (GeV/c). (Top row) near side $|\Delta\phi| < \pi/3$, (bottom row) away side $|\Delta\phi| < 2\pi/3$. Trigger angle is from out-of-plane (left) to in-plane (right).
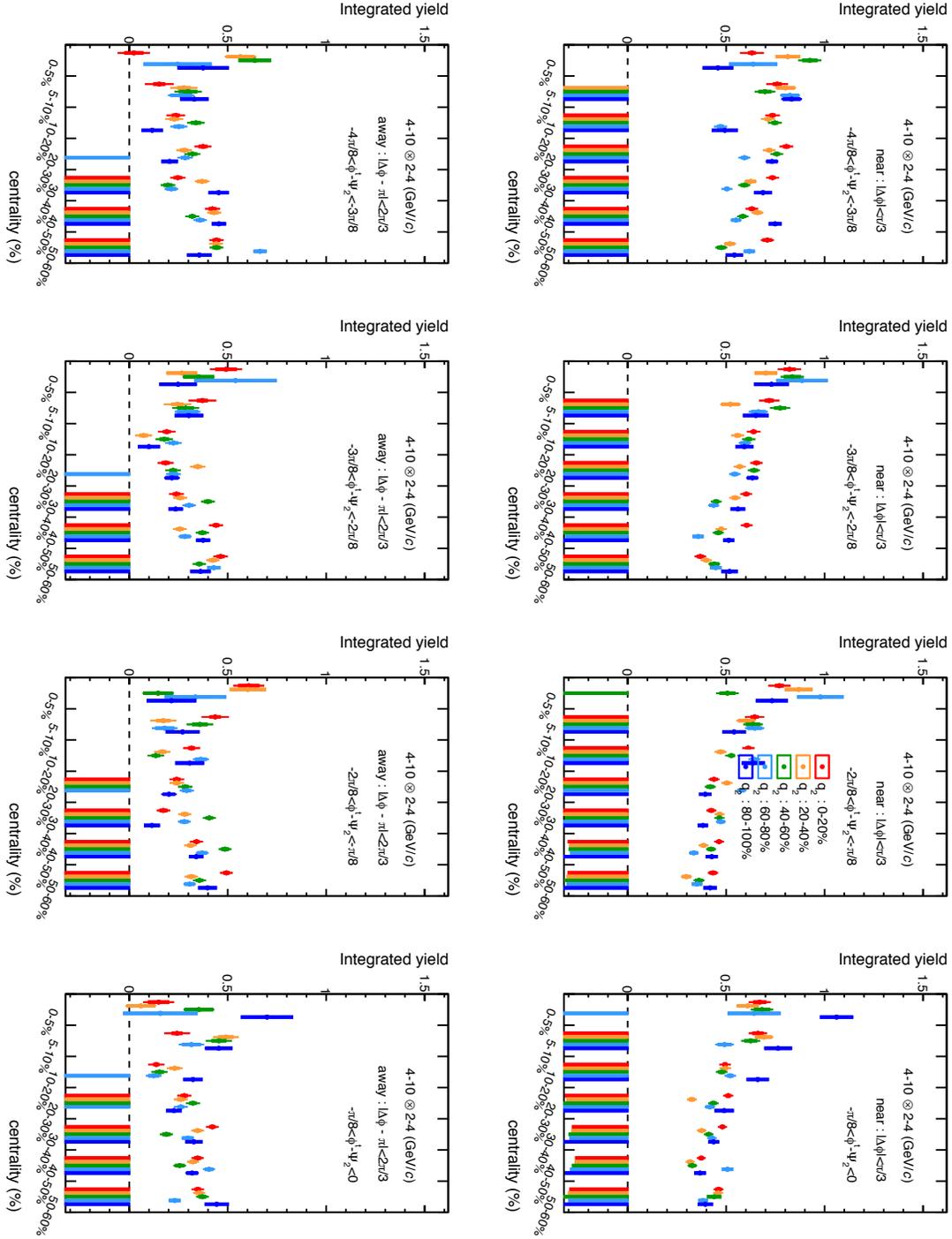
Figure A.43: Centrality and q_2 dependence of integrated yield with p_T : 4-10⊗2-4 (GeV/c). (Top row) near side $|\Delta\phi| < \pi/3$, (bottom row) away side $|\Delta\phi| < 2\pi/3$. Trigger angle is from out-of-plane (left) to in-plane (right).

A.3.1 Scaling with path length

Fig.A.44-A.47 show integrated yield as a function of path length simulated by Glauber Monte-Carlo.
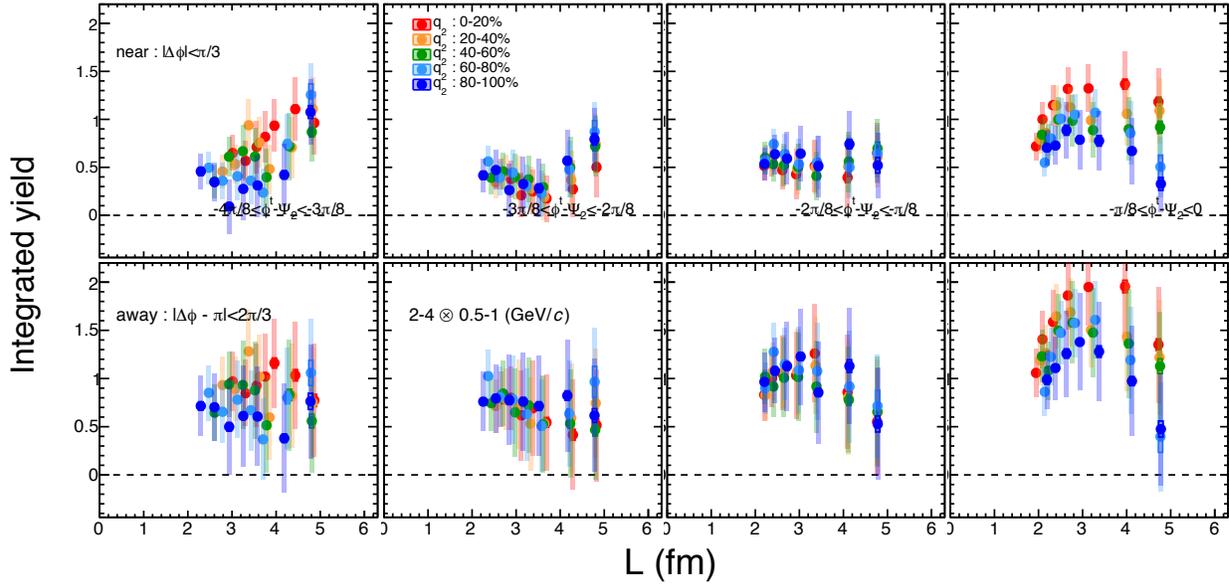
Figure A.44: Integrated yield as a function of path length L with $p_T : 2\text{-}4 \otimes 0.5\text{-}1$ (GeV/c) in the near side (top) and away side (bottom).

A.4 Azimuthal anisotropy of correlated yield

Fig.A.48 and Fig.A.49 show p_T dependence of $v_n^{Y,corr}$ as a function of p_T with q_2 selections.

A.5 Asymmetry of near-side and away-side structure

Fig.A.50-A.59 show peak asymmetry as a function of trigger angle ϕ_s in each centrality and q_2 bin.
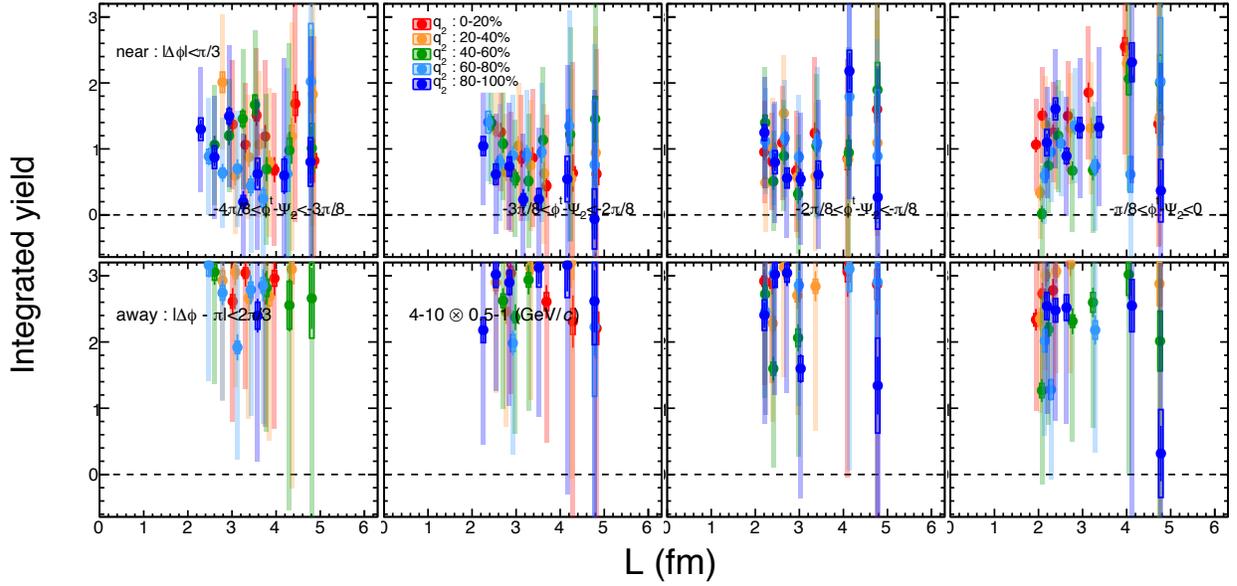
Figure A.45: Integrated yield as a function of path length L with $p_T : 4\text{-}10 \otimes 0.5\text{-}1$ (GeV/c) in the near side (top) and away side (bottom).
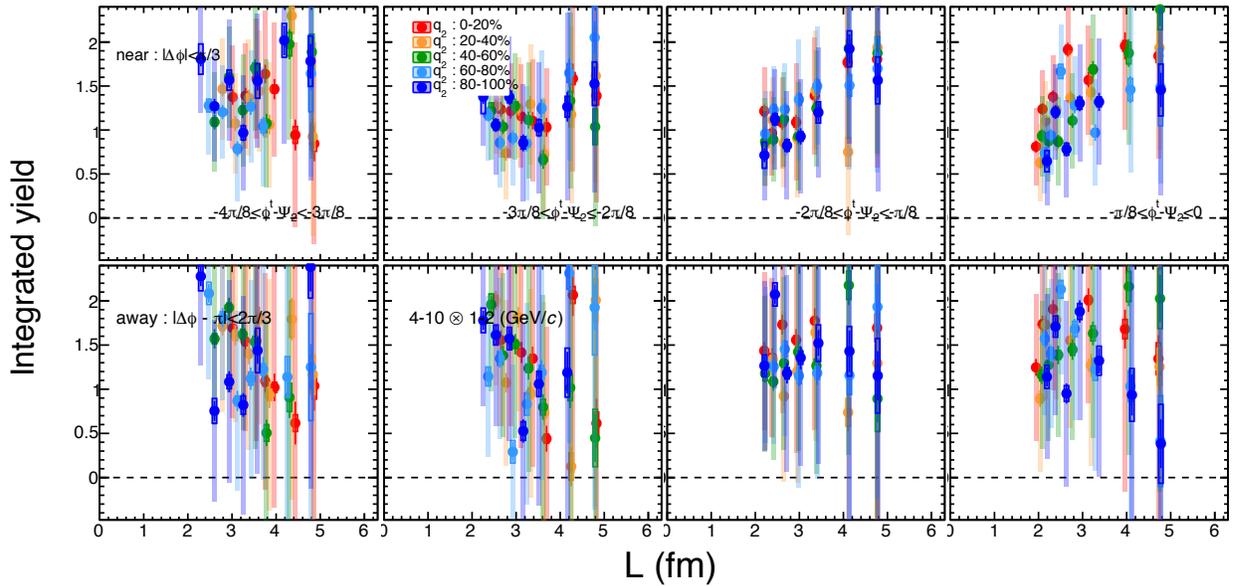
Figure A.46: Integrated yield as a function of path length L with $p_T : 4\text{-}10 \otimes 1\text{-}2$ (GeV/c) in the near side (top) and away side (bottom).
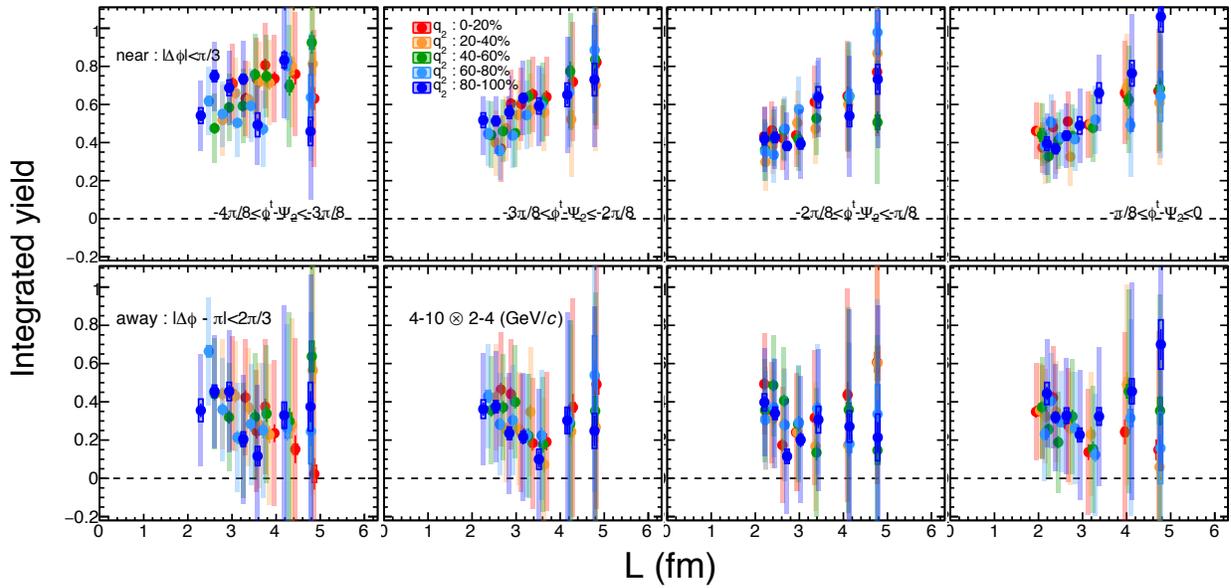
Figure A.47: Integrated yield as a function of path length L with p_T : 4-10⊗2-4 (GeV/c) in the near side (top) and away side (bottom).
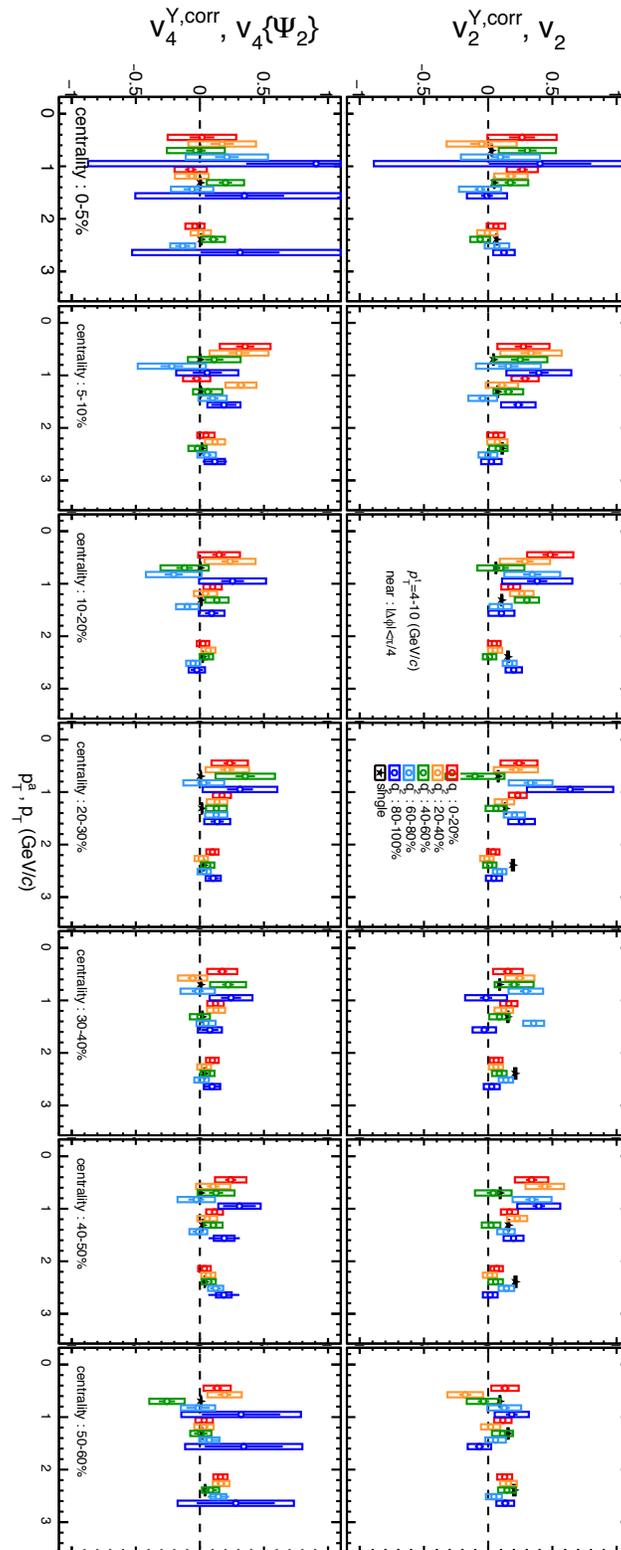
Figure A.48: Azimuthal anisotropy of correlated yield with p_T : 4-10 (GeV/c) in the near side with q_2 selections.
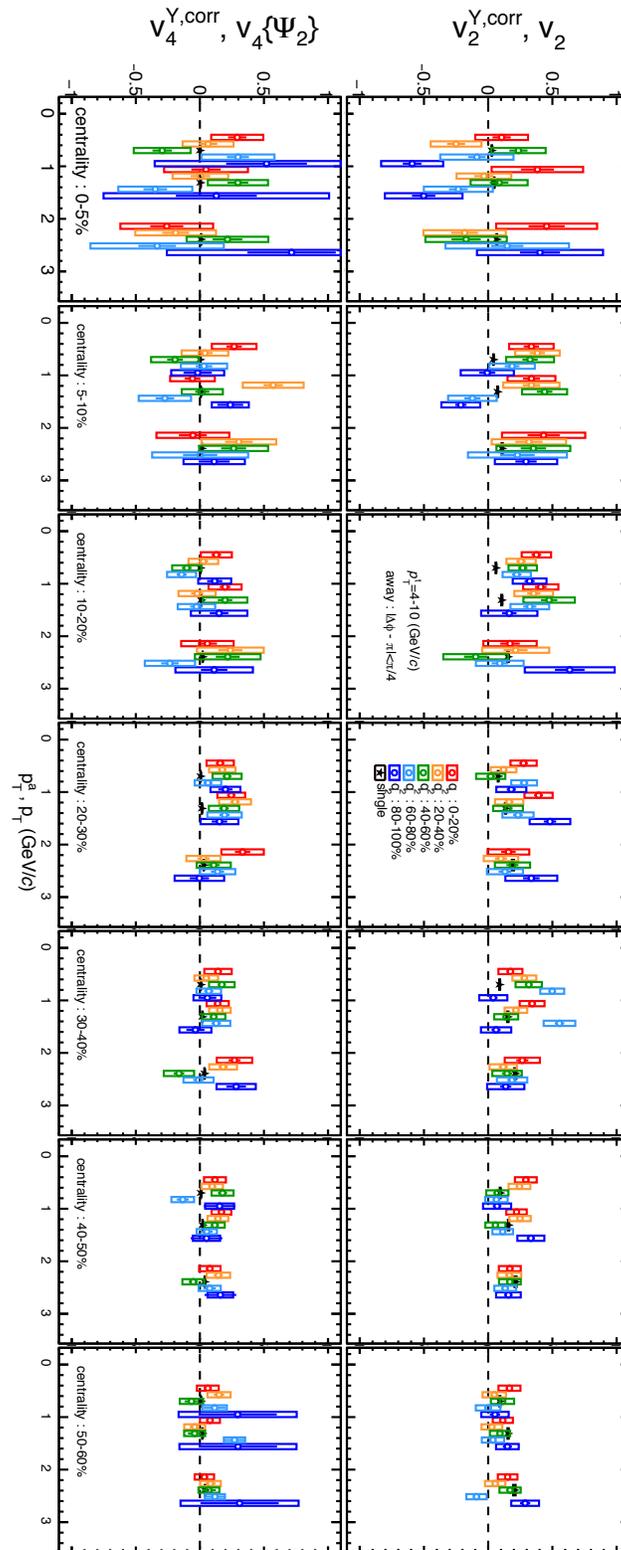
Figure A.49: Azimuthal anisotropy of correlated yield with p_T : 4-10 (GeV/c) in the away side with q_2 selections.
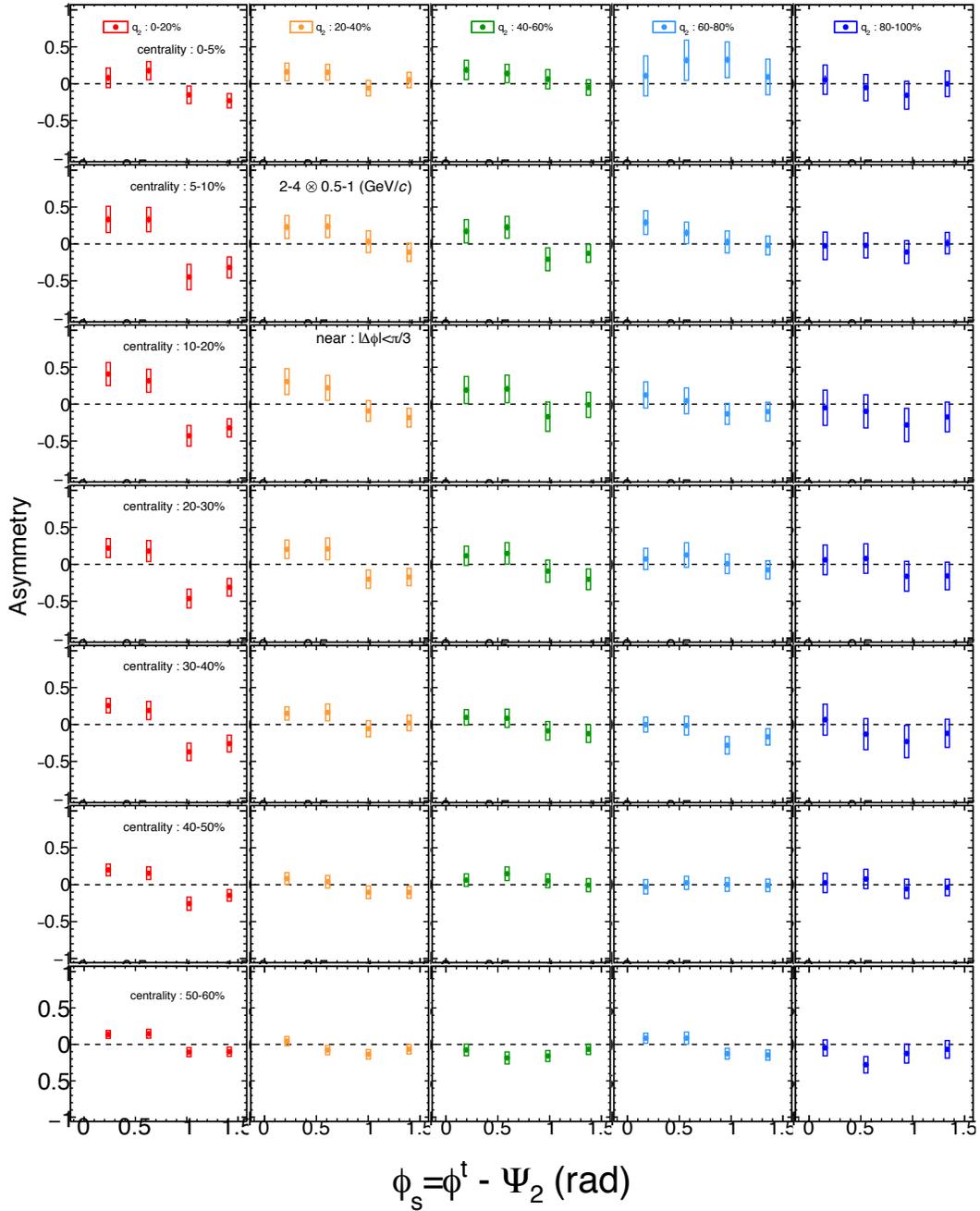
Figure A.50: Trigger angle ϕ_s dependence of near-side asymmetry with p_T : 2-4⊗0.5-1 (GeV/c) with q_2 selections from q_2 :0-20 % (left) to q_2 :80-100 % (right) in each centrality bin from 0-5 % (top) to 50-60 % (bottom).
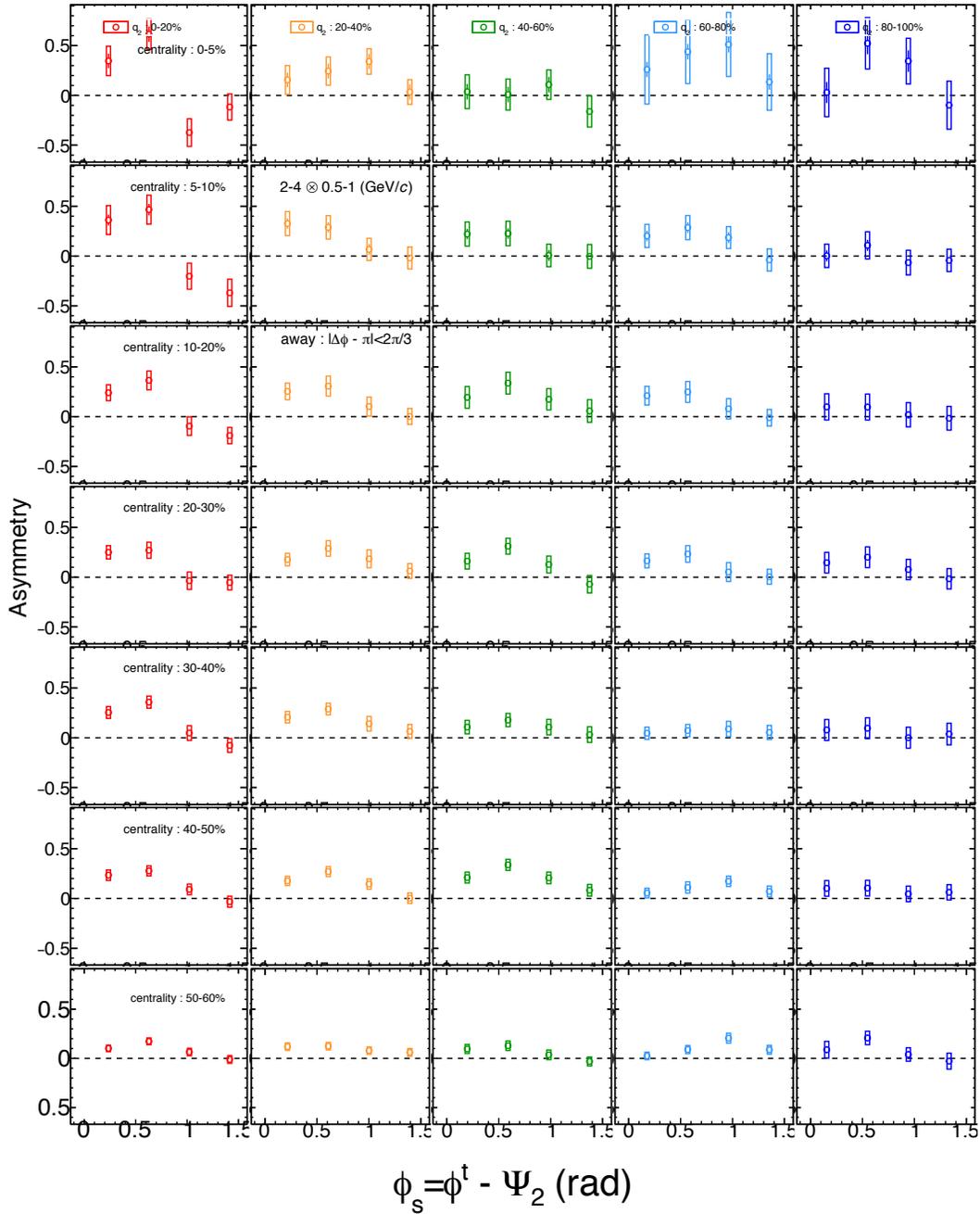
Figure A.51: Trigger angle ϕ_s dependence of away-side asymmetry with p_T : 2-4⊗0.5-1 (GeV/c) with q_2 selections from q_2 :0-20 % (left) to q_2 :80-100 % (right) in each centrality bin from 0-5 % (top) to 50-60 % (bottom).
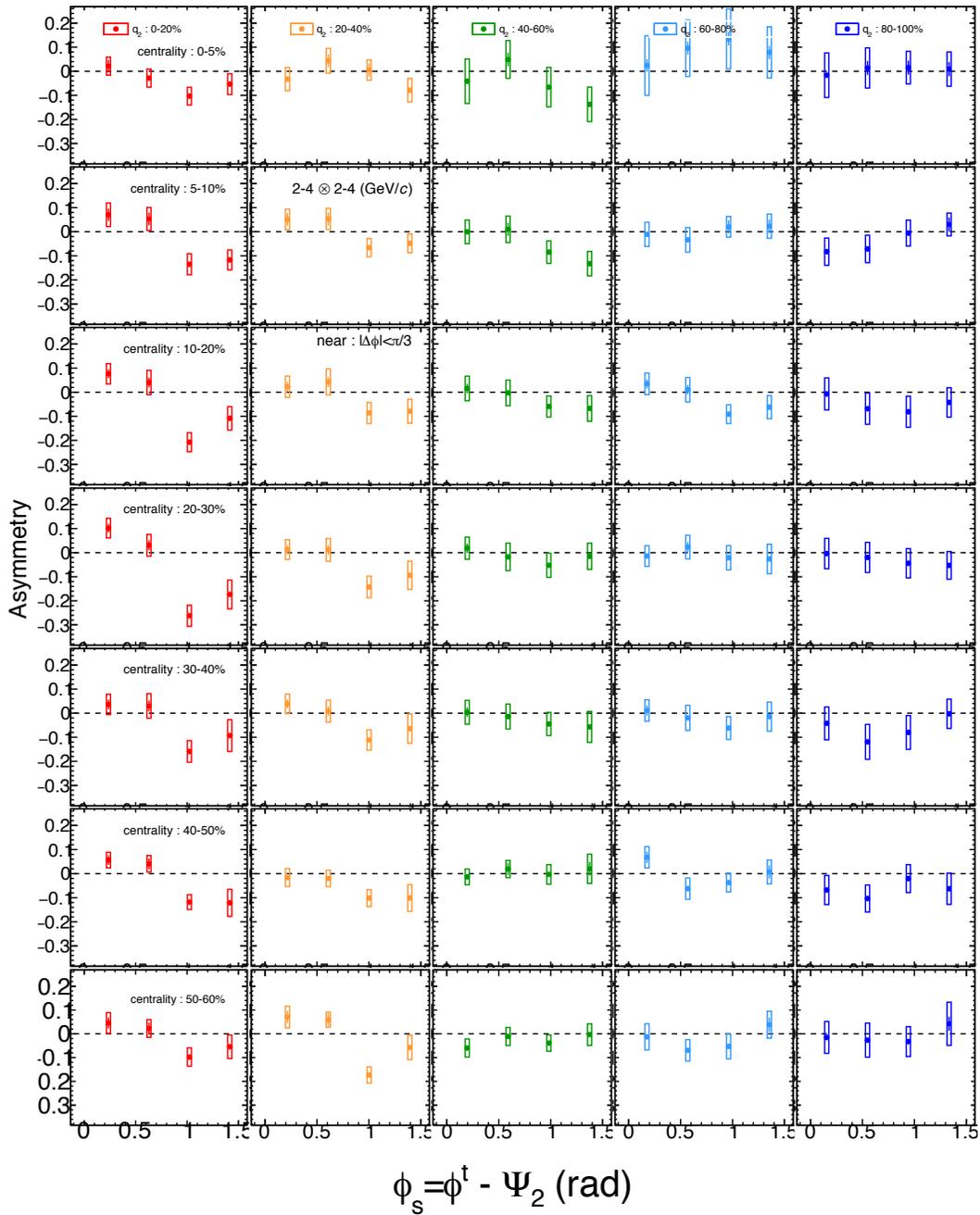
Figure A.52: Trigger angle ϕ_s dependence of near-side asymmetry with p_T : 2-4⊗2-4 (GeV/c) with q_2 selections from q_2 :0-20 % (left) to q_2 :80-100 % (right) in each centrality bin from 0-5 % (top) to 50-60 % (bottom).
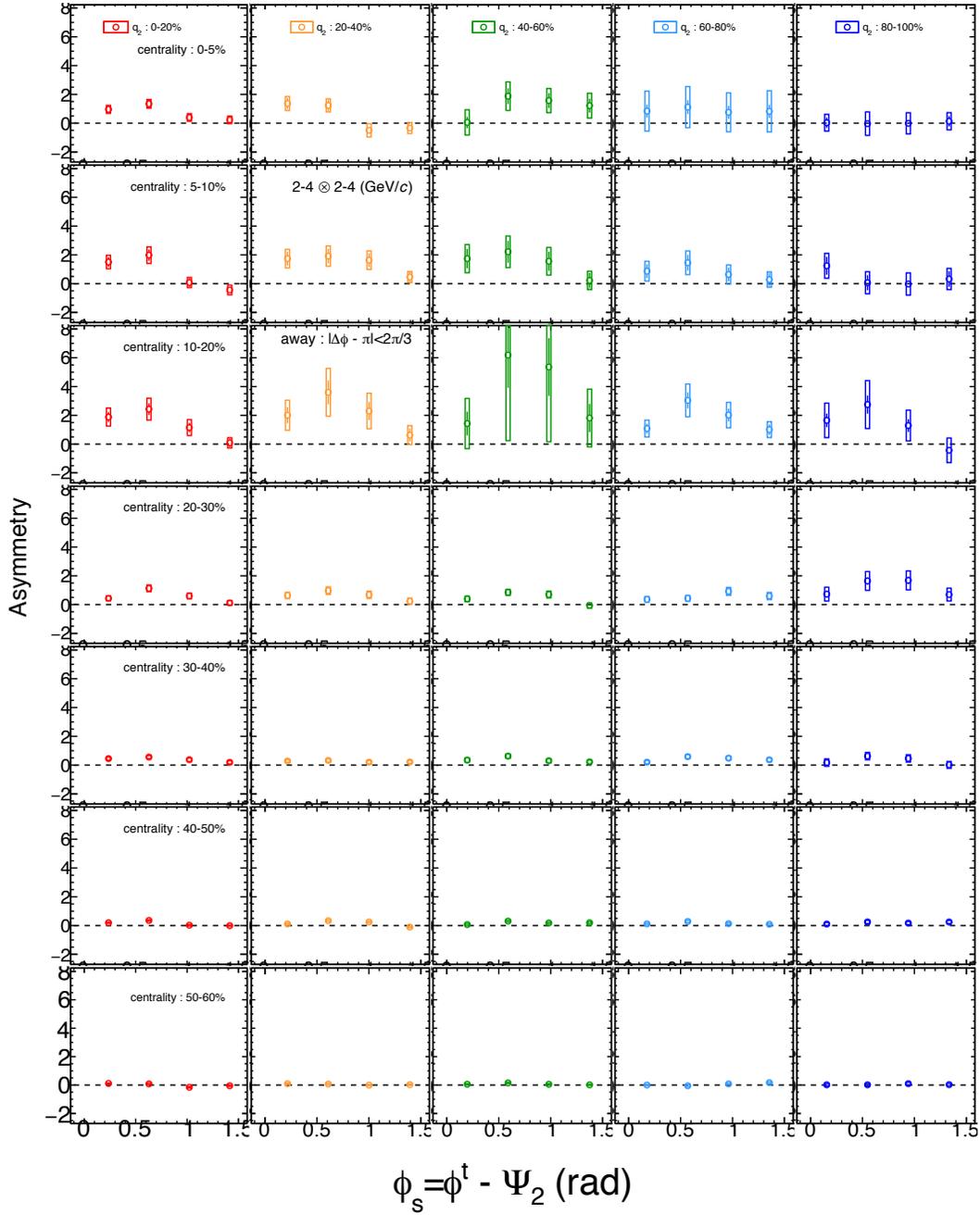
Figure A.53: Trigger angle ϕ_s dependence of away-side asymmetry with p_T : 2-4⊗2-4 (GeV/c) with q_2 selections from q_2 :0-20 % (left) to q_2 :80-100 % (right) in each centrality bin from 0-5 % (top) to 50-60 % (bottom).
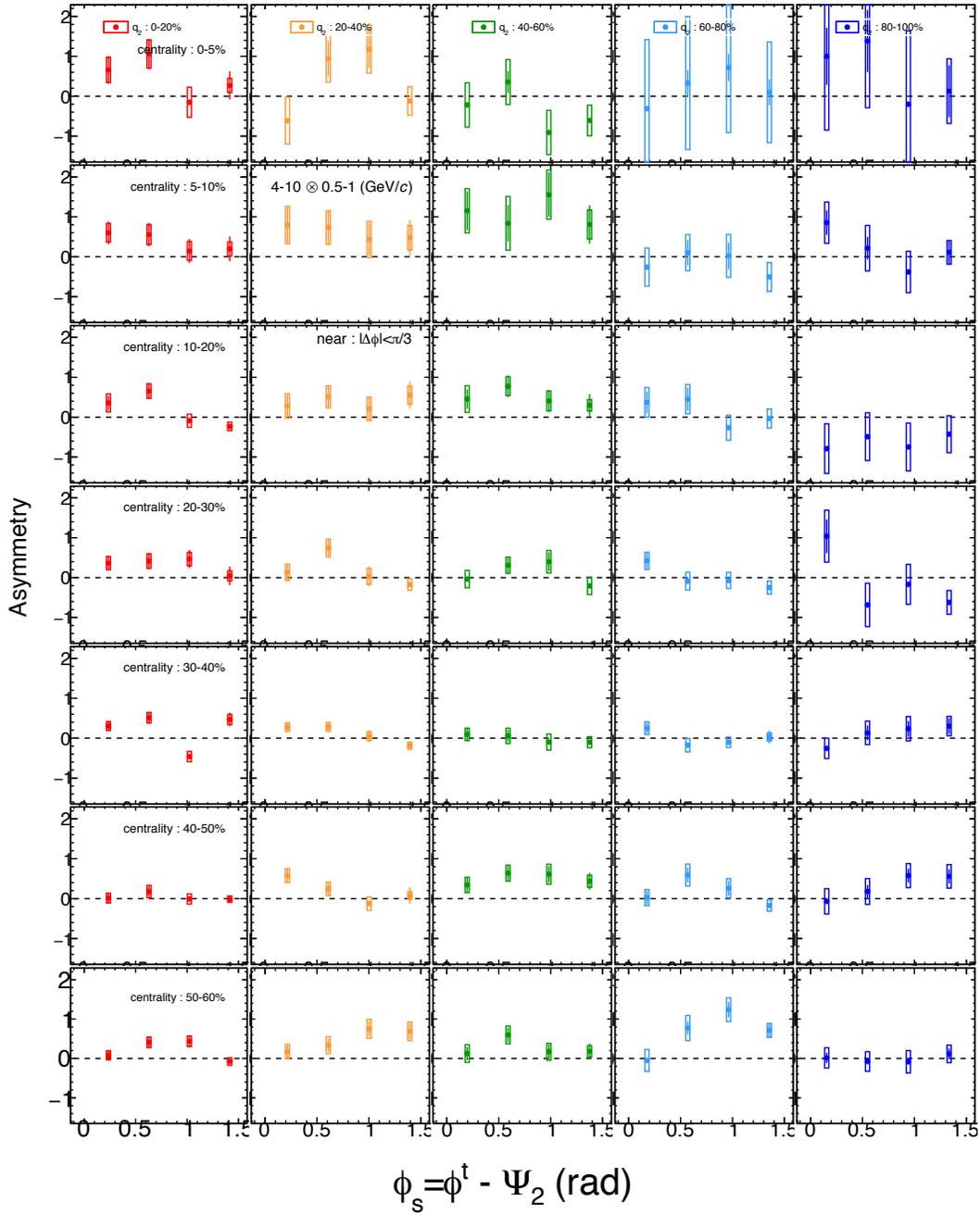
Figure A.54: Trigger angle ϕ_s dependence of near-side asymmetry with p_T : 4-10⊗0.5-1 (GeV/c) with q_2 selections from q_2 :0-20 % (left) to q_2 :80-100 % (right) in each centrality bin from 0-5 % (top) to 50-60 % (bottom).
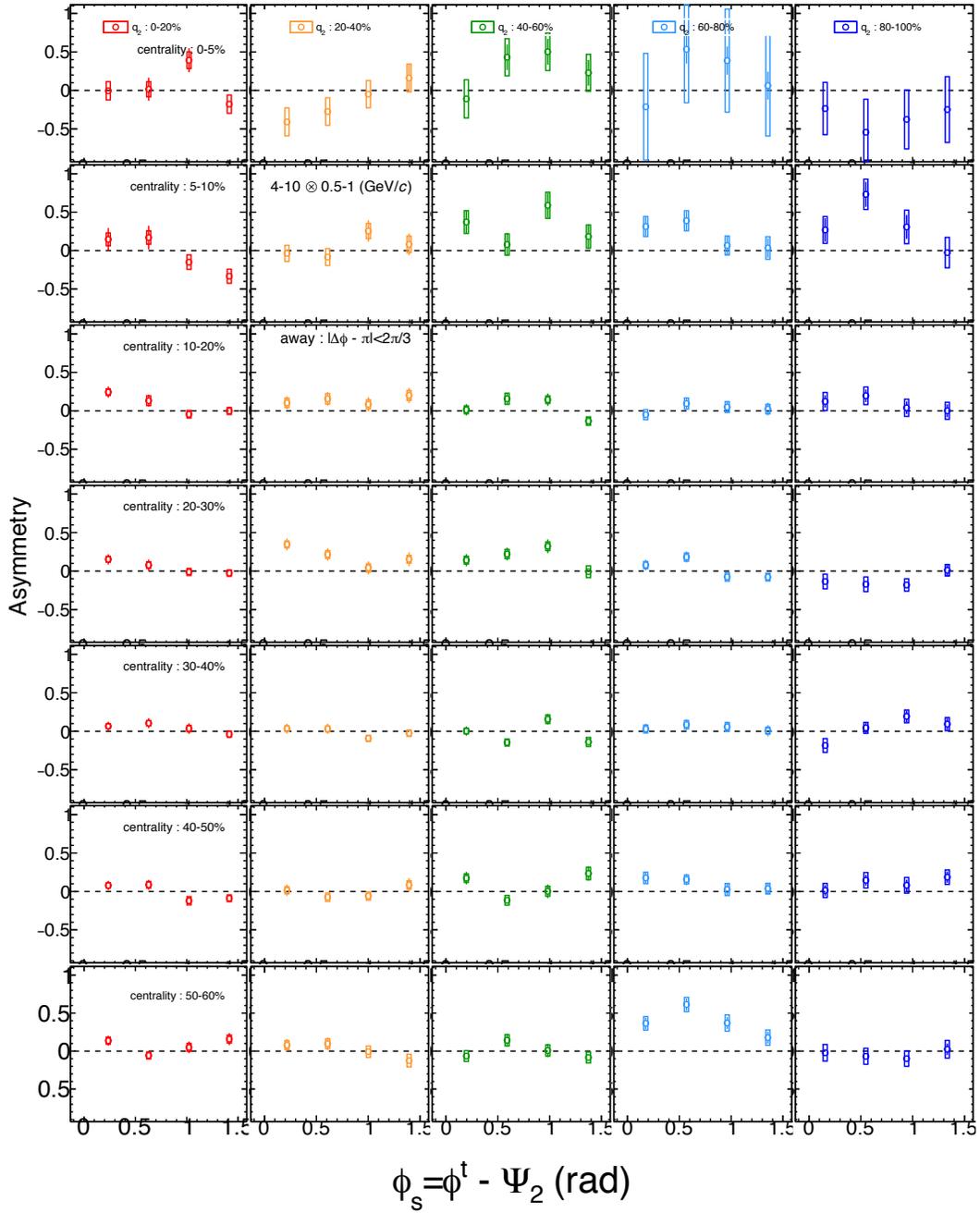
Figure A.55: Trigger angle ϕ_s dependence of away-side asymmetry with p_T : 4-10⊗0.5-1 (GeV/c) with q_2 selections from q_2 :0-20 % (left) to q_2 :80-100 % (right) in each centrality bin from 0-5 % (top) to 50-60 % (bottom).
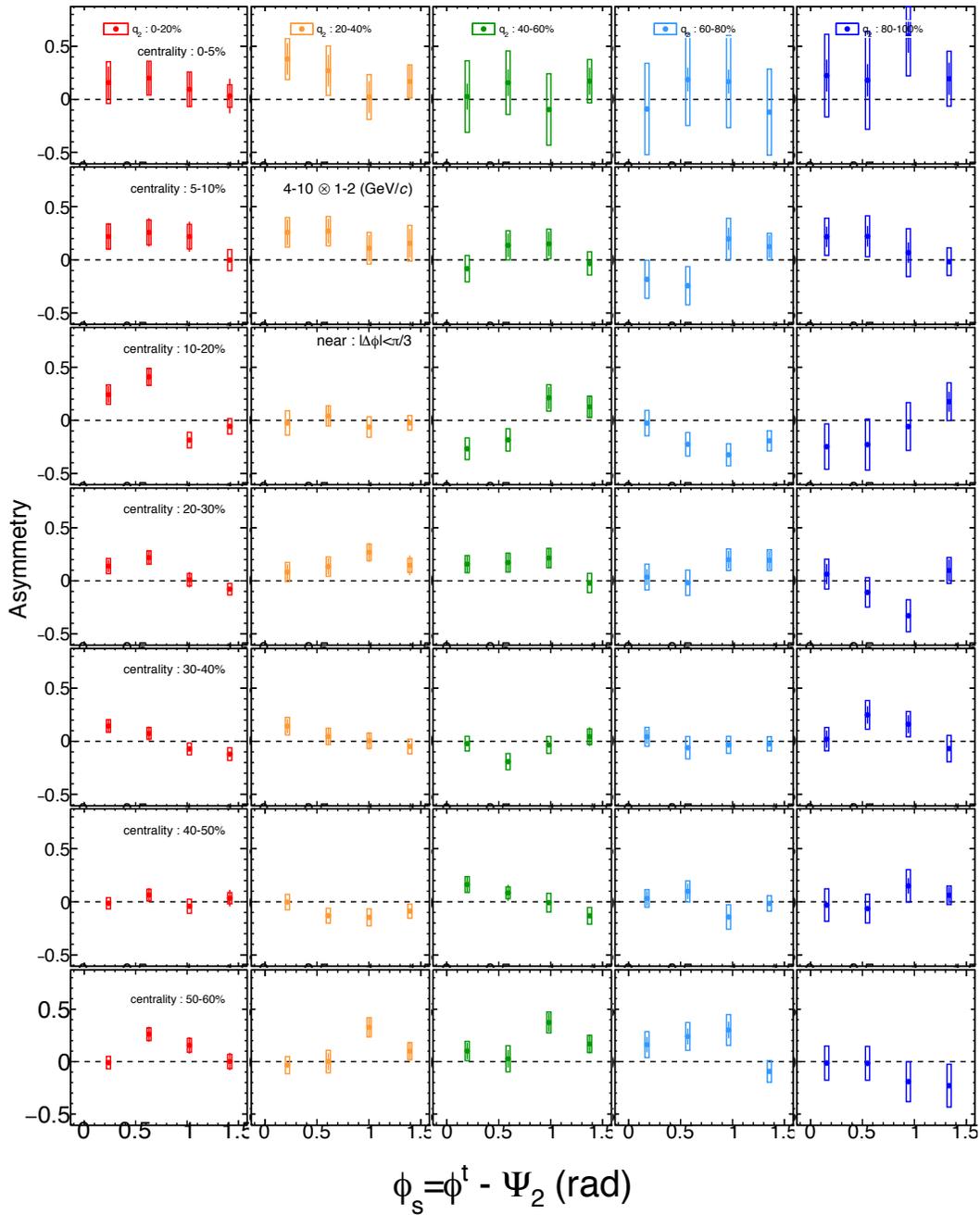
Figure A.56: Trigger angle ϕ_s dependence of near-side asymmetry with $p_T : 4\text{-}10 \otimes 1\text{-}2$ (GeV/c) with q_2 selections from $q_2 :0\text{-}20$ % (left) to $q_2 :80\text{-}100$ % (right) in each centrality bin from 0-5 % (top) to 50-60 % (bottom).
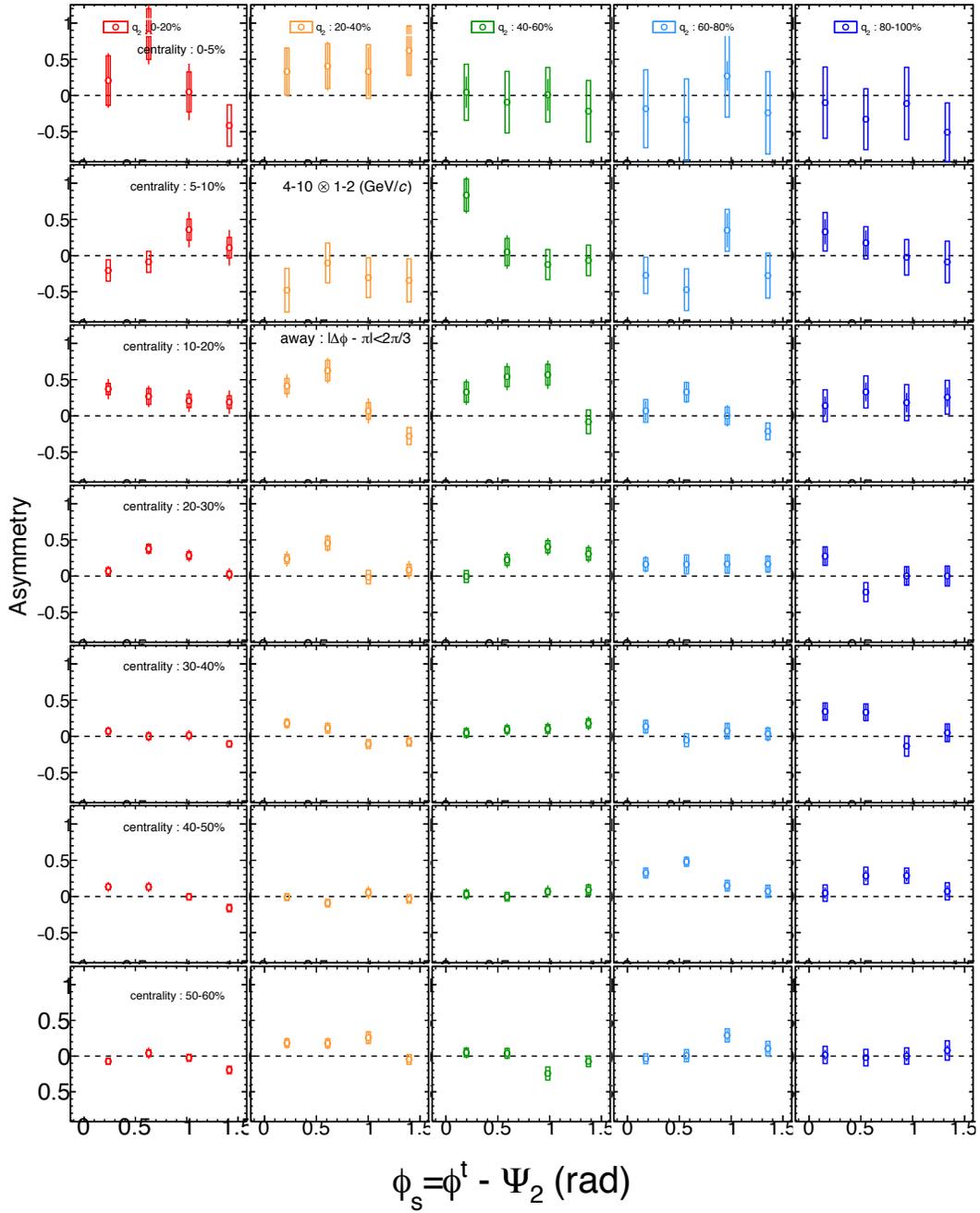
Figure A.57: Trigger angle ϕ_s dependence of away-side asymmetry with p_T : 4-10⊗1-2 (GeV/c) with q_2 selections from q_2 :0-20 % (left) to q_2 :80-100 % (right) in each centrality bin from 0-5 % (top) to 50-60 % (bottom).
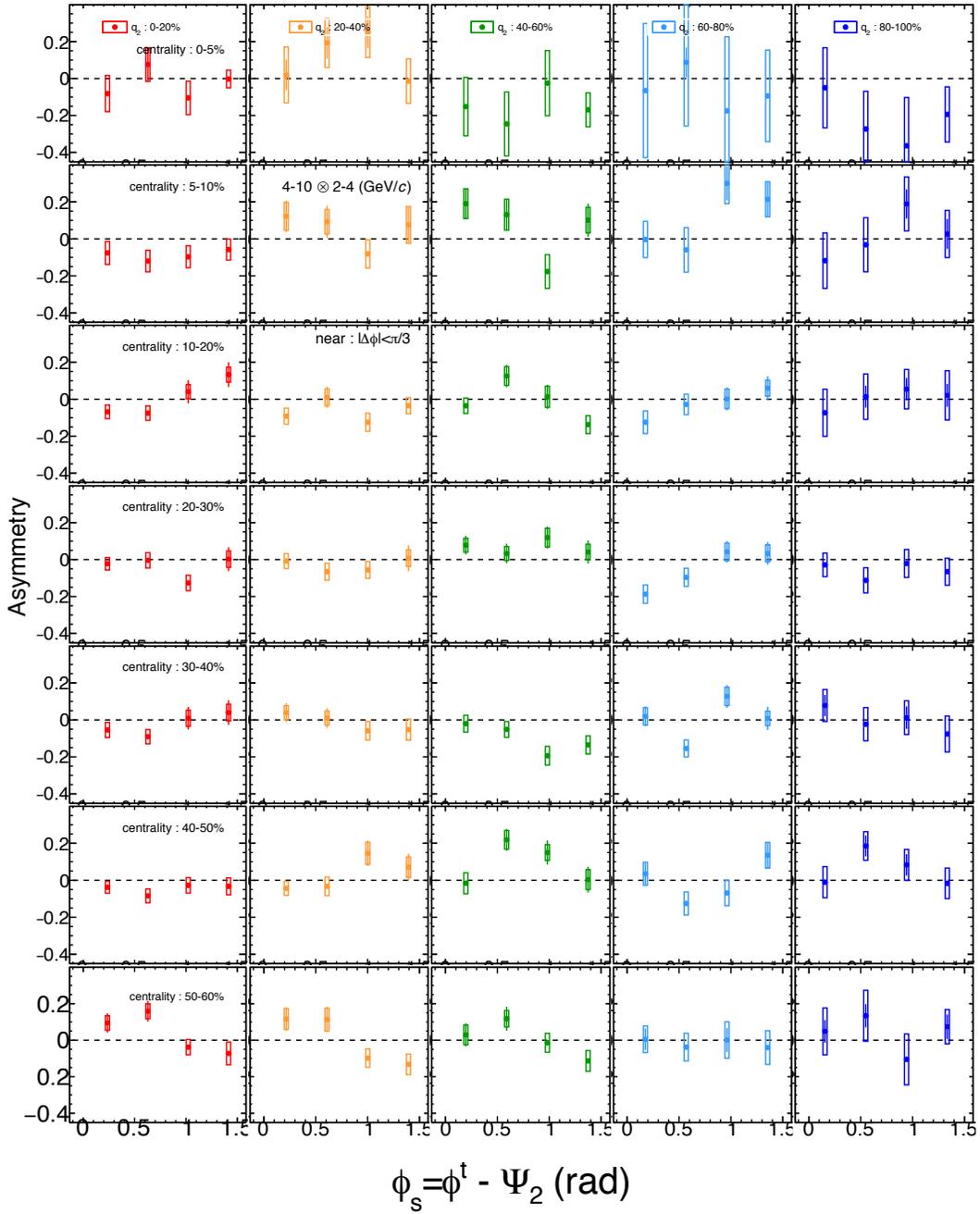
Figure A.58: Trigger angle ϕ_s dependence of near-side asymmetry with p_T : 4-10⊗2-4 (GeV/c) with q_2 selections from q_2 :0-20 % (left) to q_2 :80-100 % (right) in each centrality bin from 0-5 % (top) to 50-60 % (bottom).
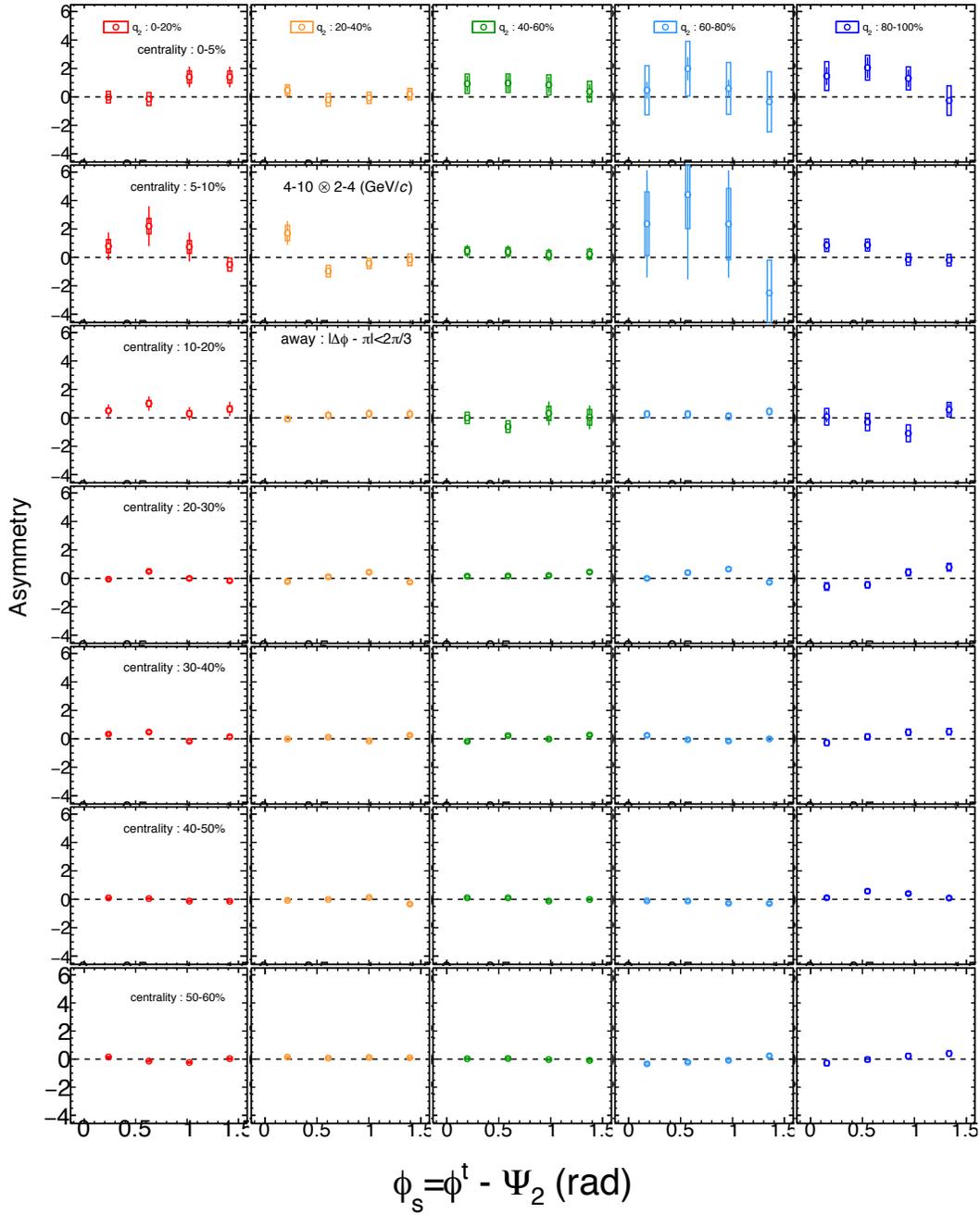
Figure A.59: Trigger angle ϕ_s dependence of away-side asymmetry with p_T : 4-10⊗2-4 (GeV/c) with q_2 selections from q_2 :0-20 % (left) to q_2 :80-100 % (right) in each centrality bin from 0-5 % (top) to 50-60 % (bottom).

Appendix B

Systematic uncertainties of correlations

B.1   Systematics of v_2 for background reconstruction

B.2   Systematics of event-plane alignment in event mixing

B.3   Systematics of ZYAM

B.4   Fraction of square of systematics
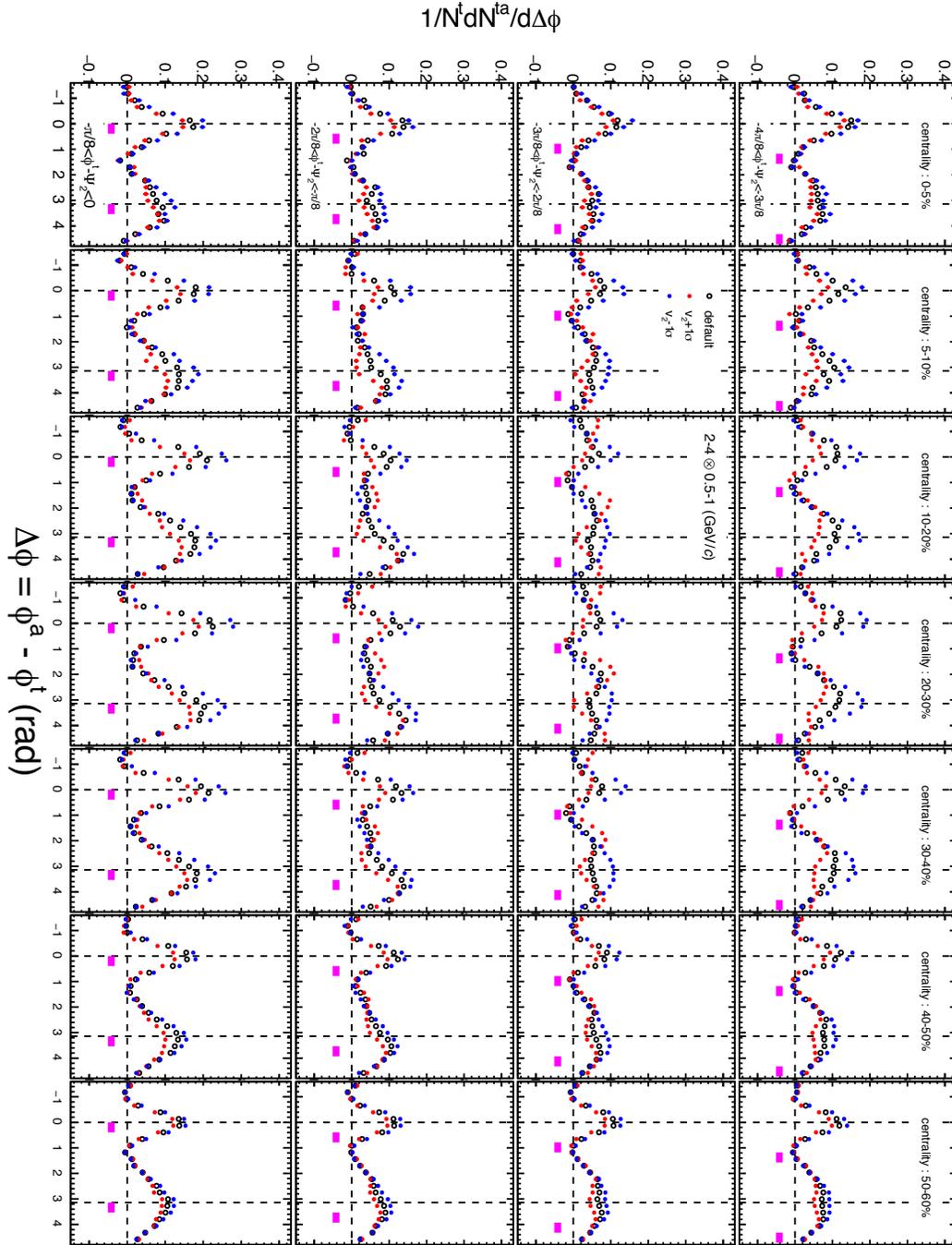
Figure B.1: Azimuthal distributions of correlated yield with subtracting $v_2 \pm 1\sigma$ with $p_T^t \otimes p_T^a =$ 2-4⊗0.5-1 (GeV/c).
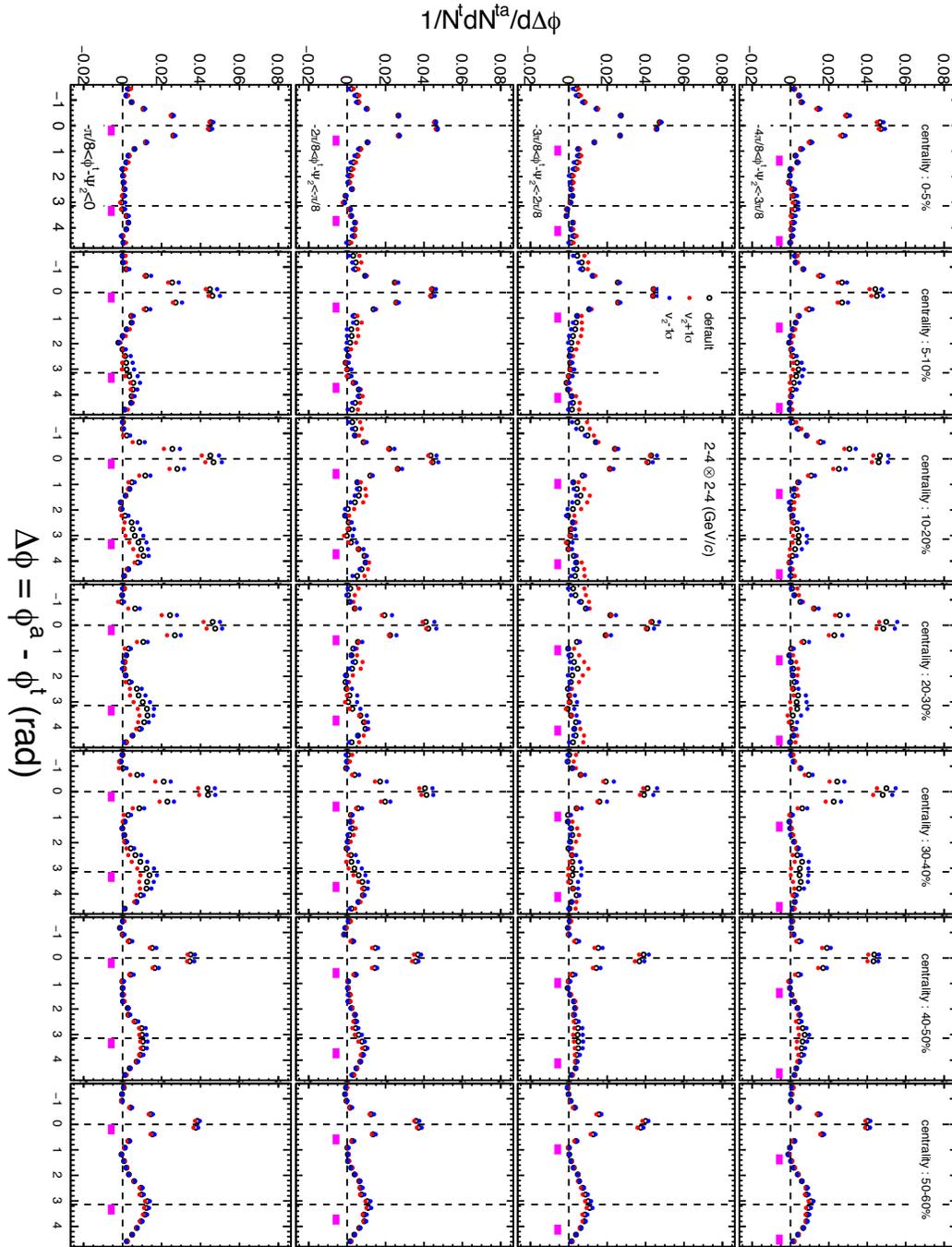
Figure B.2: Azimuthal distributions of correlated yield with subtracting $v_2 \pm 1\sigma$ with $p_T^t \otimes p_T^a = $ 2-4⊗2-4 (GeV/c).
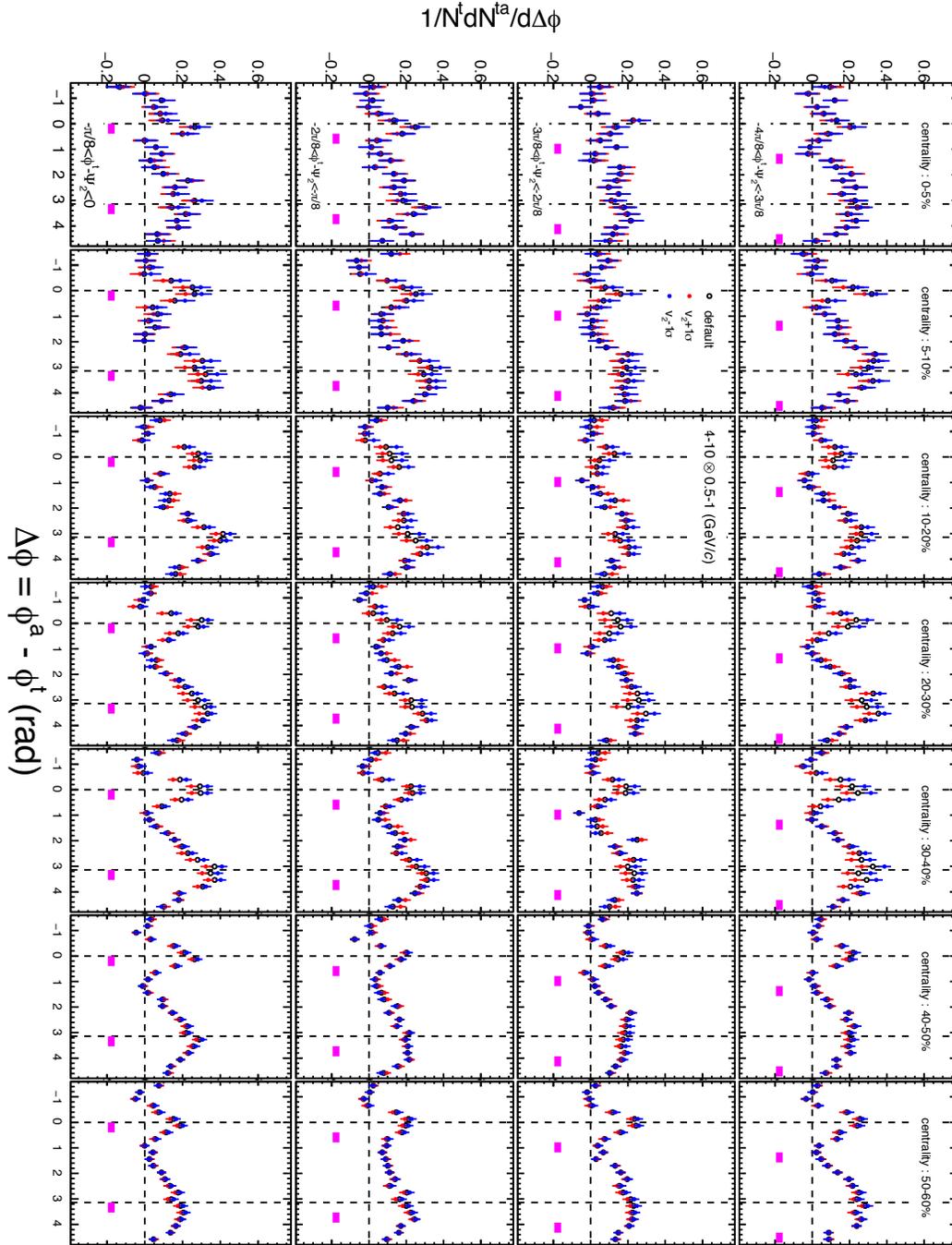
Figure B.3: Azimuthal distributions of correlated yield with subtracting $v_2 \pm 1\sigma$ with $p_T^t \otimes p_T^a = 4\text{-}10 \otimes 0.5\text{-}1$ (GeV/c).
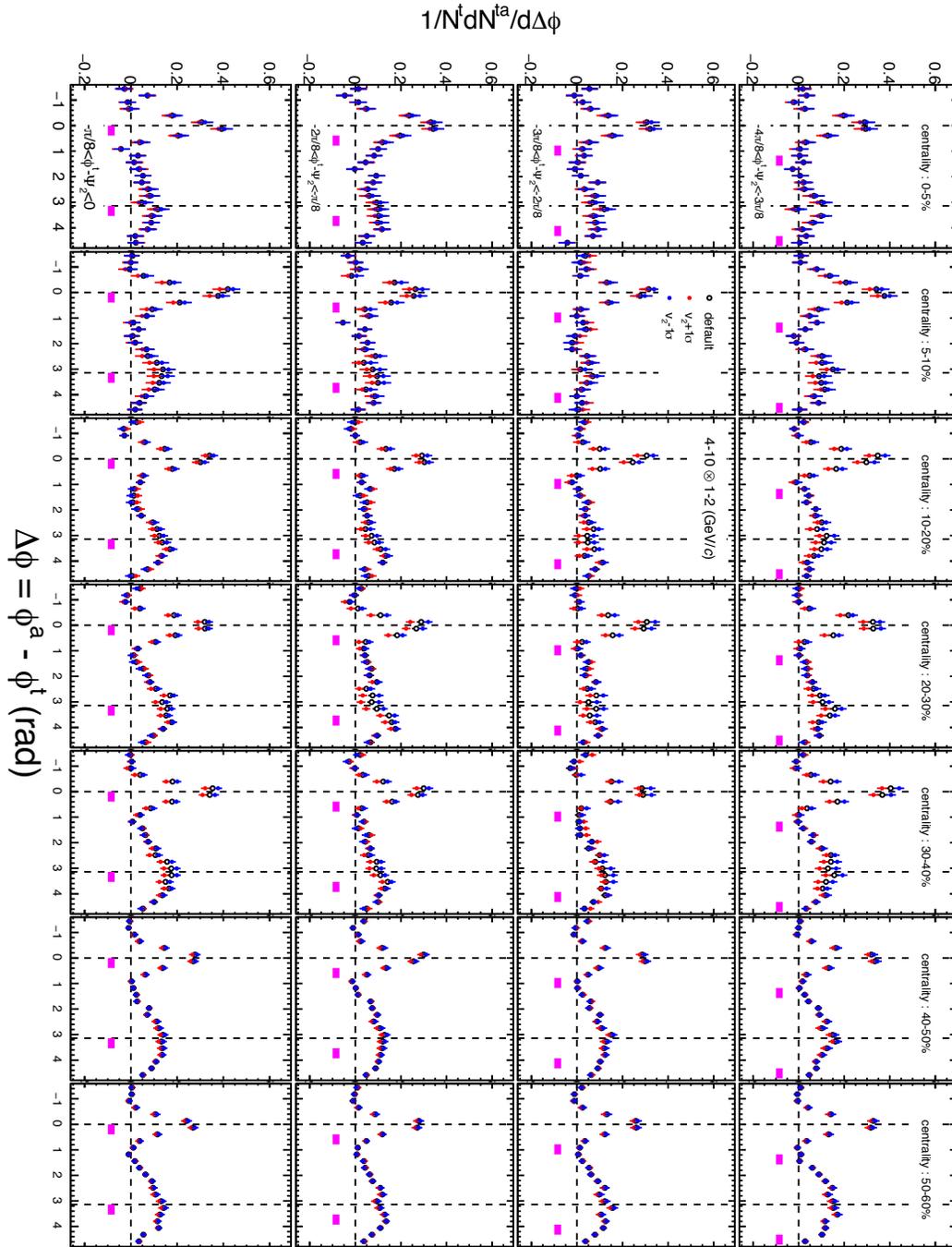
Figure B.4: Azimuthal distributions of correlated yield with subtracting $v_2 \pm 1\sigma$ with $p_T^t \otimes p_T^a = $ 4-10⊗1-2 (GeV/c).
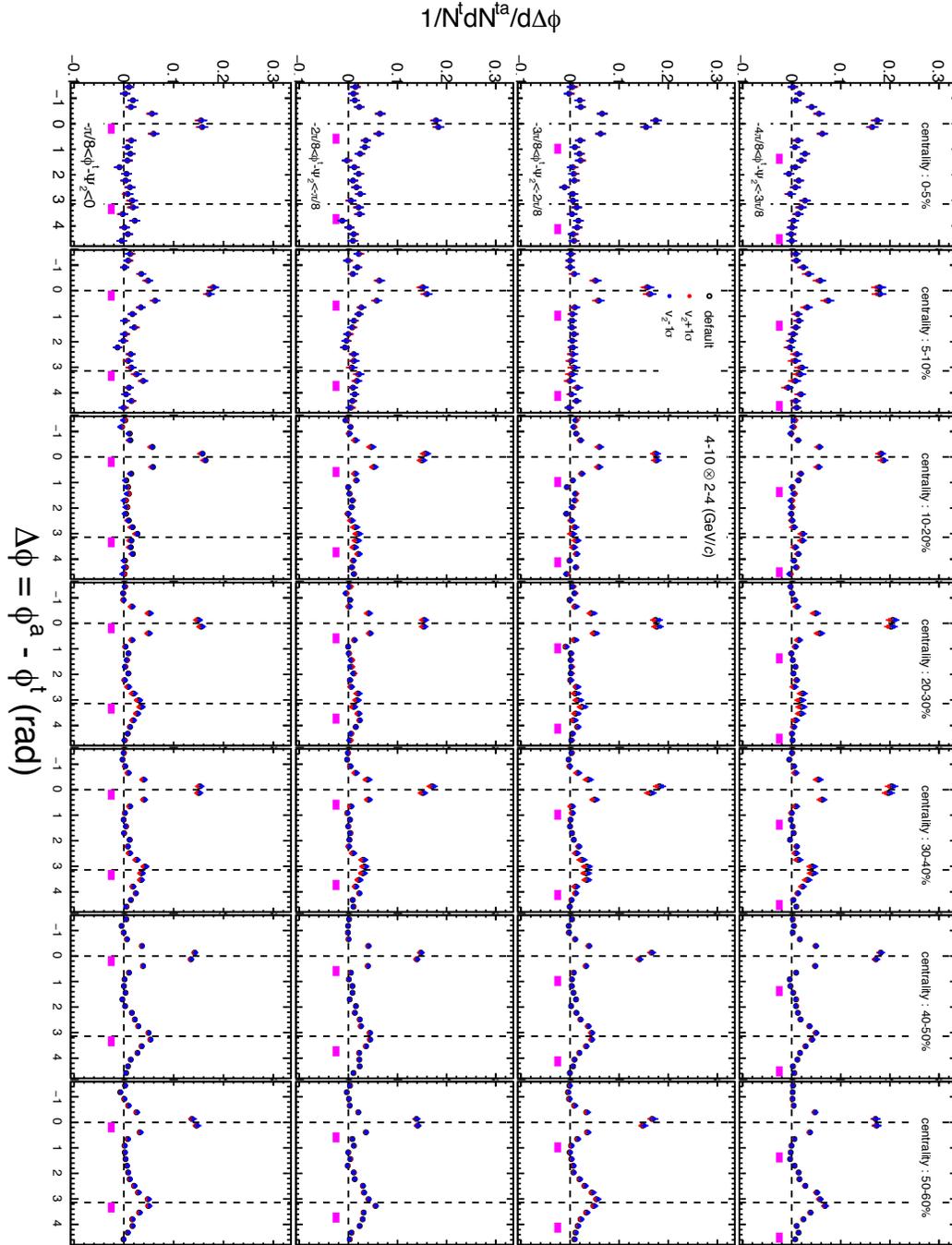
Figure B.5: Azimuthal distributions of correlated yield with subtracting $v_2 \pm 1\sigma$ with $p_T^t \otimes p_T^a =$ 4-10⊗2-4 (GeV/c).
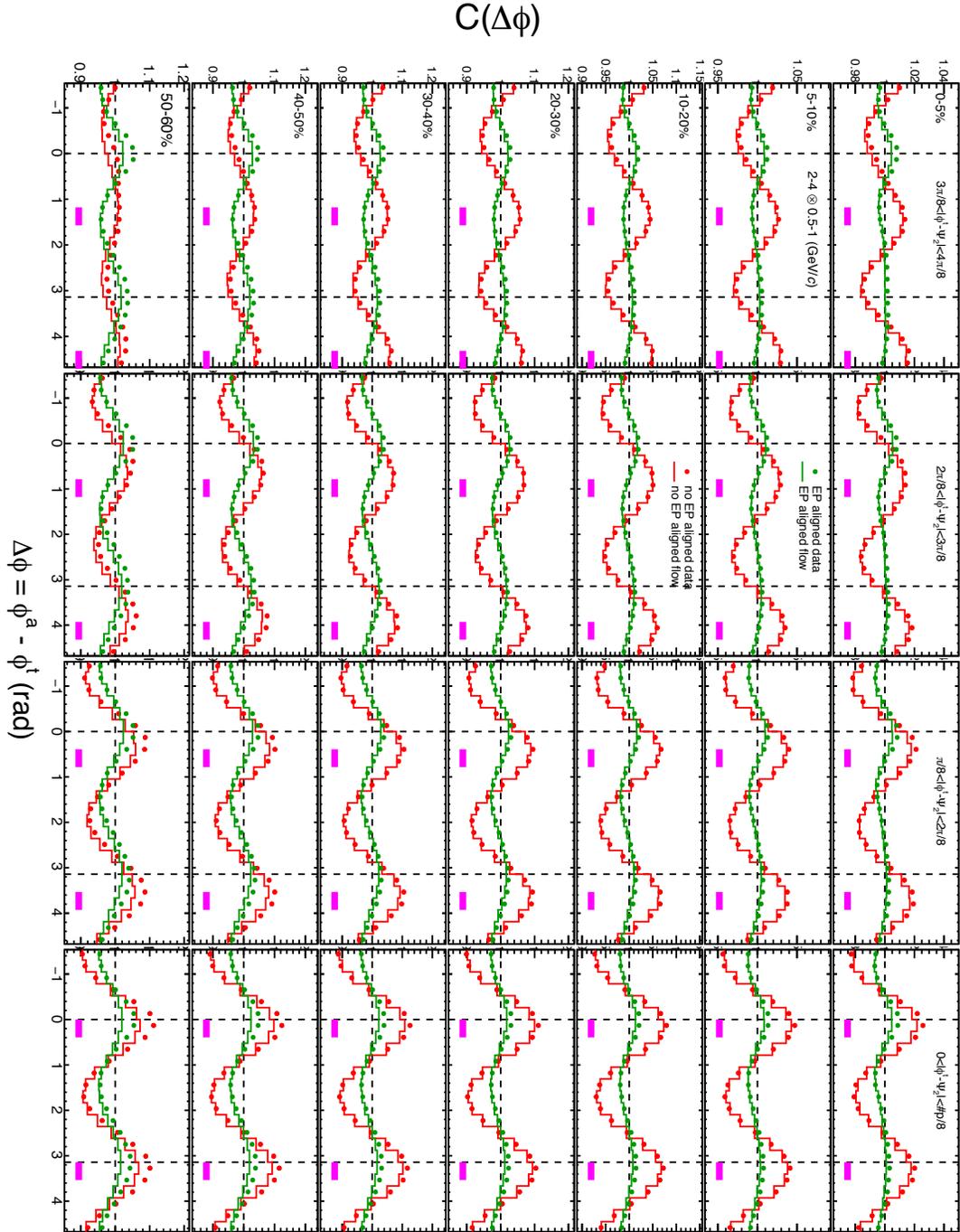
Figure B.6: Azimuthal correlation functions and flow background with and without alignment of second-order event plane (red) and inclusive-trigger correlation (blue), respectively, with $p_T^t \otimes p_T^a = 2\text{-}4 \otimes 0.5\text{-}1$ (GeV/c).
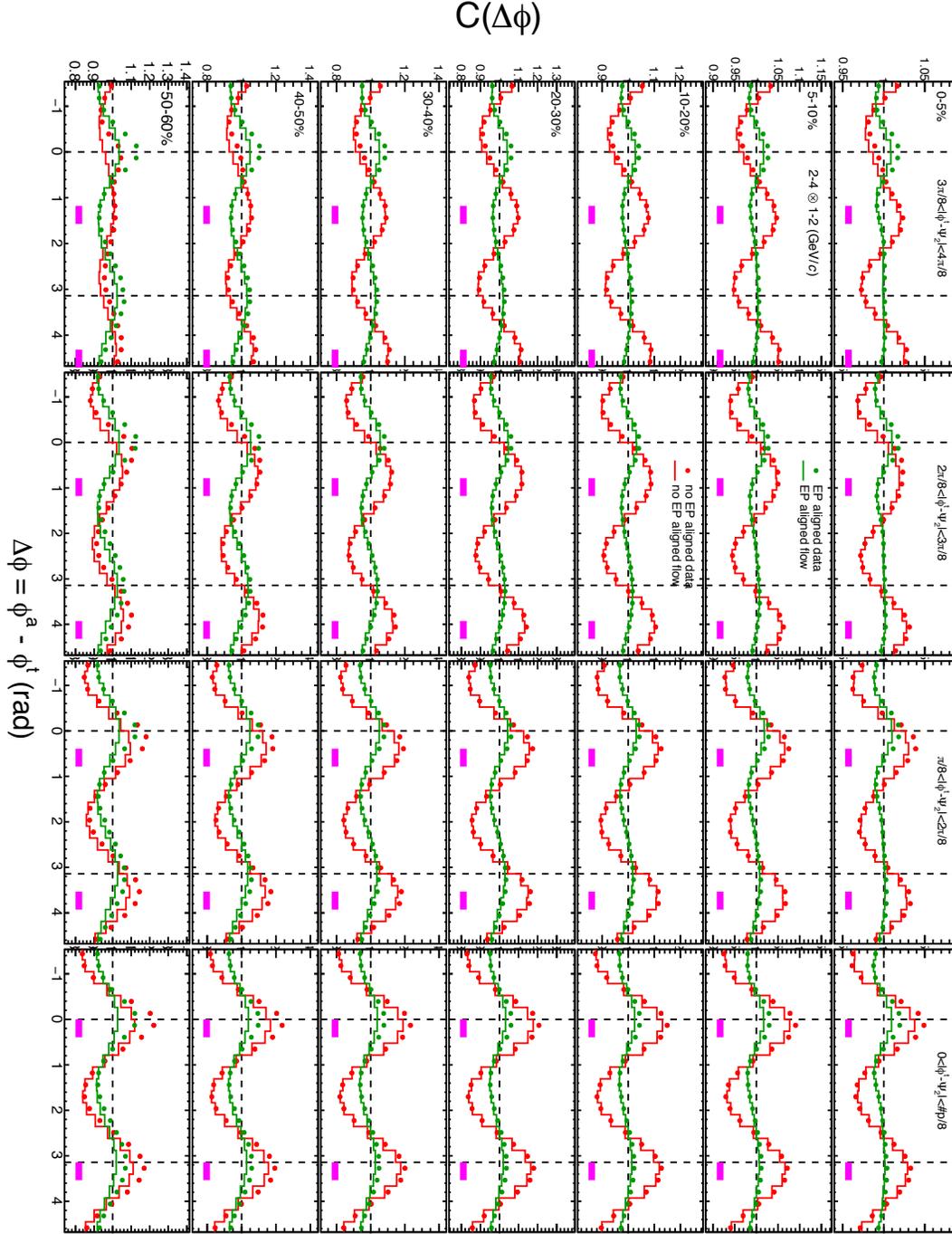
Figure B.7: Azimuthal correlation functions and flow background with and without alignment of second-order event plane (red) and inclusive-trigger correlation (blue), respectively, with $p_T^t \otimes p_T^a = 2\text{-}4 \otimes 1\text{-}2$ (GeV/c).
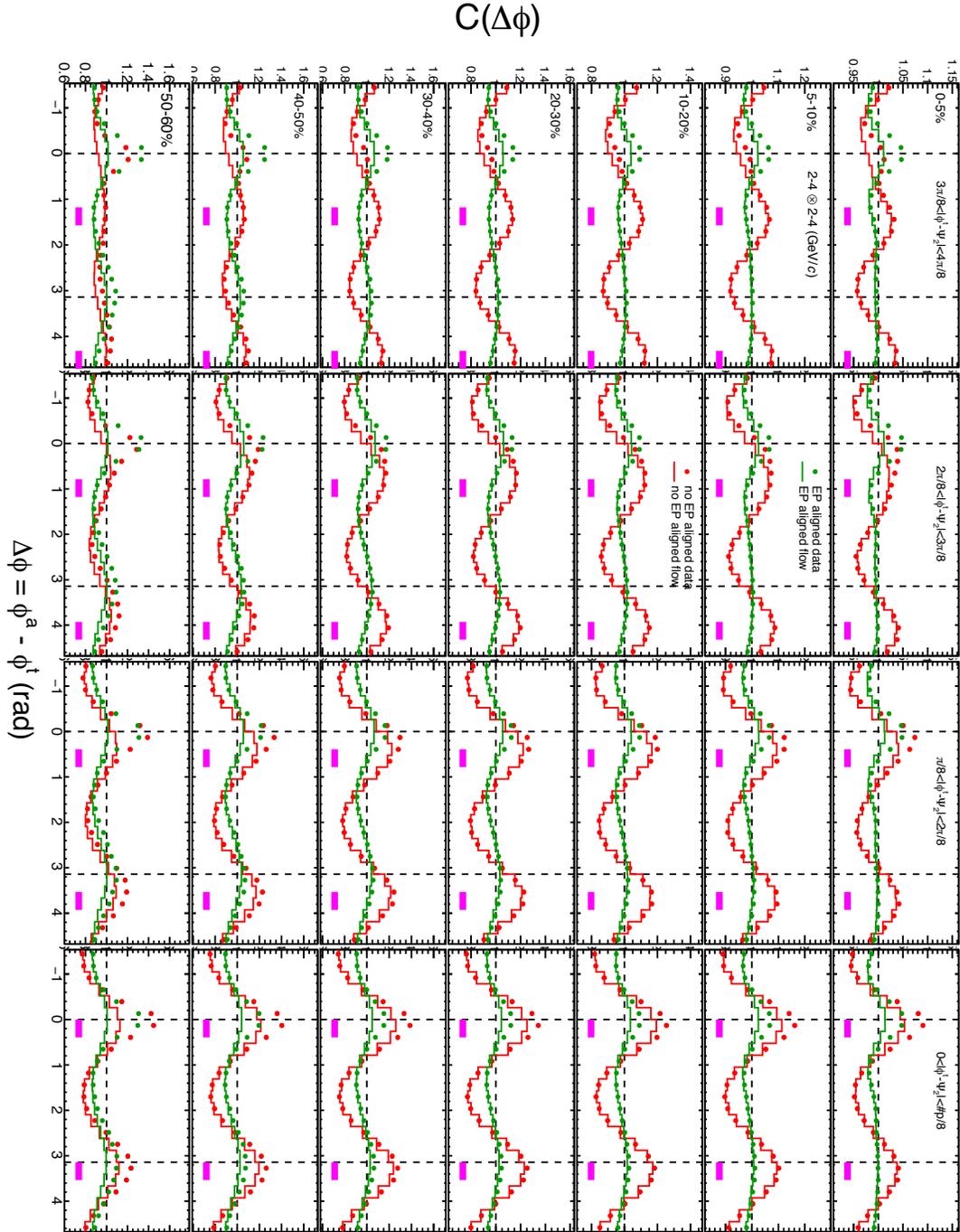
Figure B.8: Azimuthal correlation functions and flow background with and without alignment of second-order event plane (red) and inclusive-trigger correlation (blue), respectively, with $p_T^t \otimes p_T^a = 2\text{-}4 \otimes 2\text{-}4$ (GeV/c).
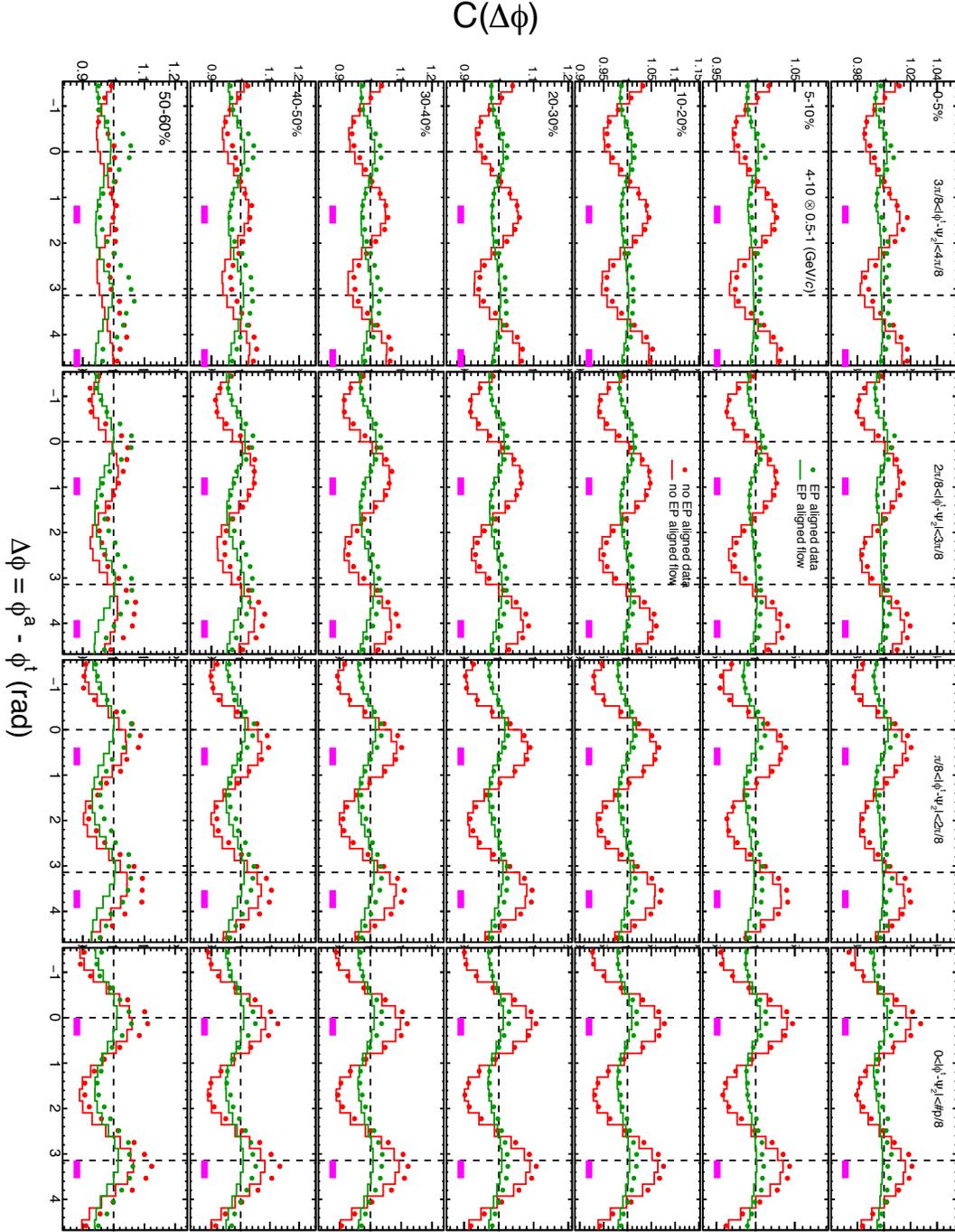
Figure B.9: Azimuthal correlation functions and flow background with and without alignment of second-order event plane (red) and inclusive-trigger correlation (blue), respectively, with $p_T^t \otimes p_T^a = 4\text{-}10 \otimes 0.5\text{-}1$ (GeV/c).
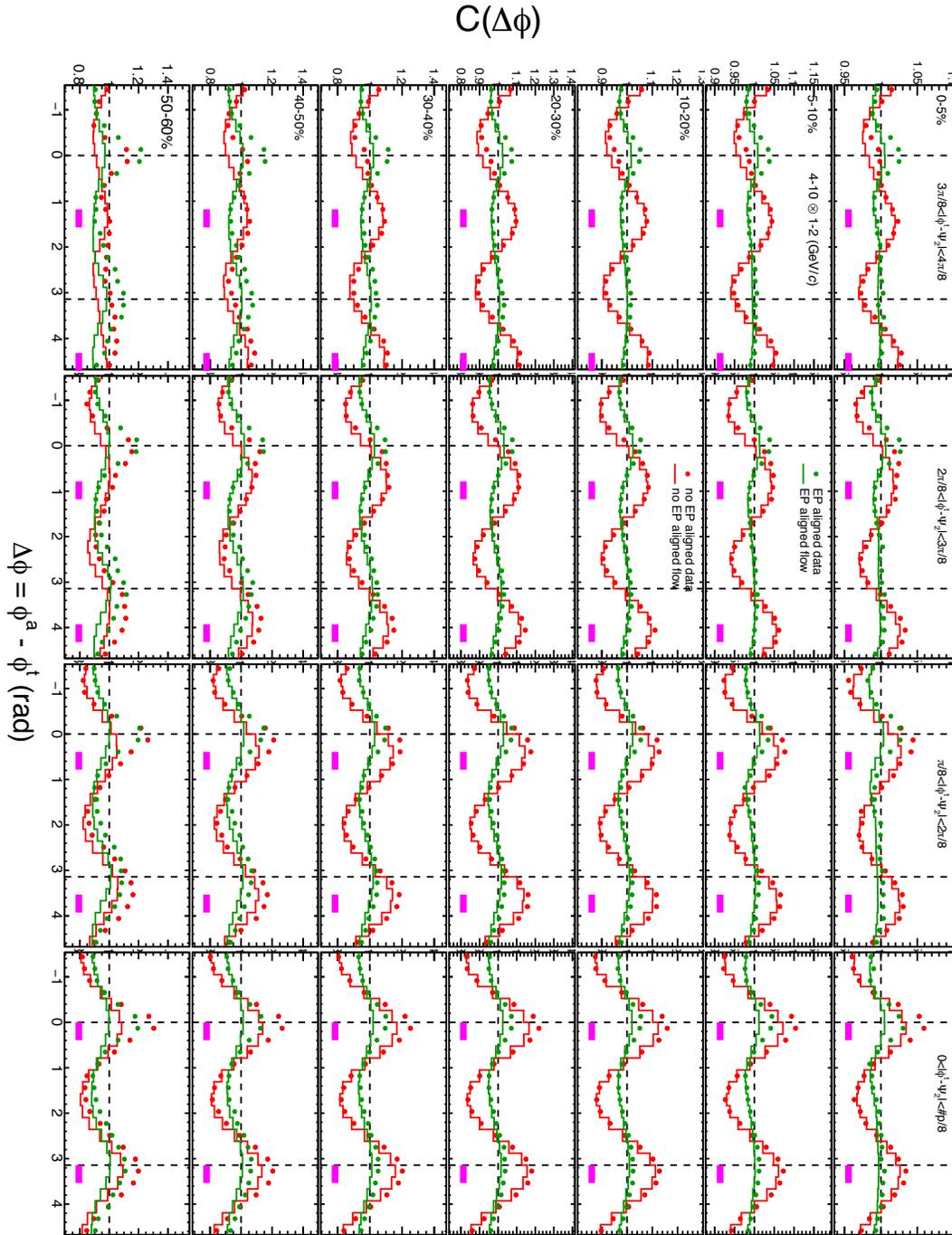
Figure B.10: Azimuthal correlation functions and flow background with and without alignment of second-order event plane (red) and inclusive-trigger correlation (blue), respectively, with $p_T^t \otimes p_T^a = 4\text{-}10 \otimes 1\text{-}2$ (GeV/c).
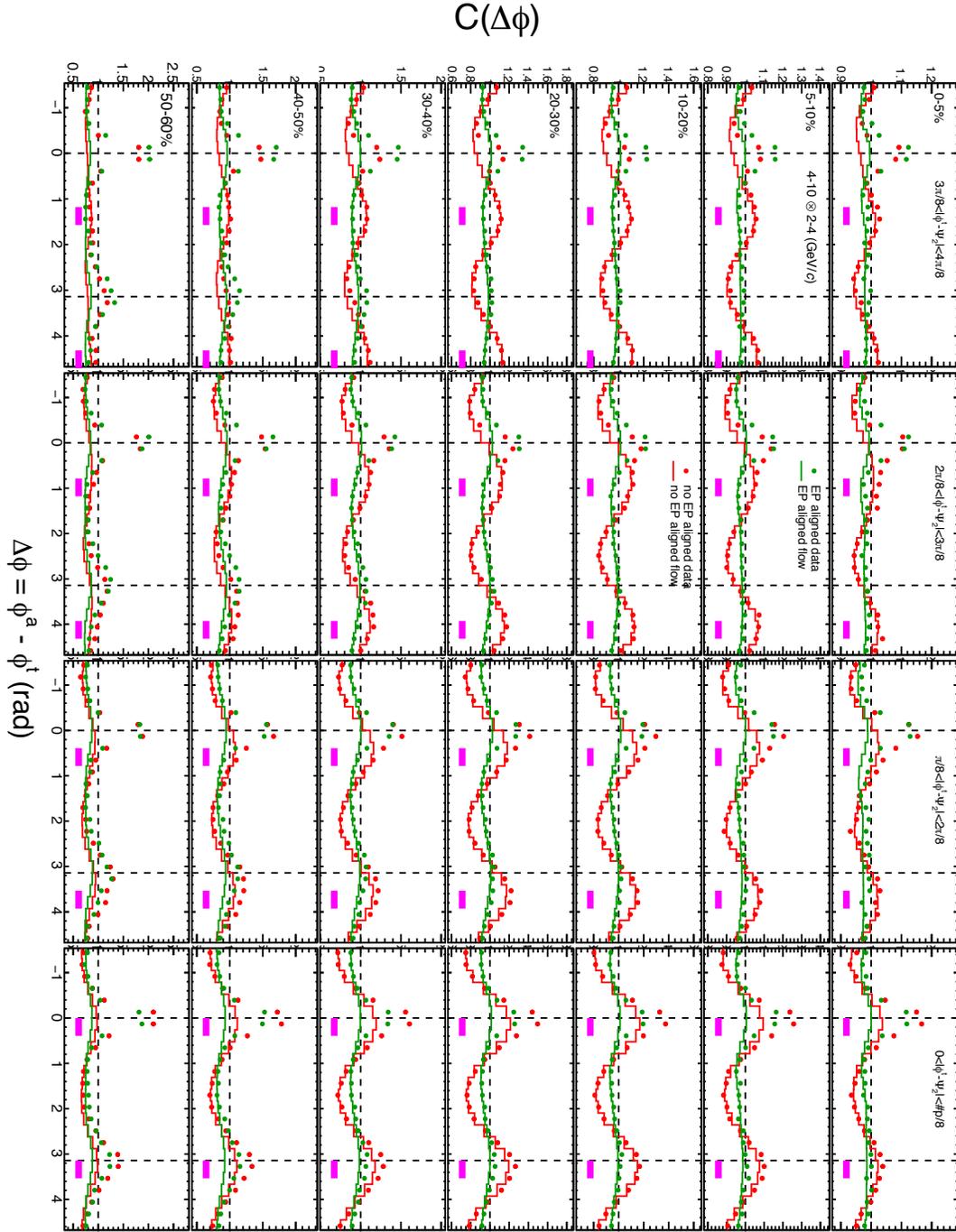
Figure B.11: Azimuthal correlation functions and flow background with and without alignment of second-order event plane (red) and inclusive-trigger correlation (blue), respectively, with $p_T^t \otimes p_T^a = $ 4-10⊗2-4 (GeV/c).
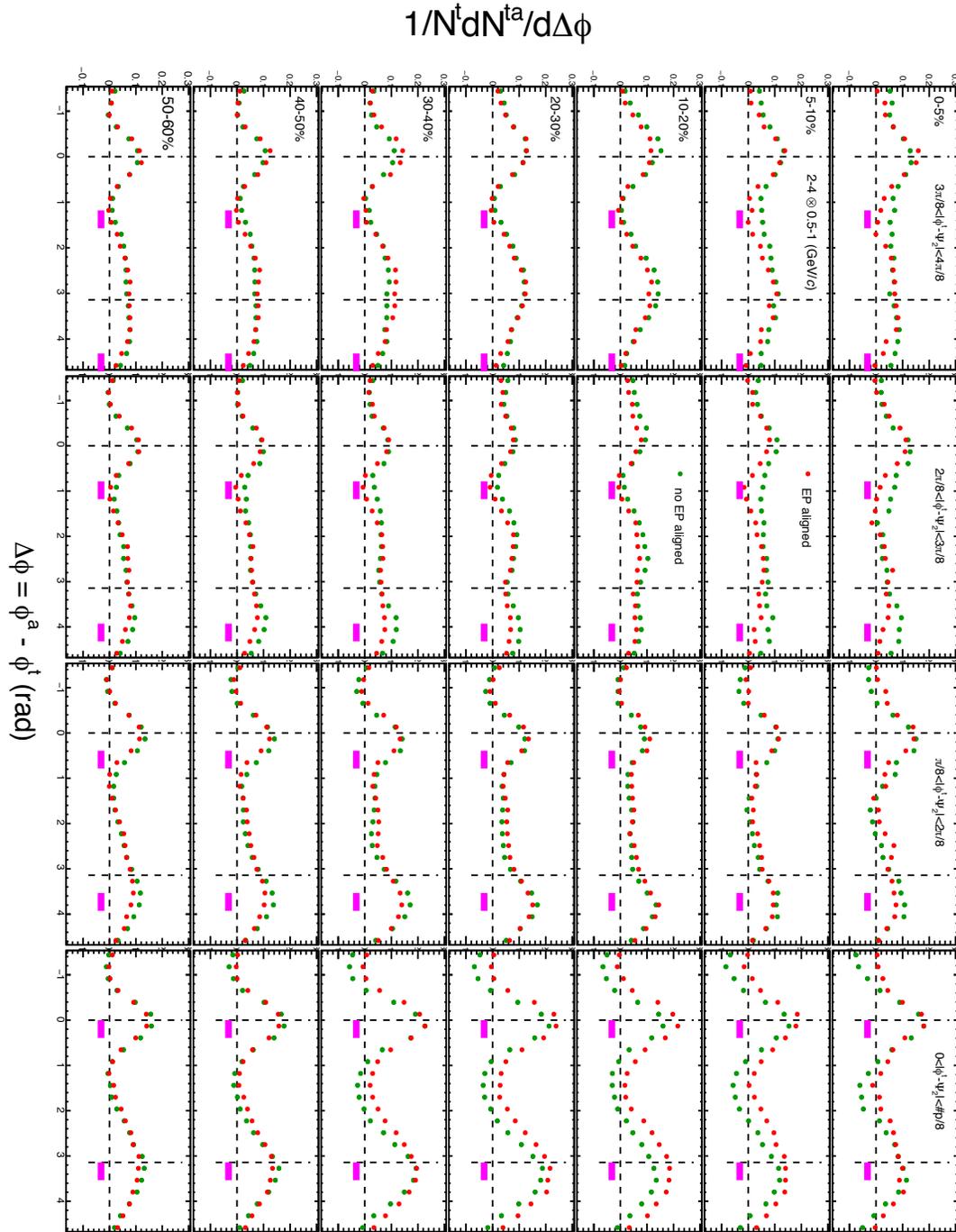
Figure B.12: Azimuthal distributions of correlated yield with and without alignment of second-order event plane (red) and inclusive-trigger correlation (blue), respectively, with $p_T^t \otimes p_T^a = 2\text{-}4 \otimes 0.5\text{-}1$ (GeV/c).
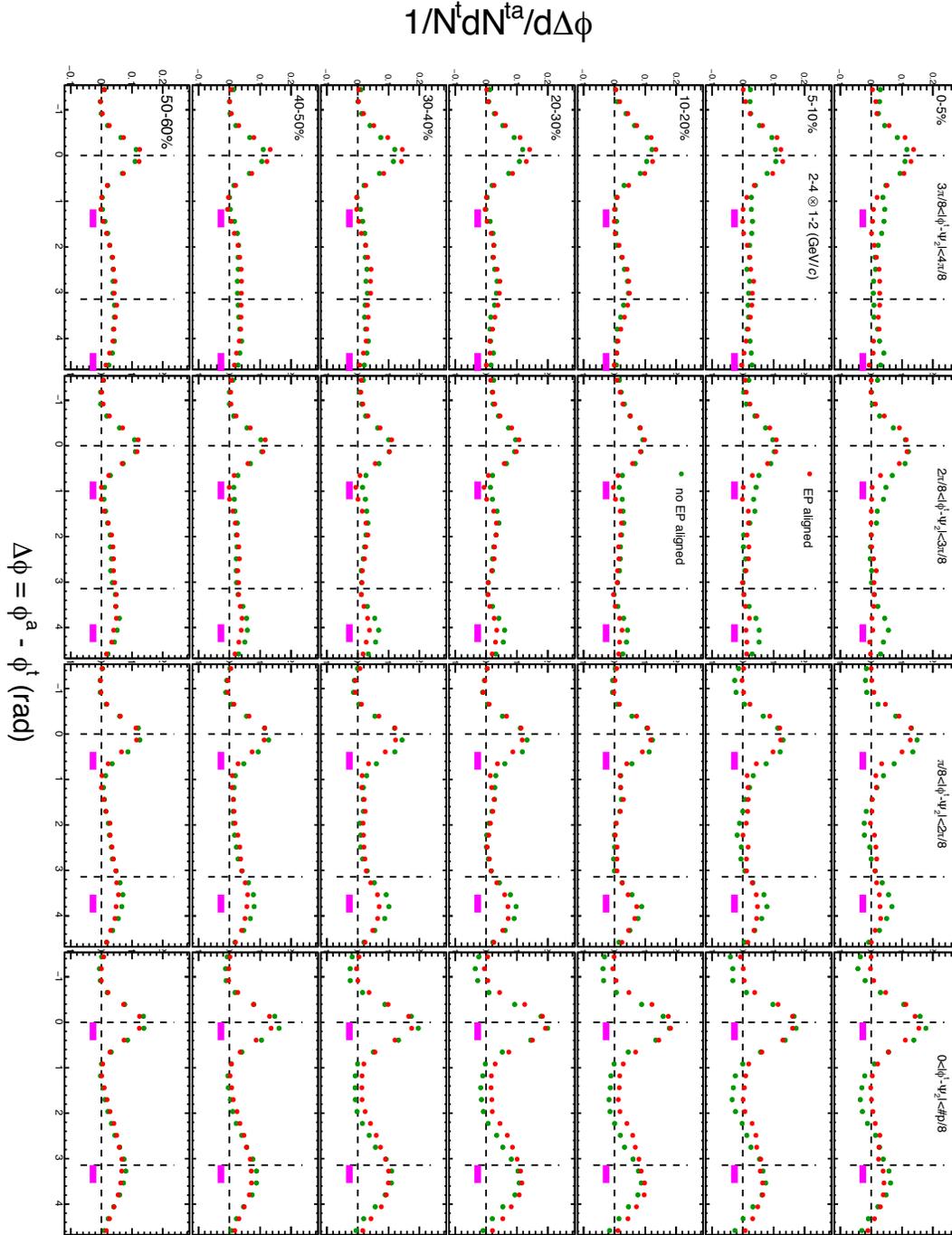
Figure B.13: Azimuthal distributions of correlated yield with and without alignment of second-order event plane (red) and inclusive-trigger correlation (blue), respectively, with $p_T^t \otimes p_T^a = 2\text{-}4 \otimes 1\text{-}2$ (GeV/c).
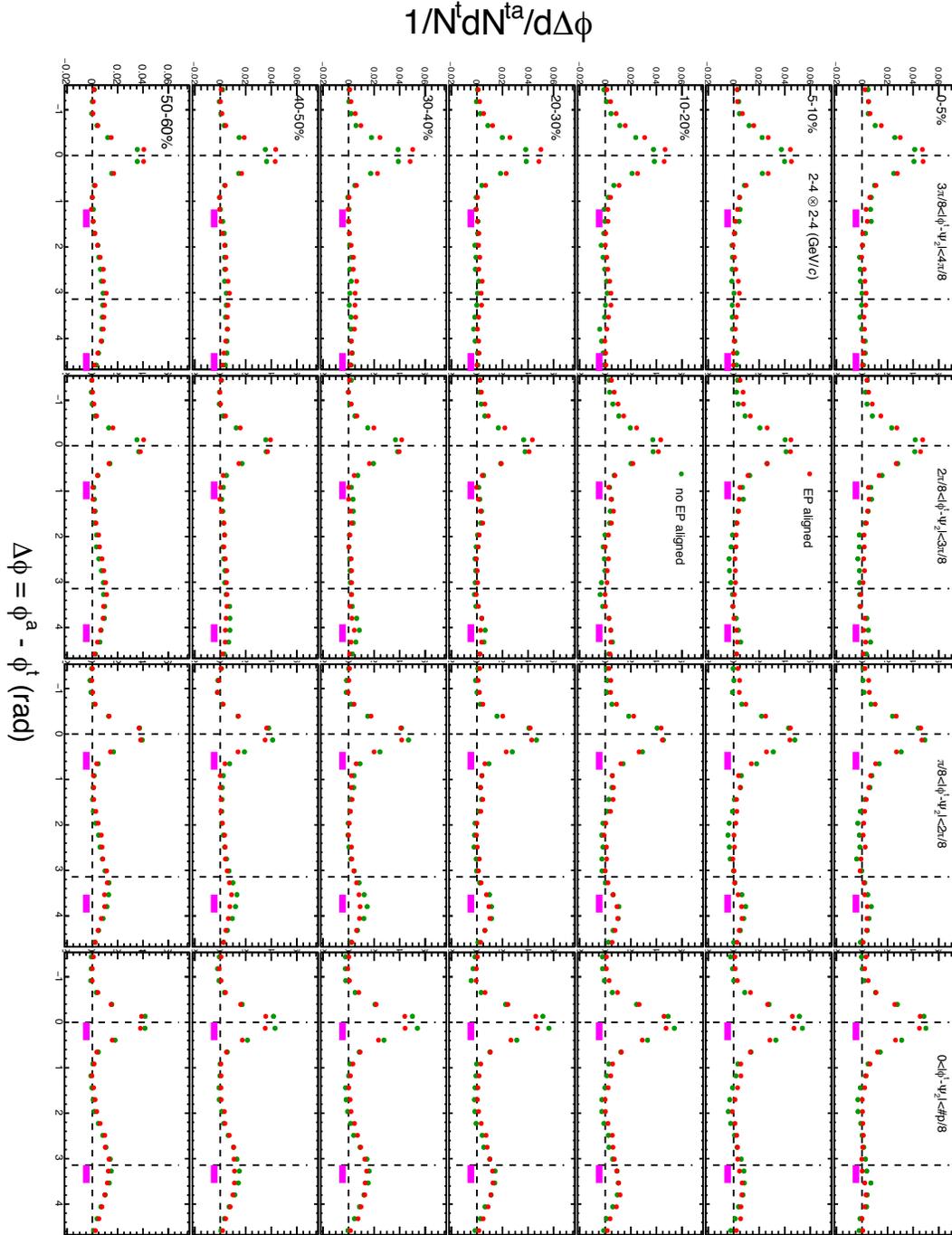
Figure B.14: Azimuthal distributions of correlated yield with and without alignment of second-order event plane (red) and inclusive-trigger correlation (blue), respectively, with $p_T^t \otimes p_T^a = $ 2-4⊗2-4 (GeV/c).
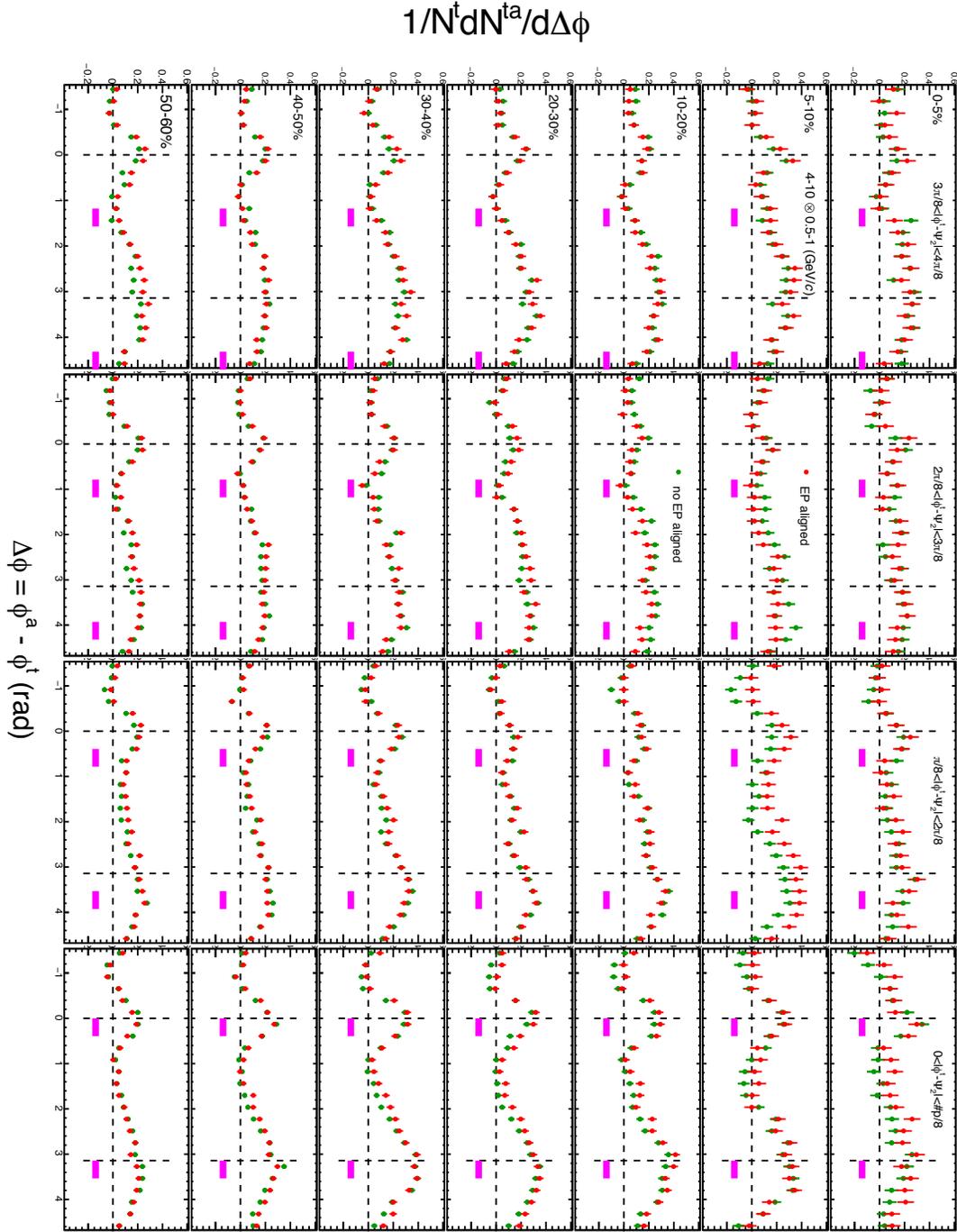
Figure B.15: Azimuthal distributions of correlated yield with and without alignment of second-order event plane (red) and inclusive-trigger correlation (blue), respectively, with $p_T^t \otimes p_T^a = $ 4-10⊗0.5-1 (GeV/c).
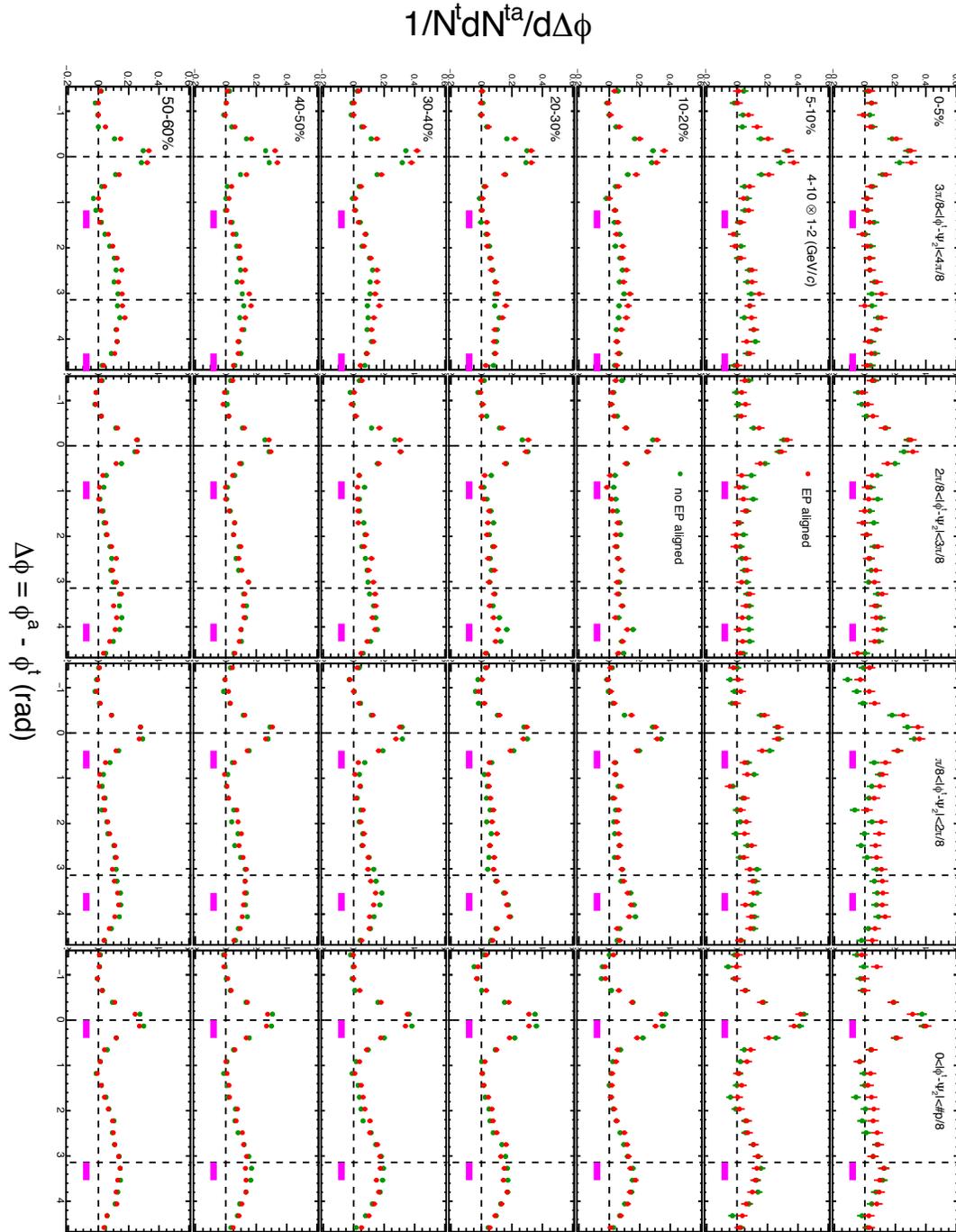
Figure B.16: Azimuthal distributions of correlated yield with and without alignment of second-order event plane (red) and inclusive-trigger correlation (blue), respectively, with $p_T^t \otimes p_T^a = 4\text{-}10 \otimes 1\text{-}2$ (GeV/c).
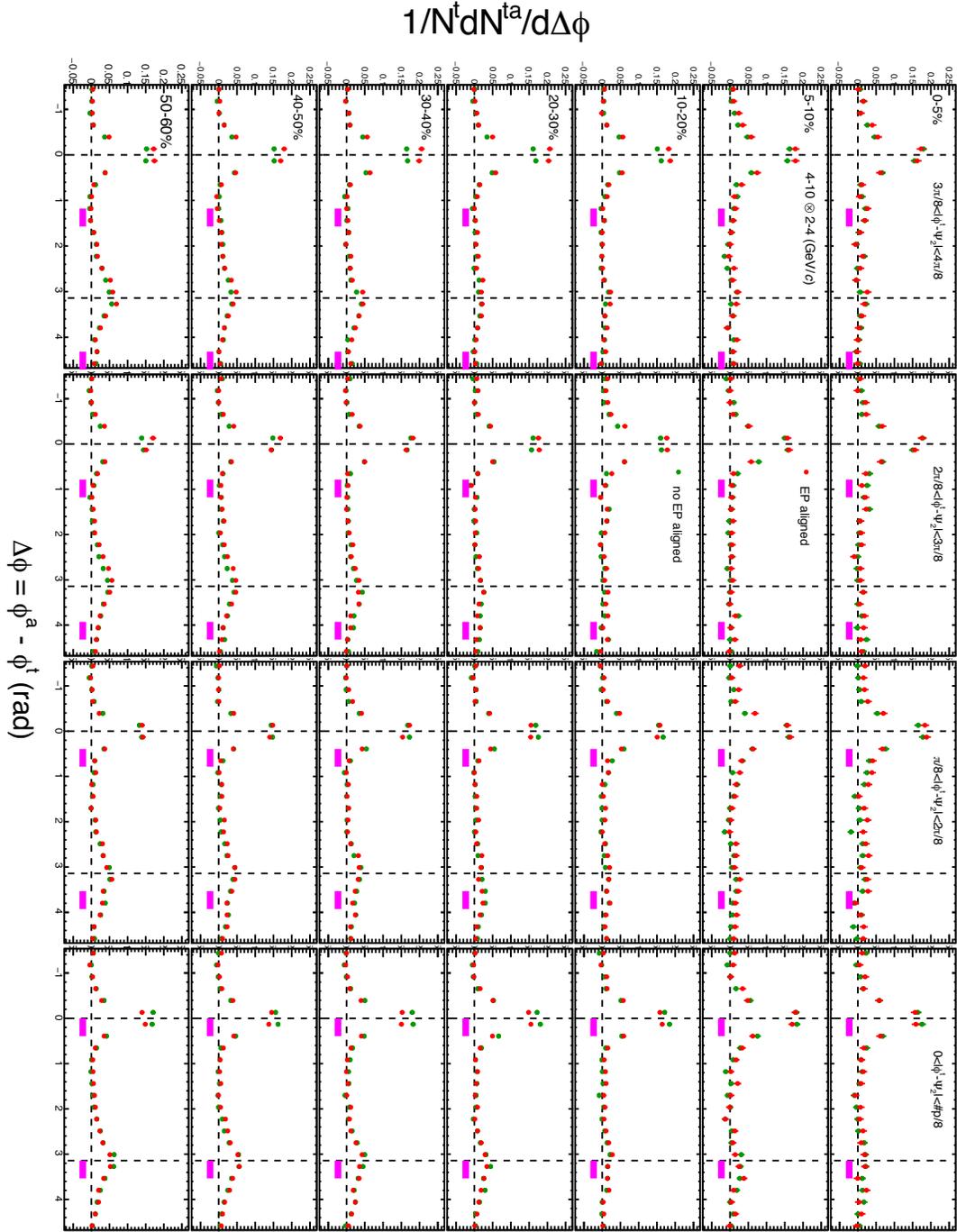
Figure B.17: Azimuthal distributions of correlated yield with and without alignment of second-order event plane (red) and inclusive-trigger correlation (blue), respectively, with $p_T^t \otimes p_T^a = 4\text{-}10 \otimes 2\text{-}4$ (GeV/c).
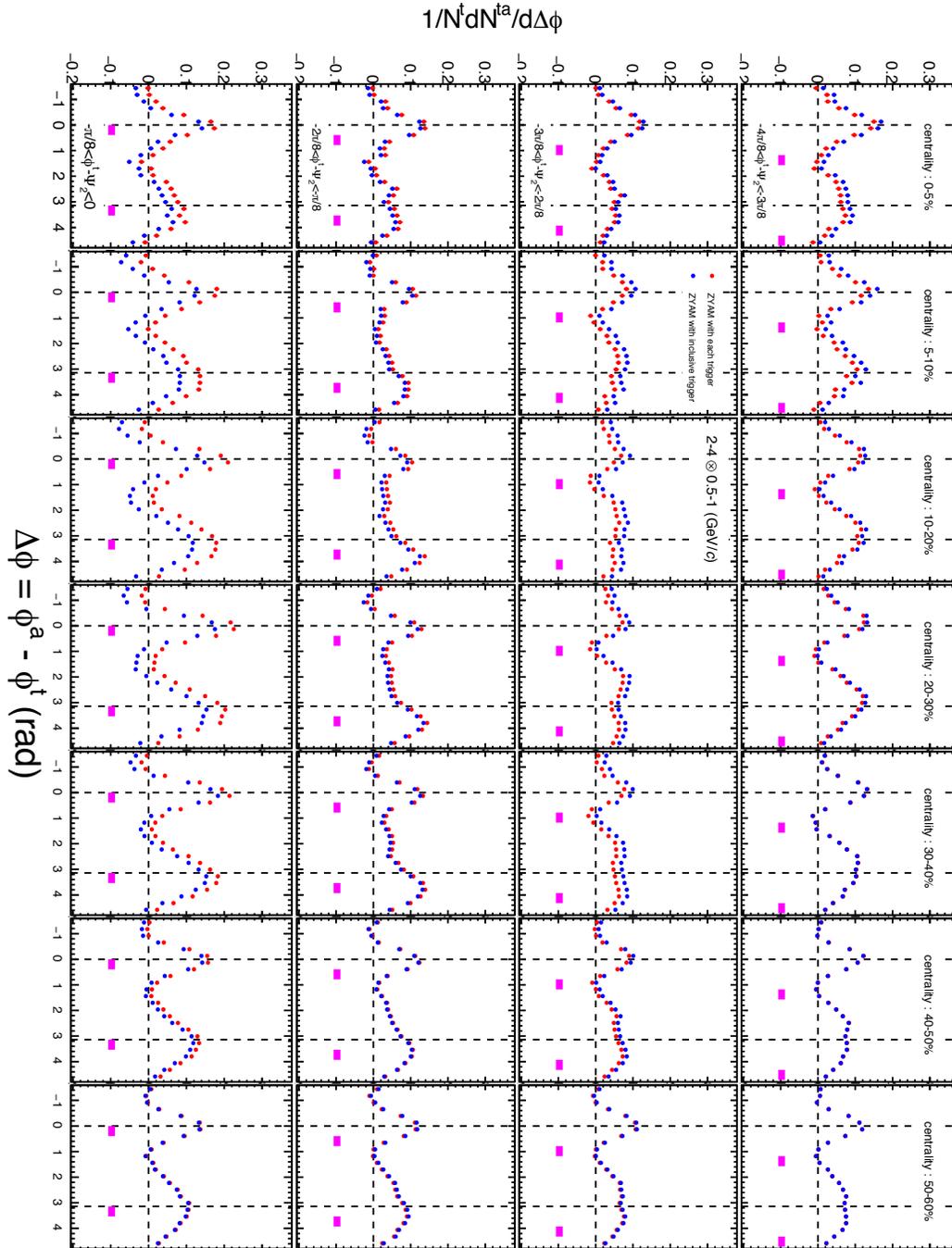
Figure B.18: Azimuthal distributions of correlated yield with ZYAM determined with trigger-angle selected correlation (red) and inclusive-trigger correlation (blue) $p_T^t \otimes p_T^a = 2\text{-}4 \otimes 0.5\text{-}1$ (GeV/c).
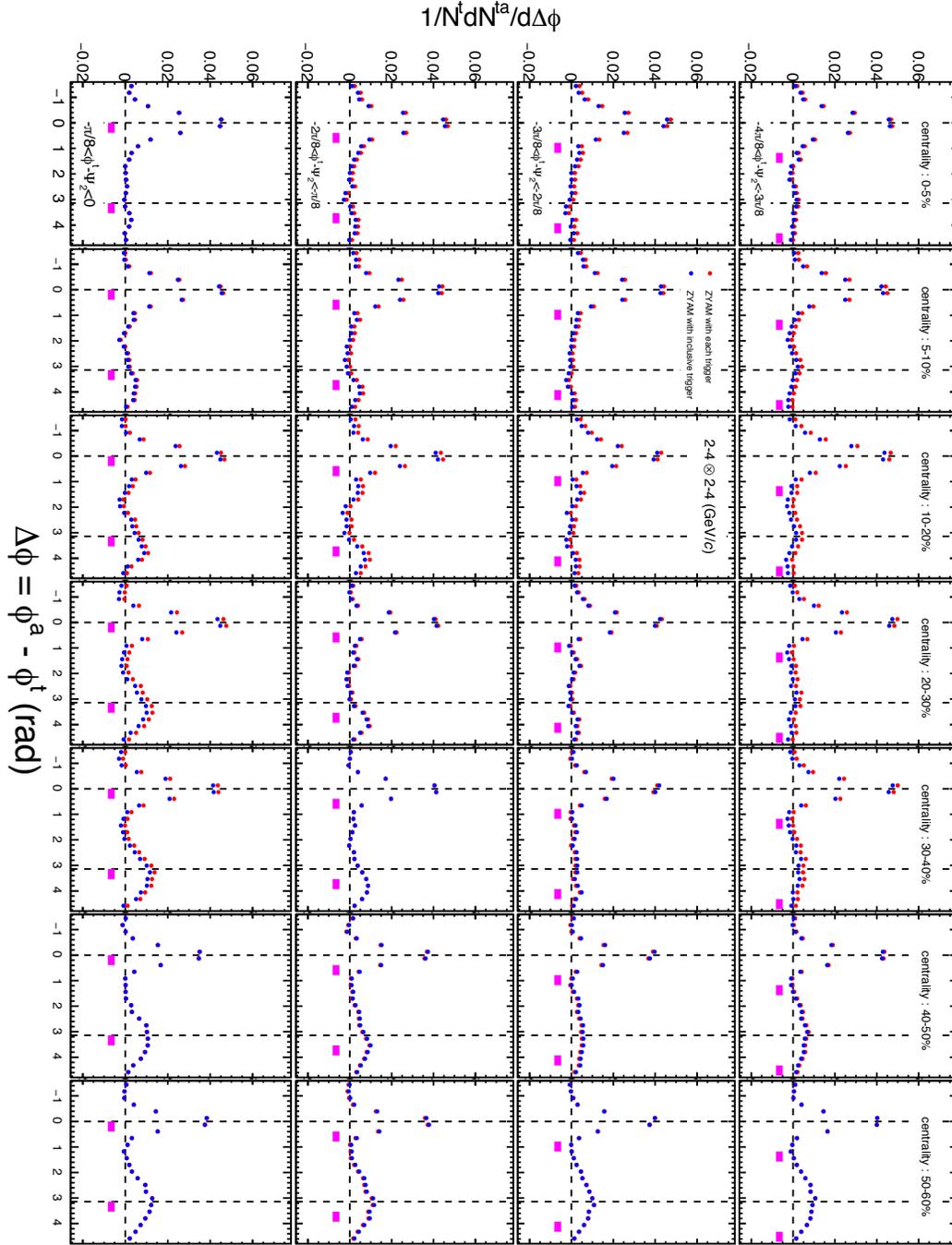
Figure B.19: Azimuthal distributions of correlated yield with ZYAM determined with trigger-angle selected correlation (red) and inclusive-trigger correlation (blue) $p_T^t \otimes p_T^a$ = 2-4⊗2-4 (GeV/c).
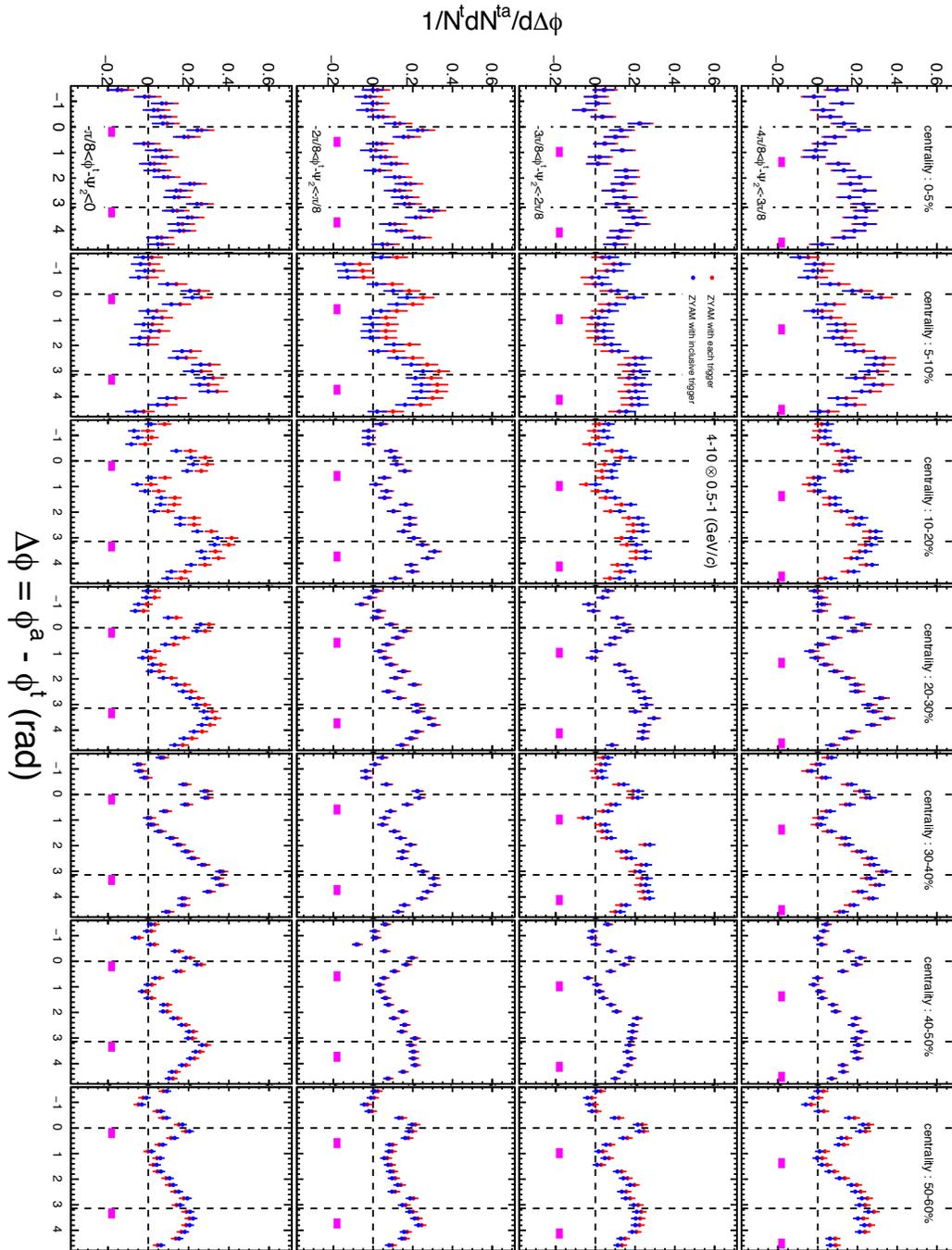
Figure B.20: Azimuthal distributions of correlated yield with ZYAM determined with trigger-angle selected correlation (red) and inclusive-trigger correlation (blue) $p_T^t \otimes p_T^a = $ 4-10⊗0.5-1 (GeV/c).
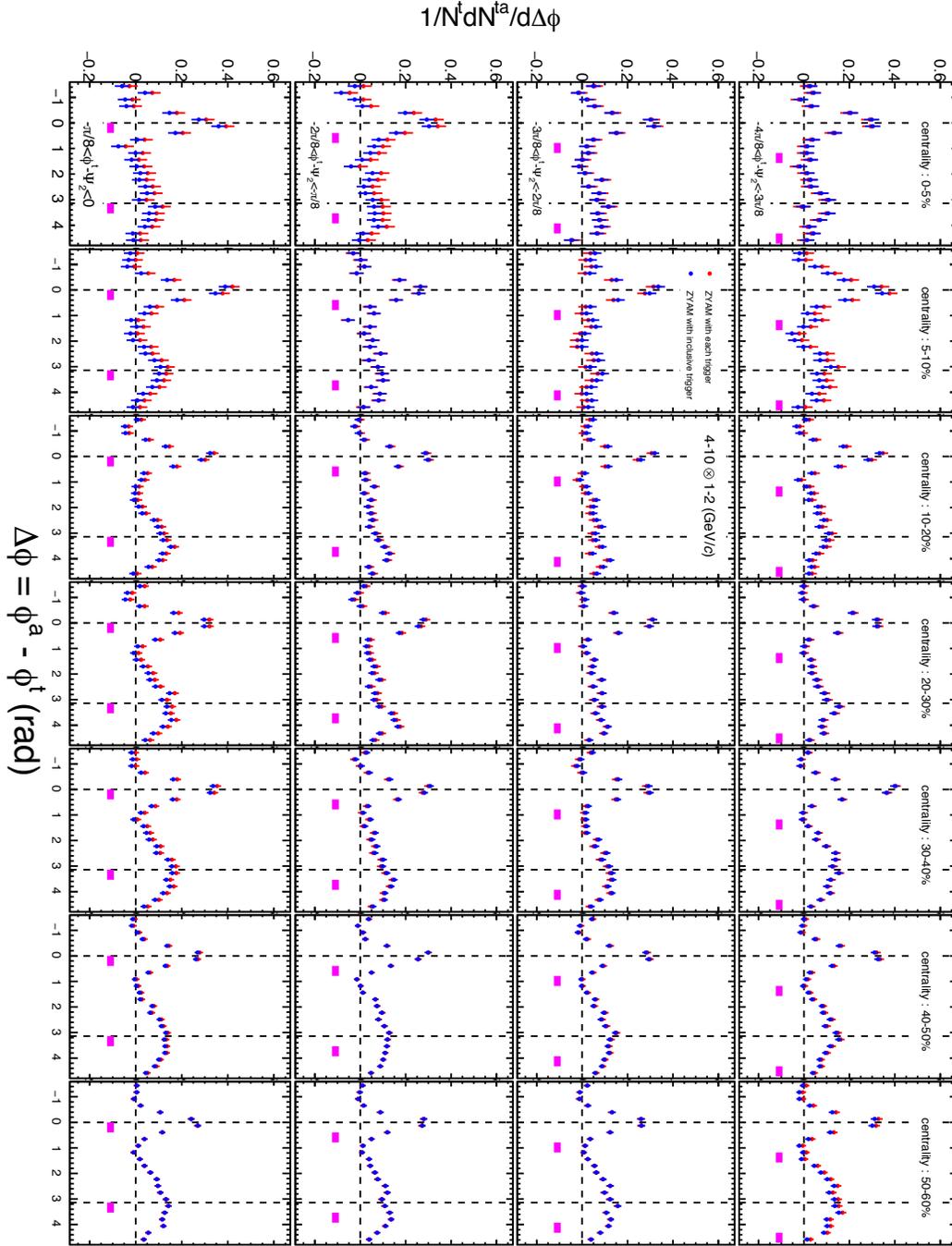
Figure B.21: Azimuthal distributions of correlated yield with ZYAM determined with trigger-angle selected correlation (red) and inclusive-trigger correlation (blue) $p_T^t \otimes p_T^a$ = 4-10⊗1-2 (GeV/c).
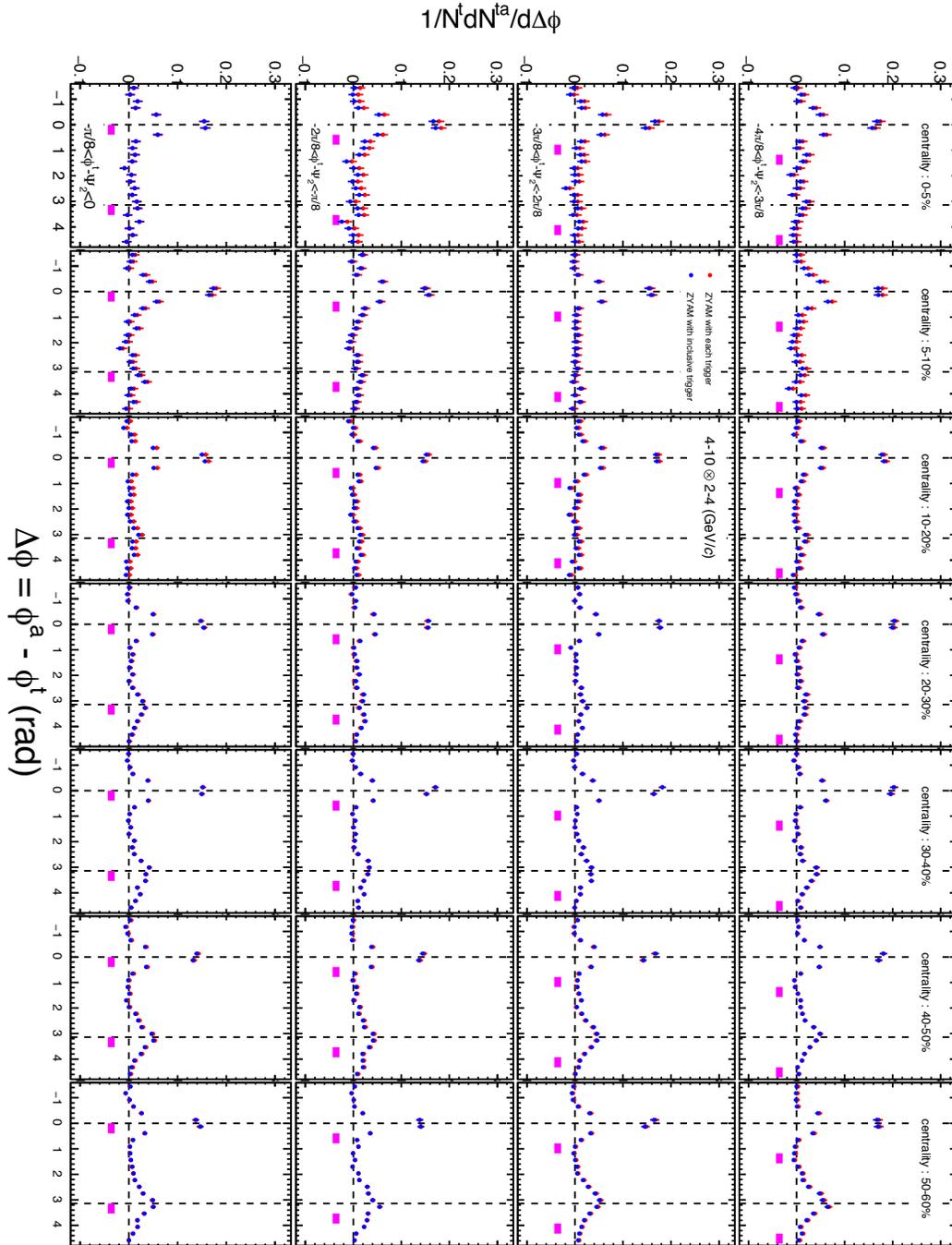
Figure B.22: Azimuthal distributions of correlated yield with ZYAM determined with trigger-angle selected correlation (red) and inclusive-trigger correlation (blue) $p_T^t \otimes p_T^a$ = 4-10⊗2-4 (GeV/c).
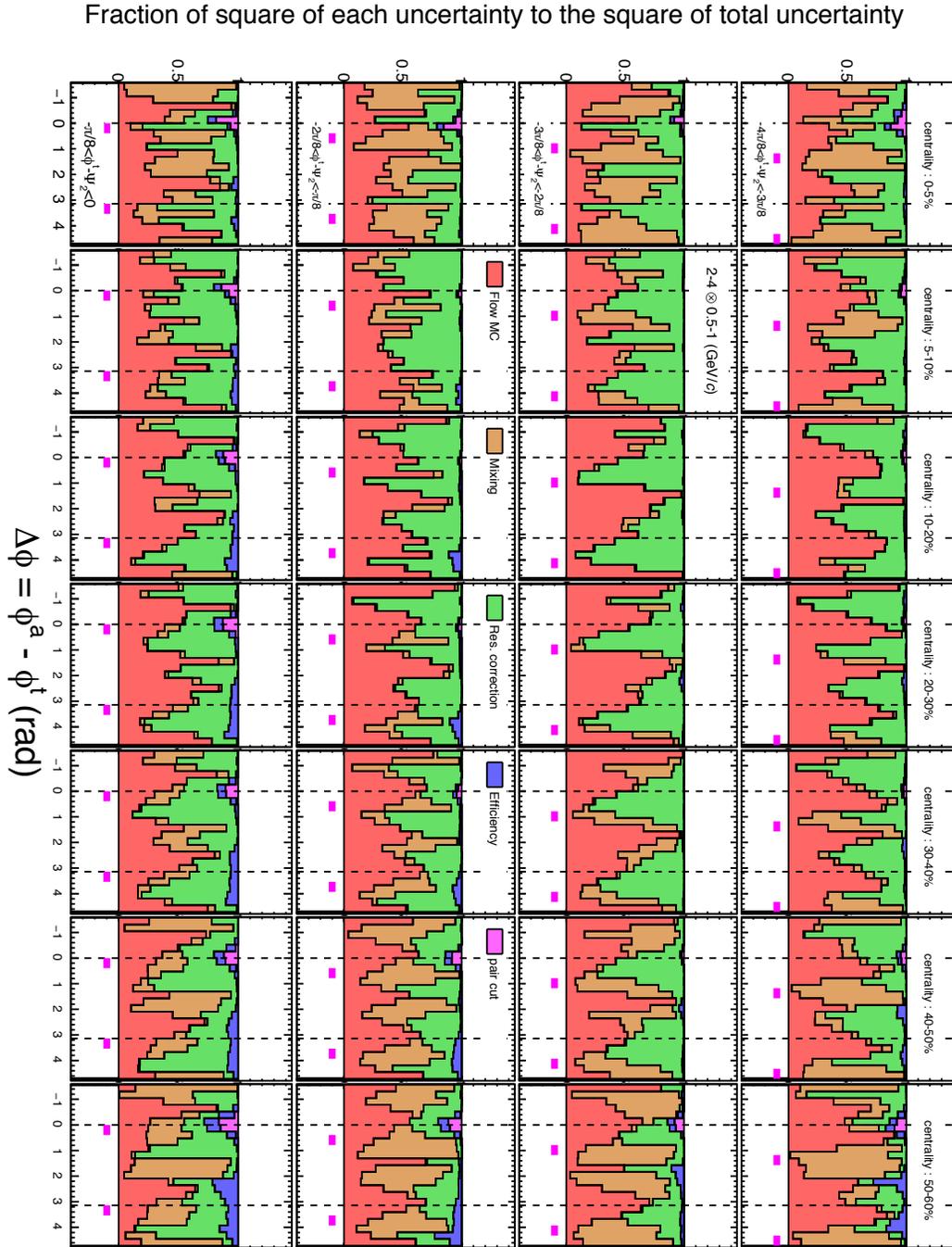
Figure B.23: Azimutal angle dependence of fraction of square of each systematic source to the square of total systematic unertainty with $p_T^t \otimes p_T^a$ = 2-4⊗0.5-1 (GeV/c).
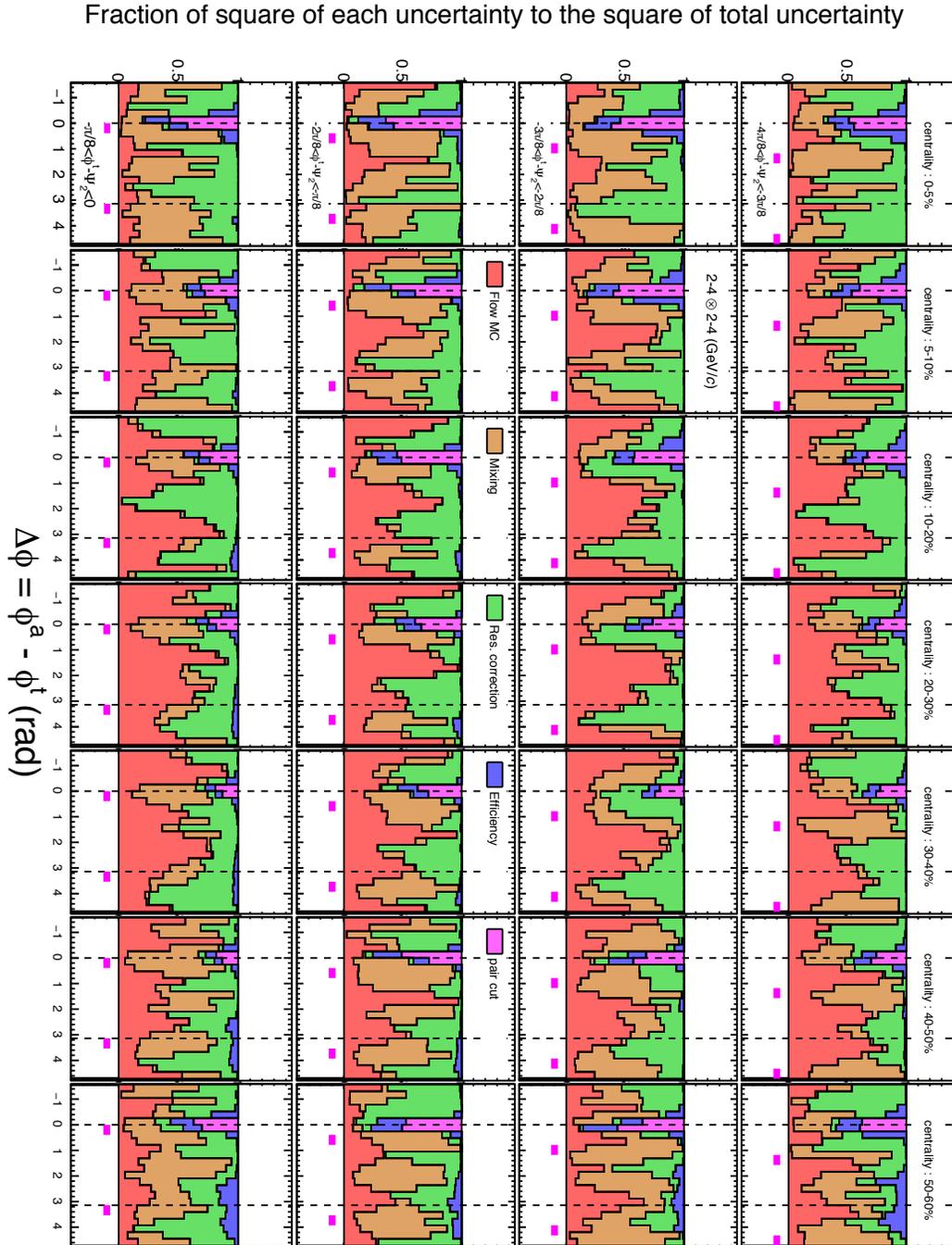
Fraction of square of each uncertainty to the square of total uncertainty

Figure B.24: Azimutal angle dependence of fraction of square of each systematic source to the square of total systematic unertainty with $p_T^t \otimes p_T^a$ = 2-4⊗2-4 (GeV/c).

Figure B.25: Azimutal angle dependence of fraction of square of each systematic source to the square of total systematic unertainty with $p_T^t \otimes p_T^a$ = 4-10⊗0.5-1 (GeV/c).
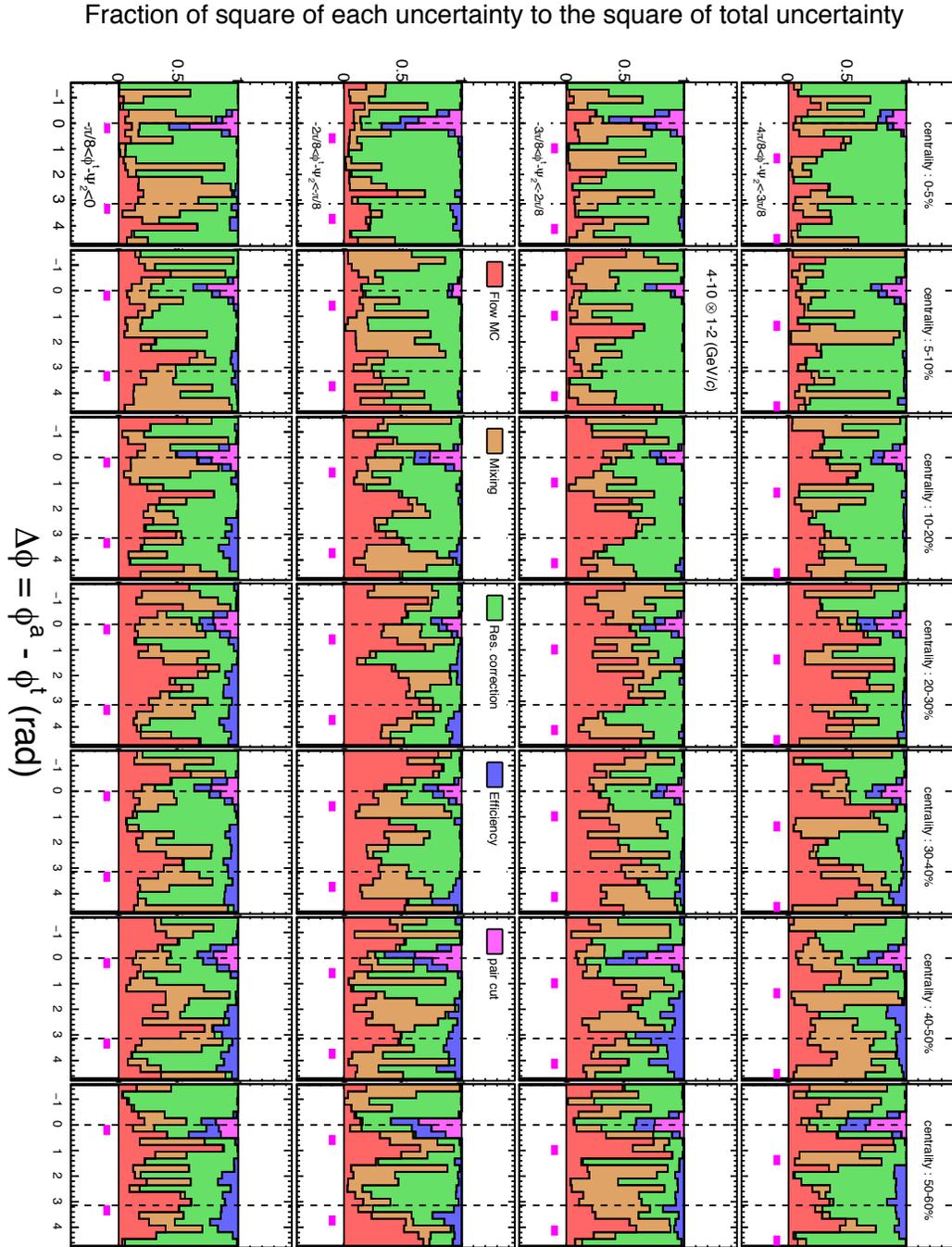
Fraction of square of each uncertainty to the square of total uncertainty

Figure B.26: Azimutal angle dependence of fraction of square of each systematic source to the square of total systematic unertainty with $p_T^t \otimes p_T^a = 4\text{-}10 \otimes 1\text{-}2$ (GeV/c).

Fraction of square of each uncertainty to the square of total uncertainty
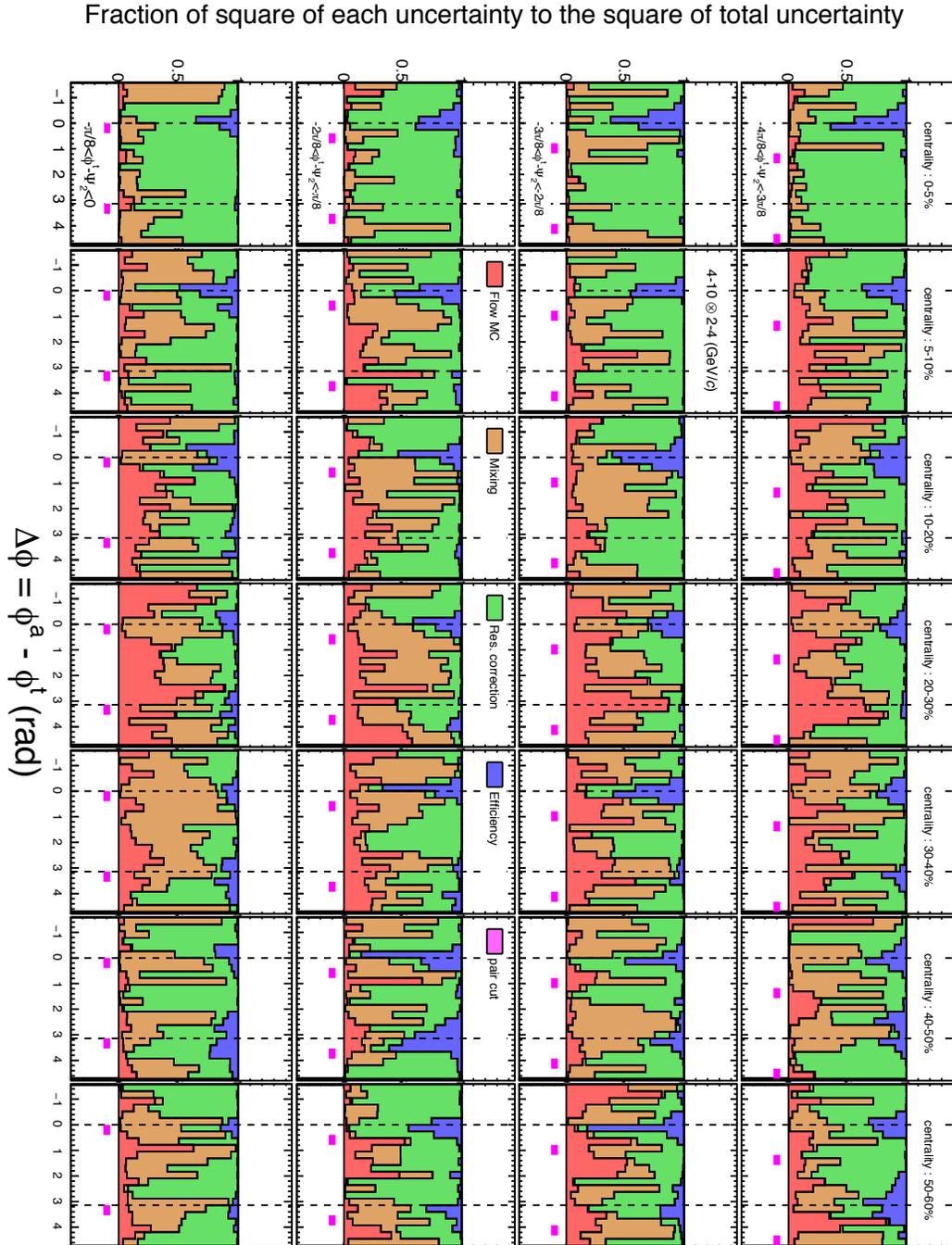
Figure B.27: Azimutal angle dependence of fraction of square of each systematic source to the square of total systematic unertainty with $p_T^t \otimes p_T^a$ = 4-10⊗2-4 (GeV/c).

Appendix C

Results of AMPT

In this chapter, results of AMPT model is presented. Centrality is determined based on imapct parameter b in the generated events in this study as shown in Table.C.1.

Table C.1: Centrality binning and impact parameter

low edge of centrality (%)	0	5	10	20	30	40	50	60	70	80
low edge of impact parameter (fm)	0	3.3	4.9	6.9	8.4	9.7	10.9	11.9	12.9	13.8

C.1   Azimuthal anisotropy v_n

C.1.1   Azimuthal anisotropy with and without jet quenching mode

Fig.C.1 shows comparison of v_2, v_3 and v_4 with and without jet quenching mode as a function of p_T in 0-50 % centrality.

C.1.2   Azimuthal anisotropy with q_2 or ε_2 selections

Fig.C.2-C.6 shows v_2, v_3 and v_4 with q_2 or ε_2 selections as a function of p_T in 0-50 % centrality.

C.2   Azimuthal distributions of correlations

C.2.1   Comparison of correlations with and without quenching mode

Fig.C.7 shows azimuthal distribution of correlated yield with various p_T combinations in 0-50 % centrality with and without quenching option in AMPT model. Quenching parameter $-dE/dx$ = 2 (GeV/fm).
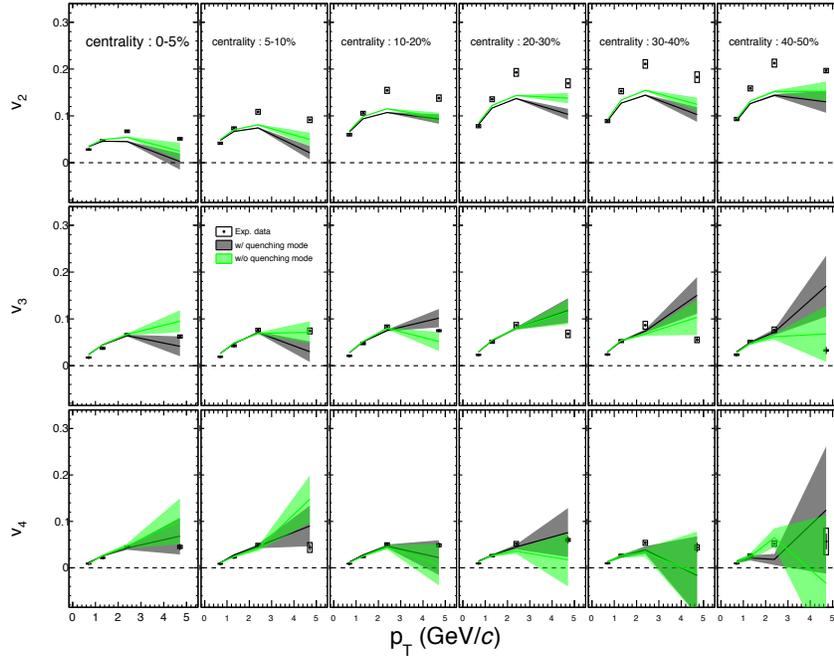
Figure C.1: Azimuthal anisotropy with 0-20 % q_2 or ε_2 selections in 0-50 % centrality in AMPT model.
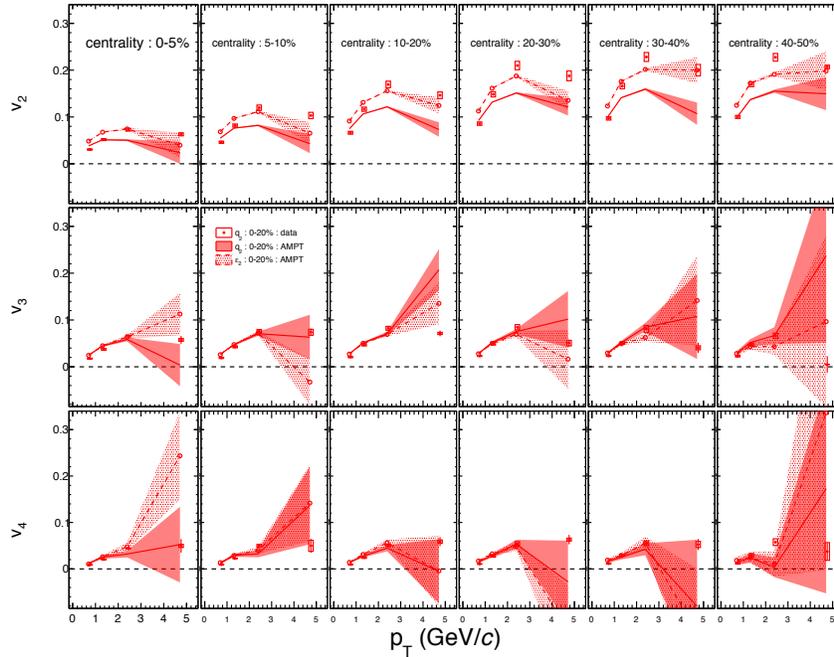
Figure C.2: Azimuthal anisotropy with 0-20 % q_2 or ε_2 selections in 0-50 % centrality in AMPT model.
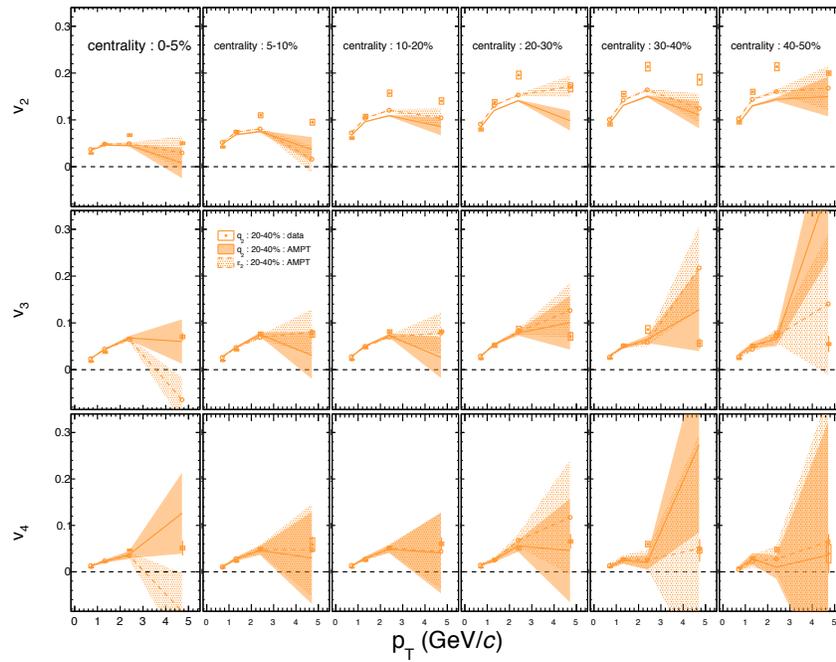
Figure C.3: Azimuthal anisotropy with 20-40 % q_2 or ε_2 selections in 0-50 % centrality in AMPT model.
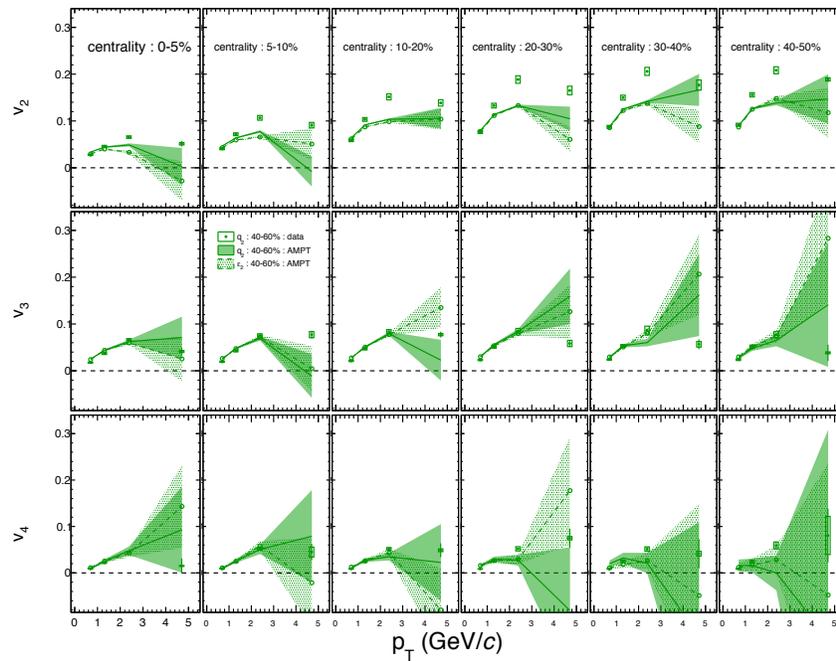
Figure C.4: Azimuthal anisotropy with 40-60 % q_2 or ε_2 selections in 0-50 % centrality in AMPT model.
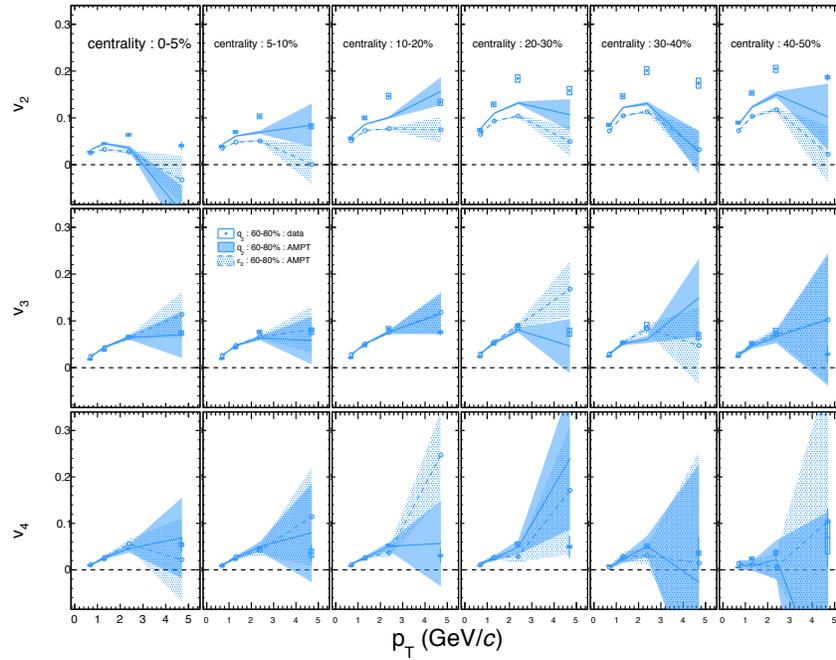
Figure C.5: Azimuthal anisotropy with 60-80 % q_2 or ε_2 selections in 0-50 % centrality in AMPT model.
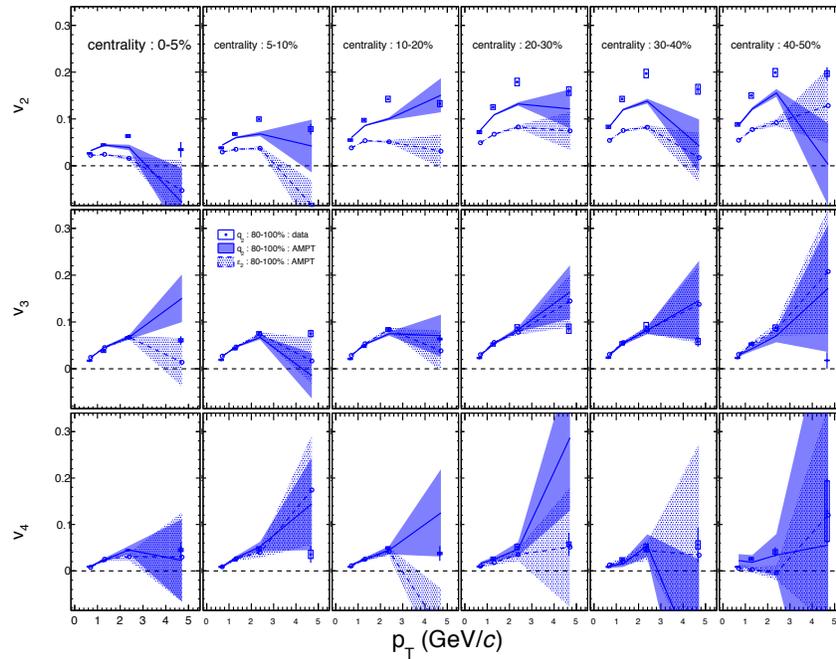
Figure C.6: Azimuthal anisotropy with 80-100 % q_2 or ε_2 selections in 0-50 % centrality in AMPT model.
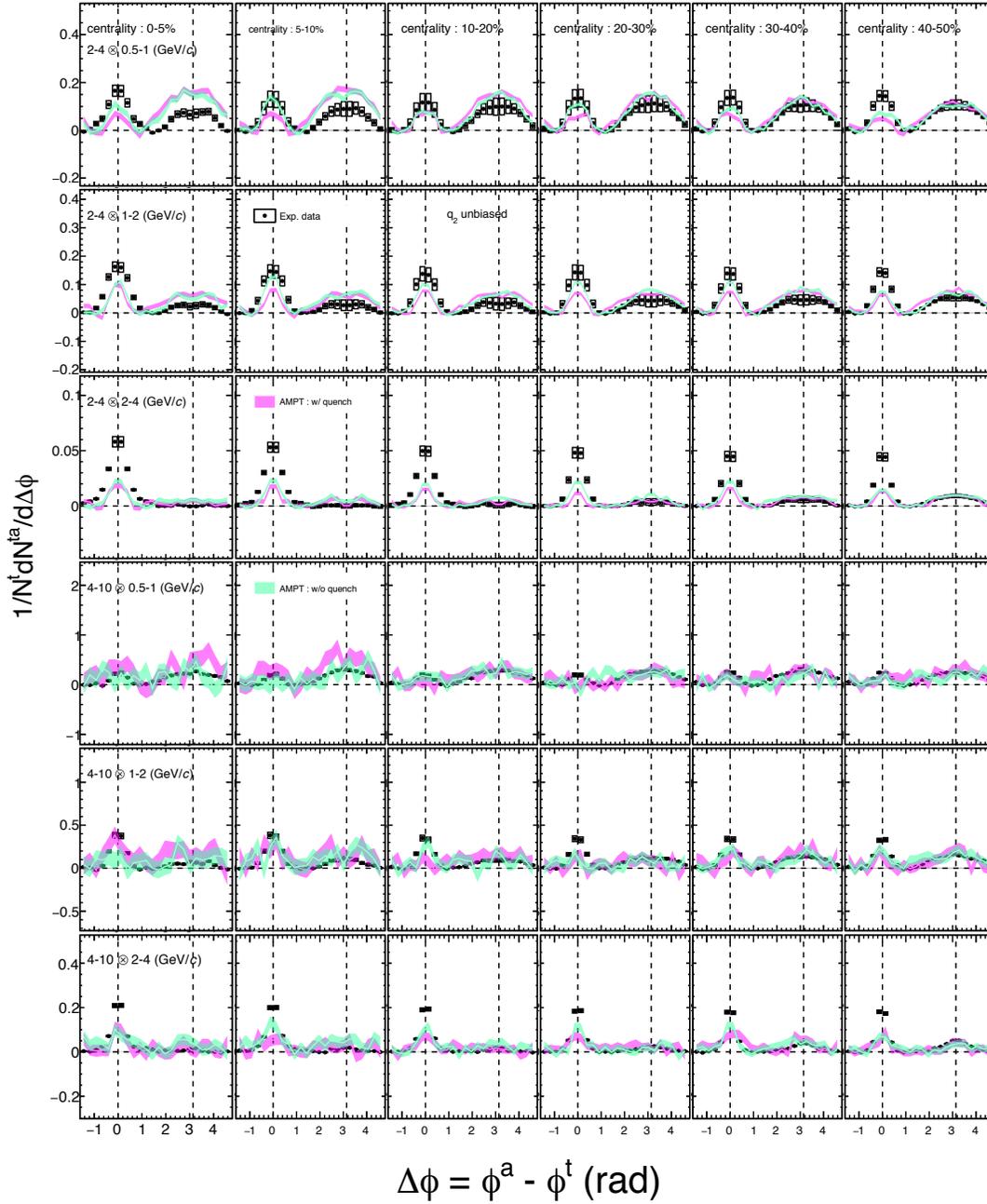
Figure C.7: Azimuthal distribution of correlated yield with various p_T combinations after v_2, v_3 and v_4 contribution subtraction in 0-50 % centrality. Trigger particle's p_T are 2-4 and 4-10 (GeV/c), and associate particle's p_T are 0.5-1, 1-2 and 2-4 (GeV/c).

C.2.2   Event plane dependent two-particle correlations

Fig.C.8 and Fig.C.9 show trigger angle ϕ_s dependence of azimuthal distribution of correlated yield with 2-4 $\otimes$ 0.5-1 and 1-2 (GeV/c) after v_2, v_3 and v_4 contribution subtraction in 0-50 % centrality.

C.2.3 q_2 selections and ε_2 selections

Inclusive triggered correlations

Fig.C.10 and Fig.C.11 show correlations with top and bottom q_2 or ε_2 selections with various p_T combinations in 0-50 % centrality with and without quenching option in AMPT model.

Trigger angle dependence
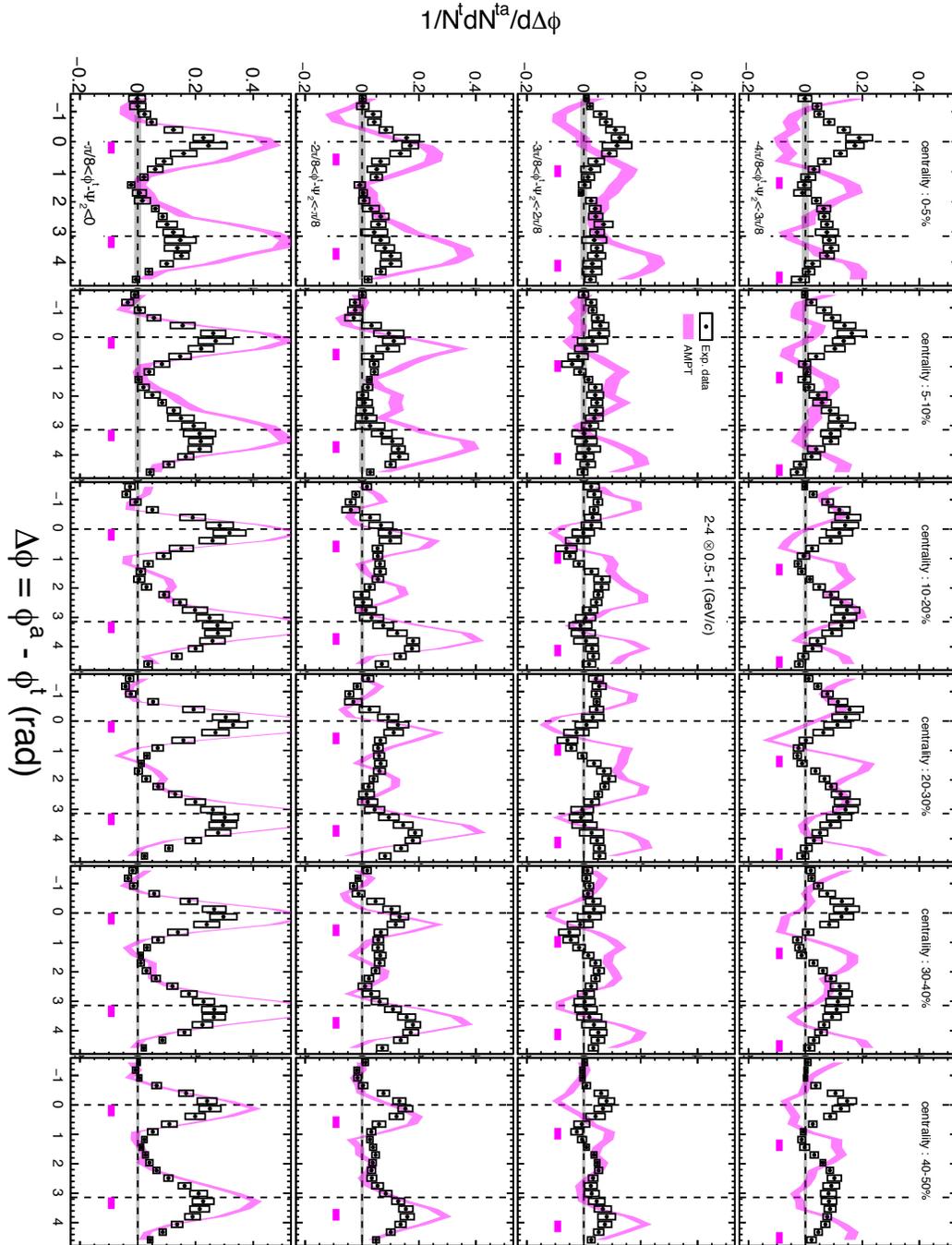
Figure C.8: Trigger angle ϕ_s dependence of azimuthal distribution of correlated yield with 2-4 $\otimes$ 0.5-1 (GeV/c) after v_2, v_3 and v_4 contribution subtraction in 0-50 % centrality.
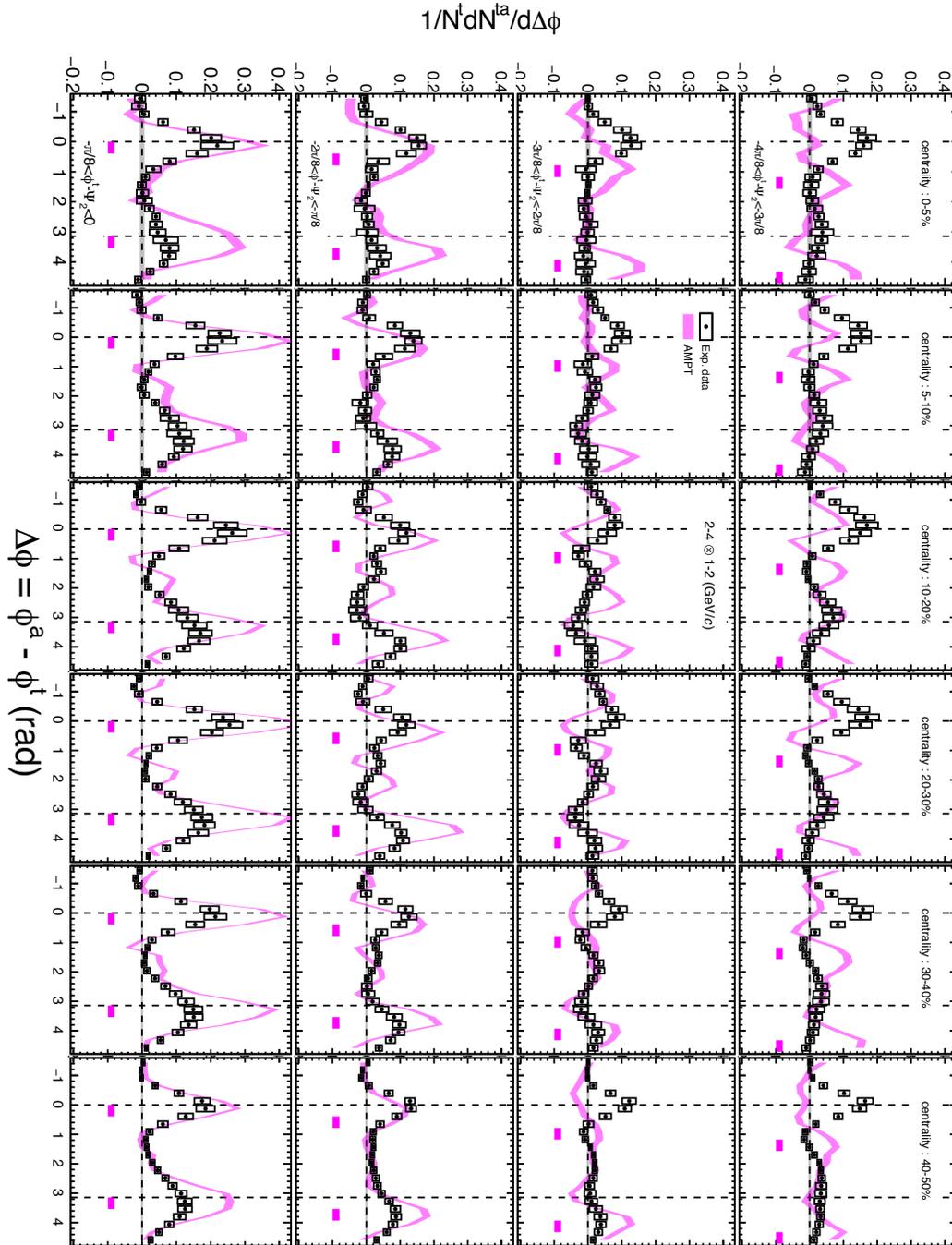
Figure C.9: Trigger angle ϕ_s dependence of azimuthal distribution of correlated yield with 2-4 $\otimes$ 1-2 (GeV/c) after v_2, v_3 and v_4 contribution subtraction in 0-50 % centrality.
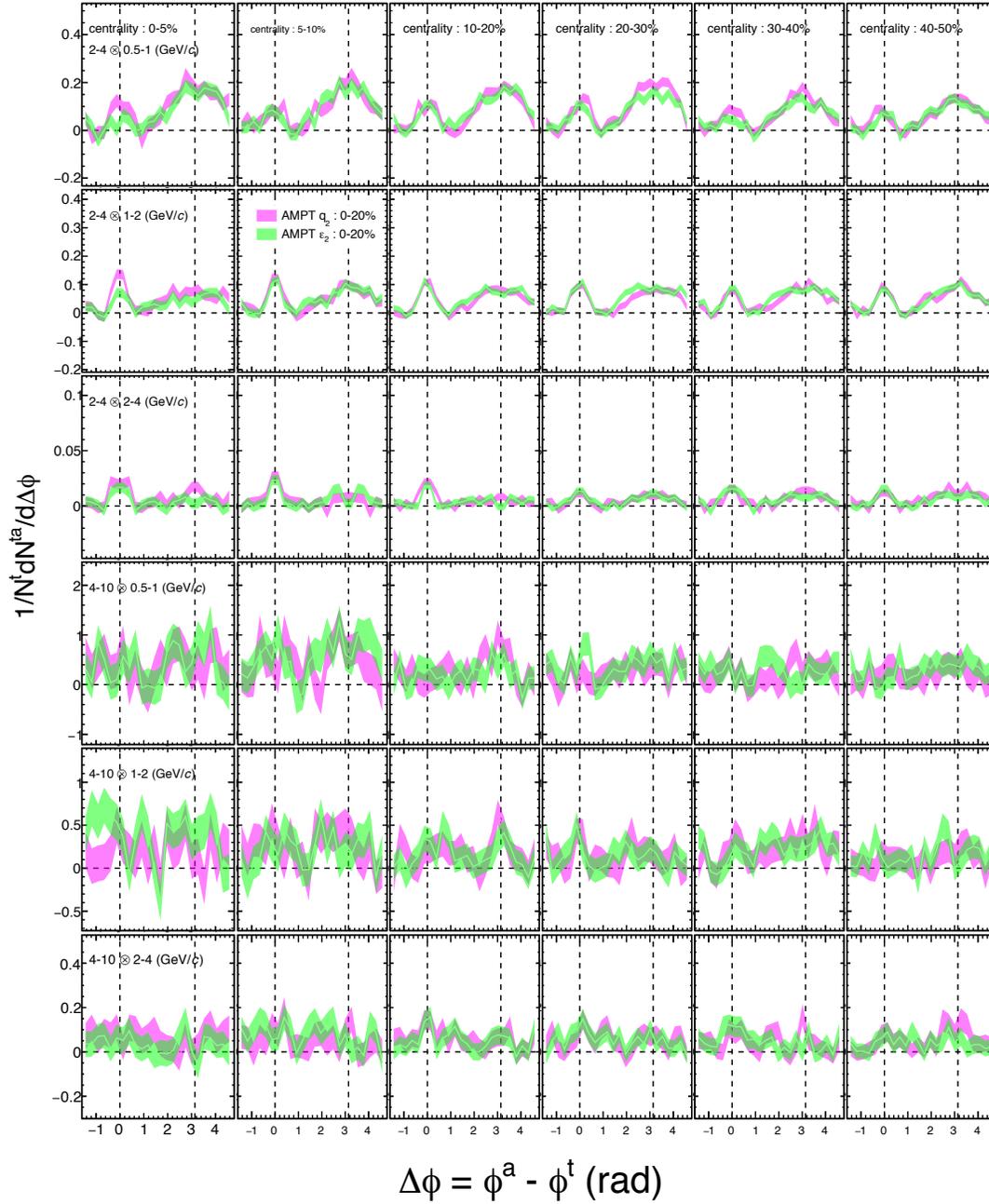
Figure C.10: Azimuthal distribution of correlated yield with various p_T combinations after v_2, v_3 and v_4 contribution subtraction with top q_2 or ε_2 selections in 0-50 % centrality. Trigger particle's p_T are 2-4 and 4-10 (GeV/c), and associate particle's p_T are 0.5-1, 1-2 and 2-4 (GeV/c).
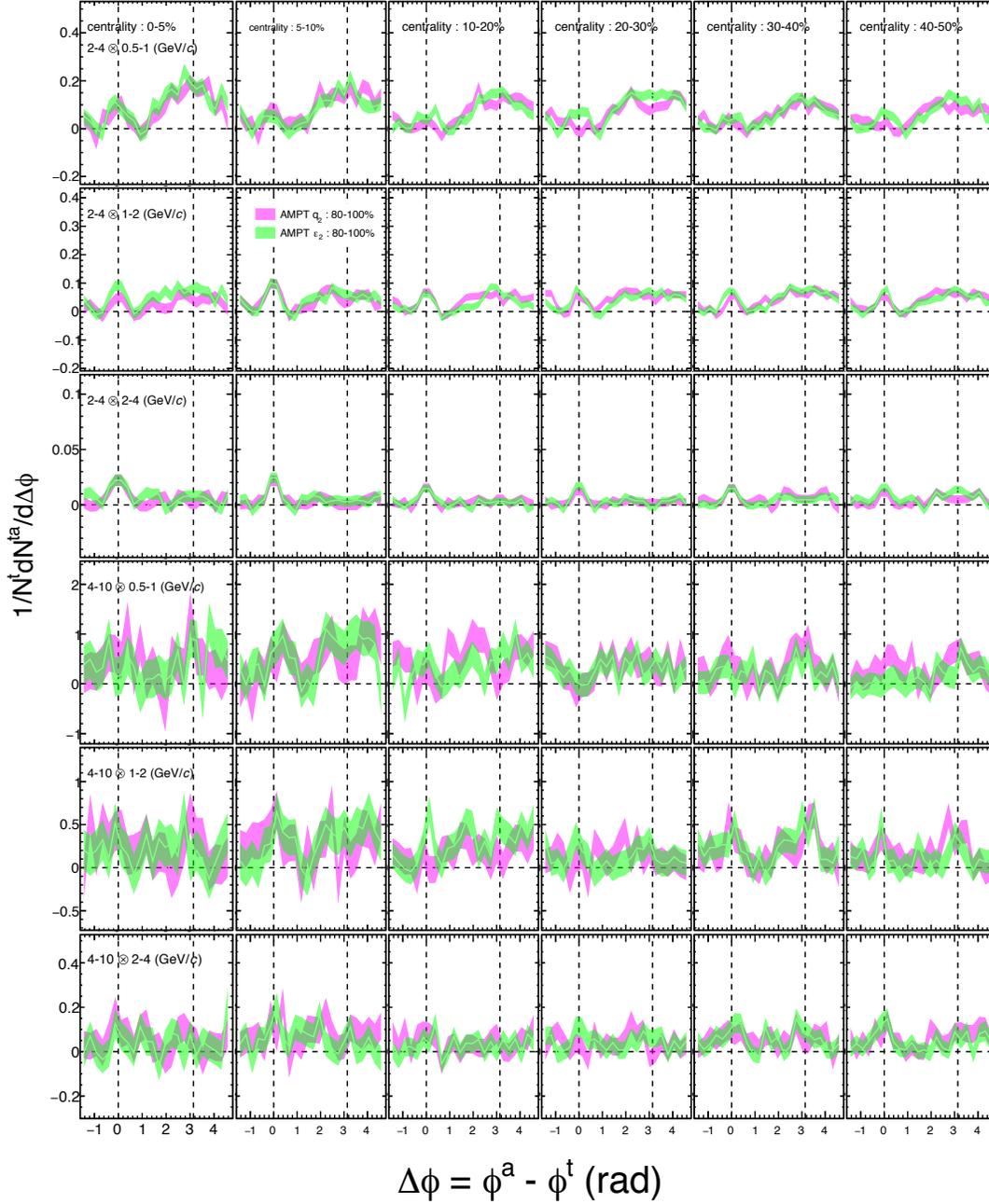
Figure C.11: Azimuthal distribution of correlated yield with various p_T combinations after v_2, v_3 and v_4 contribution subtraction with bottom q_2 or ε_2 selections in 0-50 % centrality. Trigger particle's p_T are 2-4 and 4-10 (GeV/c), and associate particle's p_T are 0.5-1, 1-2 and 2-4 (GeV/c).
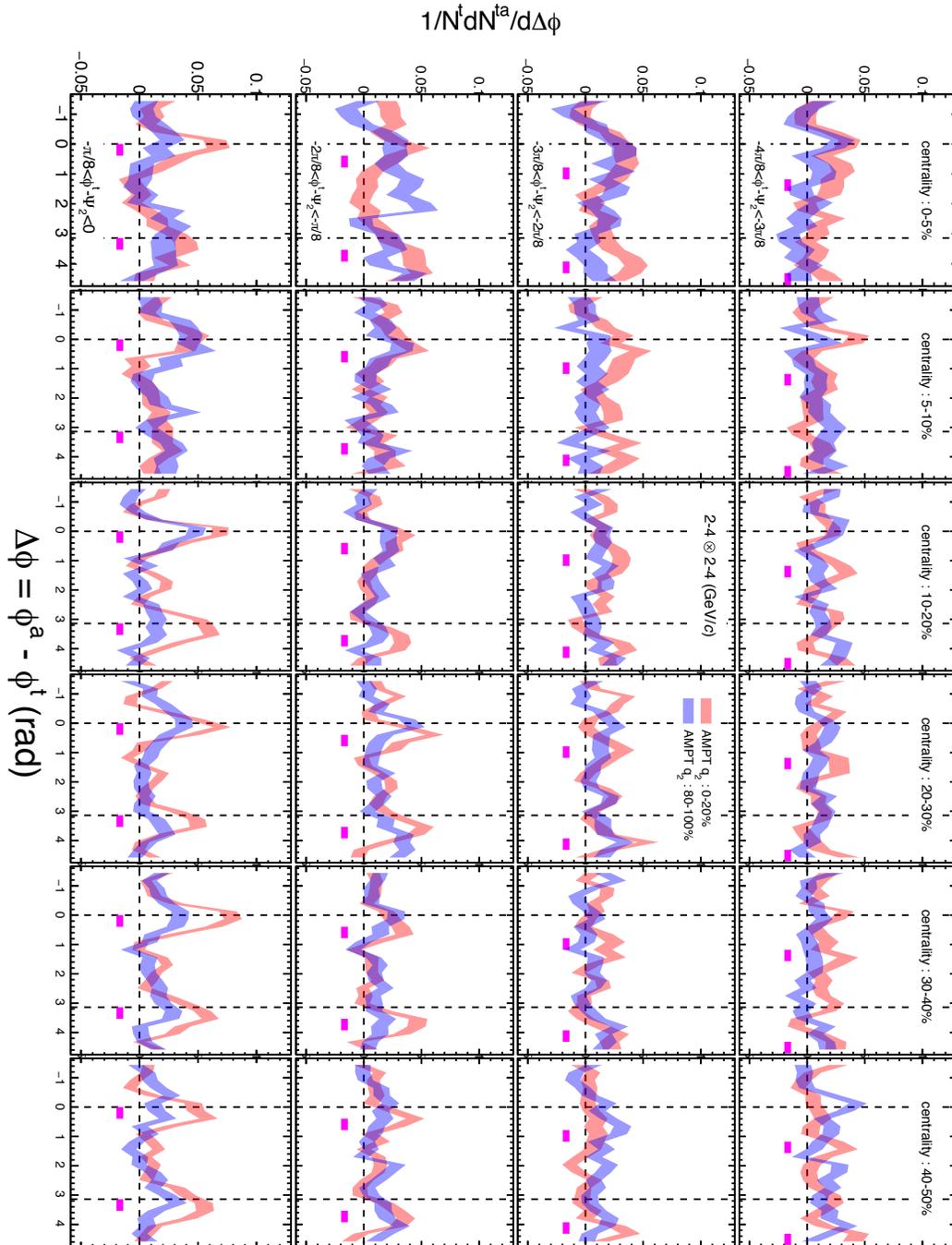
Figure C.12: Trigger angle ϕ_s dependence of azimuthal distribution of correlated yield after v_2, v_3 and v_4 contribution subtraction with top and bottom q_2 20 % selections in 0-50 % centrality. Trigger and associate p_T combination is $p_T^t \otimes p_T^a$ = 2-4⊗0.5-1 (GeV/c).
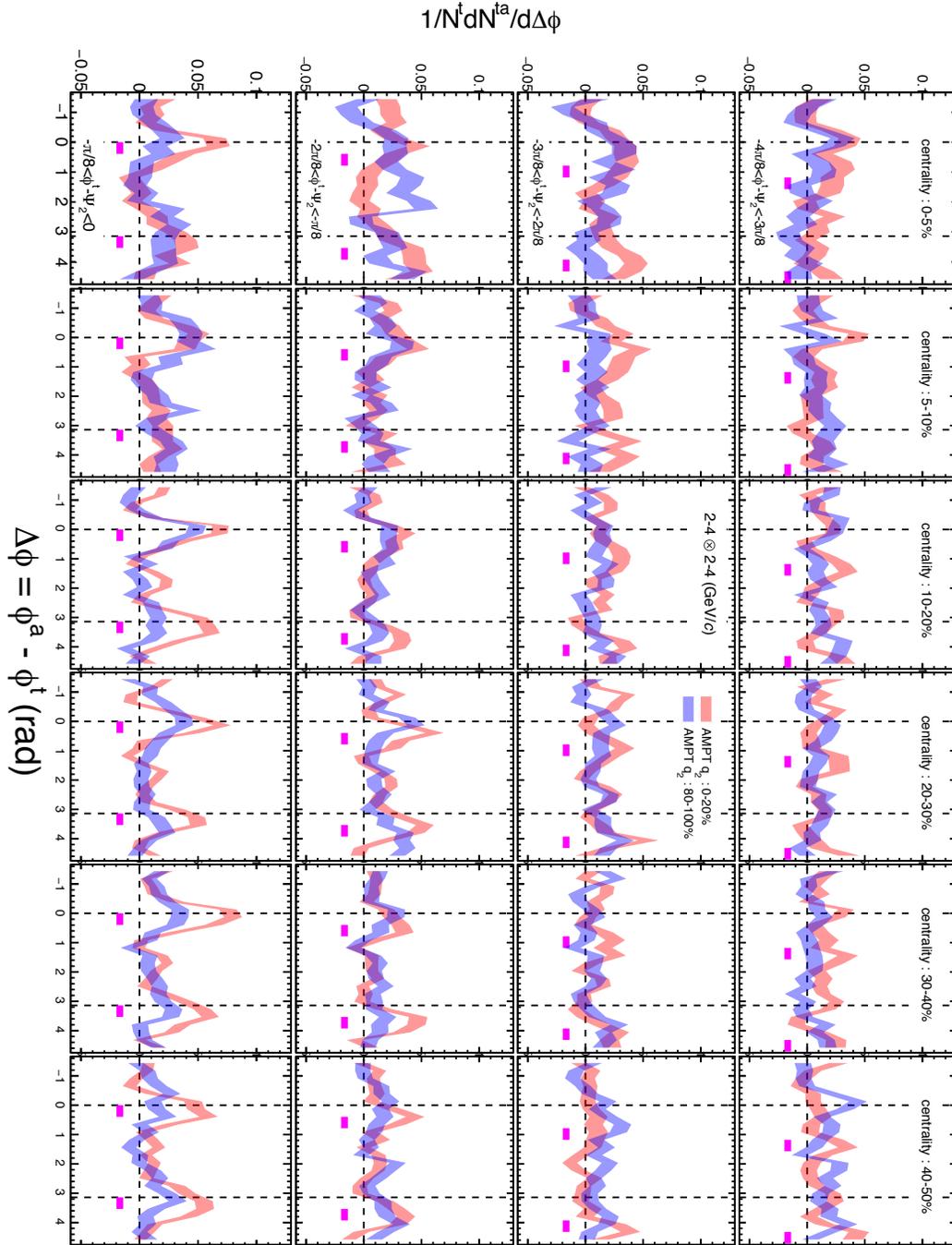
Figure C.13: Trigger angle ϕ_s dependence of azimuthal distribution of correlated yield after v_2, v_3 and v_4 contribution subtraction with top and bottom q_2 20 % selections in 0-50 % centrality. Trigger and associate p_T combination is $p_T^t \otimes p_T^a = $ 2-4$\otimes$2-4 (GeV/c).
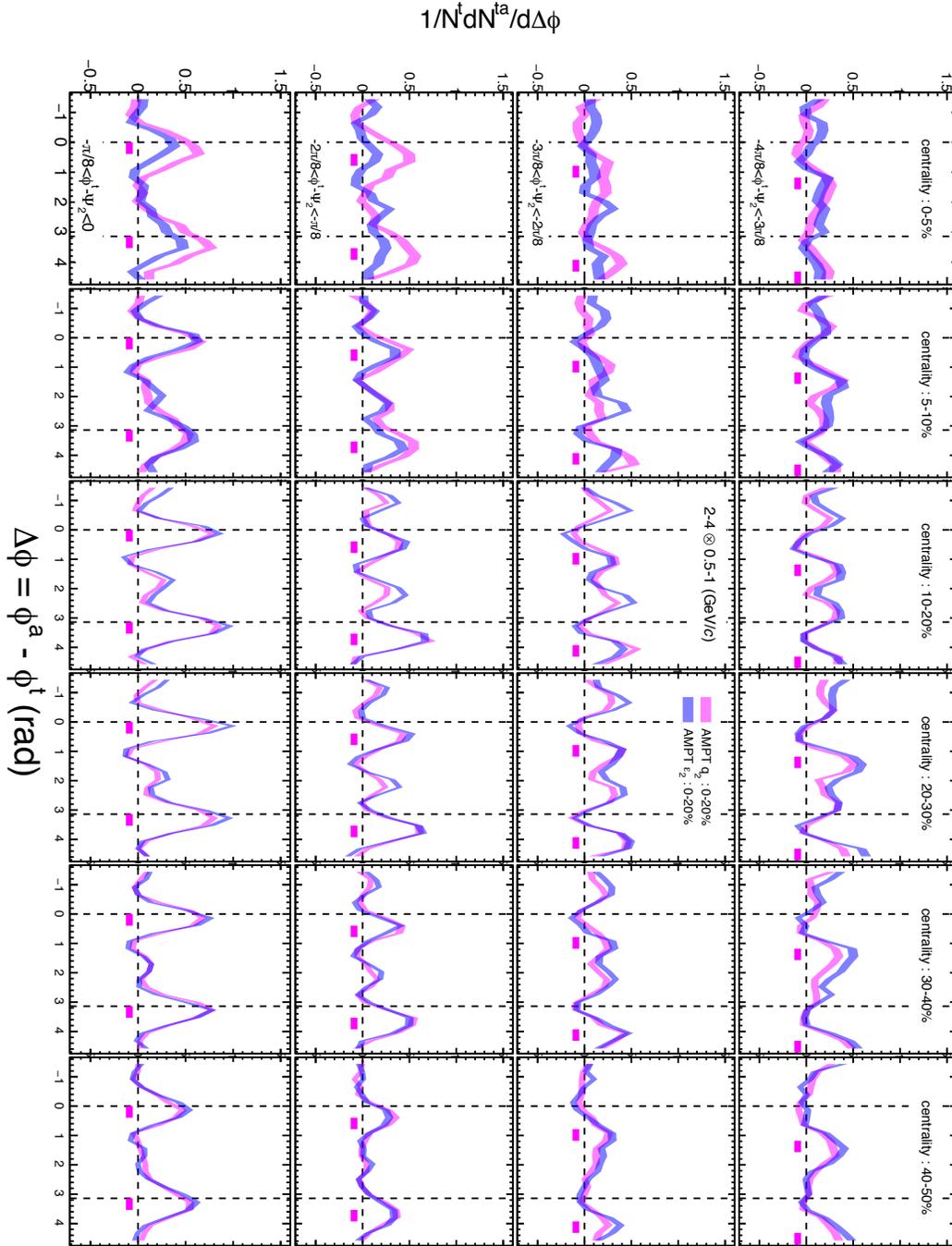
Figure C.14: Trigger angle ϕ_s dependence of azimuthal distribution of correlated yield after v_2, v_3 and v_4 contribution subtraction with top q_2 20 % and top ε_2 20 % selections in 0-50 % centrality. Trigger and associate p_T combination is $p_T^t \otimes p_T^a = $ 2-4$\otimes$0.5-1 (GeV/c).
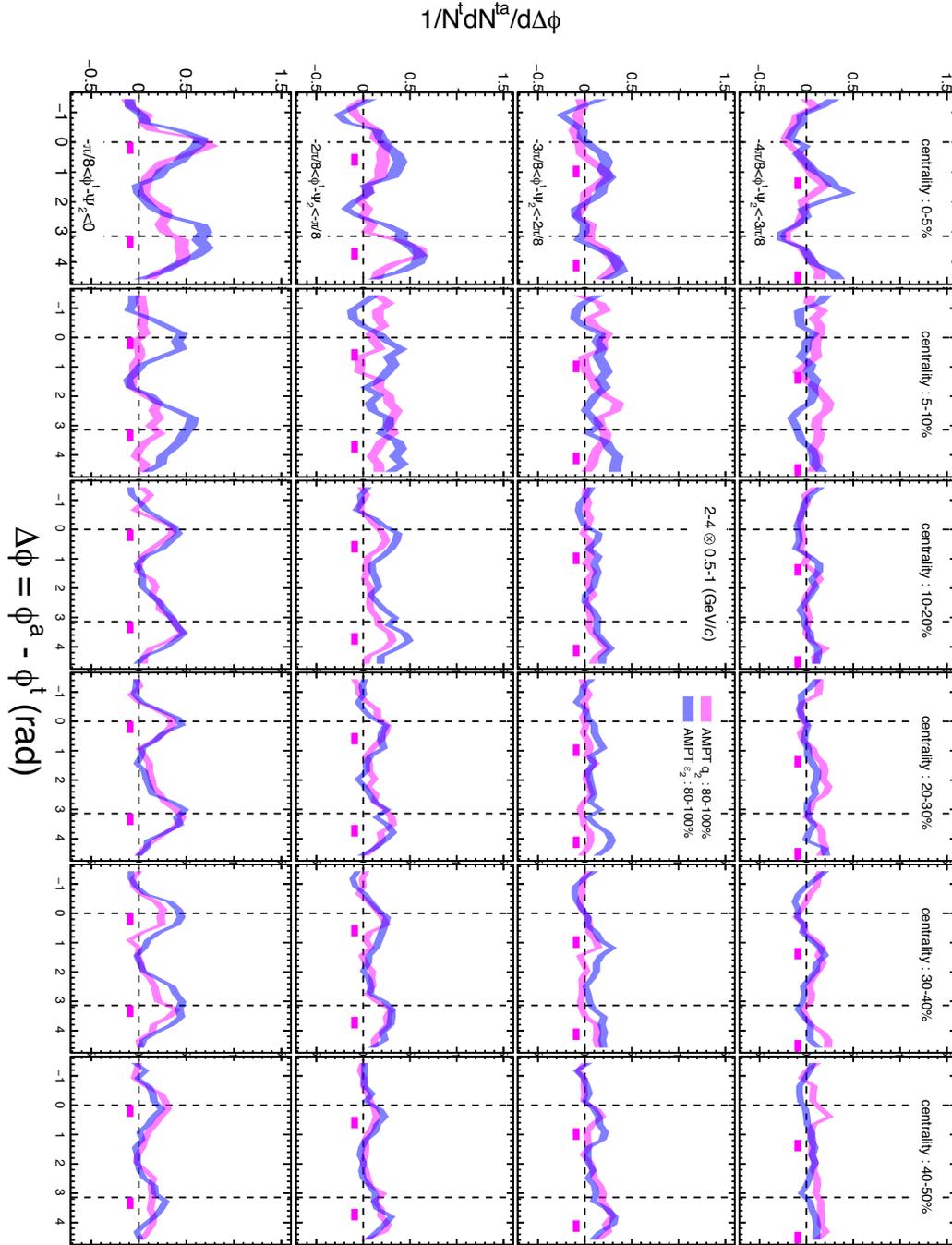
Figure C.15: Trigger angle ϕ_s dependence of azimuthal distribution of correlated yield after v_2, v_3 and v_4 contribution subtraction with bottom q_2 20 % and bottom ε_2 20 % selections in 0-50 % centrality. Trigger and associate p_T combination is $p_T^t \otimes p_T^a = 2\text{-}4 \otimes 0.5\text{-}1$ (GeV/c).
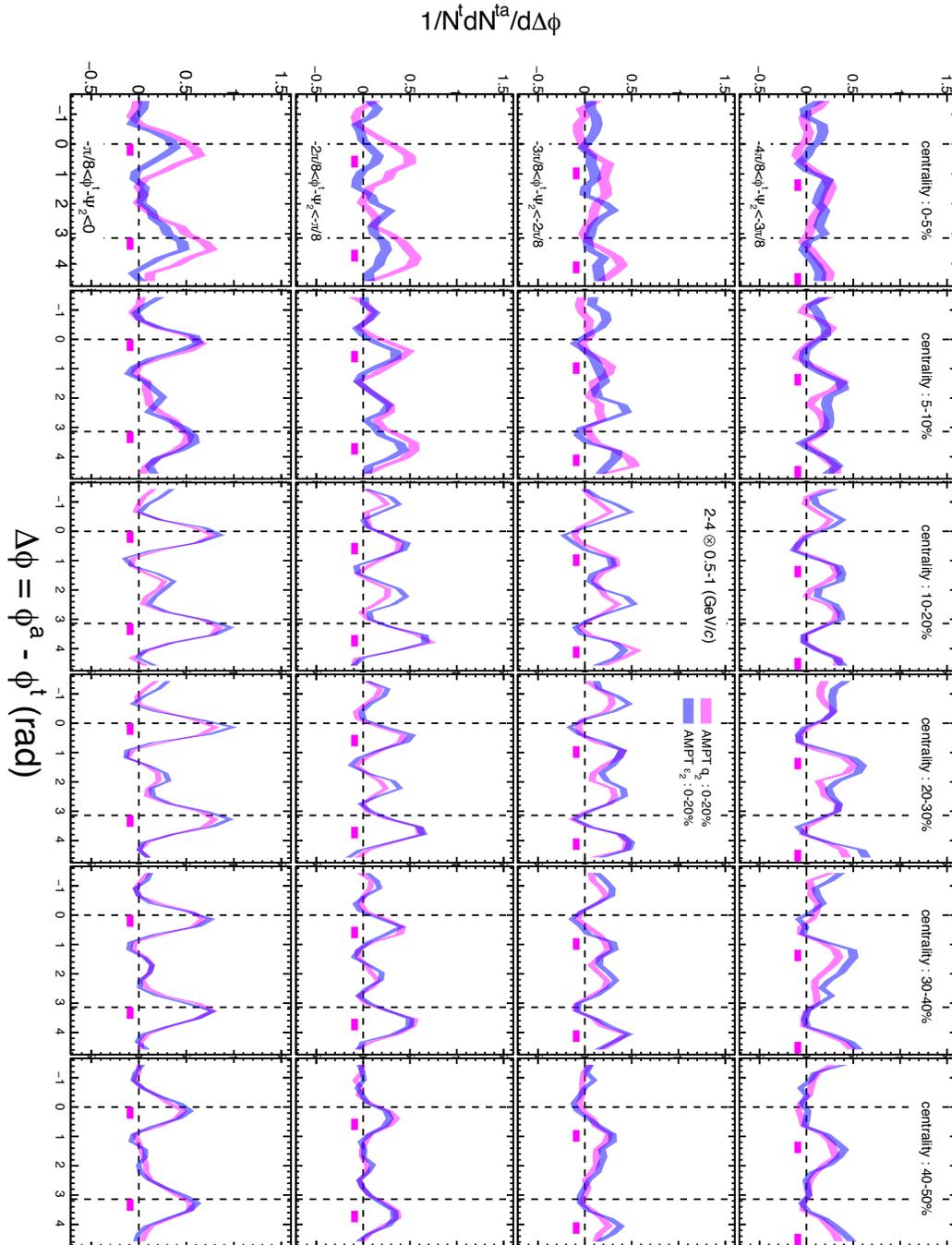
Figure C.16: Trigger angle ϕ_s dependence of azimuthal distribution of correlated yield after v_2, v_3 and v_4 contribution subtraction with top q_2 20 % and top ε_2 20 % selections in 0-50 % centrality. Trigger and associate p_T combination is $p_T^t \otimes p_T^a = 2\text{-}4 \otimes 2\text{-}4$ (GeV/c).
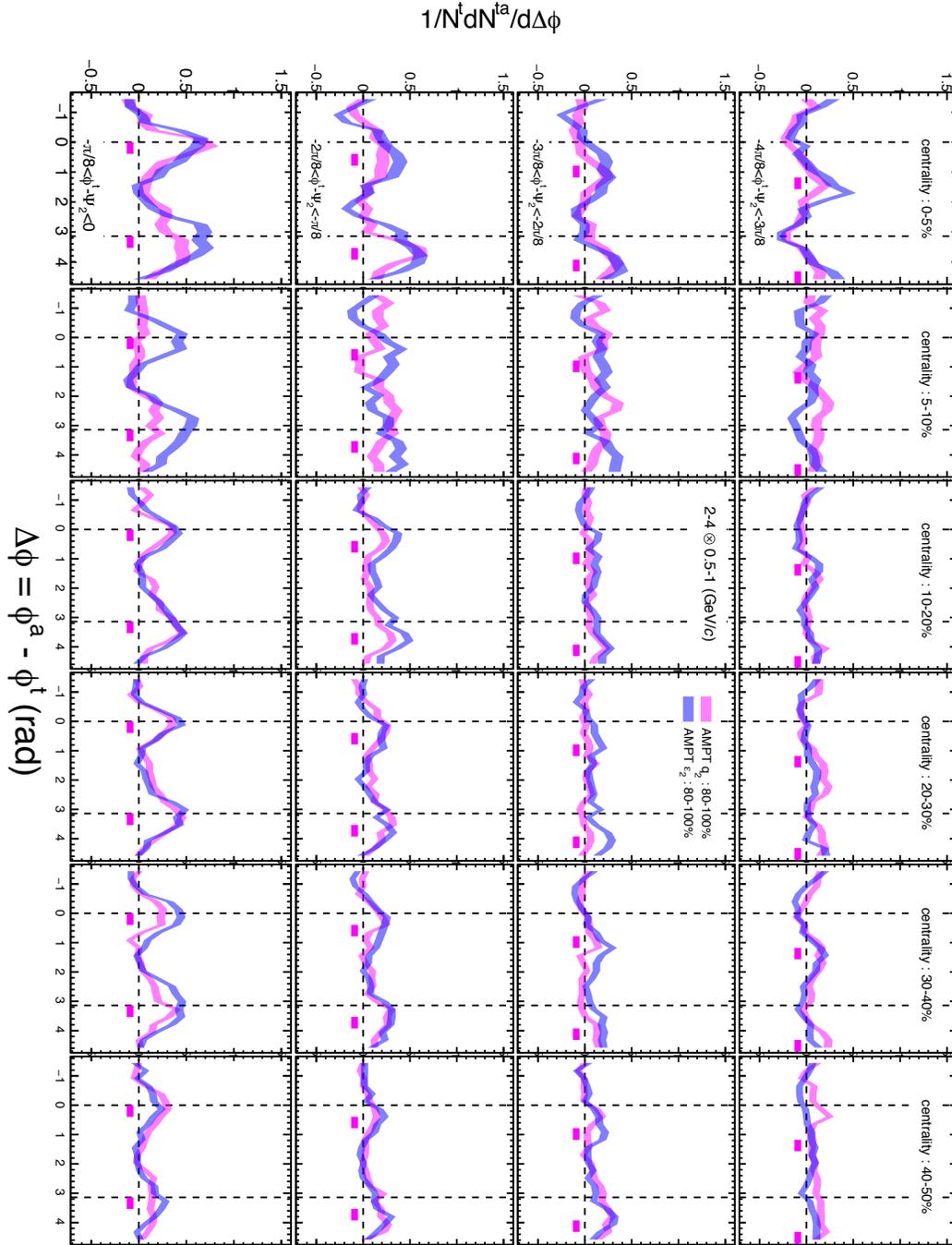
Figure C.17: Trigger angle ϕ_s dependence of azimuthal distribution of correlated yield after v_2, v_3 and v_4 contribution subtraction with bottom q_2 20 % and bottom ε_2 20 % selections in 0-50 % centrality. Trigger and associate p_T combination is $p_T^t \otimes p_T^a$ = 2-4⊗2-4 (GeV/c).

Bibliography

[1] A. B. Arbuzov, "Quantum Field Theory and the Electroweak Standard Model," 2017.

[2] X.-N. Wang, "A pQCD-based approach to parton production and equilibration in high-energy nuclear collisions," *Phys. Rept.* **280** (1997) 287–371.

[3] P. D. Group, "Review of Particle Physics," *Chin. Phy.* **38** (2015) 090001.

[4] T. Ma and S. Wang, "Unified Field Theory and Principle of Representation Invariance," in *Proceedings, 2013 Community Summer Study on the Future of U.S. Particle Physics: Snowmass on the Mississippi (CSS2013): Minneapolis, MN, USA, July 29-August 6, 2013.* 2012.

[5] G. HOOFT, "A PLANAR DIAGRAM THEORY FOR STRONG INTERACTIONS," *Nucl. Phys.* **B 72** (1974) 461–473.

[6] A. A. Migdal, "Loop equations and 1/N expansion," *Physics Reports* **102, 4** (1983) 199–290.

[7] A. Bazavov *et al.*, "Equation of state and QCD transition at finite temperature," *Phys. Rev.* **D80** (2009) 014504.

[8] R. Snellings, "Elliptic Flow: A Brief Review," *New J. Phys.* **13** (2011) 055008.

[9] R. J. Glauber and G. Matthiae, "High-energy scattering of protons by nuclei," *Nucl. Phys.* **B 21** (1970) 135–157.

[10] B. Alver and G. Roland, "Collision geometry fluctuations and triangular flow in heavy-ion collisions," *Phys. Rev.* **C81** (2010) 054905.

[11] J. D. Bjorken, "Highly Relativistic Nucleus-Nucleus Collisions: The Central Rapidity Region," *Phys. Rev.* **D27** (1983) 140–151.

[12] T. Matsui, "Dynamical Evolution of the Quark - Gluon Plasma and Phenomenology," *Nucl. Phys.* **A461** (1987) 27C–48C.

[13] L. D. McLerran and R. Venugopalan, "Gluon distribution functions for very large nuclei at small transverse momentum," *Phys. Rev.* **D49** (1994) 3352–3355.

[14] L. D. McLerran, "The Color glass condensate and small x physics: Four lectures," *Lect. Notes Phys.* **583** (2002) 291–334.

[15] P. F. Kolb and R. Rapp, "Transverse flow and hadrochemistry in Au+Au collisions at $\sqrt{s_{\mathrm{NN}}}$ = 200-GeV," *Phys. Rev.* **C67** (2003) 044903.

[16] **PHENIX** Collaboration, S. S. Adler *et al.*, "Systematic studies of the centrality and $\sqrt{s_{\mathrm{NN}}}$ dependence of the d E(T) / d eta and $dN_{ch}/d\eta$ in heavy ion collisions at mid-rapidity," *Phys. Rev.* **C71** (2005) 034908.

[17] **STAR** Collaboration, J. Adams *et al.*, "Identified particle distributions in pp and Au+Au collisions at $\sqrt{s_{\mathrm{NN}}}$ = 200 GeV," *Phys. Rev. Lett.* **92** (2004) 112301.

[18] **British-Scandinavian-MIT** Collaboration, K. Guettler *et al.*, "Inclusive Production of Low-Momentum Charged Pions at $x = 0$ at the CERN Intersecting Storage Rings," *Phys. Lett.* **64B** (1976) 111–116.

[19] **PHENIX** Collaboration, S. S. Adler *et al.*, "Identified charged particle spectra and yields in Au+Au collisions at $\sqrt{s_{\mathrm{NN}}}$ = 200-GeV," *Phys. Rev.* **C69** (2004) 034909.

[20] **PHENIX** Collaboration, S. S. Adler *et al.*, "Production of phi mesons at mid-rapidity in $\sqrt{s_{\mathrm{NN}}}$ = 200- GeV Au+Au collisions at RHIC," *Phys. Rev.* **C72** (2005) 014903.

[21] J. L. Nagle and M. P. McCumber, "Heavy Ion Initial Conditions and Correlations Between Higher Moments in the Spatial Anisotropy," *Phys. Rev.* **C83** (2011) 044908.

[22] **PHENIX** Collaboration, A. Adare *et al.*, "Measurements of Higher-Order Flow Harmonics in Au+Au Collisions at $\sqrt{s_{\mathrm{NN}}}$ = 200 GeV," *Phys. Rev. Lett.* **107** (2011) 252301.

[23] B. H. Alver, C. Gombeaud, M. Luzum, and J.-Y. Ollitrault, "Triangular flow in hydrodynamics and transport theory," *Phys. Rev.* **C82** (2010) 034913.

[24] B. Schenke, S. Jeon, and C. Gale, "Elliptic and triangular flow in event-by-event (3+1)D viscous hydrodynamics," *Phys. Rev. Lett.* **106** (2011) 042301.

[25] H. Petersen, G.-Y. Qin, S. A. Bass, and B. Muller, "Triangular flow in event-by-event ideal hydrodynamics in Au+Au collisions at $\sqrt{s_{\mathrm{NN}}}$ = 200 A GeV," *Phys. Rev.* **C82** (2010) 041901.

[26] **PHENIX** Collaboration, S. S. Adler *et al.*, "Common suppression pattern of eta and pi0 mesons at high transverse momentum in Au+Au collisions at $\sqrt{s_{\mathrm{NN}}}$ = 200-GeV," *Phys. Rev. Lett.* **96** (2006) 202301.

[27] **PHENIX** Collaboration, A. Adare *et al.*, "Suppression pattern of neutral pions at high transverse momentum in Au + Au collisions at $\sqrt{s_{\mathrm{NN}}}$ = 200-GeV and constraints on medium transport coefficients," *Phys. Rev. Lett.* **101** (2008) 232301.

[28] **STAR** Collaboration, J. Adams *et al.*, "Evidence from d + Au measurements for final state suppression of high p(T) hadrons in Au+Au collisions at RHIC," *Phys. Rev. Lett.* **91** (2003) 072304.

[29] I. Lokhtin and A. Snigirev, "A model of jet quenching in ultrarelativistic heavy ion collisions and high-pt hadron spectra at RHIC," *Eur.Phys.* **C 45** (2006) 211–217.

[30] **STAR** Collaboration, M. M. Aggarwal *et al.*, "Azimuthal di-hadron correlations in d+Au and Au+Au collisions at $\sqrt{s_{NN}}$=200 GeV from STAR," *Phys. Rev.* **C82** (2010) 024912.

[31] V. Greco, C. M. Ko, and P. Levai, "Parton coalescence and anti-proton / pion anomaly at RHIC," *Phys. Rev. Lett.* **90** (2003) 202302.

[32] R. J. Fries, B. Muller, C. Nonaka, and S. A. Bass, "Hadronization in heavy ion collisions: Recombination and fragmentation of partons," *Phys. Rev. Lett.* **90** (2003) 202303.

[33] C. M. K. Rainer J. Fries, Kyongchol Han, "Jet Hadronization via Recombination of Parton Showers in Vacuum and in Medium," *Nucl. Phys. A.* (2016) .

[34] T. Luo, Y. He, X.-N. Wang, and Y. Zhu, "Jet propagation within a Linearized Boltzmann Transport Model," *Nucl. Phys. A932* (2014) .

[35] **STAR** Collaboration, B. I. Abelev *et al.*, "Long range rapidity correlations and jet production in high energy nuclear collisions," *Phys. Rev.* **C 80** (2009) 064912.

[36] **STAR** Collaboration, B. I. Abelev *et al.*, "Indications of Conical Emission of Charged Hadrons at RHIC," *Phys. Rev. Lett.* **102** (2009) 052302.

[37] J. R. Thorsten Renk, "Mach cones in an evolving medium," *Phys. Rev.* **C 73** (2006) 011901.

[38] V. Koch, A. Majumder, and X.-N. Wang, "Cherenkov radiation from jets in heavy-ion collisions," *Phys. Rev. Lett.* **96** (2006) 172302.

[39] L. Pang, Q. Wang, and X.-N. Wang, "Effects of initial flow velocity fluctuation in event-by-event (3+1)D hydrodynamics," *Phys. Rev.* **C86** (2012) 024911.

[40] T. Todoroki, *Measurements of Two-Particle Correlations with respect to Higher-Order Event Planes in $\sqrt{s_{NN}} = 200GeV$ Au + Au Collisions at RHIC-PHENIX*. PhD thesis, University of Tsukuba, 2014.

[41] **PHENIX** Collaboration, A. Adare *et al.*, "Suppression of away-side jet fragments with respect to the reaction plane in Au+Au collisions at $\sqrt{s_{NN}}$=200 GeV," *Phys. Rev.* **C84** (2011) 024904.

[42] **STAR** Collaboration, H. Agakishiev *et al.*, "Event-plane-dependent dihadron correlations with harmonic v_n subtraction in Au + Au collisions at $\sqrt{s_{NN}}$=200 GeV," *Phys. Rev.* **C89** no. 4, (2014) 041901.

[43] **ATLAS** Collaboration, G. Aad *et al.*, "Measurement of the distributions of event-by-event flow harmonics in lead-lead collisions at = 2.76 TeV with the ATLAS detector at the LHC," *JHEP* **11** (2013) 183.

[44] J. Schukraft, A. Timmins, and S. A. Voloshin, "Ultra-relativistic nuclear collisions: event shape engineering," *Phys. Lett.* **B719** (2013) 394–398.

[45] N. Tanaka, *Measurements of Azimuthal Angle Dependence of HBT radii with respect to the event plane in $\sqrt{s_{NN}}$ = 2.76 TeV Pb-Pb collisions at LHC-ALICE*. PhD thesis.

[46] **ALICE** Collaboration, S. Acharya *et al.*, "Constraining the magnitude of the Chiral Magnetic Effect with Event Shape Engineering in Pb-Pb collisions at $\sqrt{s_{NN}}$ = 2.76 TeV," *Phys. Lett.* **B777** (2018) 151–162.

[47] **ALICE** Collaboration, J. Adam *et al.*, "Event shape engineering for inclusive spectra and elliptic flow in Pb-Pb collisions at $\sqrt{s_{NN}}$ = 2.76 TeV," *Phys. Rev.* **C93** no. 3, (2016) 034916.

[48] E. Schnedermann, J. Sollfrank, and U. W. Heinz, "Thermal phenomenology of hadrons from 200-A/GeV S+S collisions," *Phys. Rev.* **C48** (1993) 2462–2475.

[49] **ATLAS** Collaboration, G. Aad *et al.*, "Measurement of the correlation between flow harmonics of different order in lead-lead collisions at $\sqrt{s_{NN}}$ = 2.76 TeV with the ATLAS detector," *Phys. Rev.* **C92** no. 3, (2015) 034903.

[50] M. Luzum and P. Romatschke, "Conformal Relativistic Viscous Hydrodynamics: Applications to RHIC results at $\sqrt{s_{NN}}$ = 200-GeV," *Phys. Rev.* **C78** (2008) 034915.

[51] M. L. Miller, K. Reygers, S. J. Sanders, and P. Steinberg, "Glauber modeling in high energy nuclear collisions," *Ann. Rev. Nucl. Part. Sci.* **57** (2007) 205–243.

[52] H.-J. Drescher, A. Dumitru, A. Hayashigaki, and Y. Nara, "The Eccentricity in heavy-ion collisions from color glass condensate initial conditions," *Phys. Rev.* **C74** (2006) 044905.

[53] "Brookhaven National Laboratory." https://www.bnl.gov/.

[54] "RHIC." https://www.bnl.gov/rhic/.

[55] "U.S. Department of Energy, Nuclear Physics (NP)." https://science.energy.gov/np/.

[56] "PHENIX Collaboration." http://www.phenix.bnl.gov/.

[57] "STAR Collaboration." https://www.star.bnl.gov/.

[58] "PHOBOS Collaboration." https://www.bnl.gov/phobos/.

[59] "BRAHMS Collaboration." http://www4.rcf.bnl.gov/brahms/WWW/.

[60] A. J. et al, *ELECTRON BEAM ION SOURCE PRE-INJECTOR PROJECT (EBIS) CONCEPTUAL DESIGN REPORT*, 2005.

[61] **STAR** Collaboration, M. M. Aggarwal *et al.*, "An Experimental Exploration of the QCD Phase Diagram: The Search for the Critical Point and the Onset of De-confinement," `arXiv:1007.2613 [nucl-ex]`.

[62] M. Anderson *et al.*, "The STAR time projection chamber: A Unique tool for studying high multiplicity events at RHIC," *Nucl. Instrum. Meth.* **A499** (2003) 659–678.

[63] W. L. for the STAR TOF Group, "The large-area time-of-flight upgrade for STAR," *Nuclear Instruments and Methods in Physics Research* **B 241** (2005) 306310.

[64] W. J. Llope *et al.*, "The STAR Vertex Position Detector," *Nucl. Instrum. Meth.* **A759** (2014) 23–28.

[65] C. Adler, A. Denisov, E. Garcia, M. J. Murray, H. Strobele, and S. N. White, "The RHIC zero degree calorimeter," *Nucl. Instrum. Meth.* **A470** (2001) 488–499.

[66] J.-Y. Ollitrault, "Determination of the reaction plane in ultrarelativistic nuclear collisions," *Phys. Rev.* **D48** (1993) 1132–1139.

[67] A. M. Poskanzer and S. A. Voloshin, "Methods for analyzing anisotropic flow in relativistic nuclear collisions," *Phys. Rev.* **C58** (1998) 1671–1678.

[68] C. W. J. for the STAR Collaboration, "The Beam-Beam Counter: A Local Polarimeter at STAR," *AIP Conference Proceedings. 980* (2008) .

[69] Z. Tang, Y. Xu, L. Ruan, G. van Buren, F. Wang, and Z. Xu, "Spectra and radial flow at RHIC with Tsallis statistics in a Blast-Wave description," *Phys. Rev.* **C79** (2009) 051901.

[70] **STAR** Collaboration, L. Adamczyk *et al.*, "Bulk Properties of the Medium Produced in Relativistic Heavy-Ion Collisions from the Beam Energy Scan Program," *Phys. Rev.* **C96** no. 4, (2017) 044904.

[71] Z.-W. Lin, C. M. Ko, B.-A. Li, B. Zhang, and S. Pal, "A Multi-phase transport model for relativistic heavy ion collisions," *Phys. Rev.* **C72** (2005) 064901.

[72] **STAR** Collaboration, J. Adams *et al.*, "Azimuthal anisotropy and correlations at large transverse momenta in p+p and Au+Au collisions at $\sqrt{s_{\mathrm{NN}}} = 200$-GeV," *Phys. Rev. Lett.* **93** (2004) 252301.

[73] J. Jia, S. Esumi, and R. Wei, "Away-side asymmetry of jet correlation relative to reaction plane: A Sensitive probe for jet in-medium modifications," *Phys. Rev. Lett.* **103** (2009) 022301.

[74] **CMS** Collaboration, S. Chatrchyan *et al.*, "Centrality dependence of dihadron correlations and azimuthal anisotropy harmonics in PbPb collisions at $\sqrt{s_{\mathrm{NN}}}=2.76$ TeV," *Eur. Phys. J.* **C72** (2012) 10052.

[75] **PHENIX** Collaboration, S. Afanasiev *et al.*, "High-pT π^0 Production with Respect to the Reaction Plane in Au + Au Collisions at $\sqrt{s_{\mathrm{NN}}}$ = 200-GeV," *Phys. Rev.* **C80** (2009) 054907.

[76] T. H. K. YAGI and Y. MIAKE, *Quark-Gluon Plasma*. CAMBRIDGE UNIVERSITY PRESS, 2005.